Hans Kristian Rusten

Simulation and modelling of hydrogen production by sorption enhanced steam methane reforming in fixed bed reactors

Hans Kristian Rusten

Doctoral Thesis

NTNU
Norwegian University of
Science and Technology

NTNU
Norwegian University of
Science and Technology

NTNU

Hans Kristian Rusten

Simulation and modelling of hydrogen production by sorption enhanced steam methane reforming in fixed bed reactors

Thesis for the degree of philosophiae doctor

Trondheim, April 2010

Norwegian University of
Science and Technology
Faculty of Natural Sciences and Technology
Institute of Chemical Engineering

◼ NTNU
Norwegian University of
Science and Technology

Preface

This work has been carried out at the Department of Chemical Engineering at the Norwegian University of Science and Technology. The work has been financed by the Norwegian Research Council through the KLIMATEK program.

My supervisor Dr. Hugo Jakobsen deserves a thousand thanks for his patience and valuable support, specially for the input to the numerical part of the thesis. The help and work of Dr. De Chen and Dr. Esther Ochoa-Fernández has been invaluable and given me insight into the world of experimental work. Without the experimental work of Esther, the simulations presented in this thesis would not had been possible.

I would also like to thank Håvard Lindborg and Erik Hessen for their contribution to my work.

Thanks to my family and especially my parents for always believing in me, and for my genes.

Also many thanks to friends and the NTNUI B-lag for making the years in Trondheim a great pleasure even outside the office. Last but not least I would like to thank myself for hanging in there, in what has been the most challenging task of my life.

Abstract

An increased demand for hydrogen as energy-carrier and as fuel for clean power generation is expected during the 21st century. The Kyoto-protocol states that the world has to decrease it's CO_2-emissions to the atmosphere. A concept combining hydrogen production and sequestration of CO_2 is the sorption enhanced steam methane reforming (SE-SMR) process. This is an alternative to the traditional steam methane reforming (SMR) for production of hydrogen. SE-SMR is a concept that has received increased attention in recent years. The process utilizes a solid CO_2-acceptor to capture CO_2 in the reforming reactor and thereby change the normal thermodynamic limitations of steam methane reforming.

The work in this thesis has focused on simulation of hydrogen production by sorption enhanced steam methane reforming in a fixed bed reactor. A robust transient one dimensional model has been formulated and implemented for the simulations of the reforming reactor. Three main models have been formulated, one pseudo-homogeneous model and two heterogeneous model that account for intraparticle mass and heat transfer. The two heterogeneous models are different in the way the solid materials are placed in the reactor. The 1-particle model considers one type of pellet in the reactor consisting of both catalytic and sorbent material, while the 2-particle model considers two separate pellet types with catalytic and sorbent material.

Kinetic models for all major reactions must be formulated to simulate the sorption enhanced steam methane reforming reactor. The steam methane reforming reactions have been extensively studied earlier, and the kinetic model of Xiu and Froment was used in the simulations. Different solid synthetic materials for the high temperature CO_2 capture have been studied, and kinetic models for capture of CO_2 on these materials have been formulated in this thesis. Two of the materials, nanocrystalline lithium zirconate and sodium zirconate have been synthesized at NTNU, while the lithium silicate was obtained from Toshiba. The materials synthesized at NTNU showed quite similar kinetic properties, and the capture rate of CO_2 was described by a first order rate reaction with respect to fractional conversion of the solid. However, while the shape of the rate expression was similar

for the two zirconates, the reaction rates did differ substantially. The lithium zirconate had the slowest capture rate of the materials; with a kinetic constant about 100 times lower than the one for sodium zirconate, which showed the fastest kinetics. The capture rate on lithium silicate was found to be between the two other materials.

The reactor simulations of SE-SMR show that it is possible to produce hydrogen with purity above 80 % on a dry basis in a fixed bed reactor with the investigated sorbents. The reactor performance are highly dependent on the capture kinetics and while hydrogen with over 80% purity could be produced with a superficial velocity of 2 m/s and a steam to carbon ratio of 3 with Na_2ZrO_3 as sorbent, a superficial velocity of 0.3 m/s and a steam to carbon ratio of 5 was necessary for Li_2ZrO_3. The performance of Li_4SiO_4 is between these two materials. In all reactor simulations it was found that there will be large temperature gradients in the reactor even if the total reaction is not very endothermic. If a fixed bed reactor is operated without external heating, the temperature close to the inlet will decrease dramatically, while the outlet temperature will increase. This means that temperature control could be necessary during hydrogen production, and that heating/cooling not only has to be supplied during regeneration.

The results from the reactor simulations have been incorporated in computer simulations of the whole process of producing pure hydrogen by SE-SMR. Sorption enhanced reforming, regeneration of sorbent, heating and cooling of the reactor bed, CO_2 compression, H_2 purification by presure swing adsorption, and heat integration of the process are the main parts of the hydrogen production process. The data on regeneration has been limited and the process sizing and performance is mainly based on the reforming being the limiting factor. The efficiency is very dependent on the amount of heat that must be supplied to the reactor in the regeneration step and the CO_2-sorption kinetics of the sorbent. A thermal efficiency of 0.71 was calculated for an SE-SMR process with Na_2ZrO_3 as sorbent with a gas velocity of 2 m/s, a 10 m long reactor, a pressure of 10 bar, a reforming temperature of 848 K and a steam to carbon ratio of 3. The heat for regeneration was in this case supplied by combustion of methane in pure oxygen and yielded high CO_2 removal ($\approx 100\%$). The thermal efficiency is comparable and better than for autothermal reforming with CO_2 removal by an amine process.

The temperature of regeneration used for Li_2ZrO_3 as sorbent were only 52 °C higher than the reforming temperature, while it was 325 °C higher for Na_2ZrO_3. When Li_2ZrO_3 replaced Na_2ZrO_3 as CO_2-acceptor, the lower temperature increase for regeneration, which lead to less heat supplied, did make up for some of the disadvantages of Li_2ZrO_3, but in total the slower kinetics make it a less promising sorbent for SE-SMR. With all other parameters equal the thermal efficiency fell from 0.71 to 0.67 when using Li_2ZrO_3 as acceptor instead of Na_2ZrO_3. At the

same time the cross-section area of the reactor had to be increased almost 10 times to get the throughput that was necessary to have equal production of hydrogen. Producing hydrogen with a total lower heating value of 700 MW the necessary reactor cross-sectional area was about 20 m^2 for the simulation with Na$_2$ZrO$_3$ as sorbent, while the necessary crossectional area for Li$_2$ZrO$_3$ were 173 m^2.

The possibility of not producing pure hydrogen, but a mixture of hydrogen and methane by SE-SMR with Na$_2$ZrO$_3$ as sorbent has also been investigated. With the low conversion of methane, the CO$_2$-capture simulated for this process was only 62 % when the methane content in the product is calculated as CO$_2$-equivalents. The thermal efficiency of this process was about 0.83, compared to the 0.71 for the case with pure hydrogen as product. If the kinetics of CO$_2$-sorption could be increased, giving higher hydrogen content in the product, an increased CO$_2$ removal can be reached without lowering the thermal efficiency.

vi

List of publications and presentations

Publications

The thesis is partly based on the following articles published in peer-reviewed journals, where the two first are enclosed in appendix B.

I H. K. Rusten, E. Ochoa-Fernández, D. Chen, and H. A. Jakobsen. Numerical investigation of sorption enhanced steam methane reforming using CO_2 as CO_2-acceptor. *Industrial & Engineering Chemistry Research*, 46(13):4435–4443, 2007

II H. K. Rusten, E. Ochoa-Fernández, H. Lindborg, D. Chen, and H. A. Jakobsen. Hydrogen production by sorption-enhanced steam methane reforming using lithium oxides as CO_2-acceptor. *Industrial & Engineering Chemistry Research*, 46:8729–8737, 2007

III E. Ochoa-Fernández, H. K. Rusten, H. A. Jakobsen, M. Rønning, A. Holmen, and D. Chen. Sorption enhanced hydrogen production by steam methane reforming using Li_2ZrO_3 as sorbent: Sorption kinetics and reactor simulation. *Catalysis Today*, 106:41–46, 2005

Presentations

A list of oral and poster presentation that have been given in relation to the work in this thesis is given below.

- E. Ochoa-Fernández, T. Grande, H. K. Rusten, H. A. Jakobsen, A. Holmen, M. Rønning, and D. Chen. Novel solid high temperature CO_2 absorbents for the production of H_2 by sorption enhanced steam reforming. EuropaCat-VII;, August 2005

- E. Ochoa-Fernández, H. K. Rusten, M. Rønning, A. Holmen, H. A. Jakobsen, and D. Chen. H_2 production by CO_2 sorption enhanced steam methane reforming. gas-fuel 05. Oral presentation, 14-16 November 2005

- H. K. Rusten, E. Ochoa-Fernández, D. Chen, E. T. Hessen, and H. A. Jakobsen. Modeling and simulation of sorption enhanced hydrogen production. the second trondheim conference on CO_2 capture, transport and storage. Oral presentation, 10-11 October 2005

- E. Ochoa-Fernández, T. Zhao, G. Haugen, H. K. Rusten, M. Rønning, H. A. Jakobsen, and D. Chen. Application of CO_2 sorption enhanced hydrogen production with CO_2 removing: precombustion in power generation. the third trondheim conference on CO_2 capture, transport and storage. Oral presentation, 10-11 October 2005

- H. K. Rusten, E. Ochoa-Fernández, D. Chen, E. T. Hessen, H. Lindborg, and H. A. Jakobsen. Modelling and simulation of sorption enhanced hydrogen production. 8th international conference on greenhouse gas control technologies (GHGT-8). Oral presentation, 19-22 June 2006

- E. Ochoa-Fernández, G. Haugen, T. Zhao, H. K. Rusten, J.-P. Andreassen, M. Rønning, H. A. Jakobsen, I. Aartun, B. Børresen, E. Rytter, M. Rønnekleiv, and D. Chen. Design, preparation and applications of CO_2 acceptors in power generation with CO_2 management. 12th international conference on greenhouse gas control technologies, GHGT-8. Oral presentation, 19 - 22 June 2006

- H. K. Rusten, E. Ochoa-Fernández, D. Chen, and H. A. Jakobsen. Heterogeneous and pseudo-homogeneous reactor models with solution of the velocity-pressure coupling for simulation of sorption enhanced steam reforming. 17th international congress of chemical and process engineering CHISA. Oral presentation, 27-31 August 2006

- H. K. Rusten, E. Ochoa-Fernández, C. De, and H. A. Jakobsen. Modelling and simulation of hydrogen production by sorption enhanced steam reforming; integration of catalyst and adsorbent. ISCRE 19 - 19th international symposium on chemical reaction engineering. Oral presentation, 3-6 September 2006

Contents

List of Figures

List of Tables

List of symbols

Roman

Symbol	Description	Units
a_v	surface area of particles	1/m
A	area	m^2
C	concentration	mol/m^3
C_p	heat capacity	J/mol K
d	diameter	m
d_t	diameter of reactor tube	m
D	dispersion factor or diffusivity	m^2/s
E	Arrhenius activation energy	J/mol
f	friction factor	-
h	bulk-particle heat transfer coefficient	W/m K
$-\Delta H$	heat of reaction	J/kg
J	mass flux vector	kg/m^2
k	Mass transfer coefficient	m/s
K	constant in capture kinetics	1/s
L	length of reactor	m
$\dot{m}$	mass flux	$kg/m^2 s$
n	constant in capture kinetics	-
p	pressure	Pa
q	mass of CO_2 per mass of acceptor	-
Q	heat	W
r	radius , or reaction rate of components	m or kg/kg s
R	reaction rate or gas constant	kg/m^3 or J/K mol
S	component mass source term	$kg/m^3 s$
S'	heat source term	$J/m^3 s$
t	time	s
T	temperature	K
u	superficial gas velocity	m/s

Symbol	Description	Units
v	gas velocity vector	m/s
V	Volume	m^3
w	mass	kg
$\dot{w}$	mass flow	kg/s
x	fractional conversion	-
y	mole fraction	-
z	axial position	m

Greek

Symbol	Description	Units
α	ratio between volume of acceptor and catalyst	-
ε	void fraction	-
η	thermal efficiency or effectiveness factor	-
λ	conductivity	J/m s
μ	viscosity	Pa s
ρ	density	kg/m^3
τ	tortuosity	-
ω	mass fraction	-

Subscripts

Symbol	Description
b	bed
cap	capture, CO_2-acceptor
cat	catalyst
eq	equilibrium
f	feed
g	gas
i	component i
m	molar
max	maximum
p	particle
s	solid
w	wall
z	axial direction

Superscripts

Symbol	Description
d	dry
s	surface

Chapter 1

Introduction

1.1 Global warming and CO_2-capture

The intergovernmental climate panel's (IPCC) report Climate Change 2007 states that "Most of the observed increase in globally-averaged temperature since the mid 20th century is very likely due to the observed increase in anthropogenic GHG (green-house gas) concentrations".[7] Among the anthropogenic green-house gases, which mainly includes methane, nitrous oxide, carbon dioxide and fluoride compounds, CO_2 is the most important. Of the total emissions, CO_2 has a share of 76.7 % estimated in CO_2-equivalents and 74 % of this comes from the use of fossil fuel. From pre-industrial times (1750) the CO_2-concentration in the atmosphere has increased from about 280 ppm to 379 ppm (2005). It is acknowledged that a decrease in the world's CO_2 emissions is necessary to decrease and ultimately reverse the global warming due to anthropogenic green-house gas emissions. The importance of this work was underlined by the presentation of Al Gore and the IPCC as winners of the 2007 Nobel Peace Prize.

Different strategies can be employed to mitigate the CO_2-emissions, and as the world shows no desire to reduce its energy consumptions other strategies should be investigated. One strategy is carbon capture and storage. Fossil fuels is the main energy source in the world and by capturing carbon from the hydrocarbons and store it, less CO_2 will be emitted to the atmosphere. CO_2-sequestration processes can be divided into three main categories.

- **Post-combustion** systems separate the CO_2 from the combustion flue gas. This is the most mature CO_2-removal technology in the world and chemical absorption is the dominating process. CO_2 is absorbed in a liquid, typically an amine-solution, and by heating the amine solution the pure CO_2 is stripped off. Other possibilities for post-combustion systems are the use of solid sorbents and membranes.

- **Pre-combustion** systems separate out the carbon from the fuel before the combustion. This is done by converting the fuel into hydrogen and carbon dioxide and/or carbon monoxide. This produces a high energy carbon free fuel (hydrogen) which can be used both for large power generation facilities and smaller mobile units which will only emit water.

- **Oxy-fuel** systems use pure oxygen for the combustion of natural gas and with mainly CO_2 and water as the combustion products this minimizes the need for downstream separation equipment. The disadvantage is that large volumes of expensive pure oxygen are needed and that combustion in pure oxygen yields very high temperatures.

For the carbon sequestration to have any meaning, the CO_2 has to be stored in a closed environment which is secure for a long timescale. The primary possibility for this is to store it underground and the concept is already well proven. Three large scale industrial projects are presently in operation; the Sleipner project in Norway, the Weyburn project in Canada and the In Salah project in Algeria.[48] Depleted oil fields are suitable places for CO_2-storage because of the cap rock in these formations. CO_2 can also be injected in oil fields that are still in operation to maintain the pressure and thereby enhance the oil recovery (EOR).

1.2   The hydrogen economy

Hydrogen is by many viewed as the energy carrier for the future.[1] Today the use of hydrogen is mainly for ammonia/urea and methanol production and for hydrogenation of heavy hydrocarbons. About 95% of the current global hydrogen production is made and consumed on the same site in these chemical processes. This is expected to change dramatically, as hydrogen moves from being primary a reagent in production of other chemicals to being an energy carrier. This change is foreseen because hydrogen has several properties which makes it an attractive fuel:

- It has a high lower heating value per mass, 2.4, 2.8 and 4 times higher than methane, gasoline and coal, respectively.

- Combustion of hydrogen does not lead to CO_2-emissions or in the case of low temperature fuel cells, no nitrous oxide, sulphur dioxide or carbon monoxide.

- Fuel cells have high energy efficiency compared to traditional combustion ($\sim 50\%$, with a possibility to reach 60% vs. 20-38 % for internal combustion[46])

- Compared to electricity it can be stored without significant losses.

Although there are strong initiatives to make hydrogen the fuel of the future, there are several obstacles to overcome. Storage is a key issue for the use of hydrogen in the transport sector. As a gas the volume is far too large for practical use, hence it has to be pressurized or stored in other ways. Currently pressurized tanks at 350-700 atm permit storage of liquid H_2 but is very expensive ($\sim$ $ 3000/kgH$_2$).[46] The transport of pure hydrogen also pose a large explosion risk and other options for storage, such as storage in solid materials, seems to be necessary for moving units. Another obstacle on the road towards a hydrogen economy is that the fuel cell technology is not mature enough to compete with internal combustion. Technology breakthrough is needed to reduce the price, and improve the reliability and cost.[1]

For the production of hydrogen several different processes is possible and they are shown in table 1.1, and it is expected that a combination of these technologies will be used for the worlds hydrogen demand. It has to be pointed out that, in any scenario, hydrogen is an energy carrier, like electricity, and not an energy source. It has to be converted from natural hydrogen sources, typically hydrocarbons or water, and when reacting with oxygen by the exothermic reaction 1.1 it can be returned to nature as water.

$$H_2 + \frac{1}{2}O_2 \rightarrow H_2O \quad \Delta H_{298} = -286kJ/mol \tag{1.1}$$
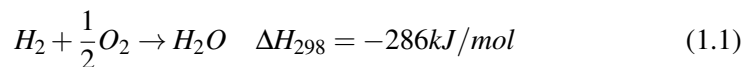
When the earth's fossil fuel reserves dries out, both the energy and the hydrogen must come from other sources, but during a slow transition to the hydrogen society reforming of natural gas will have to play a major role. The price of hydrogen produced from natural gas is still much lower than from other sources and the economics is the major driving force in industrial processes.[48]

Table 1.1: Summary of hydrogen production technologies

Hydrogen production technology	Description
Electrolysis	Water is split to hydrogen and oxygen in an electrolytic cell
Reforming and gasification	Natural gas is converted to hydrogen and carbon dioxide, or higher hydrocarbons and coal can be gasified using oxygen.
Biomass	Biological materials such as corn, sugar canes, sunflower and sawmill residues are transformed to hydrogen and CO_2. Biomass is called CO_2-neutral since it contributes to small net CO_2-emissions.
Thermochemical cycles	Using waste heat from nuclear reactors one can use a cycle involving e.g. sulphur and iodine compounds to extract hydrogen from water.
Biological production	Algae or bacteria can produce hydrogen from water

1.3 Steam methane reforming

Steam methane reforming (SMR) is the prevailing process for hydrogen production and accounts for more than half of the world production.[49] Natural gas is fed to a reactor with excess of steam, and with methane as the main component in natural gas, the main reactions in steam methane reforming are:

$$CH_4 + H_2O \leftrightarrow CO + 3H_2 \quad \Delta H_{298} = 206 kJ/mol \tag{1.2}$$

$$CO + H_2O \leftrightarrow CO_2 + H_2 \quad \Delta H_{298} = -41 kJ/mol \tag{1.3}$$
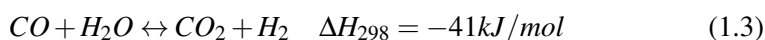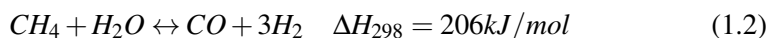
Equation (1.2) is the reforming reaction and equation (1.3) is the water-gas shift reaction.

In conventional SMR the hydrogen and CO/CO_2 are produced over a nickel catalyst at high temperatures. The catalyst is contained in reformer tubes, which are located in a box type fired furnace, where combustion of natural gas provides the heat. To get high conversions high temperatures are needed, and the conversion is favoured by low pressure. A high steam-to-carbon (S/C)-ratio will increase the conversion of methane but decreases the energy efficiency of the process and higher volumetric flow will increase the equipment cost. Typical operation temperatures for SMR are 800-950 °C, a pressure of 20-40 bar and S/C-ratio about 2.5. An overview of the steps in an SMR-process with CO_2- capture is shown in figure 1.1
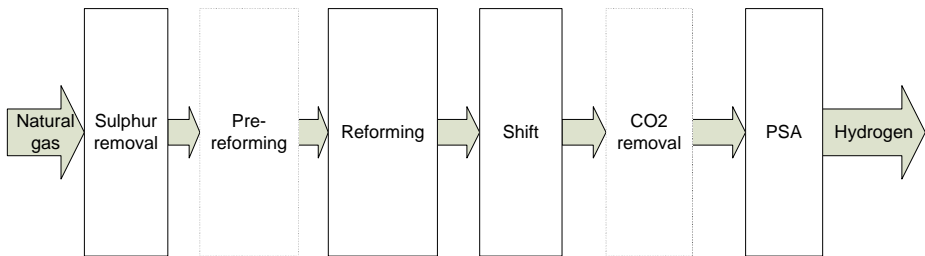
Figure 1.1: An overview of the steps in an SMR-process with CO_2-capture and hydrogen purification by pressure swing adsorption(PSA).

If the natural gas contain sulphur compounds, a pre-treating of the gas is necessary to remove the sulphur which deactivates the reforming catalyst. After the pre-treatment some processes uses a pre-reformer where heavier hydrocarbons are converted to methane. The main reforming reactions are carried out in the fired reformer where methane is converted to mainly hydrogen, carbon monoxide and carbon dioxide. Equation (1.3) is thermodynamically favoured at low temperatures and the high temperature reformer is followed by one or usually two shift reactors operated at lower temperatures, typically 300-500 °C, to convert CO and steam to hydrogen and CO_2. To get pure hydrogen a pressure swing adsorption (PSA) unit can be installed. If CO_2 sequestration is to be employed this is done before the PSA and can be done by an amine process.

Autothermal reforming and partial oxidation

Other routes to hydrogen production by converting natural gas are autothermal reforming (ATR) and partial oxidation (POX). Partial oxidation utilizes reaction

1.4 for the production of hydrogen:

$$CH_4 + 0.5O_2 \leftrightarrow CO + 2H_2 \quad \Delta H_{298} = -38 kJ/mol \tag{1.4}$$
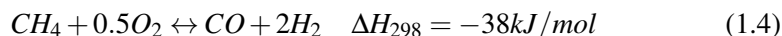
The reaction can be carried out with or without a catalyst at high temperatures (1250-1400 °C). As with SMR the gas is cooled, shifted (1.3) and CO_2 removed from the mixture after the high temperature reformer. The efficiency of POX is lower than for SMR, because less hydrogen is extracted from water, but the range of fuels that can be processed is much wider as it also can be used for hydrogen production from coal and heavy hydrocarbons.[48]

Autothermal reforming is a combination of partial oxidation and steam methane reforming. Steam, natural gas and oxygen are fed to the reactor, and the energy needed for the reforming reactions is provided by combustion of natural gas. This is done in a burner upstream to the catalytic section of the reactor, and typical reactor temperatures are 950 - 1050 °C. Because all the energy is supplied internally in the reactor the expensive furnace for the SMR is not needed, which can make ATR more cost-effective than traditional SMR. The oxygen can be supplied either by air or by pure oxygen. Pure oxygen requires an expensive air-separation-unit, but if CO_2 sequestration is wanted, combustion with pure oxygen can make the expensive amine-absorption unit obsolete.

Hydrogen purification

The hydrogen purity from the different production routes are typically 70-80% and for applications as fuel cells higher purity hydrogen is required. This process is usually performed in a pressure-swing adsorber (PSA). The PSA operates at 1-60 bar and at high pressure the impurities CO, CO_2, CH_4, etc adsorbs at a solid material, e.g. activated carbon, zeolite or silica gel, and an essentially pure hydrogen stream is produced. At a lower pressure, typically ambient or sub-atmospheric, the adsorbed species are desorbed and the PSA tail gas produced. The tail gas from the PSA-unit in a steam methane reforming process is mainly consisting of methane and un-separated hydrogen and this gas can be combusted for heat supply to the process. Typical PSA-processes consist of 4 to 16 beds dependent on the flow rate,[62] and H_2-recovery of 80-90% is possible with today's technology and the purity of the product hydrogen is typically ~99.999%.[74]

1.4   Scope of the work

Sorption enhanced steam methane reforming (SE-SMR) is an emerging technology for hydrogen production with CO_2-capture. The traditional steam methane reforming is modified by installing a CO_2 acceptor in the reactor bed together with

the catalyst. The CO_2 is thus captured in situ and the thermodynamical limitations of the process changed. Pure hydrogen can be produced for use in fuel cells or combustion turbines. To gain insight in the process and how it can be optimized, reactor modelling can be a useful tool. By describing the reactor mathematically it can be simulated under different operating conditions and one can observe the effect in changing different paramaterers. The goal of this work has been to describe a fixed bed reactor with reactor models, both heterogeneous, where the intra-particle transport is modelled, and pseudo-homogeneous where the reactor species concentrations and temperatures are averaged over the solid and the gas. The heterogeneous models can be used to study if the gas-partical mass transfer and/or the intraparticle mass transfer is a limiting step in the process and affectivity factors can be found and used in the less time-consuming pseudo-homogeneous models. The reactor models should be robust, e.g. tolerate large variations in operating conditions, be fast and accurate. Contrary to most other chemical processes mass is removed from the gas-stream in SE-SMR, and this has to be taken special care of in the modelling. For simulations of chemical reactors, the reaction kinetics is an important piece, and the kinetics have to be described matematically for the reactor simulations. The kinetics of the reforming reactions in SMR has been studied intensively and are well formulated, but in SE-SMR the CO_2-capture kinetics must be described and this has to be done specifically for each sorbent. By analyzing experimental data of uptake of CO_2 on the acceptors under different conditions it is possibile to descibe the capture process mathematically, and these expressions can be used in the reactor simulations. Different materials can be used as CO_2-acceptor but the main focus in this work has been on novel synthetic metal oxide CO_2-acceptors. When all the kinetic expressions are in place, the reactor models are used to simulate the chemical reactor performance and the possible conversions that can be achieved under different conditions can be studied. These results are also important in the sizing of a real reactor system, where the necessary space times to get the wanted conversions can be found. The goal of this work has been to study the performance of fixed bed reactors with different materials as CO_2 acceptors.

The performance of the reactors can then be used for simulations of the process of producing hydrogen by sorption enhanced steam methane reforming, and how the process is dependent of the properties of the CO_2 acceptor can be evaluated. By doing this, the thermal efficiency and the CO_2 capture for the process at different conditions can be studied.

1.5   Outline of the thesis

In *chapter 1* the motivation and some of the background for this thesis have been described.

Chapter 2 describes the sorption enhanced steam methane reforming technology, and the published literature on the subject is presented.

Chapter 3 describes the CO_2-capture kinetics for the materials Li_2ZrO_3, Li_4SiO_4, and Na_2ZrO_3, and mathematical relations are fitted to experimental data.

Chapter 4 describes the reactor models used to model the fixed bed SE-SMR reactor. One pseuso-homogenous model and different heterogeneous models are presented. All relations for the parameters used in the models are given, and the solution method for the set of partial differential equations is shown.

Chapter 5 presents the results of the reactor simulations on SE-SMR fixed bed reactors. It is divided in results from simulations with Li_2ZrO_3, Li_4SiO_4 and Na_2ZrO_3 as CO_2-acceptor.

Chapter 6 presents the results from process simulations of the SE-SMR process, and thermal efficiencies for the process are reported. Process design and sizing of reactors are also looked into.

Chapter 7 gives the conclusions and the proposed further work.

Chapter 2

Sorption enhanced steam methane reforming

2.1 Thermodynamics of SMR

The traditional steam methane reforming is a mature technology with high energy efficiency and relatively low capital investment. However, the reaction thermodynamics requires severe operating conditions for high conversion of methane. The reforming reaction is thermodynamically favoured at high temperatures, hence temperatures above 900 °C are necessary to get high conversion of methane. High temperature together with high concentrations of CO also leads to problems with coking in the reactor, which can lead to lower catalyst efficiency, higher pressure drops and in a worst case scenario, blocking of the reactor. Equilibrium methane conversion calculated from the equilibrium constants from Twigg[78] for SMR at 20 bar as function of temperature and steam to carbon - ratio is shown in figure 2.1. To reach conversions of 80-90 % at low S/C-ratios (2-3), it is seen that temperatures above 900 °C is needed. Low S/C-ratios give higher thermal efficiencies, hence SMR-processes are usually designed for S/C-ratios of about 2.5. Equilibrium dry hydrogen mole fractions that correspond to the methane conversions in figure 2.1 are shown in figure 2.2. As seen in figure 2.2, hydrogen purities just above 0.7 can be reached for a S/C - ratio of 2.5 at 900 °C. By using shift reactors at lower temperatures the hydrogen content can be increased, but the methane conversion will be almost unchanged. SMR produces a net amount of moles, hence low total pressures favours high conversion. However, to get lower investment costs total pressures in the range of 20-40 bar are common. Figure 2.3 shows the equilibrium conversion of methane as function of temperature and total pressure at a S/C-ratio of 3.

Up until today CO_2-sequestration has not been a main issue in the develop-
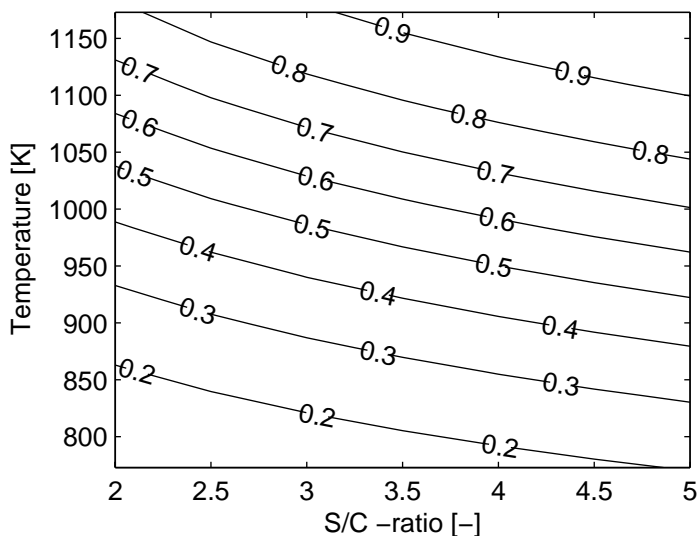
Figure 2.1: Contour plot of equilibrium SMR-conversion as function of temperature and S/C-ratio.

ment of hydrogen production processes, but with the increased awareness on global warming, this is an issue that has to be addressed. Simbeck states that hydrogen production from fossil fuels with CO_2-capture is the essential bridge to the hydrogen economy.[73] One possible process for hydrogen production with CO_2-capture is enhanced steam methane reforming.

2.2   Enhancing the SMR

The concept of sorption enhanced reaction processes is not new, and Rostrup-Nielsen[63] reports that du Motay and Marechal proposed to add a CO_2-acceptor to hydrocarbon steam reforming as early as 1868. However, the process has not received big attention until the last 20 years and first and foremost in this decade. Bruun-Tsekhevoi et al.(1988) described a continuous process using dolomite as sorbent[12], and Han and Harrison (1994) used calcium oxide to capture CO_2 in a fixed bed reactor[22]. Air products developed a process in the 1990s they called sorption enhanced reaction process (SERP).[26,82] Sorption enhanced reaction process or more precisely sorption enhanced steam methane reforming (SE-SMR) utilises a solid CO_2 acceptor, typically a metal oxide, to capture CO_2 in situ and thereby change the thermodynamical limitations.

$$MO(s) + CO_2(g) \leftrightarrow MCO_3(s) \tag{2.1}$$
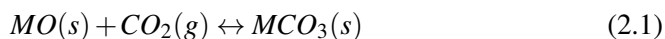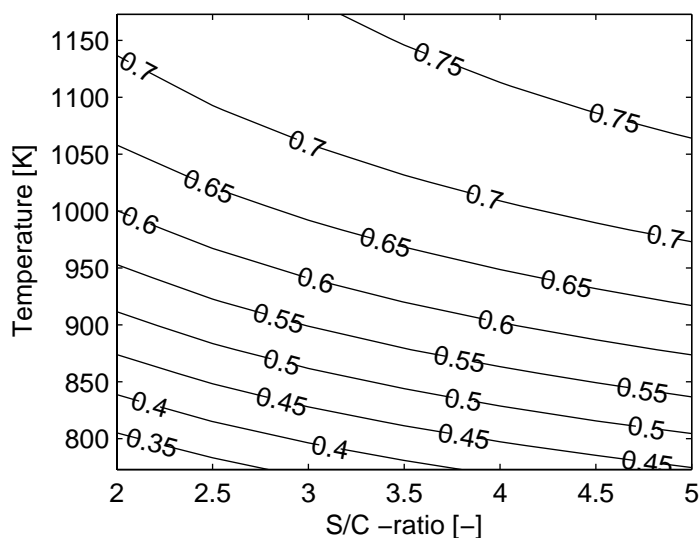
Figure 2.2: Contour plot of equilibrium dry hydrogen mole fraction as function of temperature and S/C-ratio at a pressure of 20 bar.

The total reaction for SMR, reforming reaction + water-gas shift, is:

$$CH_4(g) + 2H_2O(g) \leftrightarrow CO_2(g) + 4H_2(g) \tag{2.2}$$
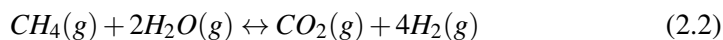
Combining equation (2.2) and equation (2.1) the total reaction for SE-SMR is:

$$CH_4(g) + 2H_2O(g) + MO(s) \leftrightarrow 4H_2(g) + MCO_3(s) \tag{2.3}$$
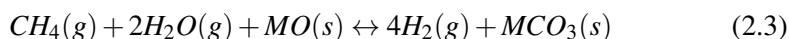
By removing CO_2 from the gas phase, the equilibrium limitations changes as described by le Chateliers principle and the reactions yield more hydrogen. This means that hydrogen can be produced at lower temperatures and with CO_2-capture in one step. The lower temperatures and the low partial pressures of CO_2 also make shift reactors redundant. Figure 2.4 shows the equilibrium methane conversion at 20 bar and a S/C-ratio of 3 as a function of temperature and partial pressure of CO_2. The equilibrium compositions is calculated from the equilibrium constants given by Twigg.[78] The CO_2 equilibrium partial pressure over CaO is also shown in figure 2.4, and it is observed that a conversion of about 0.75 can be reached at ∼600 °C in SE-SMR with CaO as CO_2-acceptor. At the same conditions the conversion of SMR is only just above 0.3 and to reach a conversion of 0.75 a temperature of about 800 °C is needed. With lithium zirconate as acceptor a conversion of 0.45 is possible. This observation shows that low partial pressures of CO_2 are necessary at these conditions for high conversions, and the equilibrium partial pressure
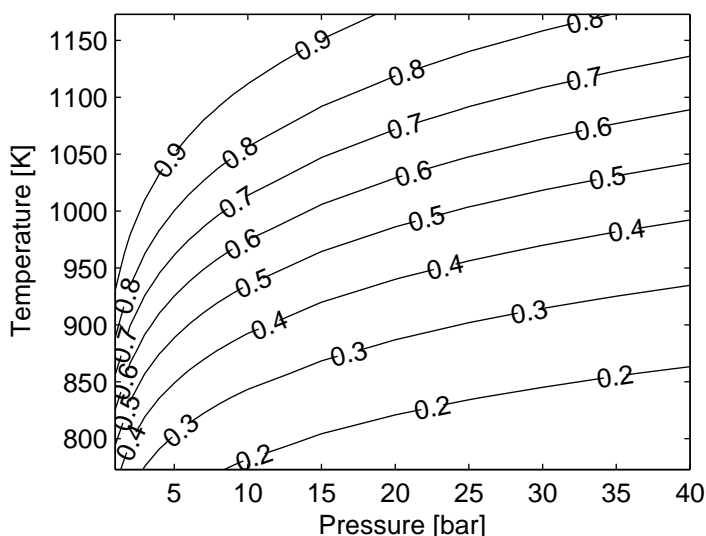
Figure 2.3: Contour plot of equilibrium SMR-conversion as function of temperature and pressure at a S/C-ratio of 3.

of CO_2 on CaO at 600 °C corresponds to a mole fraction of only 150 ppm. The equilibrium CO-fraction at these conditions is about 100 ppm.

The equilibrium dry hydrogen mole fraction at the same conditions is shown in figure 2.5: It is observed that a dry hydrogen mole fraction of 0.92 can be reached at a temperature of 600°C at these conditions with CaO as acceptor. For lithium zirconate a dry hydrogen mole fraction of 0.75 is possible, still significantly higher than the corresponding equilibrium SMR dry hydrogen mole fraction of about 0.52. Because high hydrogen purity is possible in one reactor with SE-SMR, the shift reactors that are used in SMR are not necessary.

The high hydrogen and low CO-content together with the lower temperature in SE-SMR also minimizes coking, which can be a serious problem in SMR. The total enthalpy of the reforming section of SE-SMR will be slightly endothermic or energy-neutral, dependent of the CO_2-acceptor, but the total energy requirements of the reactors will be the same as for SMR. The solid acceptor has to be regenerated, hence the heat gained from the exothermic capture must be supplied in the endothermic regeneration.
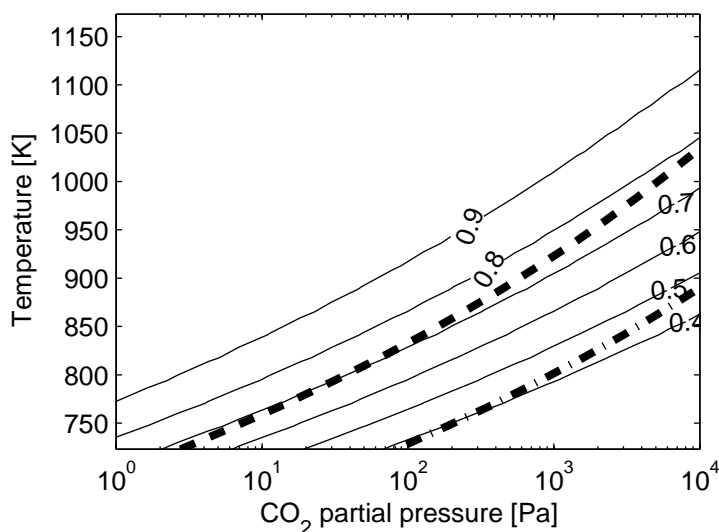
Figure 2.4: Contour plot of equilibrium SE-SMR-conversion as function of temperature and partial pressure CO_2 at a total pressure of 20 bar, the equilibrium partial pressure of CO_2 over CaO[25] (— —) and the equilibrium partial pressure of CO_2 over Li_2ZrO_3[33] (— · —) is also shown.

2.3 SE-SMR literature

Sorption of CO_2 on different materials has been studied extensively since the early 1950s. However, in most cases it has been done at low temperatures (273 - 400 K) and ambient pressures. Zeolites have good CO_2-adsorption properties under these conditions, but for temperatures in excess of 500 K the capacity is negligible.[14] For SE-SMR it is necessary to work at higher temperatures because of kinetic considerations, hence high temperature CO_2-sorbents have to be looked into. The CO_2-acceptor for SE-SMR has to fulfill certain requirements:

Fast kinetics To get high conversions in a reasonable reactor volume, the CO_2-capture rate kinetics has to be fast, particularly at low partial pressures of CO_2.

Suitable thermodynamics The material should have low equilibrium partial pressure of CO_2 at temperatures from 450-650 °C. The temperature gap between capture and regeneration must not be too high, or it must be possible to regenerate the material by pressure swing.

Stability The material must have good stability, the capture-regeneration must be reversible and it must be mechanical (Especially for fluidized bed operation)
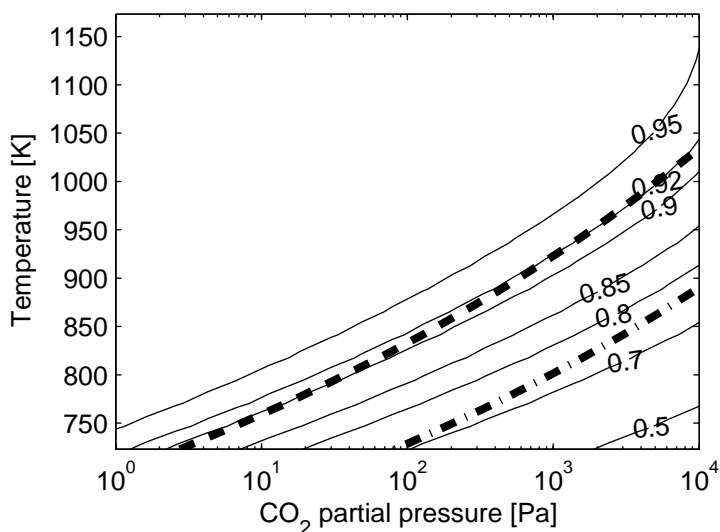
Figure 2.5: Contour plot of equilibrium SE-SMR dry hydrogen mole fraction as function of temperature and partial pressure CO_2, the equilibrium partial pressure of CO_2 over CaO[25] (— —) and the equilibrium partial pressure of CO_2 over Li_2ZrO_3[33] (— · —) is also shown

and thermal stable. The more expensive material, the more cycles must the material be able to withstand.

High capacity Particularly for fixed bed operation it is important with high capacity to get longer cycle times

Hydrotalcite

In Air Products SERP hydrotalcite was used as CO_2-acceptor and at temperatures of 450 °C and pressures of $\sim$ 5 bar they could produce high purity hydrogen ($>$95 dry mole%) with methane as the main impurity. The CO content was as low as $\sim$50 ppm. For the regeneration of the sorbent it was used a pressure swing process with depressurization to sub-atmospheric pressure (0.3-0.7 bar) and purge with steam.[82] Hydrotalcite-materials have been used in several studies of SE-SMR, and it is an anionic clay consisting of positively charged layers of metal oxide (or metal hydroxide) with inter-layers of anions, such as carbonate.[14] Hydrotalcite has quite low capacity of CO_2, Ding and Alpay reports of a working capacity of about 0.45 mol/kg, which is about 2 weight%.[14] They also studied the kinetics of CO_2-capture on hydrotalcite and modelled the sorption using a linear driving force

(LDF) - model. To get high conversions with hydrotalcite as CO_2-acceptor a high steam to carbon ratio (6) has been used. [15,26]

Limestone and dolomite

Natural occurring metal oxides as limestone and dolomite have been considered promising and cheap candidates for high temperature CO_2-capture. They are both sedimentary rocks, mainly consisting of the minerals calcite (calcium carbonate) and calcium magnesium carbonate, respectively. As the natural occurring minerals already are in a carbonized state, they must go through calcination before being used as CO_2-sorbents, and are precursors and not sorbents. Calcium oxide reacts with carbon dioxide as described in equation (2.4).

$$CaO + CO_2 \leftrightarrow CaCO_3 \quad \Delta H_{298} = -178 kJ/mol \quad (2.4)$$
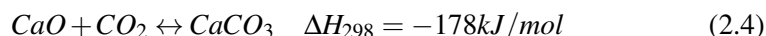
A group at Louisiana state university (USA) has done extensive research on calcium-based sorbents with dolomite and limestone as precursors and report that sorbents based on dolomite are superior to those based on limestone. Although the theoretical maximum uptake on limestone (pure calcium carbonate) is higher, in reality the dolomite-based sorbents (also containing magnesium oxide) show better kinetics, higher maximum fractional conversion and better multicycle performance. [22] Silaban et al., also from Louisiana state university, attribute the advantages of dolomite-based sorbents to the presence of MgO which does not take part in the carbonization and thereby stabilizes the sorbent. [72] The same group reports that high purity hydrogen can be produced with SE-SMR using dolomite-based sorbents. With a S/C-ratio of 4 they reached a dry hydrogen mole fraction >95% at a temperature of 650 °C and a pressure of 15 atm. [44] Johnsen et al. used dolomite as sorbent-precursor and investigated SE-SMR in a bubbling fluidized bed reactor. [30] At 600 °C and atmospheric pressures they reached equilibrium dry hydrogen mole fractions (>98 mole%) at S/C-ratios of three. The main problem with sorbents from natural CaO-sources have been the cyclic stability and Johnsen et al. report that the maximum conversion after 25 cycles is only 30 % of the initial maximum conversion (∼46 weight %).

Synthetic sorbents

Because of the poor multi-cycling stability of dolomite and limestone it has been tried to make synthetic calcium-based sorbents. Li and Cai report that they have made a sorbent based on calcium oxide and calcium aluminate (75/25 wt%) which have better stability than dolomite and limestone. [42] After 60 cycles the maximum conversion was about 40% of the initial maximum conversion while dolomite

could reach about 20% of the maximum conversion after 60 cycles. In SE-SMR with the synthetic sorbent they reached hydrogen purity >95 mole% at 650 °C, atmospheric pressure and a steam to carbon ratio of 4.

Other metal oxides than the cheap and natural occurring calcium oxide have also received attention as possible CO_2-acceptors for SE-SMR and specially lithium oxides have interesting properties. Nakagawa and Ohashi from Toshiba reported in 1998 that lithium zirconate (Li_2ZrO_3) powder can capture CO_2 up to 550 °C.[51]

$$Li_2ZrO_3 + CO_2 \leftrightarrow Li_2CO_3 + ZrO_2 \quad \Delta H_{298} = -160 kJ/mol \qquad (2.5)$$
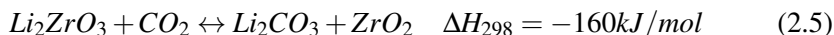
Ohashi and Nakagawa also found that the kinetics of lithium zirconate could be improved by doping it with potassium. A group at the University of Cincinnati(USA) has also worked on lithium zirconate as CO_2-acceptor and have done CO_2-uptake experiments on pure and modified lithium zirconate.[27,28,84] They also described the kinetics of the CO_2-capture by an unreacted shrinking core model.

The group from Toshiba have also studied lithium ortho-silicate as CO_2-acceptor. They found that it has better kinetic properties, could capture CO_2 at lower partial pressures and because silicate is cheaper than the expensive zirconia, the sorbent would be cheaper.[31]

$$Li_4SiO_4 + CO_2 \leftrightarrow Li_2CO_3 + Li_2SiO_3 \quad \Delta H_{298} = -143 kJ/mol \qquad (2.6)$$
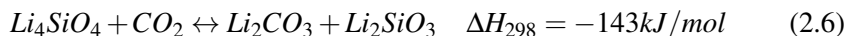
Lithium ortho-silicate have a very high theoretical maximum uptake, as Li_2SiO_3 could react with CO_2, but it is believed that it is mainly the ortho-silicate that reacts with CO_2, making the theoretical maximum uptake 36% on weight basis.[19] Kato et al found that lithium silicate could capture CO_2 at as low CO_2 concentrations as 2% at 500°C while lithium zirconate showed no significant weight change at these conditions.[31] Venegas et al. have synthesized lithium silicate by three different techniques, the solid state reaction, precipitation, and sol-gel method. Only the two first gave a satisfying material and the CO_2-capture on these have been investigated. The different methods gave different particle sizes, which in turn gave different sorption characteristics. The precipitation method gave particles sizes about a tenth of the ones with the solid state method (3μm compared to 36μm), and this gave significantly faster kinetics, and higher maximum conversion.[79]

López-Ortiz et al. tested several different synthetic sorbents with sodium titanate (Na_2TiO_3), sodium antimoniate (Na_3SbO_4) and sodium zirconate (Na_2ZrO_3) in addition to lithium zirconate and lithium silicate.[45] Sodium zirconate showed the best kinetic properties of the tested sorbents, and could be a candidate to compete with the lithium oxides. It showed faster kinetics, but was harder to regenerate. Since lithium is more expensive than sodium it can also have lower cost.

$$Na_2ZrO_3 + CO_2 \leftrightarrow Na_2CO_3 + ZrO_3 \quad \Delta H_{298} = -149 kJ/mol \qquad (2.7)$$
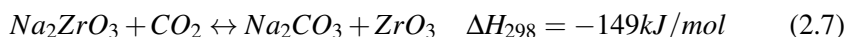
Ochoa-Fernández[52] has described the properties of the different candidates for high temperature CO_2-capture as outlined in table 2.1. The capture capacities

Table 2.1: An overview of the properties of different high temperature CO_2 acceptors.[52]

Acceptor	Capacity (gCO_2/g)	Stability	Kinetics	Regeneration temperature[K][a]
Dolomite	0.46	Poor	Good	1173
Limestone	0.79	Poor	Good	1173
$CaO/Ca_{12}Al_{14}O_{33}$	0.45	Fair	-	1173
$CaO/\gamma\text{-}Al_2O_3$	0.033	Good	-	1173
Li_2ZrO_3	0.29	Fair	Fair/Poor	1020
Na_2ZrO_3	0.24	Fair	Good	1050
Li_4SiO_4	0.36	Fair	Fair	990
Hydrotalcite	0.029	Fair/Poor	Good	PSR^b

[a]Equilibrium regeneration temperature at 1 bar and 100% CO_2
[b]Pressure swing regeneration

given in table 2.1 are the theoretical maximum and in all practical applications the capacity will be less. The volume change because of sorption will block pores and limit mass transfer, and this will reduce the capture rate or even stop the capture completely.

2.4 Reactor concepts

Two reactor concepts that are widely used in the chemical industry have been proposed for SE-SMR.

- Fluidized bed reactors

- Fixed bed reactors

Both reactor concepts offer their advantages and disadvantages for the process. The SERP process by Air Products,[26] was carried out in a fixed bed reactor system, while the early process described by Bruun-Tsekhovoi was carried out in a continuous fluidized bed process.[12]
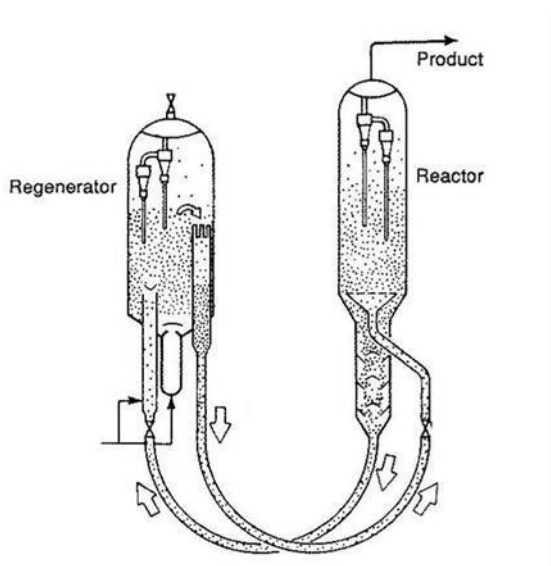
Figure 2.6: A fluidized bed reactor system.

Fluidized bed

The fluidized bed reactor had it's breakthrough in 1942 when Standard Oil started
with catalytic cracking of gasoil in a fluidized bed unit.[20] Because the catalyst de-
activates rapidly in catalytic cracking it must be regenerated continuously and until
today catalytic cracking has been the main application of fluidized bed reactors.
Though, other applications have also been introduced, like the phtalic anhydrid
and ethylene dichloride synthesis. A typical fluidized bed reactor configuration is
shown in figure 2.6. The solid flows between the two reactors, where two different
reactions are carried out and different temperatures can be employed.

The flow of solids is the main difference between a fluidized and fixed bed.
This also leads to the advantages and disadvantages compared to a fixed bed re-
actor. The positive and negative aspects of a fluidized bed reactor system for SE-
SMR are:

+ The sorbent can be continuously regenerated

+ Dependent on the sorbent an eventual small need for energy in the reforming
  reactor can be supplied by hot particles.

+ Large temperature gradients that can lead to material problems are avoided
  in a fluidized bed.

+ Low pressure drop compared to fixed bed.

- Pressure swing operation is very difficult

- It is more complex to design and operate a fluidized bed than a fixed bed.

- The mechanical strength of the particles must be high.

A fluidized bed reactor can be operated in different modes dependent on gas velocity and particle properties. In the bubbling bed regime the particles are fluidized but there is no total movement of particles through the reactor and the gas moves through the particles in bubbles. When the gas velocity is increased the bed will go into a turbulent regime, where the mixing of solids is more intense and the bed is more uniform. When the gas velocity is further increased the particles will start to blow out over the top of the reactor and we have a net entrainment of solids. If the velocity is further increased, the transport regime is reached, with a steep decline in the solid volume fraction and a large net entrainment.

Continuous operation is possible in all the regimes, even if the bubbling bed and turbulent bed does not have a "natural" transport of solids. If net transport of solids is wanted in these modes special installations have to be made so that particles are removed from the reactor bed. However, some particles and fines will be carried with the gas also in the lower velocity regimes, and these have to be separated and sent back to the bed using a cyclone. For the regimes with net entrainment of solids a cyclone will be placed on the top to separate the product gas from the particles, which are sent to the other reactor. The regime a process is operated in, depends on different properties of the process, with the reaction kinetics as one important variable. Higher velocity will both give shorter residence times and lower solid fraction in the reactor, hence the kinetics have to be fast for the fast fluidization and transport regimes to be employed.

For a sorption process the continuous regeneration is the major advantage of a fluidized bed, and for such a process all the regimes could be employed dependent on the properties of the reactions and the particles. A reactor concept could be a combination of two reactors operated in different regimes, e.g. the sorption in done in a transport reactor and the regeneration in the bubbling bed regime. One sorption process based on the fluidized bed reactor that is already commercially proven is the Lurgi CFB process where SO_2 is removed from flue gas using limestone. [34]

The fluidized bed has, as mentioned, some advantages for the process and it is claimed that for SE-SMR in an industrial scale a fluidized bed reactor system is the only alternative. [30]

Fixed bed reactor

The fixed bed reactor is used for the majority of the chemical processes in the world, and it is normally used for steam methane reforming. Different types of the

fixed bed reactor are the multitube reactor, the multibed reactor, and the single bed reactor. Figure 2.7 shows the main types of fixed bed reactors.

Single-bed Reactor   **Multi-bed Reactor**   **Multi-tube Reactor**
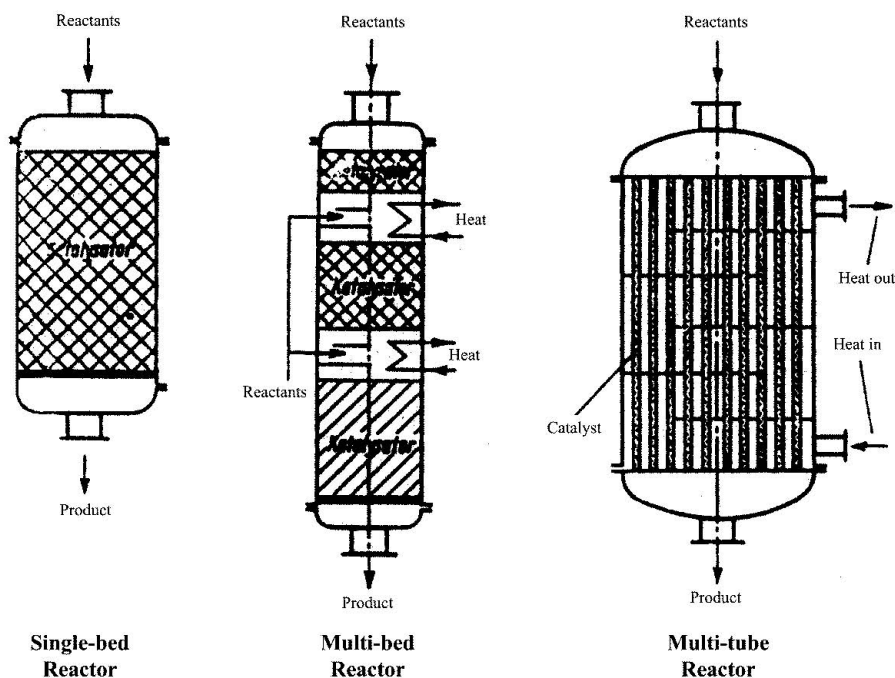
Figure 2.7: Different fixed bed reactor concepts.

The reactor or reactor tubes is packed with the catalyst which can be installed as catalyst pellets or as a structured packing. For the traditional SMR where indirect heating is used, the multitube reactor is employed and the heating is supplied by firing natural gas outside the tubes. For the more novel autothermal reactors a single bed reactor is used, with firing of natural gas directly inside the reactor. For the SE-SMR the selection of fixed bed reactor configuration is based on the heat supply. The regeneration of the sorbent demands heat and this has to be transferred to the reaction zone. The positive and negative aspects of a fixed bed reactor system are:

+ The fixed bed reactor has a simple and well-known design.

+ Pressure-swing operation can be employed.

+ The higher solid density in the fixed bed reactor can lead to lower reactor volumes.

- The pressure drop can be large

- Large temperature gradients can lead to material problems

- The process must be operated in a cyclic manner and the cycle-times of reforming and regeneration must be matched

The pressure drop is mainly dependent on the shape/size of the pellets and the gas velocity. In SMR there are steep concentration gradients inside the catalyst pellets, which mean that most of the reaction is occurring close to the outer surface of the pellet. To get a better utilization of the catalyst, smaller pellets would be favourable, but this would lead to higher pressure drops, which make the size of the particles an important trade-off in the fixed bed reactors. Typical effectiveness factors for the catalyst in SMR are below 0.1 and less than 5% of the catalyst bed loaded into a conventional reformer is not utilized.[3] To get higher effectiveness and reducing the pressure drop different particle shapes have been tried. A particle design from Haldor Topsoe is seen in figure 2.8. The shape and size of the pel-

Figure 2.8: Catalytic pellets from Haldor Topsoe.[64]

lets may also be of importance in SE-SMR, where there are two active materials with different properties. In this case the distribution of the CO_2-acceptor and the catalyst will also be an important process parameter. Both properties can be incorporated in one particle, or two different particles with one property in each can be employed. In addition, the reactor could be divided into zones with different fractions of the materials to optimize the process.

A fixed bed reactor system for SE-SMR must be operated in a cyclic manner and Waldron et al. have described the pressure swing process as follows:[82]

1 The reactants consisting of steam and methane at the high pressure and reacting temperature is passed through the bed until the carbon oxide levels in the outlet reach a preset level.

2   The reactor is depressurized to ambient pressure.

3   The reactor is evacuated to sub-atmospheric pressure and purged with steam.

4   The reactor is pressurized to the high pressure using steam.

In case of temperature swing operation this could be implemented with or without in combination with pressure swing. In a combined temperature/pressure swing the temperature has to be increased in step 2 to the wanted desorption temperature, and the temperature have to be decreased in step 4 back to the wanted reaction temperature. The gas used for desorption could be steam or other gases, but it should be easy to separate it from the product CO_2 stream, for the CO_2 to be transported to storage. Flue gas from combustion of hydrogen/methane in pure oxygen could supply the needed heat to the reactor and the CO_2/steam used as purge gas.

2.5   Modelling of SE-SMR

The reactor modelling work on SE-SMR with actual sorbent kinetics is sparse, and limited to calcium oxide and hydrotalcite as CO_2-acceptor. For fixed bed reactors, the most detailed work has been done by a group at the university of Porto, resulting in several papers.[85,86,87,88] They used hydrotalcite as CO_2-acceptor and adopted the sorption-kinetics from Ding and Alpay[14]. The models used for simulations are transient 1-D axial dispersion models, formulated both for pseudo-homogenous[85,87] and heterogeneous[88] cases. They analyzed both the possibility of different reactor configurations and the effect of intraparticular diffusion. Ding and Alpay have also done reactor simulations with their own kinetics on hydrotalcite, and compared the simulation results from a fixed bed reactor model with experimental data on SE-SMR, which gave good fit to the experimental data using the found capture kinetics and the SMR-kinetics from Xu and Froment.[89] The simulations and experiments were done with quite low residence times, which with the low capacity of hydrotalcite lead to a pure transient operation of the reactor. No pseudo-steady state with enhanced reforming was obtained. However, an enhancement of the reforming were obtained in the first 3-4 minutes of operation.[15]

A temperature swing concept for SE-SMR with hydrotalcite as CO_2-acceptor has been simulated by Lee et al. and they found that the temperature swing process showed favourable characteristics to the pressure swing.[41] The reforming was carried out at 490 °C and the regeneration at 590 °C. With an S/C-ratio of 4 and a pressure of 1.5 bar hydrogen fraction of 0.9999 was obtained(!). The model used for the simulation was a transient pseudo-homogeneous CSTR-in-series model. Koumpouras et al. have proposed a reactor system based on a monolith catalytic

reactor with the sorbent pneumatically conveyed through the reactor.[36] They modelled this using a steady state plug flow model. Hydrotalcite was used as acceptor and with a temperature of 450°C and a S/C-ratio of 6 a methane conversion of 0.75 was reached. The same group has also done simulations of a fixed bed reactor looking at the effect of sorbent characteristics and state that an ideal sorbent has the capacity of lithium zirconate and the kinetics of hydrotalcite.[35]

Another Lee found an expression for the kinetics of CO_2-capture on calcium oxide in 2004[38] and have used this for simulations of a fixed bed reactor[39] and a moving bed reactor.[40] The fixed bed reactor was simulated using a transient pseudo-homogenous plug flow model. It was found that inlet temperatures above 650 °C had to be used to get a satisfying conversion. In the moving bed reactor, the solid flows counter-current to the gas at a fixed circulation rate and it was used a steady state pseudo-homogenous plug flow model. For the simulations of both reactor types it were used an efficiency factor of 0.3 for the carbonation. In both reactors hydrogen purities above 0.97 was obtained.

Johnsen et al. used calcined dolomite as CO_2-acceptor and simulated a fluidized bed model using a steady state two-phase model for the reformer. The cyclic process with calcination was simulated, but for the regenerator no actual kinetics was used, and it was assumed that the regeneration was at equilibrium. Only heat and mass balances were solved for this reactor. The reforming was performed at 600°C and the regeneration between 850 and 900 °C. For an S/C-ratio of 3 at 600°C a hydrogen purity of 0.97 was obtained.

Li and Cai have synthesized $CaO/Ca_{12}Al_{14}O_{33}$ and modelled the CO_2-capture kinetics and the regeneration kinetics.[42] Using these kinetic models they have simulated the SE-SMR cycle for a thermal swing process in a fixed bed reactor. The reactor model used was a transient pseudo-homogeneous plug flow model, and the reforming temperature 650 °C and the regeneration temperature about 900 °C. Argon was used as purge gas for the regeneration.

Zagoruiko and Okunev[91] have also simulated SE-SMR with Calcium Oxide as sorbent, with the regeneration method as the novelty. 1% methane in air was fed to the regeneration reactor and the combustion heat used to supply the heat for the endothermic calcination. The simulations show that this way of regeneration is possible and the highest efficiency is obtained when feeding the combustion mixture counter-currently to the feed direction used for the reforming step. The material balance was formulated as a quasi-steady state plug flow model, while the heat balance was formulated in terms of a transient enthalpy balance. No data was given on the product gas composition from the reforming reactor.

Table 2.2 shows an overview of some of the modelling work done on SE-SMR. It is observed that for both hydrotalcite and calcium oxide purities above 0.9 can be reached, and both in fluidized bed and fixed bed reactors. The working temperature

for hydrotalcite is lower than for the calcium oxide, but it does not show quite as fast kinetic as the pure calcium oxide. The main difference is, as earlier mentioned, the capacity, and it can be produced significantly more hydrogen per mass of solid with calcium oxide as sorbent.

Table 2.2: An overview of some of the modelling work done on SE-SMR

Reference	Sorbent	Reactor	Model	P(bar)	S/C	T(K)	$y_{H_2}^d$	mol CH$_4$ s/kg s	mol H$_2$/kg s
Xiu et al. [88]	Htlc[a]	FB[b]	D Het[c]	4.45	6	723	0.93	5290	0.30
Lee et al. [41]	Htlc	FB	SS CSTR[d]	1.5	4	763	0.9999	1186	0.39
Lee et al. [40]	CaO	MB[e]	SS P-H[f]	3	3	973	0.94	720	2.9
Johnsen et al. [30]	CaO (dolomite)	BB[g]	SS 2-P[h]	1.013	3	873	0.97	1216	7.3
Li and Cai [42]	CaO/Ca$_{12}$Al$_{14}$O$_{33}$	FB	D P-H	1.013	4	923	0.97	538	17

[a]Hydrotalcite
[b]Fixed bed
[c]Dynamic heterogeneous
[d]Steady state CSTR in series
[e]Moving bed
[f]Steady state pseudo-homogeneous
[g]Bubbling bed
[h]2-phase model

Chapter 3

Kinetic modelling

To be able to simulate SE-SMR by reactor models all major chemical kinetic rate expressions must be formulated mathematically. A steady state kinetic model for reforming reactions have been given by Xu and Froment[89], and it was confirmed by Ding and Alpay[15] that this model is applicable to transient reactor model, both in the presence and absence of a sorbent. This means that the kinetic rate expression for the CO_2-capture is the missing part in the chemical reaction kinetics in SE-SMR. By measuring the transient weight uptake on a sorbent as function of operating parameters such as CO_2-partial pressure and temperature, a kinetic model can be fitted to the experimental data.

Gas-solid reaction chemistry has been studied extensively but still there are difficulties in understanding and modelling the actual reaction rates. This is because the mechanisms are complex, with the overall reaction rates influenced not only by chemical reactions but by physical adsorption, mass and/or energy transfer. These mechanisms are also affected by changes in morphology, crystallite orientations, crystallite size, impurities, etc.

For many gas-solid reactions the rate is determined by the rate of physical adsorption on the surface, and a common way of modelling this is by a linear driving force (LDF) model. The LDF-model is expressed as in equation (3.1)

$$\frac{\partial q_i}{\partial t} = K(q_i^{eq} - q_i) \tag{3.1}$$

Where q is the mass uptake per pass of sorbent. For physical adsorption, there are several different isotherms that can describe the equilibrium between the gas phase and the adsorbed species (q_i^{eq}), e.g. the linear, Toth and Langmuir isotherms. Ding and Alpay found that the CO_2-capture on hydrotalcite was well described by the LDF mode with a Langmuir isotherm.[14] The sorption capacity was strongly dependent of the partial pressure of CO_2, which indicates that physical adsorption is the rate limiting step. Ding and Alpay reports that there are indications

that there is some strong irreversible chemisorption on fresh material, followed by weak physical adsorption.

For the other materials described in section 2 other models have been used to describe the kinetics. In most cases of kinetic modelling of gas-solid reactions the starting point is the general diffusional mole balance:

$$\varepsilon \frac{\partial c_a}{\partial t} = \frac{1}{r^m} \frac{\partial}{\partial r} \left(r^m D_e \frac{\partial c_a}{\partial r} \right) - (-r_a)$$
(3.2)

The *m* takes different values dependent of the geometry (0 for slab, 1 for cylinder, and 2 for sphere) A concept frequently used to model gas-solid reactions is the shrinking unreacted core model.[83] A schematic representation of a spherical sorbent particle is shown in figure 3.1. The largest section in figure 3.1 is a repre-
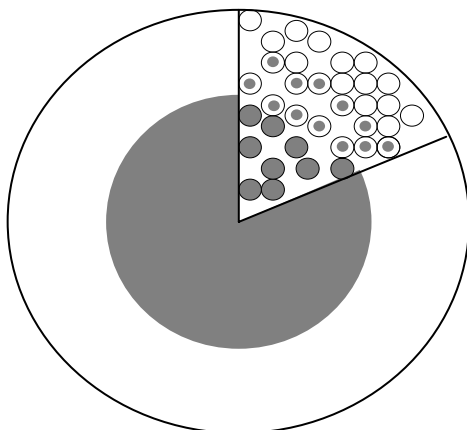
Figure 3.1: A schematic representation of a particle, showing a particle reacting with the shrinking core model, and in one segment grains reacting by the grain model.

sentation of a spherical particle reacting by the shrinking core model. The model considers a spherical particle where a fluid reacts with the solid (gray) to produce a porous solid product layer(white). The unreacted solid is impervious to the fluid, and the reaction occurs at the front between the unreacted and reacted solid. For the unreacted shrinking core model the term $(-r_a)$ in equation (3.2) is set to zero because all reaction happens at the front between the unreacted and reacted solid, and the reaction rate is accounted for in the boundary conditions between the solid phases of unreacted solid and reaction product. With a first order reaction with respect to gas concentration, Johnsen solved equation equation (3.2) analytically

for the fractional conversion (x) and got the result: [30]

$$\frac{dx}{dt} = \frac{3}{r_p} \frac{(1-x)^{2/3} \frac{1.27}{\rho_s RT} (p_a - p_{a,eq})}{\frac{1}{k} + \frac{r_p((1-x)^{1/3} - (1-x)^{2/3})}{D_p} + \frac{(1-x)^{2/3}}{k_g}} \tag{3.3}$$

Shieh and Lee have solved the shrinking core model for slab, cylindrical and sphere geometry for a random reaction order. [71] They also included an induction period to account for nucleation at the surface. The resulting equation was on the form:

$$t** = g(x) + \frac{2}{2D_p} \frac{V_p}{a_p} (1 + 1/K^{eq}) P(x) \tag{3.4}$$

Where

$$t** = \frac{vka_p}{\rho_s f_g V_p} (C_a^n - C_a^{eq})(t - t_{ind}(1 - e^{-t/t_{ind}})) \tag{3.5}$$

$$g(x) = 1 - (1-x)^{1/f_g} \tag{3.6}$$

$$P(x) = \begin{cases} 1 - 3(1-x)^{2/3} + 2(1-x) & f_g = 3 & \text{for a sphere} \\ x + (1-x)ln(1-x) & f_g = 2 & \text{for a long cylinder} \\ x^3 & f_g = 1 & \text{for an infinite slab} \end{cases} \tag{3.7}$$

Except the term for the induction period $(-t_{ind}(1 - e^{-t/t_{ind}}))$ this model is similar to the shrinking core model in Szekely. [76] Two alternatives to the shrinking core model are the pore model and the grain model proposed by Szekely and Evans. [75] Referring to figure 3.1 the pore model assumes that the diffusion through the pores is rate-limiting and the pore structure changes with reaction. The grain model assumes that the rate limiting step is in the smaller solid grains, but is in many ways similar to the shrinking core model. The diffusion in the grains is solid state diffusion contrary to the shrinking core model which accounts for pore diffusion.

The shrinking core model and the grain model can also be combined, then the grain kinetics is employed in the r_a.

In general terms the kinetics of a gas-solid reaction can be described as: [21]

$$\frac{dx}{dt} = Kf(P_a)F(x) \tag{3.8}$$

Some of the different expressions for F(x) in equation (3.8) given by Gomez-Barea et al. are listed in table 3.1. [21] Here, the kinetic expression is divided in two parts, i.e. one part that is dependent on the fractional conversion of the solid material (F(x)), and one part that is dependent of the gas partial pressure. The kinetic constant (K), will in most cases be dependent of the temperature. The formulations

can be based on a mechanical explanation, or they can be purely empirical with no attempt to explain how the reaction occurs. The advantages of a mechanistic based model can be that it can be used outside the intervals where the experiments were conducted, but still there are risks that the kinetic mechanisms can change. Models that explain the mechanism can also be of use in the synthesis of new and improved materials. If the mechanisms of kinetics are known, the materials can be made in such a way that the known limitations are minimized. However, the mechanistic based models need more detailed testing of the materials because more parameters have to be determined, and in reactor modelling the most important aspect is that the model give the correct reaction kinetics and not that the model describes the reaction mechanisms, even if it ideally does both.

Table 3.1: Some expression for F(x) in equation (3.8)[21].

Name	F(x)	Reference
Volumetric model	$(1-x)$	Szekely[76]
Grain model	$(1-x)^{2/3}$	Szekely[76]
Random pore model	$(1-x)(1-\psi_0 \ln(1-x))^{1/2}$	Bhatia and Perlmutter[8]
Avrami-Erofeev	$n(1-x)(-\ln(1-x))^{(n-1)/n}$	Avrami-Erofeev[4,5,6,24]
Traditional	$(1-x)^n$	—

3.1 A kinetic model for the CO_2-capture on Li_2ZrO_3

The kinetics of the gas-solid reaction between lithium zirconate and carbon dioxide has earlier been modelled by Ida and Lin with a double-shell unreacted core mechanism.[27] After an initial stage the dense Li_2ZrO_3 core is covered by two layers, an inner layer with ZrO_2 and an outer layer of Li_2CO_3. The rate-limiting step was found to be the diffusion of CO_2 in the Li_2CO_3-layer. The lithium zirconate from Ida and Lin was made by the solid state method, and the pure lithium zirconate needed >24 h to reach a 18% weight gain in a CO_2 atmosphere at 500 °C. Nair et al. states that lithium zirconate made by sol-gel procedures are superior in terms of sorption properties.[50] Using a novel soft-chemistry route our group have synthesized nanocrystalline lithium zirconate and by that minimizing the grain sizes. The detailed synthesis method is presented by Ochoa-Fernández et al.[59] The CO_2-capture properties of this lithium zirconate material were evaluated using a tapered-element oscillating microbalance (TEOM). A TEOM calculates the mass change in the fixed bed by measuring the changes in natural frequency of an oscillating quartz element containing the sample and has short response times which
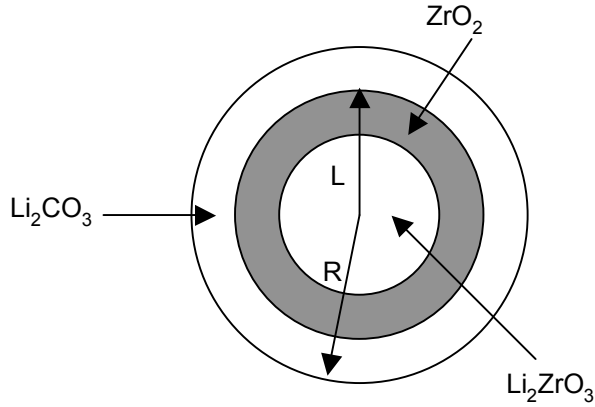
Figure 3.2: Illustration of the particle used in Ida and Lins shrinking core mechanism for Li_2ZrO_3

make it suitable for measuring fast sorption reactions. While exposing lithium zirconate to gas flows with different partial pressures at different temperatures, the uptake of CO_2 was measured, and on the basis of these data a kinetic rate expression was determined. To avoid the influence of external mass transfer, the gas flow was increases until no change in initial uptake rate was observed. The uptake of CO_2 is measured at three temperatures, 530, 550 and 575 °C and at partial pressures in the range of 0.3-1 bar. The experimental setup and procedures of the TEOM measurements are described in detail by Ochoa-Fernández et al.[59] The double shell shrinking core model from Ida and Lin is based on equation (3.2) and the description of the particle is shown in figure 3.2. By defining y as L/R the weight uptake on Li_2ZrO_3 by the double shell shrinking core mechanism could be expressed as:

$$\frac{\Delta w}{w_0} = 29(1 - y^3) \tag{3.9}$$

where y is the solution of the cubic equation:

$$y^3 - 3/2y^2 + \frac{2\alpha C_{CO_2}t + 1}{2} = 0 \tag{3.10}$$

When trying to fit the model from Ida and Lin to the experimental data, it was evident that it could not explain the uptake measurements and the same applied for variations of the shrinking core model, like the grain model of Szekely. Figure 3.3

shows the best fit of two of the experimental data at 848 K and partial pressures of CO_2 of 1 and 0.7 bar. The fit is not satisfying, and other kinetic expressions had to be looked into. Szekely describes a model he calls the volumetric model,

(a) T = 848 K, p_{CO_2} = 1 bar   (b) T = 848 K, p_{CO_2} = 0.7 bar
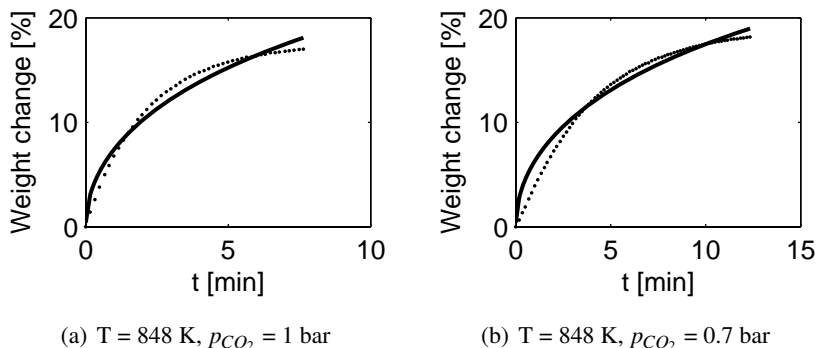
Figure 3.3: Experimental data $(\cdots)$ and the fitted shrinking core model from Ida and Lin[27](—) for capture of CO_2 on lithium zirconate.

where the uptake rate is a function of $(1-x)$, where x is the fractional conversion of the acceptor.[76] The small crystal sizes in the material can make the kinetics limited by nucleation and crystal growth. These processes have been described by the Avrami-Erofeev model where the function of conversion in general terms is formulated as:[4,5,6,24]

$$F(x) = n(1-x)(-\ln(1-x))^{(n-1)/n} \tag{3.11}$$

The n in the Avrami-Erofeev model can take the value of 1, 2, and 3, and for n = 1 the model describes random nucleation and reduces to:

$$F(x) = (1-x) \tag{3.12}$$

The fractional conversion, x, is 1 at full saturation of the CO_2-acceptor and defined by:

$$x = \frac{q}{q_{max}} \tag{3.13}$$

q is the mass of CO_2 captured per mass of lithium zirconate, q_{max} is q at maximum capture and is found to be 0.22 for this sample of Li_2ZrO_3. The experimental data showed good fit to this model which can be called random nucleation by the Avrami-Erofeev model or the model which Szekely just calls the volumetric model without giving a mechanistic explanation. The Avrami-Erofeev model was originally used to describe phase transformations of steel, later on it has been used for several other chemical processes, like the oxidation of nickel.[24] The measured

data show a dependency of the partial pressure of CO_2 close to 2, a number which can indicate that the chemical reaction rate can be a limiting step or it can mean that the rate limiting step changes with changes in partial pressure. Because of the good fit to the experimental data, the expression chosen for the dependency of partial pressure was on the form:

$$f(p_{CO_2}) = (p_{CO_2} - p_{CO_2,eq})^2 \qquad (3.14)$$

The total expression for the capture rate is then given as:

$$\frac{dx}{dt} = K(p_{CO_2} - p_{CO_2,eq})^2(1-x) \qquad (3.15)$$

The equilibrium partial pressure of CO_2, $p_{CO_2,eq}$, is modelled using thermodynamical data.[33] K is the effective reaction rate constant for which an Arrhenius expression is used for the temperature dependence.

$$K = K_0 e^{-\frac{E_{cap}}{R}\left(\frac{1}{T} - \frac{1}{T_0}\right)} \qquad (3.16)$$

T_0 in equation (3.16) is set as 848 K. The fitted parameters in equation 3.15 and 3.16 are given with standard deviations in table 3.2. An in-house Matlab code for

Table 3.2: Parameters fitted to equation (3.15)

$K_0 (s^{-1})$	$8.07 \times 10^{-13} \pm 7 \times 10^{-15}$
$E_{cap} (J/mol)$	$7.7 \times 10^4 \pm 2 \times 10^3$

nonlinear model fitting using a secant version of Marquardt's[47] method of least squares was used to determine the parameters in the model. The experimental data and the model fit at different partial pressures of CO_2 and temperatures are shown in figure 3.4. There is a short induction period at lower partial pressures which give small discrepancy to the model, but we find the model sufficiently good to be able to simulate the SE-SMR. A maximum in the capture kinetics is observed at a temperature around 585 °C that this model is not able to explain, thus the model should not be used at temperatures significantly higher than the ones used in the measurements.

3.2 A kinetic model for CO_2-capture on lithium ortho-silicate

Contrary to the lithium zirconate material that was studied, the Li_4SiO_4 is a commercial material obtained from Toshiba. The material is made by solid state synthesis and the detailed synthesis method is reported by Kato et al.[32] The kinetics of
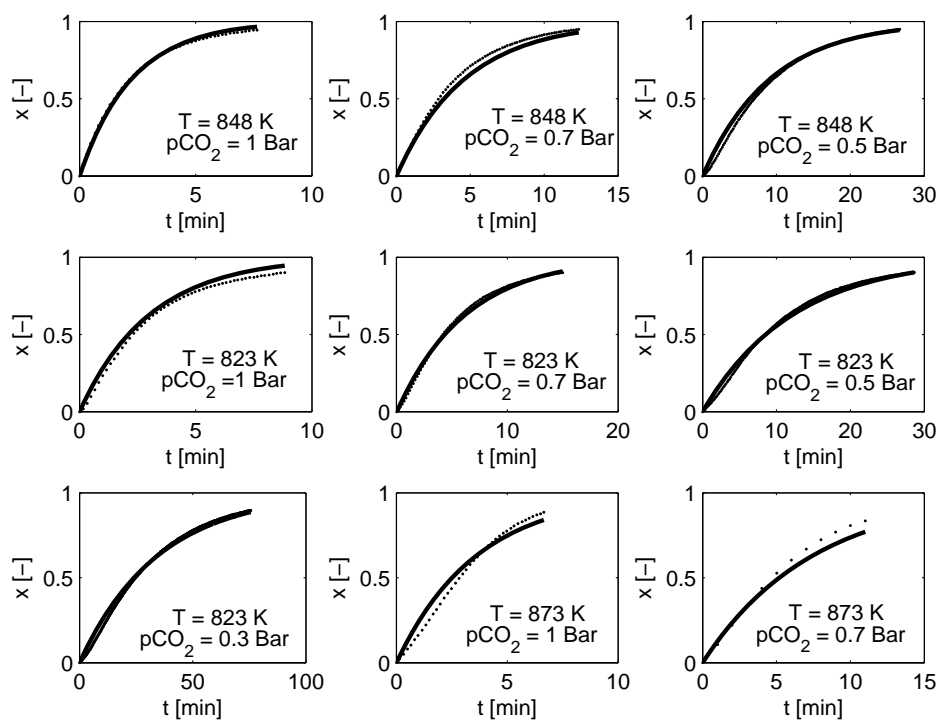
Figure 3.4: Experimental data $(\cdots)$ and the kinetic model (—) for capture of CO_2 on lithium zirconate.

CO_2-capture on the Li_4SiO_4-based material from Toshiba have been examined in a tapered element oscillating microbalance (TEOM) at three different temperatures, 803, 823 and 848 K, and at partial pressures of CO_2 in the range 0.05-1 bar. The material was grounded to a fine powder before the experiments and the flow rates used in the measurements were high enough to assure no external mass-transfer limitations. The experimental setup and procedures of the TEOM measurements are described in detail by Ochoa-Fernández et al.[57]

As already reported different expressions for F(x) have been given in the literature and a selection of these is listed by Gomez-Barea and Ollero[21]. A commonly applied model is the shrinking unreacted core model for spheres[76] where $F(x) = (1-x)^{2/3}$. Other used models are the random pore model[8] and the volumetric model[76]. None of these models or variations of these, like the shrinking core model with different geometries and including an induction period[71], showed satisfying fit to the experimental data over the whole range of operating conditions. Neither did any variation of the Avrami-Erofeev model. For the gathered experimental data an expression with $F(x) = (1-x)^n$ and an n-value of 2 gave best fit to

the data. This formulation does not explain the capture mechanism, but indicates that the rate limiting step is changing with fractional conversion, as reported by Lee[38] for the reaction of calcium oxide with CO_2. A rigorous mechanistic model for the CO_2-capture should include the change in rate-limiting step during the course of reaction and with change in temperature and partial pressure of CO_2, but for the purpose of this work, which is the modelling of SE-SMR, a simpler model is considered sufficient. To be able to formulate a more descriptive model which explains the different steps in the capture of CO_2 further experimental analysis is needed.

After determining the expression for F(x) the reaction rate expression is given as:

$$\frac{dx}{dt} = Kf(p_{CO_2})(1-x)^2 \tag{3.17}$$

Mechanistic models based on first order reaction kinetics with respect to the CO_2 partial pressure use $f(p_{CO_2}) = p_{CO_2} - p_{CO_2,eq}$, but the experimental data clearly showed that the kinetics were not first order with respect to partial pressure. Similar to the function of fractional conversion this indicates that the rate-limiting step changes with partial pressure. Non-linear dependencies of the partial pressure has also been found and modelled for other gas-solid reactions, like the reaction of CO_2 with calcium oxide.[30] The expression found for the modelling of the capture kinetics is shown in equation (3.18).

$$\frac{dx}{dt} = K(p_{CO_2} - p_{CO_2,eq})^n(1-x)^2 \tag{3.18}$$

Experiments have also been carried out to get the equilibrium partial pressure of CO_2 for the material, and this was done by finding the highest partial pressure of CO_2 at different temperature which did not lead to weight-gain after several hours in the TEOM. This was done because according to the thermodynamic data from the literature[33] equilibrium partial pressures were much higher than the partial pressures where CO_2-capture was observed, e.g. at 848 K the equilibrium partial pressure from the literature is 0.1 bar, while capture was observed at partial pressures down to 0.025 bar. From these experimental data an expression for the equilibrium partial pressure of CO_2 as a function of temperature was found:

$$ln(\frac{1}{p_{CO_2,eq}}) = -0.0066T - 2.25 \tag{3.19}$$

The experimental data and the equilibrium partial pressure from equation (3.19) are shown in figure 3.5. By integrating equation (3.18) in time the expression fitted to the experimental data was found:

$$x = 1 - \frac{1}{1 + K(p_{CO_2} - p_{CO_2,eq})^n t} \tag{3.20}$$
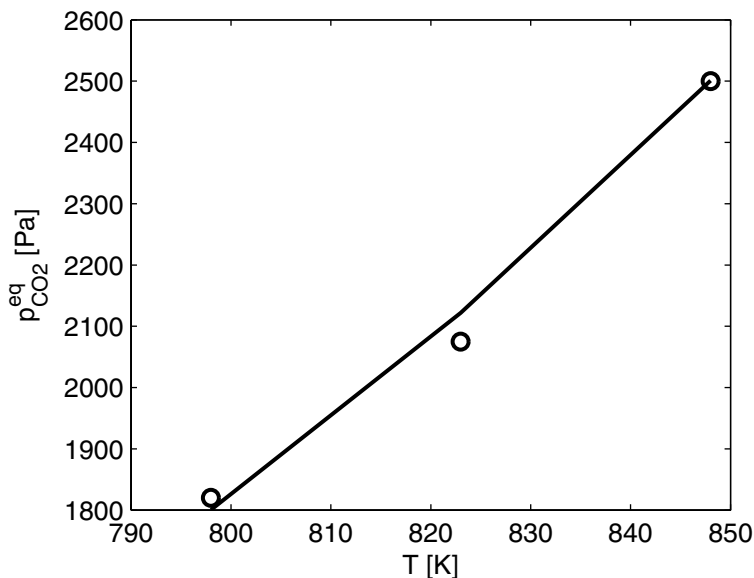
Figure 3.5: The modelled equilibrium partial pressures (—) and the experimentally found equilbrium partial pressures (◦) as a function of temperature for lithium ortho-silicate

x is the fractional conversion of sorbent, defined as q/q_{max} where q is the mass uptake of CO_2 per mass of sorbent, and q_{max} is the maximum of q found for this material, which was 0.20. For the kinetic constant (K) an Arrhenius expression (3.16) is used for the temperature dependence with T_0 set to 848 K.

The fitted parameters in equation (3.18) and equation (3.16) with standard deviations for lithium ortho-silicate are given in table 3.3. Figure 3.6 shows the

Table 3.3: Capture kinetic parameters

$K_0(s^{-1})$	$1.84 \times 10^{-4} \pm 1.7 \times 10^{-5}$
$E_{cap}(J/mol)$	$1.1 \times 10^5 \pm 3 \times 10^3$
$n(-)$	0.26 ± 0.01

experimental data and the model fit at all examined partial pressures and temperatures. The fit is reasonably good, particularly since the material will undergo minor changes as it is used in several cycles. Changes in the morphology during the capture-regeneration cycles will have some effect on the sorption kinetics which will lead to discrepancies to any kinetic model. Though, the model fit is found sufficient to model the SE-SMR with Li_4SiO_4 as CO_2-acceptor.

(a) T = 848 K, p_{CO_2} = 1 bar   (b) T = 848 K, p_{CO_2} = 0.5 bar   (c) T = 848 K, p_{CO_2} = 0.3 bar

(d) T = 848 K, p_{CO_2} = 0.05 bar   (e) T = 823 K, p_{CO_2} = 1 bar   (f) T = 823 K, p_{CO_2} = 0.5 bar

(g) T = 803 K, p_{CO_2} = 1 bar   (h) T = 803 K, p_{CO_2} = 0.5 bar
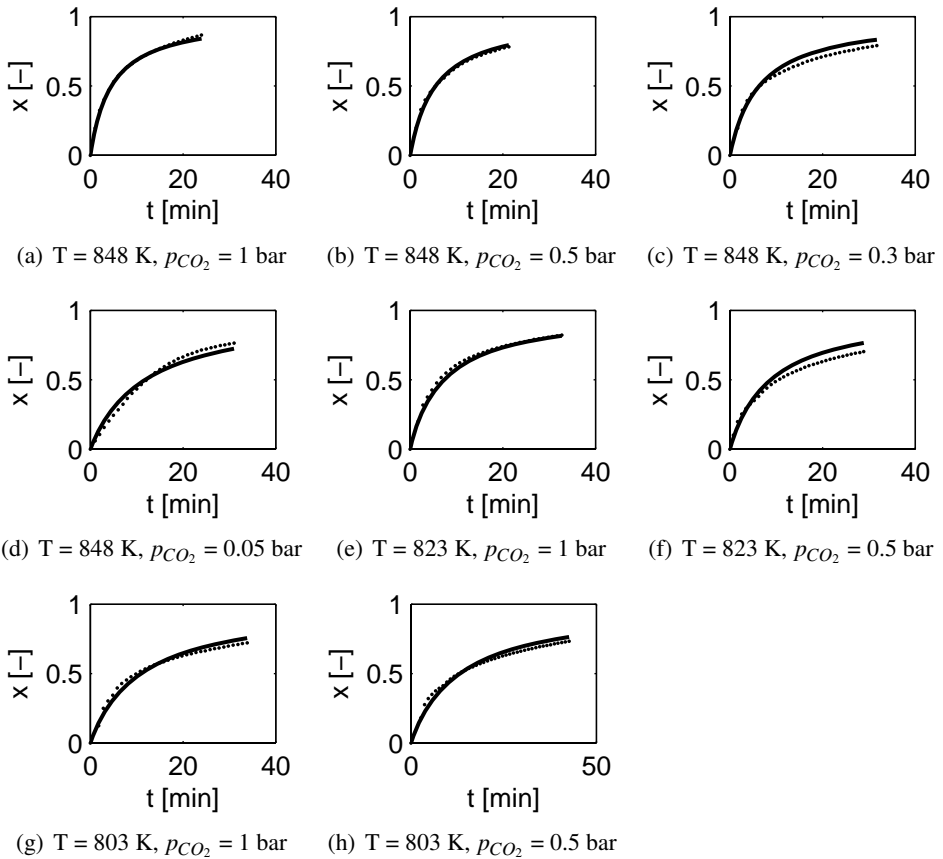
Figure 3.6: Experimental data ($\cdots$) and the kinetic model (—) for capture of CO_2 on lithium ortho-silicate.

3.3 A kinetic model for CO_2-capture on sodium zirconate

The last material that has been investigated experimentally is sodium zirconate. Because it had promising thermodynamic properties and it was reported by López-Ortiz et al.[45] that it could compete well with the lithium oxides as CO_2-acceptor, a sodium zirconate material was synthesized. Because of the superior properties of the lithium zirconate made with the novel soft-chemistry route[57] compared to other lithium zirconate powders, the sodium zirconate was also synthesized using this method and it is described in detail by Zhao et al.[92]

The CO_2-capture properties were measured in the TEOM at partial pressures in the range 0.05 - 0.14 bar and temperatures in the range 753-848 K. Because the material is made in the same way as the lithium zirconate, it could be expected

that it followed much of the same kinetic mechanisms. Although the kinetics is much faster than the capture on Li_2ZrO_3, the same kinetic expression was found to fit well to the CO_2-capture on Na_2ZrO_3. The other gas-solid reaction models described, such as the shrinking core model, the random pore model, and others, did not give satisfactory fit to the experimental data. This means that the expression fitted to the capture data was on the form:

$$\frac{dx}{dt} = K(p_{CO_2} - p_{CO_2,eq})^2(1-x) \tag{3.21}$$

The maximum uptake, q_{max}, of this Na_2ZrO_3-material was found to be 0.172 and the Arrhenius expression given in equation (3.16) with 848 K used as T_0 was used for the temperature dependence of the kinetic constant. In the same way as for lithium silicate the experimental data showed that the equilibrium partial pressure of CO_2 from the literature was higher than the partial pressures where capture was observed. At 848 K capture of CO_2 were observed down to partial pressures of 150 Pa while the equilibrium partial pressure is at about 2000 Pa. The expression found for the temperature dependency of the equilibrium partial pressure was:

$$ln(\frac{1}{p_{CO_2,eq}}) = -0.0018T - 3.5 \tag{3.22}$$

The experimental data and the equilibrium partial pressure from equation (3.22) are shown in figure 3.7. Then, using the same in-house code as earlier for model fitting, the parameters for the model was found. These are given in table 3.4 together with the respective standard deviations. The model and the experimental data are shown in figure 3.8. Especially the initial rates show a very nice fit to the model, while there are some discrepancies at higher conversions for a few of the experimental series. This could occur because the material morphology can change during the capture-regeneration cycles and this simple model is not able to describe these changes accurately. However, the model is found sufficiently accurate to model the SE-SMR, and the fit is good for such a simple model.

Table 3.4: Parameters fitted to equation (3.21)

$K_{10}(s^{-1})$	$9.0 \times 10^{-11} \pm 1 \times 10^{-12}$
$E_1(J/mol)$	$1.57 \times 10^5 \pm 1 \times 10^3$
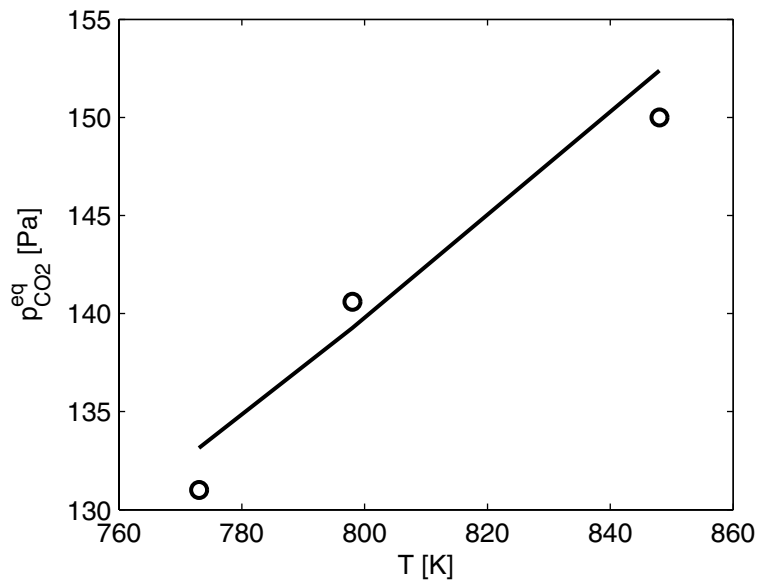
Figure 3.7: The modelled equilibrium partial pressures (—) and the experimentally found equilibrium partial pressures (○) as a function of temperature for sodium zirconate
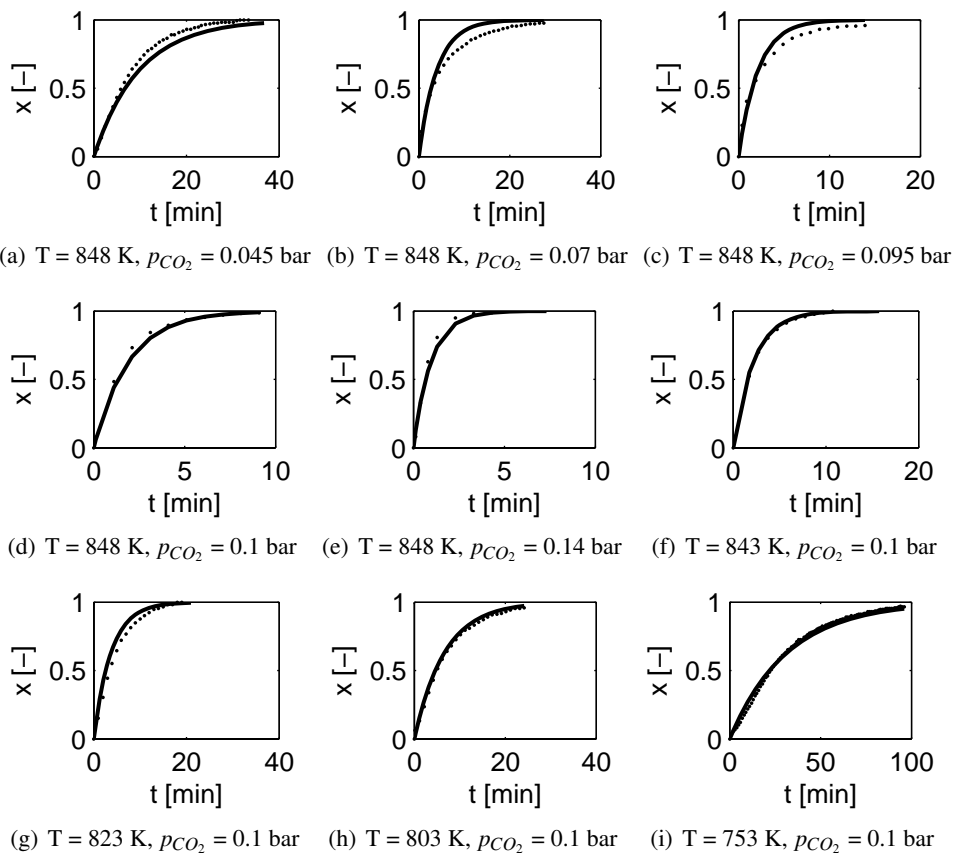
Figure 3.8: Experimental data $(\cdots)$ and the kinetic model (—) for capture of CO_2 on sodium zirconate.

Chapter 4

Reactor models

For simulations of a chemical reactor there a several different approaches, from simple plug flow models to rigorous CFD-models. A more complex model requires more computation and programming time. The goal of this work has been to develop a model that is able to describe the SE-SMR process in a fixed-bed reactor with large differences in operating conditions and that are stable and fast.

4.1 Transport equations

A starting point for a chemical reactor model is the general mass balance equation for a chemical species i in reacting fluid flow with varying density, temperature, and composition, which is written as:

$$\frac{\partial \rho_i}{\partial t} + \nabla \cdot (\rho_i \mathbf{v}) + \nabla \cdot J_i = S_i \tag{4.1}$$

The first term considers time variations in specific density of species i and the second part describes the transport of i by convective transport. The third term is the dispersion term which covers diffusion, transport by turbulence effects and backmixing due to packing. On the right hand side is the source term for the chemical species and it is typically a reaction rate term in a chemical reactor.

A transient model, i.e. a model that includes the first term in equation (4.1), is chosen in this work because the capture of CO_2 has a time-dependent nature. When the fractional conversion of the acceptor increases the capture rate decreases and eventually the conversion in the reactor drops below a set point. Then the acceptor has to be regenerated before a new cycle of hydrogen production can start. The model chosen is one-dimensional, but particularly if the reactor has indirect heating through the tube walls, a 2-D model could be useful to investigate the

41

radial temperature profiles in the reactor tube. However, this property has been neglected to reduce the computational time. In traditional SMR the gas velocities are high and modeling of this process has been done without including the dispersion term. [20] The capture kinetics on most sorbents are much slower that the reforming kinetics, though lower gas velocities have to be used to get satisfying conversion. Because of this, the convection does not necessarily dominate over the dispersion, and the dispersion term is taken into account in the reactor model. The dispersion term is described with an expression analogue to Fick's law, using an effective dispersion coefficient instead of the molecular diffusion:

$$J_i = D_{z,i}\rho_g \frac{\partial \omega_i}{\partial z} \tag{4.2}$$

After doing these assumptions a cross-sectional average of equation (4.1) reduces the model to one dimension, and after introducing mass fractions, the transport equation for porous media flow is given as:

$$\varepsilon_b \frac{\partial \rho_g \omega_i}{\partial t} + \frac{\partial}{\partial z}(\rho_g \omega_i u) = \frac{\partial}{\partial z}\left(\varepsilon_b D_{z,i}\rho_g \frac{\partial \omega_i}{\partial z}\right) + S_i \tag{4.3}$$

Equation (4.3) is solved for the components H_2, CO, CH_4 and CO_2. H_2O is the dominating component in the system and the mass fraction of H_2O is obtained from equation (4.4).

$$\sum_{i=1}^{5} \omega_i = 1 \tag{4.4}$$

For fast reactions in the catalyst pellet the transport to and inside the pellets can be a rate limiting step of the process. Pseudo-homogeneous models do not model the pellets explicitly and the reactor is modeled as one phase averaged over the gas and solid volumes. To account for a limiting intraparticle transport, efficiency factors between 0 and 1 are introduced in pseudo-homogeneous models. A heterogeneous model also models the transport and reaction inside the catalyst pellets and with this higher resolution the computational time will be higher. However, if the efficiency factors for the reaction in the pellets are unknown a heterogeneous model can be used to get necessary information whether the intraparticle transport is a rate limiting step and what effectiveness factor that has to be used in the pseudo-homogeneous model to account for this. In this work both a pseudo-homogeneous and two heterogeneous models has been programmed. The two different heterogeneous models have been made to investigate the difference in reactor performance when the sorbent and the catalyst are located in the same particle, and when they are placed in two different particles. In the latter case the conversions could be lower because of higher transport resistance when the CO_2 is not captured close to the catalyst.

For all the three different models, the mass balance of species i in the reactor bed is modelled by equation (4.3), the only difference is the source term, S_i, with the expressions shown in equation (4.5). For the one-particle (1-P) and two-particle (2-P) heterogeneous models the source term contains particle-bulk mass transfer terms and for the pseudo-homogeneous model (P-H) S_i is a reaction-rate term.

$$S_i = \begin{cases} a_{v,cat}k_i\rho_g(\omega^s_{i,cat} - \omega_i) + a_{v,cap}k_i\rho_g(\omega^s_{i,cap} - \omega_i) & \text{2-P} \\ a_{v,p}k_i\rho_g(\omega^s_{p,i} - \omega_i) & \text{1-P} \\ \frac{1-\varepsilon_b}{1+\alpha\frac{1-\varepsilon_{p,cat}}{1-\varepsilon_{p,cap}}}(1 - \varepsilon_{p,cat})\rho_{cat}v_i r_i & \\ \quad + \frac{1-\varepsilon_b}{1+\frac{1-\varepsilon_{p,cap}}{\alpha(1-\varepsilon_{p,cat})}}(1 - \varepsilon_{p,cap})\rho_{cap}v_{cap}r_{cap,i} & \text{P-H} \end{cases} \tag{4.5}$$

The bulk-particle mass transfer is modelled using a linear relationship between the mass transfer and the difference in bulk and particle surface mass fractions. The mass transfer resistance is included using a mass transfer coefficient. For the two-particle model, the mass-transfer term considers both mass-transfer from the catalyst and CO_2-acceptor particles; hence two terms are included in this case. There are also two terms in the source term for the pseudo-homogeneous model; the capture rate on the CO_2-acceptor and the reforming kinetics on the catalyst. For a case with both materials in one particle, the void fractions ($\varepsilon_{p,cat}$ and $\varepsilon_{p,cat}$) will be the same and the source term can be simplified.

The general heat balance in terms of temperature yields:

$$\rho C_p \frac{\partial T}{\partial t} + \rho C_p \mathbf{v} \nabla \cdot T = \nabla(\lambda \nabla T) + Q \tag{4.6}$$

Using the general heat balance (4.6) as a starting point and making the same assumptions as for the mass balance a one dimensional energy balance can be formulated for the temperature in the fixed bed reactor:

$$(\rho_g C_{pg}\varepsilon_b + \rho_s C_{ps})\frac{\partial T}{\partial t} + \rho_g u C_{pg}\frac{\partial T}{\partial z} = \frac{\partial}{\partial z}\left(\lambda_z \frac{\partial T}{\partial z}\right) + S'_i \tag{4.7}$$

In the same way as that for the component transport, the source term (S'_i) is

different for the different models, as defined in equation (4.8).

$$S_i' = \begin{cases} a_{v,cat}h(T - T_{cat}^s) + a_{v,cap}h(T_{cap}^s - T) + Q & \text{2-P} \\[2ex] a_{v,p}h(T_p^s - T) + Q & \text{1-P} \\[2ex] \dfrac{1-\varepsilon_b}{1+\alpha\frac{1-\varepsilon_{p,cat}}{1-\varepsilon_{p,cap}}}(1 - \varepsilon_{p,cat})\rho_{cat}\sum_i^3 \Delta H_{R_i}R_i \\[2ex] \qquad + \dfrac{1-\varepsilon_b}{1+\frac{1-\varepsilon_{p,cap}}{\alpha(1-\varepsilon_{p,cat})}}(1 - \varepsilon_{p,cap})\rho_{cap}\Delta H_{cap}r_{cap} + Q & \text{P-H} \end{cases} \tag{4.8}$$

The terms are analogous to the terms in the component transport equation, with heat-transfer terms for the heterogeneous models and a heat-of-reaction term for the pseudo-homogeneous model. Q in equation (4.8) is the heat transferred from the reactor walls. This term is given as:

$$Q = \frac{4U}{d_t}(T_w - T) \tag{4.9}$$

For the catalyst pellets the basis is also the general mass balance for a chemical species (4.1), but the assumptions made are different. Inside the catalyst and capture pellets convective terms are assumed not significant, because the pressure gradients will be very small, which make the convective term obsolete.[13] It is assumed spherical catalyst pellets, hence spherical coordinates is a natural choice. The general mass balance may be reduced to one dimension due to symmetry and using spherical coordinates the resulting equation for the chemical species i yields:

$$\varepsilon_p\frac{\partial \rho_g \omega_{p,i}}{\partial t} = \frac{1}{r^2}\frac{\partial}{\partial r}(r^2 D_{p,i}\rho_g\frac{\partial \omega_{p,i}}{\partial r}) + \bar{r}_i \tag{4.10}$$

Two different models based on these equations are simulated, one model with one particle (1-P) consisting of both the sorbent and the catalyst, and one model with two different particles (2-P). For the model with one type of particle the term $\bar{r}_i$ consists of both the reforming reaction-rates and the capture reaction-rate. For all components but CO_2, the capture-rate is zero. The reaction-rates in the pellets can then be expressed as:

$$\bar{r}_i = \begin{cases} \frac{1-\varepsilon_p}{1+\alpha}\rho_{cat}r_i + \frac{1-\varepsilon_p}{1+\frac{1}{\alpha}}\rho_{cap}r_{cap,i} & \text{1-P} \\[2ex] (1 - \varepsilon_{p,cat})\rho_{cat}r_i & \text{2-P, cat} \\[2ex] (1 - \varepsilon_{p,cap})\rho_{cap}r_{cap,i} & \text{2-P, cap} \end{cases} \tag{4.11}$$

In the model with two types of particles, equation (4.10) is solved for both of them. Like the equations for bulk component transport, equation (4.10) is solved

for four components and H_2O is calculated from the sum of mass fractions (4.4). In the sorbent particle, all components but CO_2 are inert, and only one component equation is solved in addition to the energy equation (4.12).

$$(\varepsilon_p \rho_g C_{pg} + (1-\varepsilon_p)\rho_p C_{ps})\frac{\partial T_p}{\partial t} = \frac{1}{r^2}\frac{\partial}{\partial r}(r^2 \lambda_p \frac{\partial T_p}{\partial r}) + \Delta H_R \tag{4.12}$$

The temperature equation for the particles (4.12) are solved in the same manner as the component equations, with different ΔH_R for the different models.

$$\Delta H_R = \begin{cases} \frac{1-\varepsilon_p}{1+\alpha}\rho_{cat}\sum_i^3(-\Delta H_{R_i})R_i + \frac{1-\varepsilon_p}{1+\frac{1}{\alpha}}\rho_{cap}r_{cap,i}(-\Delta H_{r,cap}) & \text{1-P} \\[3mm] (1-\varepsilon_{p,cat})\rho_{cat}\sum_i^3(-\Delta H_{R_i})R_i & \text{2-P, cat} \\[3mm] (1-\varepsilon_{p,cap})\rho_{cap}r_{cap,i}(-\Delta H_{r,cap}) & \text{2-P, cap} \end{cases} \tag{4.13}$$

Steady state reactor models, which are the most common in reactor simulations, do not usually use the full formulation of the pressure-velocity coupling. A very common way of modelling the pressure profile in the reactor is by using the Ergun equation:

$$\frac{dp}{dz} = -f\frac{\rho_g|u|u}{d_p} \tag{4.14}$$

This formulation has also been used in models with time variations, but problems were encountered when trying to employ this model in our case. At low gas velocities the Ergun formulation gave nice results and it is under these conditions that it was used by Xiu et al.[85] When the gas velocities were increased no stable solutions were found even at very short time-steps. Due to this problem it was decided to formulate the pressure-velocity coupling more rigorously including the transient and convectional terms of the momentum equation. The momentum equation for an averaged 1-D fixed-bed reactor can be given as[29]:

$$\frac{\partial}{\partial t}(\rho_g u) + \frac{\partial}{\partial z}(\frac{\rho_g uu}{\varepsilon_b}) = -\varepsilon_b\frac{\partial p}{\partial z} - \varepsilon_b f\frac{\rho_g|u|u}{d_p} \tag{4.15}$$

Viscous forces, gravitational forces and the wall friction forces are small compared to the friction term in porous media for reactor conditions used in these simulations and hence neglected in the momentum equation. Compared to a standard momentum equation for gas flow, a porous media friction term, $(-\varepsilon_b f\rho_g|u|u/d_p)$, is added to the right hand side.

The continuity equation has to be solved in addition to the momentum equation to determine the pressure and velocity profiles. The bulk gas continuity equation yields:

$$\varepsilon_b\frac{\partial \rho_g}{\partial t} + \frac{\partial}{\partial z}(\rho_g u) = -R_{cap} \tag{4.16}$$

The capture kinetics, R_{cap}, are accounted for in the continuity since mass in terms of CO_2 is removed from the gas phase of the reactor bed.

4.2 Boundary conditions

To get a well-formulated set of equations for the reactor, boundary conditions have to be defined. At the inlet the properties of the inlet stream are used as boundary condition:

$$\left.\begin{array}{rl} \omega_i & = \omega_{i,f} \\ T & = T_f \\ \dot{m} & = \dot{m}_f \end{array}\right\} \text{ at } z = 0 \tag{4.17}$$

At the outlet the compositions and temperatures are not known, hence a different approach has to be used. It is common to assume that there are no gradients at the outlet and use the Danckwerts boundary condition, and this condition is used for the temperature and the mass fractions. The pressure at the outlet is assumed to be known, and is set as a constant pressure in the model. All the boundary equations at the outlet are given in equation (4.18).

$$\left.\begin{array}{l} \dfrac{\partial \omega_i}{\partial z} = 0 \\[2mm] \dfrac{\partial T}{\partial z} = 0 \\[2mm] p = p_{out} \end{array}\right\} \text{ at } z = L \tag{4.18}$$

In the particle phase the spherical particles are assumed to be symmetric, which means that there will be no gradients in the middle. At the outer surface, the species mass boundary condition is set based on the mass transfer to the particle. The diffusional transport at the surface equals the mass transport between the gas phase and the particles. Similar conditions are applied for the temperature at the surface.

$$\left(D_{p,i} \frac{\partial \omega_i}{\partial r} \right)_{r=r_p} = -k_i(\omega_{p,i} - \omega_i) \tag{4.19}$$

$$\left(\lambda_p \frac{\partial T_p}{\partial r} \right)_{r=r_p} = -h(T_p - T) \tag{4.20}$$

$$\left(D_{p,i} \frac{\partial \omega_i}{\partial r} \right)_{r=0} = 0 \tag{4.21}$$

$$\left(\lambda_p \frac{\partial T_p}{\partial r} \right)_{r=0} = 0 \tag{4.22}$$

4.3 Thermodynamics and parameters

The gas phase modeled is at moderate pressure and high temperatures and the ideal gas law should be sufficient to describe it, and the gas densities are calculated by using the ideal gas law:

$$\rho_g = \frac{p}{RT} \sum_i M_i y_i \tag{4.23}$$

The thermodynamic properties viscosity, heat capacity and heat conductivity of the gases are all calculated from relations in Poling et al.[61]
Gas viscosity:

$$\mu_i = \frac{A_i T^{3/2}}{T + B_i} \tag{4.24}$$

Gas heat capacity:

$$C_{pgi} = A_i T + B_i T^2 + C_i T^3 + D_i T^4 \tag{4.25}$$

Gas conductivity:

$$\lambda_i = A_i + B_i T + C_i T^2 + D_i T^3 \tag{4.26}$$

A, B, C and D in the relations given above are all material-specific constants. To get the property of the gas mixture a mole weighted sum is used for the properties listed above:

$$\mu_g = \sum_i y_i \mu_i \tag{4.27}$$

In reactor modeling there are some dimensionless groups that are commonly used in different contexts. The ones used in this work are given here:

$$\text{Reynold number:} \qquad Re_p = \frac{\rho u d_p}{\mu_g} \tag{4.28}$$

$$\text{Schmidts number:} \qquad Sc = \frac{\mu_g}{\rho_g D_m} \tag{4.29}$$

$$\text{Sherwood number:} \qquad Sh = \frac{k}{D_m d_p} \tag{4.30}$$

$$\text{Nusselt number:} \qquad Nu = \frac{h}{\lambda_g d_p} \tag{4.31}$$

$$\text{Prandtl number:} \qquad Pr = \frac{C_{pg}\mu}{\lambda_g} \tag{4.32}$$

Several different parameters are necessary in the model and these are based on empirical correlations from the literature. The axial dispersion coefficient ($D_{z,i}$) is calculated from equation (4.33):[18]

$$D_{z,i} = 0.73 D_{im} + \frac{0.5 u d_p}{1 + 9.49 D_{im}/(u d_p)} \tag{4.33}$$

The molecular diffusivities (D_{im}) of component i in the gas-mixture are calculated from the Wilke equation (4.34)[9] and the molecular binary diffusivities are calculated from relations in Poling et al.[61]

$$\frac{1}{D_{im}} = \sum_{k \neq i} \frac{y_k}{D_{ki}} \tag{4.34}$$

A correlation for the mass-transfer coefficient between the gas phase and the particle is given by:[81]

$$Sh = 2 + 1.1(Sc)^{1/3}(Re_p)^{0.6} \tag{4.35}$$

In equation (4.10), the effective diffusion coefficient in the particle $(D_{p,i})$ is calculated from the relationship in equation (4.36).

$$D_{p,i} = D_{im}\varepsilon_p/\tau \tag{4.36}$$

The heat-transfer coefficient between the gas phase and the particles are calculated using the analogy between heat- and mass-transfer replacing Sh and Sc with Nu and Pr in equation (4.35).

$$Nu = 2 + 1.1(Pr)^{1/3}(Re_p)^{0.6} \tag{4.37}$$

A relation for the effective axial bed conductivity is given by Yagi et al.:[90]

$$\frac{\lambda_z}{\lambda_g} = \frac{\lambda_z^0}{\lambda_g} + 0.75(Pr)(Re_p) \tag{4.38}$$

$\frac{\lambda_z^0}{k_g}$ in equation (4.38) is given by equation (4.39):

$$\frac{\lambda_z^0}{k_g} = \varepsilon_b + \frac{1 - \varepsilon_b}{0.139\varepsilon_b - 0.0339 + 2/3(\lambda_g/\lambda_p)} \tag{4.39}$$

Gas conductivities (λ_g) are estimated from the Eucken formula[10].

The void fraction in the bed is dependent of the size of the particles and a relation has been given that is valid for $\frac{d_p}{d_t} \leq 0.5$[16]:

$$\varepsilon_b = 0.4 + 0.05\frac{d_p}{d_t} + 0.412\left(\frac{d_p}{d_t}\right)^2 \tag{4.40}$$

A relation for the friction factor used in equation (4.15) is given in equation (4.41).[23]

$$f = 6.8\frac{(1 - \varepsilon_b)^{1.2}}{\varepsilon_b^3}Re_p^{-0.2} \tag{4.41}$$

4.4 Reaction kinetics

The steam methane reforming and the water-gas shift reaction kinetics can be described by three equations, two of which are independent:

$$1. \quad CH_4 + H_2O \Leftrightarrow CO + 3H_2 \tag{4.42}$$

$$2. \quad CO + H_2O \Leftrightarrow CO_2 + H_2 \tag{4.43}$$

$$3. \quad CH_4 + 2H_2O \Leftrightarrow CO_2 + 4H_2 \tag{4.44}$$
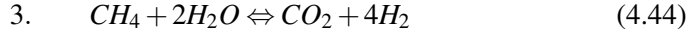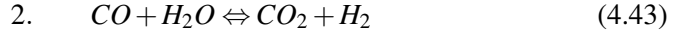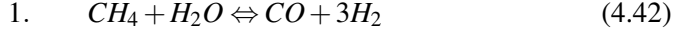
The kinetics of these reactions have been described by Xu and Froment:[89]

$$R_1 = \frac{k_1}{p_{H_2}^{2.5}} \left(p_{CH_4} p_{H_2O} - p_{H_2}^3 p_{CO}/K_1 \right) /DEN^2 \tag{4.45}$$

$$R_2 = \frac{k_2}{p_{H_2}} \left(p_{CO} p_{H_2O} - p_{H_2} p_{CO_2}/K_2 \right) /DEN^2 \tag{4.46}$$

$$R_3 = \frac{k_3}{p_{H_2}^{3.5}} \left(p_{CH_4} p_{H_2O} - p_{H_2}^4 p_{CO_2}/K_3 \right) /DEN^2 \tag{4.47}$$

DEN is given as $1 + K_{CO} p_{CO} + K_{H2} p_{H_2} + K_{CH_4} p_{CH_4} + K_{H_2O} p_{H_2O}/p_{H_2}$ and the kinetic constants taken from Xu and Froment are given below:[89]

$$k_1 = 0.01618 e^{-240100/R(1/T - 1/648)} \tag{4.48}$$

$$k_2 = 2.10 \cdot 10^{-5} e^{-67130/R(1/T - 1/648)} \tag{4.49}$$

$$k_3 = 0.001926 e^{-243900/R(1/T - 1/648)} \tag{4.50}$$

$$K_{CH4} = 0.1790 \cdot 10^{-5} e^{38280/R(1/T - 1/823)} \tag{4.51}$$

$$K_{CO} = 40.910 \cdot 10^{-5} e^{70650/R(1/T - 1/648)} \tag{4.52}$$

$$K_{H2O} = 0.4152 \cdot 10^{-5} e^{-88680/R(1/T - 1/823)} \tag{4.53}$$

$$K_{H2} = 0.0296 \cdot 10^{-5} e^{82900/R(1/T - 1/648)} \tag{4.54}$$

The equilibrium constants are taken from Twigg[78], and are given as a function of Z, where $Z = 1000/T - 1$.

$$K_1 = \frac{1.027 \cdot 10^{10}}{e^{(0.2514Z^4 - 0.3665Z^3 - 0.58101Z^2 + 27.1337Z - 3.2770)}} \tag{4.55}$$

$$K_2 = e^{(-0.29353Z^3 + 0.63508Z^2 + 4.1778Z + 0.31688)} \tag{4.56}$$

$$K_3 = K_1 K_3 \tag{4.57}$$

The capture reaction-rate ($r_{cap,i}$) is given by equation (4.58) where the relation for $\frac{dx}{dt}$ is different for the different sorbents.

$$r_{cap} = q_{max} \frac{dx}{dt} \tag{4.58}$$

The relationships and parameters for $\frac{dx}{dt}$ are given in chapter 3.

4.5 The algorithm

To solve the set of partial differential equations formulated for the reactor, they have to be discretized and the result is a set of algebraic equations. There are in principal three types of discretization methods: finite differences, finite element and finite volume method. The finite volume method is chosen in this case, because it is easy to implement and the conservative form assures that the conservation principle fulfilled. In this method the equations are integrated over the cell volumes, which are subvolumes of the reactor volume. The conservative general mass balance for a chemical species (4.1) is used as starting point in the following discussion. After introducing the relation for J_i from equation (4.2) the equation becomes:

$$\frac{\partial \rho_i}{\partial t} + \nabla \cdot (\rho_i u) = \nabla \cdot (D\rho \nabla \omega_i) + S_i \tag{4.59}$$

For the finite volume method the equation is first integrated over the cell volume ΔV:

$$\int_{\Delta V} \frac{\partial \rho_i}{\partial t} dV + \int_{\Delta V} \nabla \cdot (\rho_i u) dV + \int_{\Delta V} \nabla \cdot (D\rho_g \nabla \omega_i) dV = \int_{\Delta V} S_i dV \tag{4.60}$$

The Gauss divergence theorem states that:

$$\int_{\Delta V} \nabla \cdot f \, dV = \int_A \mathbf{n} \cdot f \, dA \tag{4.61}$$

The reactor is divided into cells and an illustration of one cell is shown in figure 4.1. The area, A, is the cross-section of the reactor, and the reactor is divided axially into subsections with length Δz.

Using equation (4.61) the volume integrals in equation (4.60) can be rewritten as surface integrals and by integrating over the time interval Δt the resulting equation is:

$$\int_{\Delta t} \frac{\partial}{\partial t} \left(\int_{\Delta V} \rho_i dV \right) dt + \int_{\Delta t} \int_A (\rho_i u) \cdot \mathbf{n} dA dt$$

$$+ \int_{\Delta t} \int_A ((D\rho_g \nabla \omega_i)) \cdot \mathbf{n} dA dt = \int_{\Delta V} S_i dV \tag{4.62}$$
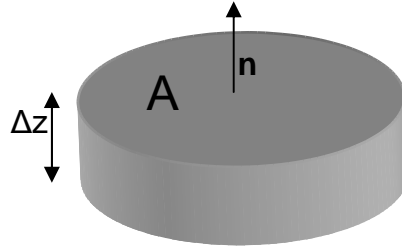
Figure 4.1: Illustration of one cell volume, ΔV with the surface of one cell, A, the normal vector, **n**, and the height of one cell, Δz, specified.
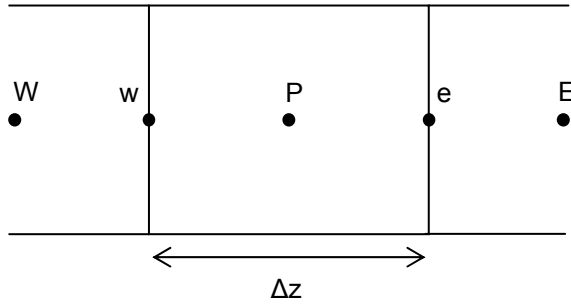
Figure 4.2: The cell volume, with the positions used in the dicretization marked.

When performing the integration over the surface area, reducing equation (4.62) to one dimension, and introducing mass fractions, the result becomes equation (4.63). The time derivative is approximated by a first order forward difference, $\frac{\partial f}{\partial t} = \frac{f - f^0}{\Delta t}$, where f^0 is the value in the previous time step. An implicit scheme is used which means that all variable values except one in the time derivative, are in the new time step. One cell volume for a one-dimensional model is shown in figure 4.5.

$$\varepsilon_b \frac{\rho_g \omega_i - \rho_g^0 \omega_i^0}{\Delta t} \Delta V + (\rho_g u \omega_i A)_e - (\rho_g u \omega_i A)_w$$
$$= (\varepsilon_b D_z \rho_g \frac{d\omega_i}{dz} A)_e - (\varepsilon_b D_z \rho_g \frac{d\omega_i}{dz} A)_w + S_i \Delta V \quad (4.63)$$

The surface areas of all cell volumes are equal and when setting $\Delta V = A\Delta z$ the area A can be cancelled out. First order upward differences is used for ω_i in the

convective terms, which means that if the flow direction is from left to right in figure 4.5 the value in point W is used for the variable in point w and the value in P is used for the point e. Central differences are used for the dispersion term, which means that $\frac{d\omega_i}{dz}\big|_e = \frac{\omega_{iE}-\omega_{iP}}{\Delta z}$. The mass flux $\rho_g u$ is written as F and the values on the cell faces is taken as the arithmetic mean between the nodal points. The algebraic equation then becomes for a flow direction from left to right:

$$\varepsilon_b \frac{\rho_{gP}\omega_{iP} - \rho_P^0\omega_{iP}^0}{\Delta t}\Delta z + (F_e\omega_{iP} - F_w\omega_{iW})$$
$$= \left(\varepsilon_b D_{ze}\rho_{ge}\frac{(\omega_{iE}-\omega_{iP})}{\Delta z}\right)$$
$$- \left(\varepsilon_b D_{zw}\rho_{gw}\frac{(\omega_{iP}-\omega_{iW})}{\Delta z}\right) + S_i\Delta z \quad (4.64)$$

For the solution of the discretized equation the equation is rearranged on the form shown in equation (4.65), where ω_i is the variable the equation is solved for.

$$a_P\omega_{iP} = a_W\omega_{iW} + a_E\omega_{iE} + S \quad (4.65)$$

For the general mass balance equation the expressions for the coefficients a_P, a_W, a_E and S for the inner volumes are shown below for a random flow direction.

$$a_W = D_w + \max(F_w, 0) \quad (4.66)$$
$$a_E = D_e + \max(-F_e, 0) \quad (4.67)$$
$$S = \varepsilon_b\rho_g\omega_{iP}^0\frac{\Delta z}{\Delta t} + S_{iP}\Delta z \quad (4.68)$$
$$a_P = a_W + a_E + F_e - F_w + \varepsilon_b\rho_P\frac{\Delta z}{\Delta t} \quad (4.69)$$

S_i is the source term for the different models given in equation (4.5). The energy equation is treated in the same way as the component mass balance, and the coefficients for the energy equation (4.7) are:

$$a_W = \lambda_{zw} + \max(F_W C_{pg}, 0) \quad (4.70)$$
$$a_E = \lambda_{zw} + \max(-F_E C_{pg}, 0) \quad (4.71)$$
$$S = (\varepsilon_b\rho_g C_{pg} + \rho_s C_{ps}) T_P^0\frac{\Delta z}{\Delta t} + S'_{iP}\Delta z \quad (4.72)$$
$$a_P = a_W + a_E + (\varepsilon_b\rho_g C_{pg} + \rho_s C_{ps})\frac{\Delta z}{\Delta t} \quad (4.73)$$

The term S'_i is the terms in equation (4.8) evaluated in the center point, P.
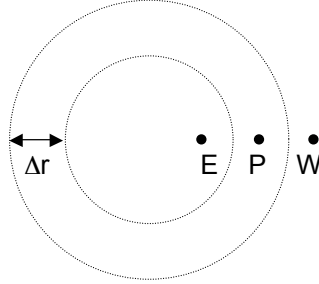
Figure 4.3: A planar projection of one cell volume ΔV in the solid particles.

For the catalyst pellets the procedure will be somewhat different. Contrary to the cylindrical reactor volume, the surface area of the cell in the spherical particle is different at different radial positions. A planar projection of one cell volume in the spherical particle is shown in figure 4.3. In the reactor transport equations the intercell-areas are equal and cancel out each other, while in the spherical case they do not cancel out. The cell surface areas are functions of the radius and are equal to $4\pi r^2$. The coefficients for the species mass balance in the catalyst pellet are:

$$a_W = \frac{\rho_{gw} D_p r_w^2 \Delta t}{\Delta r r_P^2 \varepsilon_p \rho_{gP}} \tag{4.74}$$

$$a_E = \frac{\rho_{ge} D_p r_e^2 \Delta t}{\Delta r r_P^2 \varepsilon_p \rho_{gP}} \tag{4.75}$$

$$S = \omega_P^0 + \frac{r_i \Delta t}{\varepsilon_p \rho_{gP}} \tag{4.76}$$

$$a_P = 1 + a_E + a_W \tag{4.77}$$

The parameters for the energy equation in the pellet are derived in the same way as for the species mass balance and given as:

$$a_W = \frac{\lambda_p r_w^2 \Delta t}{\Delta r r_P^2 (\varepsilon_p \rho_g C_{pg} + (1 - \varepsilon_p) \rho_p C_{ps})} \tag{4.78}$$

$$a_E = \frac{\lambda_p r_e^2 \Delta t}{\Delta r r_P^2 (\varepsilon_p \rho_g C_{pg} + (1 - \varepsilon_p) \rho_p C_{ps})} \tag{4.79}$$

$$S = T_P^0 + \frac{\Delta H_R \Delta t}{(\varepsilon_p \rho_g C_{pg} + (1 - \varepsilon_p) \rho_p C_{ps})} \tag{4.80}$$

$$a_P = 1 + a_E + a_W \tag{4.81}$$

The pressure-velocity coupling of the bulk phase is treated in a different way than the other equations. It is used a staggered grid for the velocity, which means that while all other variables are solved for in the ordinary nodal points, the velocity nodal points lie on the cell faces, i.e. in point e and w in figure 4.5. This is to avoid an instability called "the checker board problem" where a highly non-uniform field can act like a uniform field in the discretized equations.[80] To solve the momentum equation (4.15) and the continuity equation (4.16) an algorithm called semi implicit method for pressure linked equations (SIMPLE) is used.[60] Because there are no own differential equation for pressure, the pressure field is instead solved for a pressure correction. An initial pressure field is guessed and the velocities are calculated from this pressure field. Then the pressure corrections are found, and the pressure field and the velocities are corrected. This is done in an iteration loop until the pressure correction terms are zero. The pressure field that is calculated by this algorithm will only give a relative pressure field. To get the total pressure the absolute pressure in one of the nodal points has to be known. In this case the outlet pressure is set as the known pressure, and all pressures are calculated relative to this outlet pressure. The momentum equation equation (4.15) is discretized using the same method as the other transport equations, and the resulting coefficients for solution of the velocity field are:

$$a_E = \max(-F_e, 0) \tag{4.82}$$

$$a_W = \max(F_w, 0) \tag{4.83}$$

$$S = p_W - p_E + \rho_g^0 u^0 \frac{\Delta z}{\Delta t} \tag{4.84}$$

$$a_P = a_W + a_E + F_e - F_w + \varepsilon_b f \frac{\rho_g |u| \Delta z}{d_p \Delta t} + \rho_g \frac{\Delta z}{\Delta t} \tag{4.85}$$

A parameter called d_u is used in the pressure correction equation and is calculated as $1/a_P$ where a_P is calculated from equation (4.85). The coefficients for the pressure correction equation are:

$$a_E = \rho_{gE} d_{uE} \tag{4.86}$$

$$a_W = \rho_{gW} d_{uW} \tag{4.87}$$

$$S = F_w - F_e + \varepsilon_b (\rho_g^0 - \rho_g) \frac{\Delta z}{\Delta t} - R_{cap} \frac{\Delta z}{\Delta t} \tag{4.88}$$

$$a_P = a_W + a_E + \varepsilon_b \frac{\sum_i M_i y_i}{RT} \frac{\Delta z}{\Delta t} \tag{4.89}$$

The pressure fields and the velocities are updated using the calculated pressure

corrections:

$$p^{new} = p^{old} + p_c \qquad (4.90)$$

$$u^{new} = u^{old} + d_u(p_{ce} - p_{cw}) \qquad (4.91)$$

When the algebraic equations are solved directly the change in the variables can be large, and lead to oscillations and divergence of the solution. To avoid divergence, under-relaxation is used for all the equations. This means that instead of using the new calculated value, the variables is updated using partly the old iteration value and the new calculated value. Using the species mass fractions as an example, the iteration values are then updated like:

$$\omega_i = (1 - \beta)\omega_i^{old} + \beta\omega_i^{new} \qquad (4.92)$$

ω_i^{old} is the value from the previous iteration step, while ω_i^{new} is the value calculated from the coefficients. β is the relaxation factor and is between 0 and 1.

Solution of all the algebraic equations is done using the tri-diagonal matrix algorithm (TDMA).[77] It solves one-dimensional problems directly. By using the coefficients described in the previous section and the boundary conditions for each equation, the value of the variables in each nodal point are calculated.

A time splitting scheme is employed to make the algorithm more efficient, which means that not all equations are solved implicitly in each time step. At t = 0 the velocity-pressure coupling is implicitly solved without the component and energy transport equations in an initialization procedure to start the algorithm with consistent flow and pressure fields. For $t > 0$ the algorithm can be sketched like:

1. The temperature and component species equations are solved implicitly in an iteration procedure until convergence is reached. The pressure and the velocity are held constant in these calculations while the gas density, ρ_g, is updated continuously with the change in gas composition and temperature.

2. The pressure-velocity coupling is solved by an adapted SIMPLE-algorithm

3. The variables are stored and the algorithm proceeds to the next time-step with calculation of new temperature and component mass fractions.

In the heterogeneous models the particle equations are solved in step 1 simultaneously with the bulk transport equations using an implicit scheme. The particle equations and the bulk transport equations are thus solved in an iteration-loop until convergence is reached in the specific time-step, because the reaction rate terms and heat of reaction are non-linear.

Chapter 5

Simulation results

In this chapter of the thesis the results of simulations with the models described in the previous sections are presented. The kinetic models of section 3 have been used to simulate the capture reactions, and the results for SE-SMR with the different CO_2-acceptor materials are given in three separate sections of the chapter. The numerical computer environment Matlab has been used for all simulations, except for the simulations of a fluidized bed reactor used for comparison.

5.1   Simulations with Li_2ZrO_3 as CO_2-acceptor

A tube reactor with dimensions given in table 5.1 is simulated for SE-SMR with lithium zirconate as CO_2 acceptor. It is operated at a total pressure of 10 bar. Because the reforming kinetics are fast compared to the sorption rate, a high ratio between CO_2-acceptor and catalyst is used. The reactor is filled with steam (97 mole%) and a small amount of hydrogen at the desired temperature, 848K, at startup. The input to the reactor is methane and steam, in which the steam to methane ratio is set to 6. A high steam to carbon ratio is necessary to reach high conversions. A typical set of reactor conditions is presented in table 5.2 and these are referred to as standard conditions in the subsequent parts of the paper. The inlet mass flux, which is set to 0.77 kg/m^2s in the simulations, corresponds to a superficial gas velocity of 0.3 m/s. Physical properties of the reactor and materials are given in table 5.1.   A measure used for the performance of the reactor is the dry hydrogen mole fraction, which is the hydrogen mole fraction of the gas after steam is removed. The dry mole fractions are calculated as in equation (5.1).

$$y_i^d = \frac{y_i}{1 - y_{H_2O}} \tag{5.1}$$

Table 5.1: Physical parameters used in the simulations

$d_p(m)$	0.005
$d_t(m)$	0.1
$L(m)$	4
$\varepsilon_p(m)$	0.5
$\tau(-)$	3
$\rho_{cap,p}(kg/m^3)$	2500
$\rho_{cat,p}(kg/m^3)$	2300
$\lambda_p(W/mK)$	0.2
$C_{ps}(J/kgK)$	1000

Table 5.2: Standard reactor conditions

$P_{out}(bar)$	10
$T_f(K)$	848
$T_w(K)$	848
$\dot{m}_f(kg/m^2s)$	0.77
$\alpha(-)$	4

5.1.1 Assessing the need for heterogeneous models

For steam reforming, heterogeneous models or pseudo-homogeneous models including an effectiveness factor have been used to simulate the process. The methane steam reforming process has been found to be strongly intra-particular diffusion-controlled[20] and to check if this is the case also for the SE-SMR, heterogeneous models have been formulated. Dry hydrogen mole fractions at t = 200 s are plotted in figure 5.1 and no significant differences are observed in the reactor performances for the pseudo homogenous, one-particle heterogeneous and two-particle heterogeneous models. No advantage of heterogeneous models is observed at standard conditions because the capture of CO$_2$ is the limiting step of the process. In contrast to the steam methane reforming where the reactions are very fast, the capture kinetics are slow compared to the diffusion processes. The search for new and better CO$_2$-acceptors is in progress, and with faster kinetics, heterogeneous models or pseudo-heterogeneous with effectiveness factors may be needed. In the present case, a pseudo-homogeneous model with effectiveness factors of one gives satisfying results for the particle dimensions used.

With larger particles the process will move towards being controlled by intra-particle diffusion. Figure 5.2 shows the dry hydrogen outlet mole fraction at standard conditions for both one and two particles after 50 seconds. The conversion in the reactor decreases with larger particles. The effect is, as expected, greater for the two-particle model and occurs at smaller particle sizes. The reason for this is that for two particles the CO$_2$ have to diffuse out of the catalyst particle, through the bulk phase, and into the sorbent and this becomes the limiting step. For one particle the diffusion to and from the bulk phase becomes the limiting step at larger particle diameters.
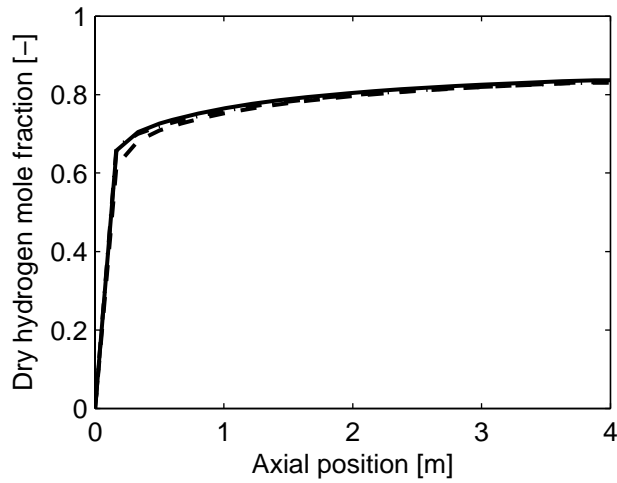
Figure 5.1: Comparison in dry hydrogen mole fraction with pseudo-homogeneous model (——),one-particle heterogeneous model ($\cdot$ —) and two-particle heteroge-neous model (— —) at t = 200 s, standard conditions, Li_2ZrO_3 as acceptor.
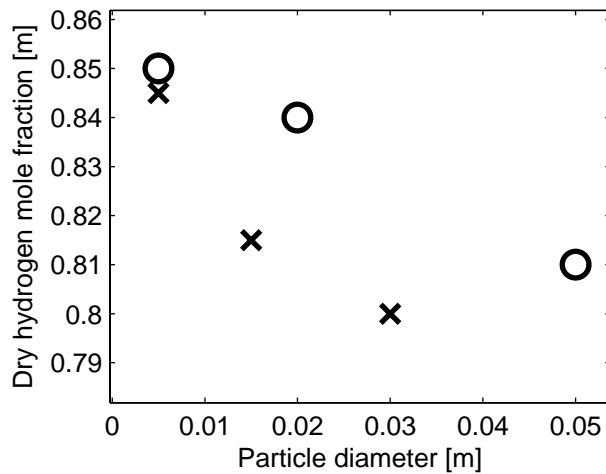
Figure 5.2: Outlet dry hydrogen mole fraction at standard conditions for different particle sizes from one-particle (o) and two-particle (x) heterogeneous models at t = 50 s, Li_2ZrO_3 as acceptor.

5.1.2 Effects of solving the full momentum equation

A full velocity-pressure coupling is solved for the models described in section 4. This part of the simulation is computationally expensive and the necessity for this model part is tested by comparing its results with other simpler model formulations. The two alternative approaches used are to assume constant gas velocity through the reactor or assume a constant mass flux through the reactor. When the full total continuity equation is not solved, the solution might be different. Comparisons of the velocity and hydrogen mole fraction that were obtained in the reactor are shown in figure 5.3 and figure 5.4 respectively. As seen in figure 5.3, the velocity in the reactor is clearly different in these cases. These phenomena
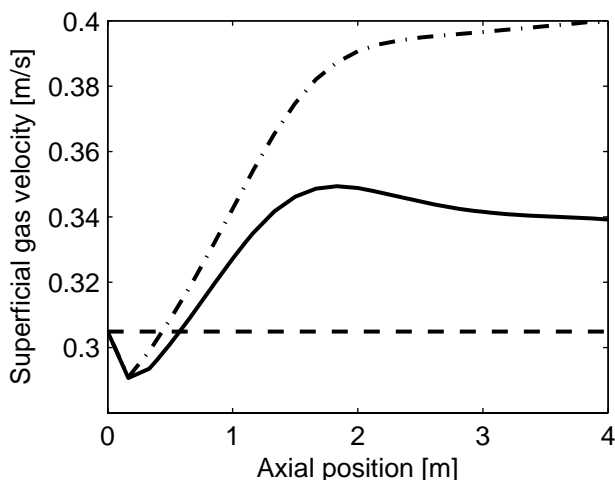
Figure 5.3: Comparisons of velocity in the reactor with full solution of the momentum and continuity equations (———), constant mass flux (— —) and constant velocity (·—), reactor profiles at t = 200 s, standard conditions, Li$_2$ZrO$_3$ as acceptor.

affects the solution of all other transport equations and the impact on the hydrogen mole fractions is seen in figure 5.4. Comparing the results from the different models, the simulation with constant velocity is more similar to the rigorous model than the one with constant mass flux, although the difference is fairly equal with opposite signs. The effect of removal of mass can be observed in figure 5.3. After a decrease in velocity in the first part of the reactor due to changes in temperature and gas composition, the velocity reaches a maximum before it slightly drops in the last part of the reactor. An important future goal in the process development is to find CO$_2$-acceptors with faster kinetics than the one used in this work.
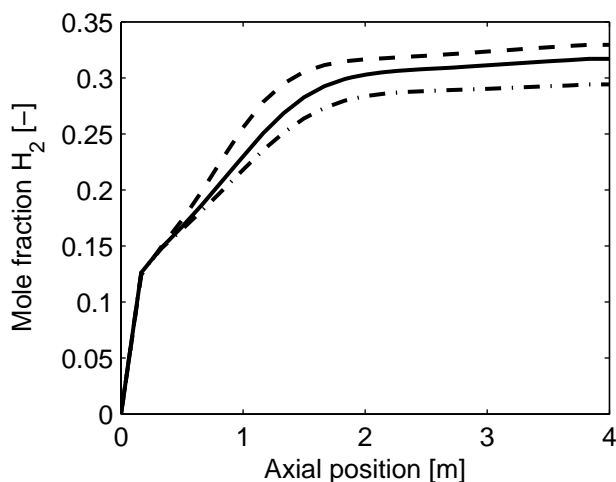
Figure 5.4: Comparisons of hydrogen mole fraction in the reactor with full solution of the momentum and continuity equations (——), constant mass flux (— —) and constant velocity (·—), reactor profiles at t = 200 s, standard conditions, Li_2ZrO_3 as acceptor.
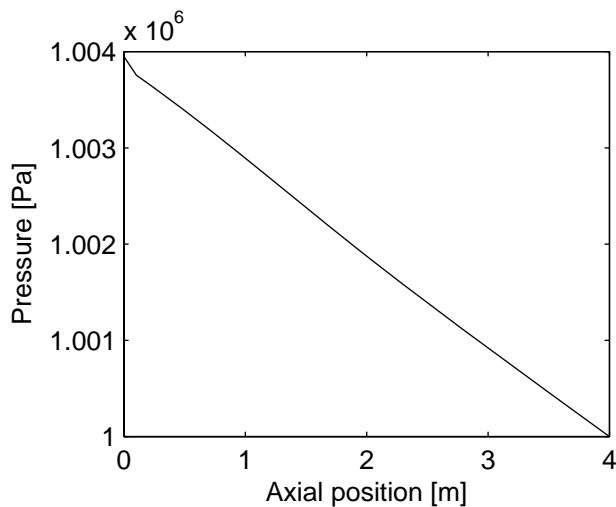
Figure 5.5: Pressure in the reactor as function of axial position, at t = 200 s, standard conditions, Li_2ZrO_3 as acceptor.

In cases with faster capture kinetics the effect of not solving the continuity equation is most likely even larger. The pressure drop in the system is dependent

of the gas velocity and since small velocities have to be used to get satisfying conversion, the pressure drop in the system is small. Figure 5.5 shows the pressure as a function of axial position, Li_2ZrO_3 as acceptor. It is observed that the pressure is approximately constant through the reactor. It is known that low pressure drops in the reactor could lead to misdistribution of flow which is not taken into account in this model. With faster capture kinetics higher gas velocities can be used, which will lead to significantly higher pressure gradients in the reactor and thus removing a possible misdistribution of flow. An important drawback for the model with solution of the momentum and total continuity equations is the computational cost. The simulations with the full model can take as much as four times the computational time used for the other two cases. To calculate the pressure and velocities a rigorous model including the transient and convective terms in the momentum-equation (4.15) are used. Other models for transient sorption reactors contain a simpler formulation with only the Ergun equation (4.14) to get the pressure[88], but a full formulation was chosen because it makes the model much more robust. The simpler Ergun formulation is sufficient in reactors with small changes in gas volume, but with changes both in gas composition, temperature and removal of CO_2 these terms should be included.

$$\frac{dp}{dz} = -f \frac{\rho_g |u| u}{d_p} \tag{5.2}$$

Figure 5.6 shows the density profile in the reactor and the large changes in gas density is seen.
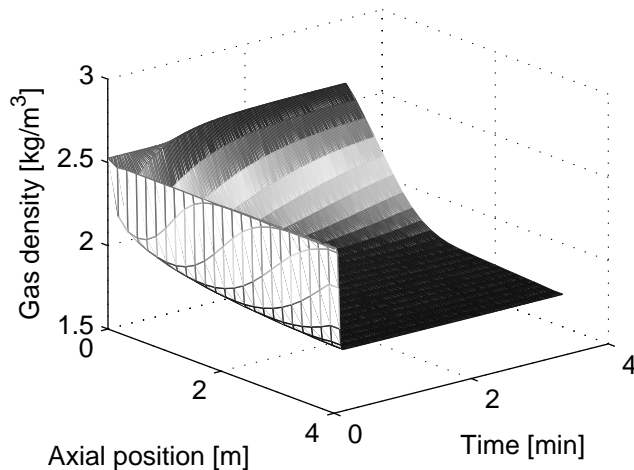
Figure 5.6: Gas density as a function of time and axial position, standard conditions, Li_2ZrO_3 as acceptor.

The Ergun equation is not on a transient form, hence the pressure will be set up instantaneously as a function of velocity. This means that changes in density because of variation in temperature, composition and total mass not will affect the pressure directly as it does in the full formulation. In some cases, dependent on the initial and boundary conditions, this will give non-physical solutions like reversal of the flow in the reactor, solutions that are not observed when using the more rigorous model. Therefore, the more rigorous model is chosen to be able to handle different kind of operating conditions although it is computationally more expensive.

5.1.3   Reactor performance

A long tube reactor of 20 meters is simulated to show the performance of the reactor as a function of the length. The thermodynamic upper limit of hydrogen purity on dry basis at 10 bar total pressure and a temperature of 848 K with lithium zirconate as acceptor is 91 mole%. Very long reactors and low space velocities are required to reach the equilibrium composition due to the limitations of the CO_2-capture kinetics. Contour plots for the dry hydrogen fraction are shown in figure 5.7. It is observed that a dry hydrogen mole fraction of 0.8 is reached just after 2 meters of the reactor, but to get close to the thermodynamical limit a significantly longer reactor is needed. At 10 meters a dry mole fraction of 0.88 is reached, but after ten more meters the dry hydrogen fraction has only increased by about 0.02 and equilibrium conversion is not reached. The main reason for this is the slow capture kinetics at low partial pressures of CO_2. A reaction order of 2 with respect to partial pressures of CO_2 in equation (3.15) makes the process slow as it reaches the thermodynamical limitation.

The partial pressure contour profiles of CO_2 are shown in figure 5.8, and it can be observed that the partial pressure is decreasing very slowly in the second half of the reactor. The partial pressure is about 10000 Pa after 4 meters, after that the capture kinetics decreases considerably and 16 meters of reactor are needed to reach a partial pressure of 5000 Pa. The equilibrium partial pressure is about 3500 Pa at 848 K. The CO_2 content is also shown in figure 5.9, but here in terms of dry mole fraction. This mole fraction is considerably less than for the traditional steam methane reforming, where the outlet dry CO_2 mole fraction is in the region 0.10-0.15. This is obviously due to the capture of CO_2 in the reactor and it also affects the CO-content, which is shown as dry mole fraction in figure 5.10. For SMR typical values for dry CO mole fractions is 0.02-0.03, hence the amount of CO in the reactor is considerably less for the SE-SMR. The same tendency as with longer reactors is observed when lowering the gas velocity. Figure 5.11 shows dry hydrogen purity as function of axial position in a 4 meter long reactor at t = 200 s,
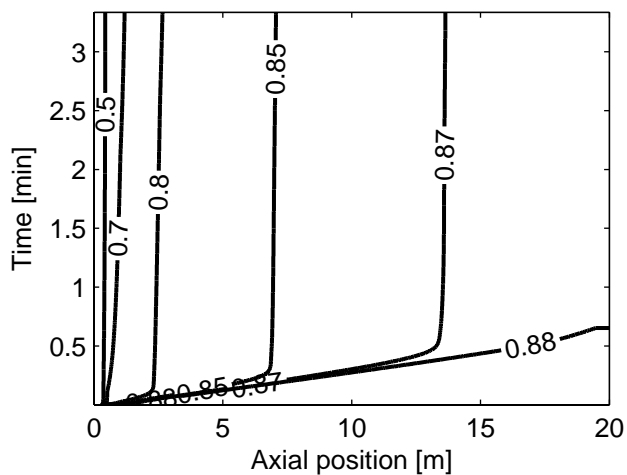
Figure 5.7: Contour plots of the dry hydrogen mole fraction as function of time and axial position at standard conditions, Li_2ZrO_3 as acceptor.
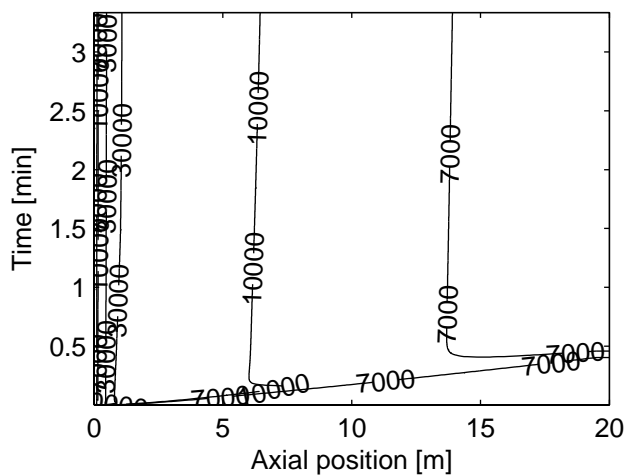
Figure 5.8: Contour plots of the partial pressure of CO_2 [Pa] as function of time and axial position at standard conditions, Li_2ZrO_3 as acceptor.
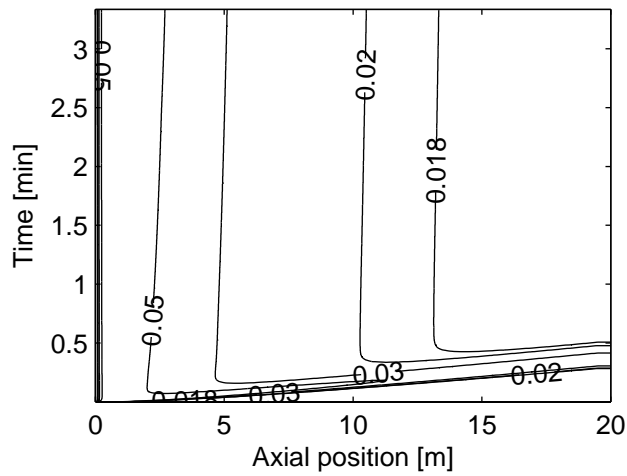
Figure 5.9: Contour plot of the dry CO_2 mole fraction as function of time and axial position at standard conditions, Li_2ZrO_3 as acceptor.
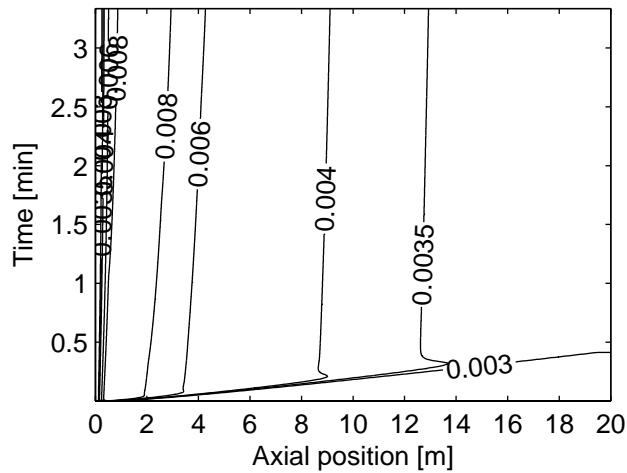
Figure 5.10: Contour plot of the dry CO mole fraction as function of time and axial position at standard conditions, Li_2ZrO_3 as acceptor.
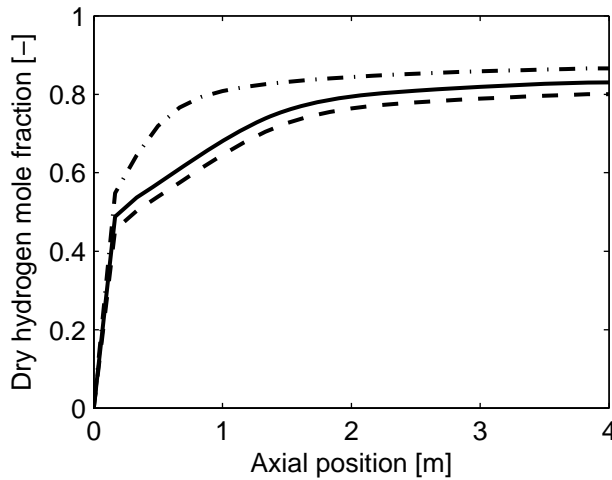
Figure 5.11: Comparison in dry hydrogen mole fraction at different inlet superficial gas velocities. u_f = 0.6 m/s (— —), 0.3 m/s(——), 0.1 m/s (· —) at t = 200 s, Li_2ZrO_3 as acceptor.

and the conversion is strongly dependent on the gas velocity.

As mentioned, there are equilibrium limitations for the process, and with lower steam to carbon ratios the equilibrium conversion will be lowered. A relatively low throughput of steam is desirable to get a more energy-efficient process, but as seen in figure 5.12 product purity is considerably lowered when the S/C ratio is lowered. This ratio is an important aspect for the process and must be evaluated carefully in a full design. Traditional SMR uses S/C-ratios down to 3 and has at this point an advantage to the SE-SMR with Li_2ZrO_3 as acceptor[57]. The CO_2-capture kinetics are dependent on the fractional conversion of the CO_2-acceptor. Thus, the sorption kinetics will be slower with time. This will lead to lower conversion in the reactor as shown in figure 5.13. The dry hydrogen mole fraction falls from about 0.84 in the first minute and slowly decreasing to below 0.8 after 40 minutes. After that the hydrogen content decreases even more, and after 50 minutes it is down to just above 70%, which is close to the thermodynamic limit for steam methane reforming without CO_2-acceptor at these conditions. The lower dry hydrogen mole fraction in the reactor is due to the decreasing capture kinetics. The decrease in kinetics is mainly due to the dependence of fractional conversion, but also because the temperature in the reactor is lowered. The reactor is heated with a constant temperature at the wall which is set equal to the inlet gas temperature. As observed in figure 5.14 this is not sufficient to sustain the temperature in the reactor. This leads to slower sorption kinetics and hence lower conversion. Fig-
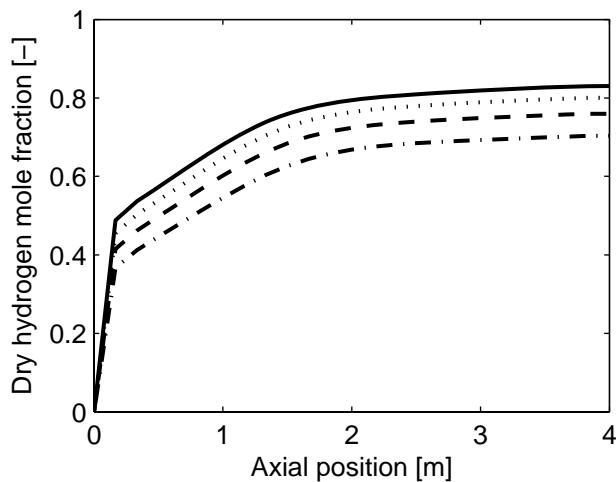
Figure 5.12: Comparison in dry hydrogen mole fraction at different steam to carbon ratio at t = 200 s. S/C = 6(——), 5 (···), 4 (— —), 3 (— ·), Li_2ZrO_3 as acceptor.
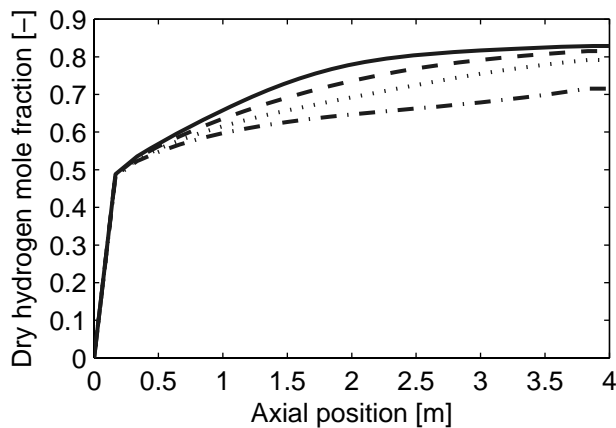
Figure 5.13: Dry hydrogen mole fraction as function of axial position, at 5 min (—), 20 min (— —), 40 min (···), and 70 min (· —), standard conditions, Li_2ZrO_3 as acceptor.
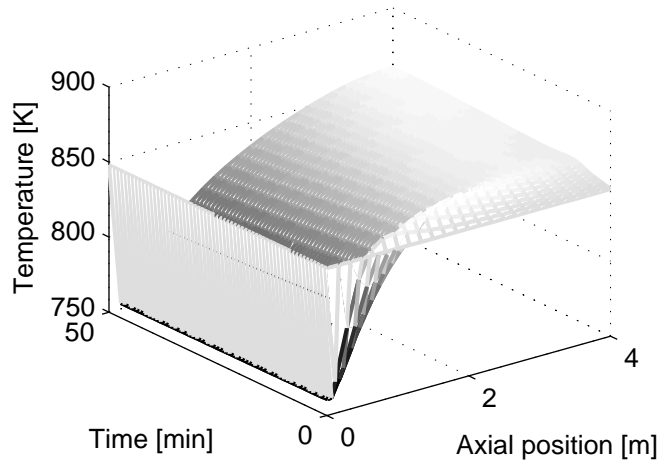
Figure 5.14: Temperature in the reactor as function of time and axial position, standard conditions, Li$_2$ZrO$_3$ as acceptor.

ure 5.15 shows the fractional conversion of the acceptor. In the timespan used in the simulations, which is about an hour, the acceptor has reached about 80% of its capacity.

It is observed that high conversions of methane can be reached with Li$_2$ZrO$_3$ as acceptor, but high steam to carbon ratios and long residence times have to be used. The simulations show that the capture kinetics is the limiting step in the process and a pseudo-homogenous model is sufficient for the reactor simulations. The inclusion of the rigorous formulation of the momentum equation was found to give significant differences in the solution of the models and the model including this formulation is used in the following parts of the thesis.
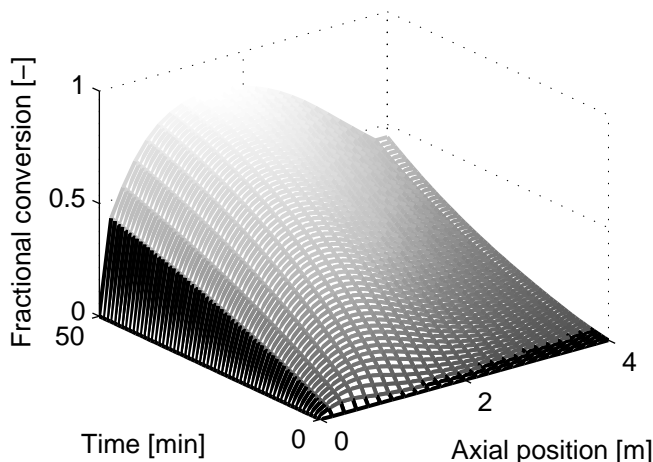
Figure 5.15: Fractional conversion of the acceptor as function of time and axial position, standard conditions, Li_2ZrO_3 as acceptor.

5.2   Simulations with Li_4SiO_4 as CO_2-acceptor

A 6 meter long reactor with an outlet pressure of 20 bar is simulated for SE-SMR with lithium silicate as CO_2-acceptor. The reactor is a multitube reactor with tube diameters of 10 cm, which is a typical diameter in SMR. At startup the reactor is filled with steam (97 mole %) and a small amount of hydrogen (3 mole %) at a temperature of 848 K. The feed to the reactor is steam and methane at a steam-to-carbon ratio of 5 with a temperature of 848 K. The inlet mass flux is set to 5 kg/m^{2}s. This gives an inlet superficial gas velocity of about 1 m/s. An acceptor-to-catalyst ratio of 4 is used in the reactor. The operating conditions are chosen to yield a dry hydrogen mole fraction out of the reactor above 0.85 and the highest production capacity possible. The steam-to-carbon ratio is an important parameter for the energy efficiency of the process. High S/C-ratios give lower thermal efficiency, but give higher equilibrium conversion. For traditional SMR typical S/C-ratios are about 3, but in SE-SMR with Li_4SiO_4 as acceptor a S/C-ratio of 5 is needed to get satisfying conversion. This gives a feed to the reactor consisting of 16.7 % methane and 83.3 % steam on molar basis. The physical parameters of the reactor and the materials are given in table 5.3.

Table 5.3: Physical parameters used in the simulations

$d_p(m)$	0.005
$d_t(m)$	0.1
$L(m)$	6
$\varepsilon_p(-)$	0.5
$\tau(-)$	3
$\rho_{cap,p}(kg/m^3)$	2600
$\rho_{cat,p}(kg/m^3)$	2300
$\lambda_p(W/mK)$	0.2
$C_{ps}(J/kgK)$	1000

5.2.1   Assessing the need for a heterogeneous model

Heterogeneous models or pseudo-homogeneous models including an efficiency factor are conventionally used to simulate the steam methane reforming. The sorption enhanced process has been simulated with heterogeneous models to see if there were any significant intra-particular resistances. Two different ways of installing the CO$_2$-acceptor in the reactor is looked into: one particle with both catalytic and capture properties or two different types of particles with catalytic and capture properties. Figure 5.16 shows the dry hydrogen mole fraction as function of axial position at t = 50 s. Particles with diameter of 5 mm have been used and the results from the heterogeneous simulations with one type of particle is about the same as for the pseudo-homogeneous model, but for the two-particle model the results are different. With two particles, the CO$_2$ has to diffuse out of the catalytic particle, through the bulk phase and into the acceptor-particle and according to the simulations this is a limiting step in the process. With one particle, this is not a problem, since the CO$_2$ is captured in the same particle as it is produced. This is contrary to the results with Li$_2$ZrO$_3$ as acceptor, where no mass-transfer limitations were found for two particles. A pseudo-homogeneous model with efficiency factors of one is used for simulating the fixed-bed reactor in the latter parts of this article, thus one particle with both properties is assumed.
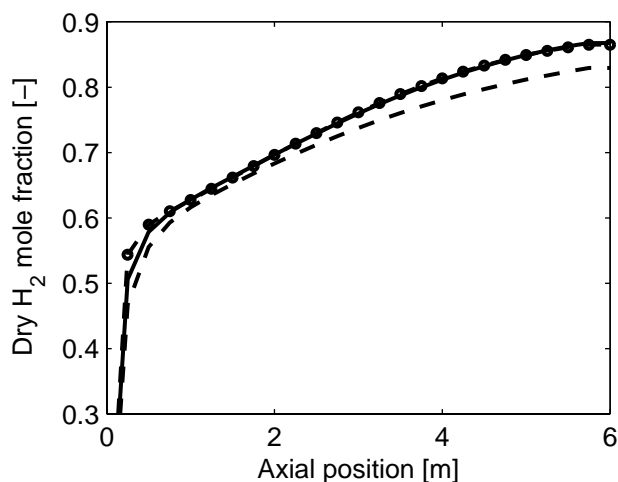
Figure 5.16: Comparison of dry hydrogen mole fraction between pseudo-homogeneous model (——), one-particle heterogeneous model (∘ ∘ ∘) and two-particle heterogeneous model (— —) with Li_4SiO_4 as acceptor, P = 20 bar, T_f= 848 K, S/C-ratio = 5, u_f = 1 m/s.
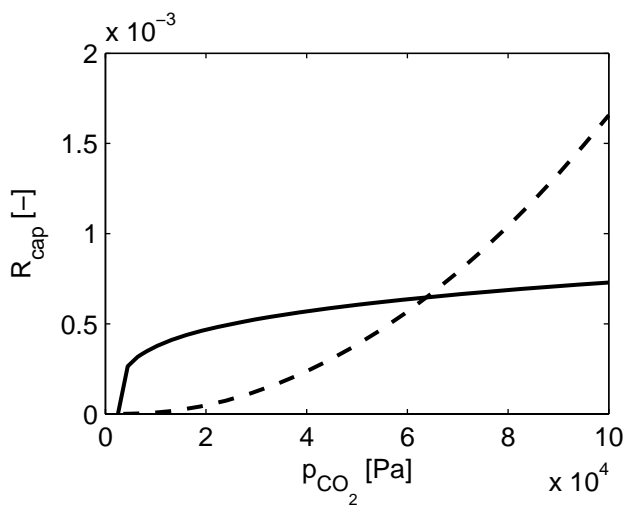
Figure 5.17: CO_2-capture kinetics for fresh sorbent as a function of partial pressure of CO_2 for Li_2ZrO_3 (— —) and Li_4SiO_4 (—).

The work reported in section 5.1 was with Li_2ZrO_3 as the CO_2-acceptor and the results show that the kinetics of Li_2ZrO_3 are slow, particularly at low partial

pressures of CO$_2$, which lead to low production capacities if a dry hydrogen fractions in the range 0.8-0.85 should be reached. The kinetics of Li$_4$SiO$_4$ are faster, and this can be clearly observed in figure 5.17, where the capture kinetics of both Li$_2$ZrO$_3$ and Li$_4$SiO$_4$ are shown as a function of partial pressure of CO$_2$. Figure 5.18 shows the outlet dry hydrogen mole fraction as a function of time, and the large difference in performance with the two different acceptors is seen. A dry hydrogen mole fraction of 0.87 can be reached at the outlet of the reactor when Li$_4$SiO$_4$ is used as acceptor, compared to 0.75 for the Li$_2$ZrO$_3$. However, it is observed that high purity of hydrogen can only be sustained for a short period of time in the case of Li$_4$SiO$_4$ as acceptor. This is because the capture kinetics is decreasing with fractional conversion of the sorbent and the conversion of methane is not sustained when the kinetics is slower.
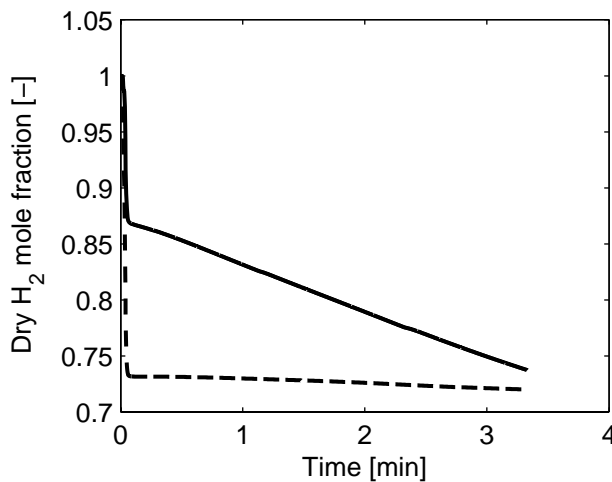
Figure 5.18: Dry hydrogen mole fraction at the outlet as function of time for Li$_2$ZrO$_3$ (— —) and Li$_4$SiO$_4$ (—), P = 20 bar, T$_f$= 848 K, S/C-ratio = 5, u$_f$ = 1 m/s, Li$_4$SiO$_4$ as acceptor.

Figure 5.19 and figure 5.20 show contour plots for inlet mass fluxes of respectively 2 kg/m^{2}s and 5 kg/m^{2}s, corresponding to gas velocities of 0.4 and 1 m/s. It is observed that the maximum conversion is the same in both cases, but that the conversion is sustained for a longer period for the lower throughput. The equilibrium dry hydrogen mole fraction with Li$_4$SiO$_4$ as acceptor is just below 0.88 at the working conditions and as observed in figure 5.18 and figure 5.20 the conversion is close to equilibrium at low fractional conversion of the acceptor.

Figure 5.21 shows the fractional conversion of sorbent as a function of time and space for the inlet mass flux of 5 kg/m^{2}s, and at a fractional conversion of 0.1
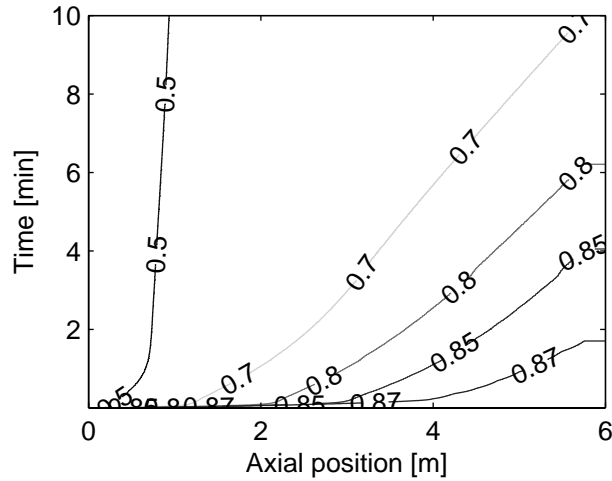
Figure 5.19: Contour plot of dry hydrogen mole fraction as function of time and axial position at an inlet mass flux of 2 kg/m²s with Li_4SiO_4 as acceptor, P = 20 bar, T_f= 848 K, S/C-ratio = 5, Li_4SiO_4 as acceptor.
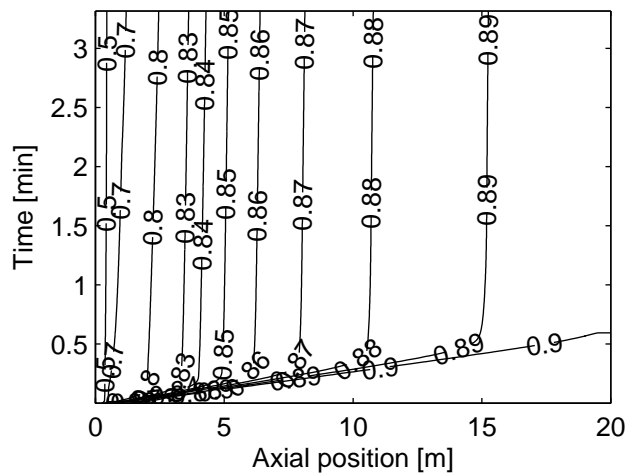
Figure 5.20: Contour plots of dry hydrogen mole fraction as function of time and axial position at an inlet mass flux of 5 kg/m²s, P = 20 bar, T_f= 848 K, S/C-ratio = 5, Li_4SiO_4 as acceptor.

the kinetics have decreased in such a way that the conversion of CH$_4$ reached at the outlet of the reactor is lowered considerably. The capture kinetics is second order with respect to fractional conversion and decreases rapidly as CO$_2$ reacts with the sorbent. Clearly, this is also the reason why the conversion is high for a longer period at lower gas throughput, where the sorbent is kept at lower fractional conversion for a longer period of time. Longer reactors and/or less gas throughput is necessary if the dry hydrogen fraction should be kept at a high level for longer periods in a fixed-bed reactor.
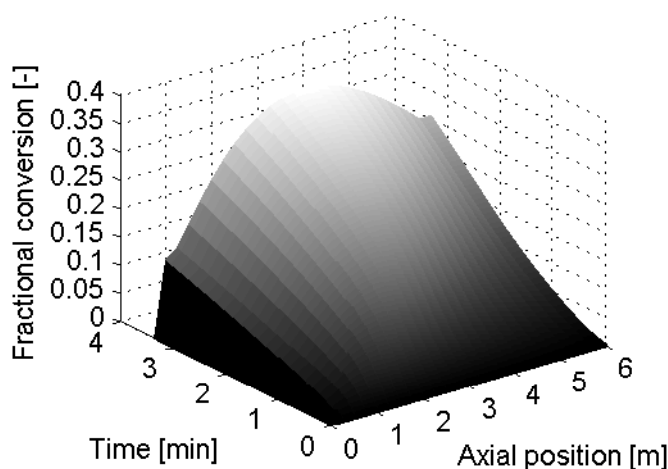
Figure 5.21: Fractional conversion of CO$_2$-acceptor as function of time and space, P = 20 bar, T$_f$= 848 K, S/C-ratio = 5, u$_f$ = 1 m/s, Li$_4$SiO$_4$ as acceptor.

Figure 5.22 shows the temperature in the reactor as a function of time and space for a simulation of 200 s. It can be observed that the temperature in the reactor is dropping dramatically, especially near the inlet. A wall temperature of 848 K is used to heat the reactor but that is not enough to attain the temperature at a constant level. The total enthalpy of reaction is positive for the process and energy has to be supplied if the temperature in the reactor should be kept constant and this has to be done more efficiently than in the simulations.
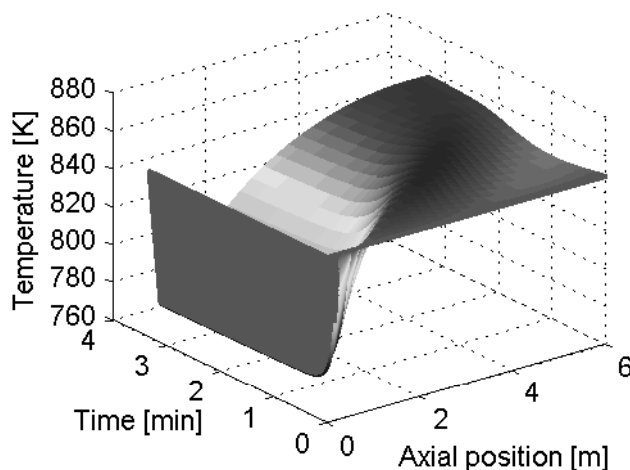
Figure 5.22: Reactor temperature as function of time and space with Li_4SiO_4 as CO_2-acceptor, P = 20 bar, T_f= 848 K, S/C-ratio = 5, u_f = 1 m/s.

5.2.2   Comparisons with fluidized bed

A possible alternative to the fixed-bed reactor is a fluidized bed reactor. The fluidized bed offers some advantages in terms of heat integration and possibilities for continuous regeneration of the sorbent. Simulations of a bubbling-bed reactor have been carried out to compare some of the results to the fixed-bed reactor. The model used to simulate the fluidized bed reactor is a rigorous 2-dimensional dynamic model based on granular theory described by Lindborg et al.[43] In Figure 5.23 the dry hydrogen mole fraction as function of axial position is shown for a fixed-bed reactor and a fluidized bed reactor. The reactor beds have equal length and the reactors are operated adiabatically at the same operating conditions. It is observed in figure 5.23 that the conversion in the fixed-bed reactor is considerably higher than for the fluidized bed reactor at equal bed heights. This could result from several reasons: the bubbles in the fluidized bed reactor give inferior contact between the gas-phase and the particles, the fluidized bed reactor has a higher void fraction which give lower particle density, the fluidized bed reactor gives a lower outlet temperature. The difference in temperature profiles can be seen in figure 5.24 and an almost constant temperature in the fluidized bed is observed. This could be an advantage compared to the fixed-bed reactor in terms of easier heat supply, but in these simulations which are adiabatic, it leads to a lower outlet temperature. This results in a lower equilibrium conversion, and the importance of controlling the outlet temperature is seen.
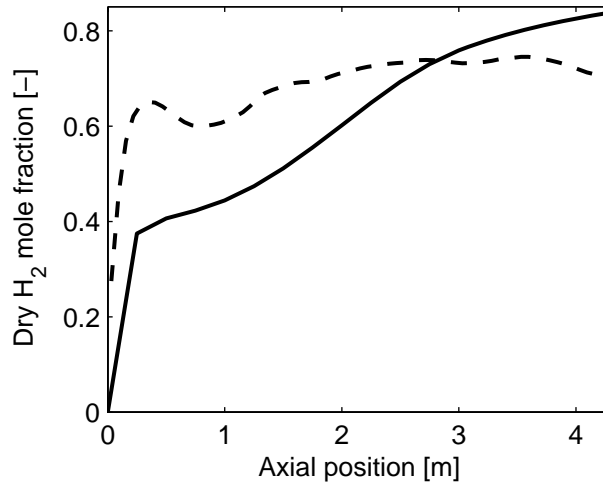
Figure 5.23: Comparison of dry hydrogen mole fraction as function of axial position between the fixed-bed reactor model(——) and fluidized bed reactor model(— —) with Li_4SiO_4 as acceptor at t = 85 s, adiabatic conditions, P = 20 bar, T_f= 848 K, S/C-ratio = 5, u_f = 0.4 m/s.
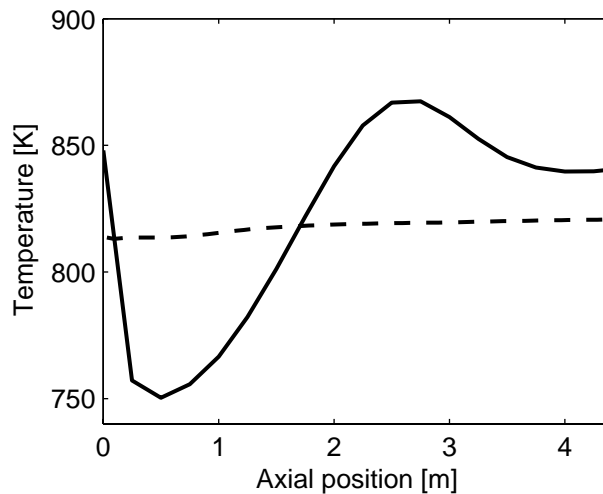
Figure 5.24: Comparison of temperature as function of axial position between the fixed-bed reactor model(——) and fluidized bed reactor model(— —) with Li_4SiO_4 as acceptor at t = 85 s, adiabatic conditions, P = 20 bar, T_f= 848 K, S/C-ratio = 5, u_f = 0.4 m/s.

The lower particle density in the fluidized bed does not have a large effect on the simulated composition. In the fluidized bed reactor an average void fraction of about 0.6 is observed while the void-fraction in the fixed-bed reactor is just above 0.4. A fixed-bed reactor with the same void-fraction as the average void-fraction in the fluidized bed was simulated to test for the effect of lower particle density. The results from these simulations are quite similar to the results from the lower void-fraction. This is because the actual local gas velocity is lowered when the void fraction is increased, which weighs up for the lowered total reaction-rates due to lower particle density, and the conversion is not affected significantly. In figure 5.25 the outlet dry hydrogen mole fraction as a function of time is shown, and the conversion is consistently lower in the fluidized bed reactor due to the already listed reasons.
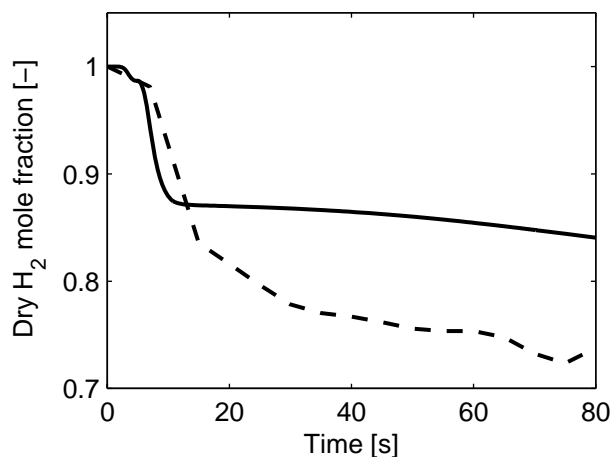
Figure 5.25: Comparison of the outlet dry hydrogen mole fraction between the fixed-bed reactor model(——) and fluidized bed reactor model(— —) as a function of time with Li_4SiO_4 as acceptor at adiabatic conditions, P = 20 bar, T_f = 848 K, S/C-ratio = 5, u_f = 0.4 m/s

Isothermal simulations for the two reactor concepts were also carried out. This was done to see if the lower conversion was solely due to the lower outlet temperature or if there is a combination of mechanisms. Figure 5.26 shows the dry hydrogen mole fractions in the reactors at isothermal conditions. Here, it is observed that the conversion in the fluidized bed reactor also is lower for the isothermal case. This means that the inferior gas-particle contact in the fluidized bed give a significant decrease in the reactor performance. In a reactor design this means that even if the heat integration is in such an efficient manner that the reactor is close to isothermal, a longer fluidized bed reactor is needed to reach comparable

conversions with the fixed-bed reactor. To reach more definite conclusions in the comparison between the reactor concepts, the regeneration of the sorbent also has to be looked into.
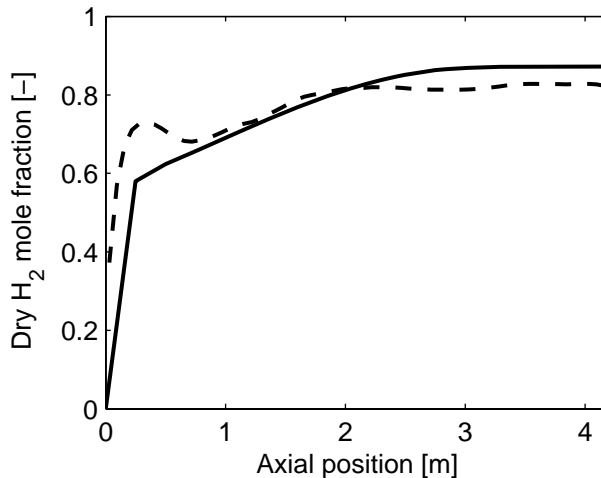
Figure 5.26: Comparison of the outlet dry hydrogen mole fraction between the fixed-bed reactor model(——) and fluidized bed reactor model(— —) as a function of time with Li$_4$SiO$_4$ as acceptor at t = 85 s, isothermal conditions, P = 20 bar, T$_f$= 848 K, S/C-ratio = 5, u$_f$ = 0.4 m/s

The simulations performed show that hydrogen with a purity of 0.87 can be produced at a temperature of 848 K, steam-to-carbon ratio of 5 and a pressure of 20 bar with Li$_4$SiO$_4$ as CO$_2$-acceptor. This is a significant improvement compared to the process with Li$_2$ZrO$_3$ as CO$_2$-acceptor. The capture rate decreases with fractional conversion of the sorbent and high conversion of CH$_4$ can not be sustained for more than a couple of minutes with high gas throughput in the reactor. Simulations also show that if one type of particle with both catalytic and capture properties is used, the capture rate is the limiting step of the process. This changes when two particles are used, where some intra-particular diffusion resistance occurs. This yields for a particle diameter of 5 mm. If a fluidized bed reactor is used for the SE-SMR the large temperature gradients will be smaller. The simulations also show that for larger production capacities the cycling times for the fixed-bed reactor will be very short, a problem that will vanish using a fluidized bed reactor with continuous regeneration of particles. The simulations of a fluidized bed reactor show that a longer reactor-bed is needed to reach satisfying conversions compared to a fixed-bed reactor. In the simulations the lower conversion in the fluidized bed is because of the lower outlet temperature and because of inferior

gas-particle contact due to gas-bubbles.

5.3 Simulations with Na_2ZrO_3 as CO_2-acceptor

Simulations of a fixed bed reactor has also been carried out using Na_2ZrO_3 as CO_2-acceptor. The kinetic expression is taken from section 3.3 and the capture rate is significantly faster than for Li_4SiO_4 and Li_2ZrO_3. The equilibrium partial pressure is also lower, and this means that higher gas velocities and lower S/C-ratios can be used and still get high conversions of methane. A comparison between the capture kinetics as a function of partial pressure of CO_2 with fresh sorbent is shown in figure 5.27. Except for a small pressure interval where the kinetics of Li_4SiO_4 is comparable, the capture kinetics on Na_2ZrO_3 is much faster than for the two sorbents used in the SE-SMR simulations in the previous subsections. It has also much lower equilibrium partial pressure at this temperature, which means that the maximum conversion at equal operating conditions is higher. The equilibrium partial pressure of the sorbent is the partial pressure where $r_{cap} = 0$ in figure 5.27.
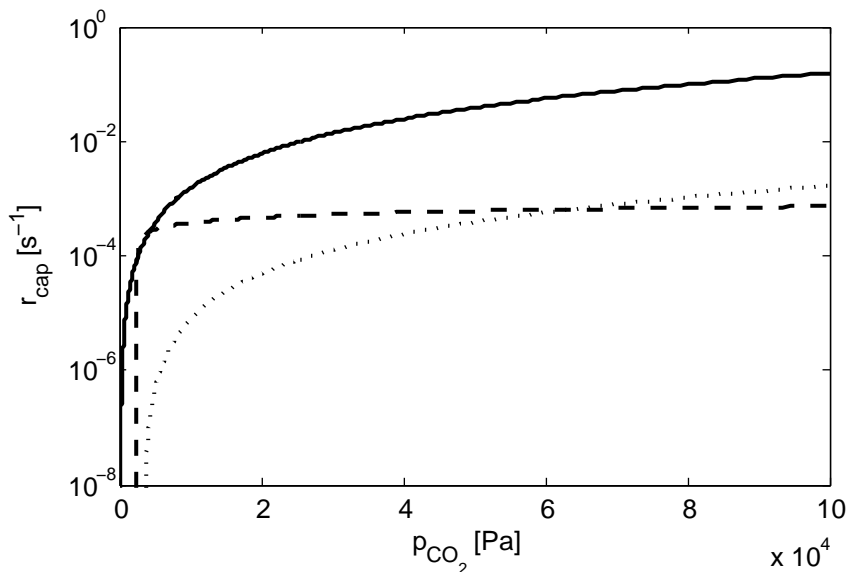
Figure 5.27: Comparison of the capture rate as function of partial pressure of CO_2 on Na_2ZrO_3 (—), Li_4SiO_4 (— —), and Li_2ZrO_3 ($\cdots$) with fresh sorbent.

Table 5.4: Standard reactor conditions for simulations with Na_2ZrO_3 as CO_2-acceptor

$P_{out}(bar)$	10
$T_f(K)$	848
$T_w(K)$	848
$\dot{m}_f(kg/m^2s)$	5
$\alpha(-)$	3

The simulations of the reactor are carried out under different operating conditions to observe the effect of changing these, but the standard conditions are given in table 5.4. The pressure drop in the reactor is dependent primarily on gas velocity and particle size, and with better reaction kinetics, higher gas velocities can be used in the reactor. This leads to higher pressure drops and with a particle diameter of 5 mm and gas velocity of 2 m/s, the pressure drop in the 10 meter long reactor would be about 3 bar. To get lower pressure drop a particle diameter of 1 cm has been used in most of the simulations. This gives a pressure drop in the 10 m long reactor of about 1.2 bar. The physical properties used in the simulations are shown in table 5.5.

Table 5.5: Physical parameters used in the simulations with Na_2ZrO_3 as acceptor

$d_p(m)$	0.01
$d_t(m)$	0.1
$L(m)$	10
$\varepsilon_p(m)$	0.5
$\tau(-)$	3
$\rho_{cap,p}(kg/m^3)$	2000
$\rho_{cat,p}(kg/m^3)$	2300
$\lambda_p(W/mK)$	0.2
$C_{ps}(J/kgK)$	1000
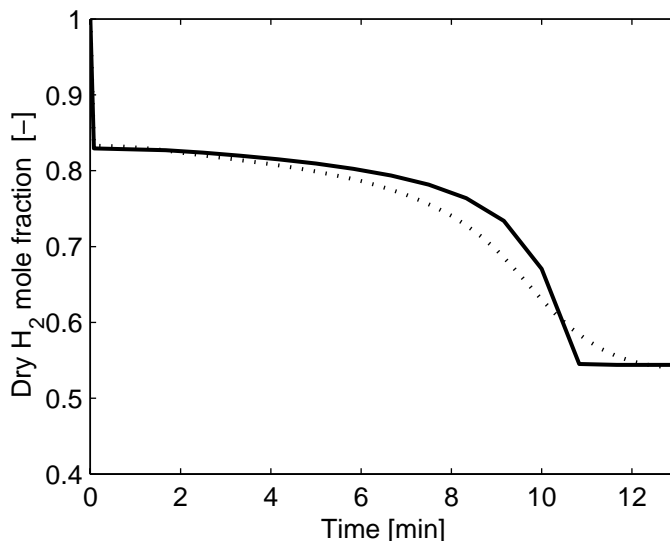
Figure 5.28: Comparison between a pseudo-homogeneous model (——) and a one-particle heterogeneous model (···) for simulation of SE-SMR with Na_2ZrO_3 as CO_2-acceptor

5.3.1   Assessing the need for a heterogeneous model

For the simulations of Li_4SiO_4 and Li_2ZrO_3 the simulations with heterogeneous models showed no significant mass-transfer resistance between the bulk phase and the particles or inside the particles with the one-particle model. The faster kinetics of Na_2ZrO_3 could change the rate limiting step, and simulations have been carried out to assess if a pseudo-homogenous model is sufficient for the simulations of SE-SMR. The equilibrium dry hydrogen mole fraction at standard conditions is about 0.92, but with the operating conditions from table 5.4 it is not possible to reach this. In figure 5.28 a comparison between the one-particle heterogeneous model and the pseudo-homogeneous model is shown. Figure 5.28 shows that there are some differences in the results from the two models. Particularly after some time, when the sorption rate drops, the transport have an effect on the results. Because the capture rate is time dependent, a time dependent efficiency factor would be necesarry to address this. The standard way to define the effectiveness factor is:[20]

$$\eta = \frac{\text{rate of reaction with pore diffusion resistance}}{\text{rate of reaction with surface conditions}} \tag{5.3}$$

In figure 5.29 the CO_2 mole fraction fields inside the pellets at 4, 6 and 8 minutes are shown. Here it is observed how the capture zone moves down the reactor with

(a) t = 4 min

(b) t = 6 min

(c) t = 8 min
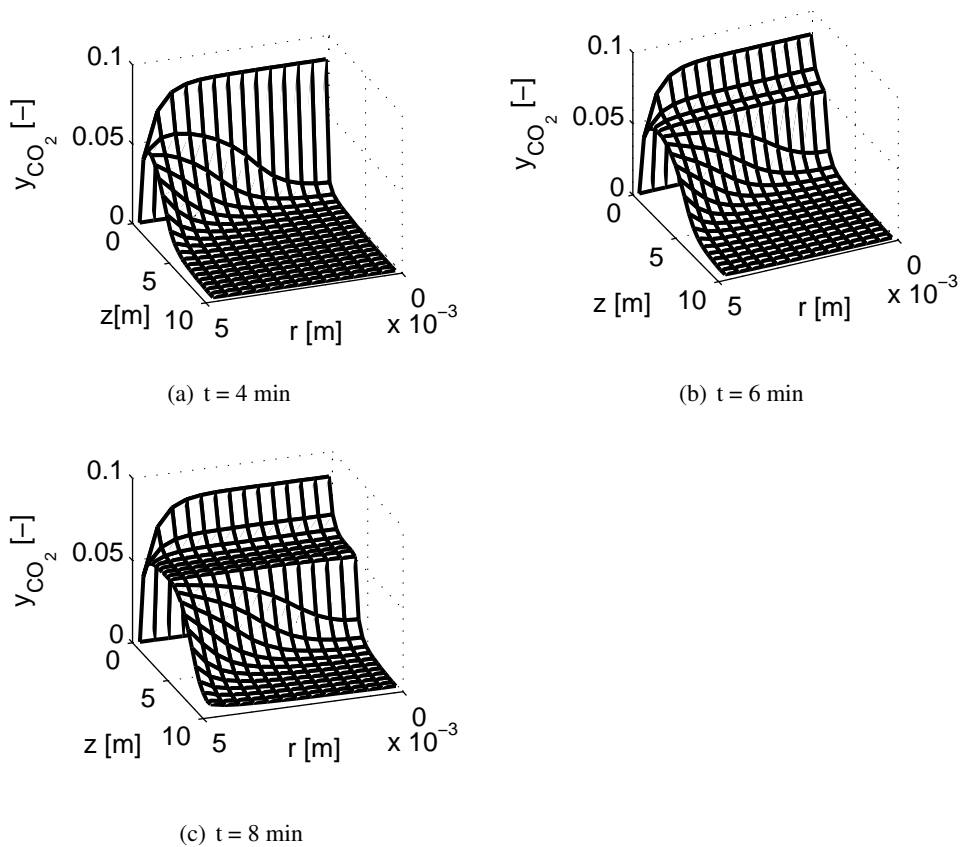
Figure 5.29: The mole fraction of CO$_2$ as function of radial position in the particle (r) and the axial position in the reactor (z) at 4, 6, and 8 minutes for SE-SMR with Na$_2$ZrO$_3$ as acceptor with operating conditions given in table 5.4.
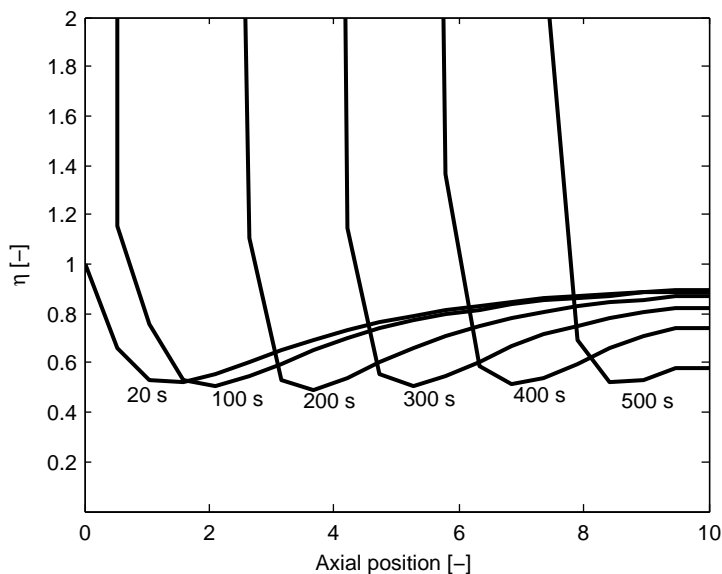
Figure 5.30: The effectiveness factor (η) for the capture reaction in SE-SMR with Na_2ZrO_3 as acceptor as function of axial position at 100, 200 300, 400, and 500 s, operating conditions given in table 5.4.

time. At 4 minutes the CO_2 is captured within the same particles as the main conversion of methane, and there are intraparticle gradients of the CO_2 mole fraction in the whole reactor. As the acceptor close to the reactor entrance is filled with CO_2 the capture-zone moves, but the main production of CO_2 from the reforming reactions is still in the beginning of the reactor. As it is seen in figure 5.29(b) and more clearly in figure 5.29(c) it is a zone in the reactor where equilibrium of SMR has been reached and no CO_2 is captured because the sorbent is filled with CO_2. This plateau with constant CO_2-fraction is clearly observed in figure 5.29(c). When the gas reaches a zone with fresh sorbent, the CO_2-content decreases and hence the conversion of the SMR reactions increases. Figure 5.30 shows the effectiveness factor for the capture reaction as function of axial position at different times in the reactor. This is calculated as in equation (5.4).

$$\eta = \frac{1}{V_p} \frac{\int_V r_{cap,p} dV}{r_{cap}^s} \tag{5.4}$$

Figure 5.30 shows how the zone with transport limitations moves through the reactor with time. Just after startup the sorbent surfaces are fresh in the whole reactor and the surface reaction is fast. For all times, but 20 seconds, there is a

(a) t = 4 min

(b) t = 6 min

(c) t = 8 min
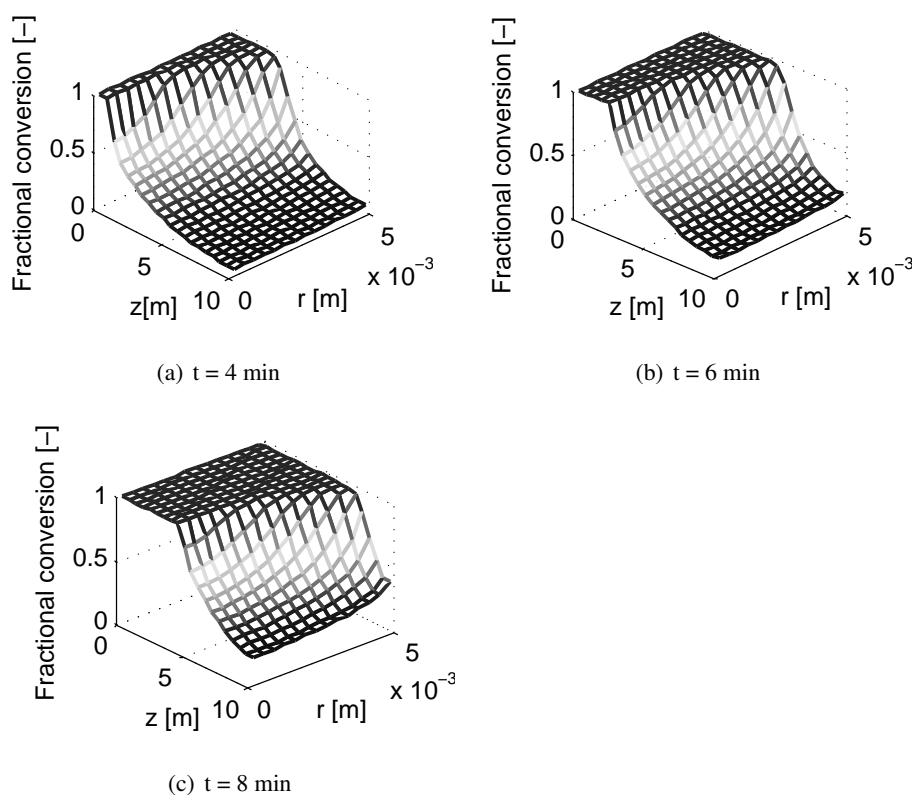
Figure 5.31: The fractional conversion of the solid as function of radial position in the particle (r) and the axial position in the reactor (z) at 4, 6, and 8 minutes for SE-SMR with Na$_2$ZrO$_3$ as acceptor with operating conditions given in table 5.4

zone with very high effectiveness factor downstream from the entrance, because the acceptor-surface is saturated with CO$_2$. This leads to a very low capture rate and the denominator in equation (5.4) is close to zero. The zone with very high effectiveness factor becomes longer with time as more and more solid is converted. The area with the lowest effectiveness factor is where the capture rate is highest and hence the diffusivity is lowest compared to the CO$_2$-capture rate. The conversion of the solid as function of radial position in the particle and of axial position after 4, 6 and 8 minutes are shown in figure 5.31 and the gradients in solid conversion in the particle are seen. In the zone where the capture rate is highest, the gradients inside the particles are highest, and this will also give the lowest effectiveness factor. The heterogeneous simulations discussed up until now have been isothermal to isolate the mass transfer effects. Adiabatic simulations have also been carried out, and the

(a) t = 4 min

(b) t = 6 min

(c) t = 8 min
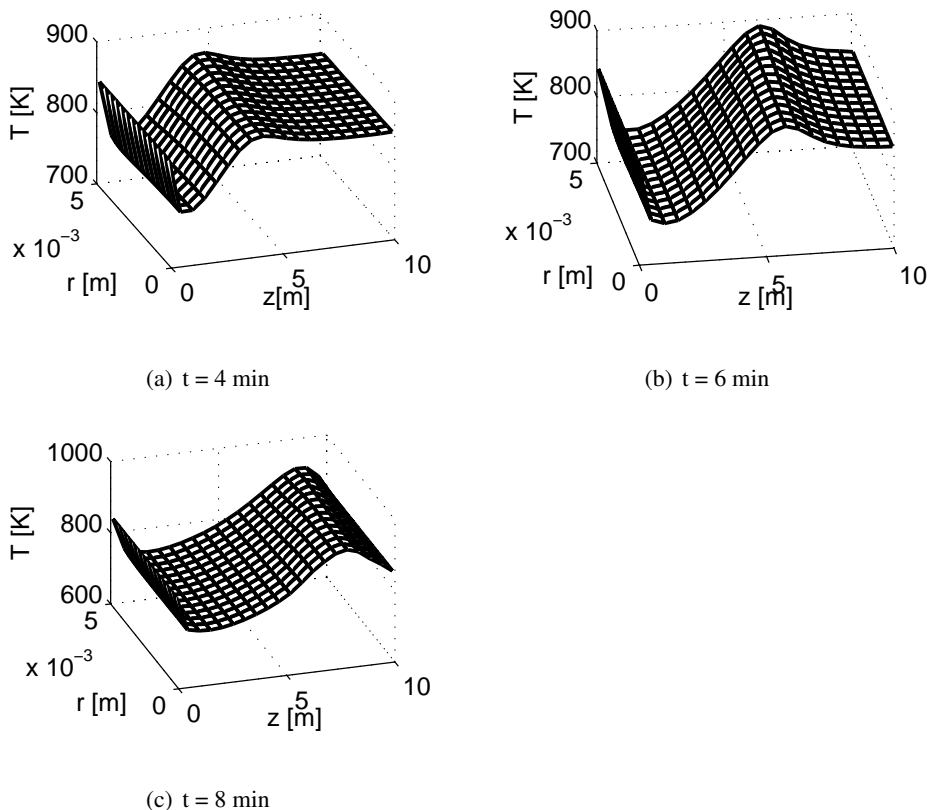
Figure 5.32: The temperature in the solid as function of radial position in the particle (r) and the axial position in the reactor (z) at 4, 6, and 8 minutes for SE-SMR with Na_2ZrO_3 as acceptor with operating conditions given in table 5.4

change in reactor temperature does affect the reactor performance, and this will be discussed more throughout later. However, the temperature gradients inside the solids will be small. This is shown in figure 5.32 where the solid temperature as a function of radial position in the solid pellets and the axial position is presented at 4, 6, and 8 minutes. As shown in this section, there are some mass-transfer effects that influence the performance of the reactor. It is also difficult to use a pseudo-homogenous model with an effectiveness factor, because this factor would change with time. The heterogeneous model with one-particle is therefore used in the following sections.

5.3.2 Reactor performance

The reactor have been simulated with different operating conditions and as previously shown in figure 5.28, the dry hydrogen mole fraction with the conditions given in table 5.4 gives a dry hydrogen outlet mole fraction about 0.83-0.84. A contour diagram of the dry hydrogen mole fraction for an isothermal simulation is shown in figure 5.33. It is seen that a dry hydrogen mole fraction above 0.8 is sustained for about 5 minutes. The contour plot of the CO$_2$ dry mole fraction for the same simulation is shown in figure 5.34. It is observed that to achieve a dry hydrogen mole fraction above 0.8 the dry mole fraction of CO$_2$ has to be below 0.003. For a steam to carbon ratio of 3 this corresponds to a wet mole fraction of below 0.002. The outlet pressure of this reactor is 10 bar, which means that the partial pressure of CO$_2$ has to be kept below 2000 Pa to achieve a dry hydrogen mole fraction above 0.8. However, this is quite far from the equilibrium CO$_2$ partial pressure at 848 K. The equilibrium is at about 150 Pa, and the conversion is controlled by the kinetics for the reactor conditions used in this simulation. If equilibrium had been reached at these conditions, a dry hydrogen mole fraction of about 0.92 would be observed.
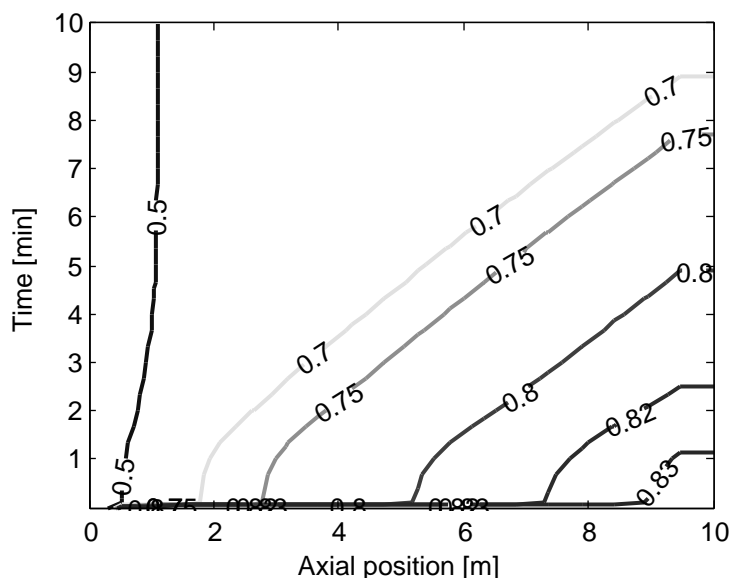
Figure 5.33: Contour plot of the dry hydrogen mole fraction as function of time and axial position in an isothermal SE-SMR reactor with Na$_2$ZrO$_3$ as acceptor at standard conditions.
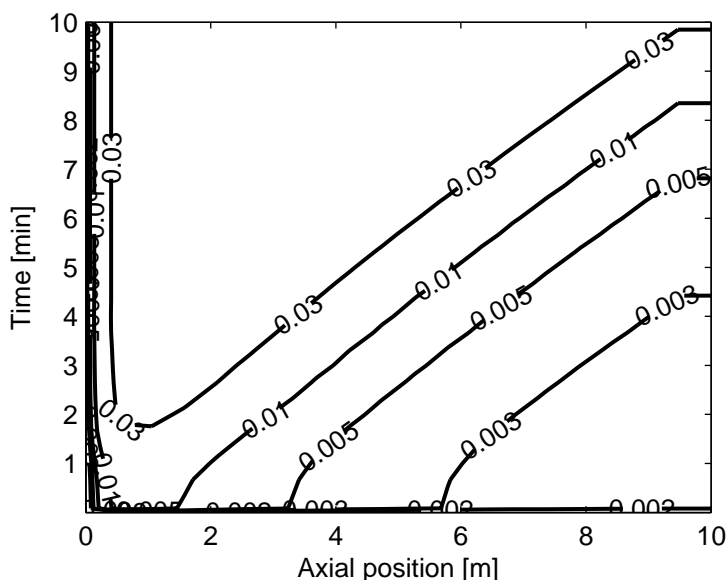
Figure 5.34: Contour plot of the dry CO_2 mole fraction as function of time and axial position in an isothermal SE-SMR reactor with Na_2ZrO_3 as acceptor at standard conditions.

An isothermal reactor is mostly an academic exercise, specially for this process, where there are a mixture with endothermic and exothermic reactions, an extremely high heat transport through the reactor walls would be necessary to keep it close to isothermal. Since the total reaction is close to energy neutral, one could try to operate the reactor without heating or cooling. This reactor would then be close to adiabatic, with no heat transferred between the reactor and the surroundings.

When simulating the reactor as adiabatic, the performance naturally changes, but the outlet purity of hydrogen does not change significantly. The contour plot of dry hydrogen purity as a function of time and axial position for the adiabatic simulations is shown in figure 5.35.

It is seen in figure 5.35 that the hydrogen purity is above 0.8 for a longer period in the adiabatic simulations. Although the total reaction is slightly endothermic, the temperature close to the outlet will increase because the capture is slower than the reforming and CO_2 produced in the reforming will be captured downstream of the reforming reactions. It is seen from figure 5.36 that the temperature increases up to almost 950 K, which is 100 K above the inlet temperature, due to the exothermic capture reaction. The temperature in the reactor falls near the entrance because the endothermic reforming is dominant and more CO_2 produced than captured.
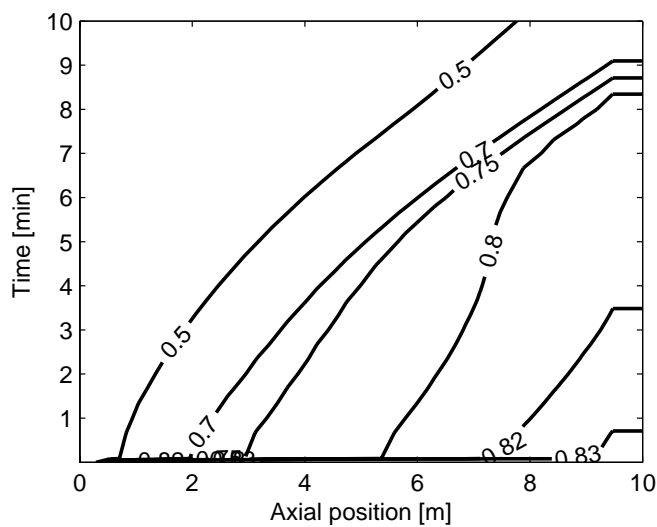
Figure 5.35: Contour plot of the dry hydrogen mole fraction as function of time and axial position in an adiabatic SE-SMR reactor with Na$_2$ZrO$_3$ as acceptor at standard conditions.
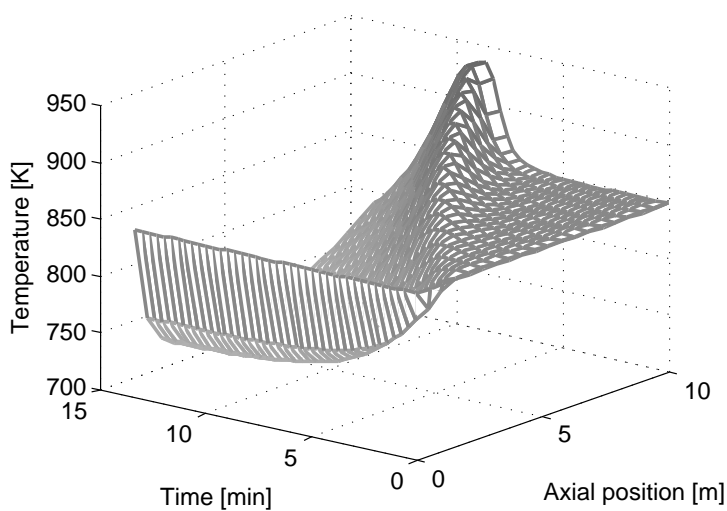
Figure 5.36: Plot of the temperature as a function of time and axial position in an adiabatic SE-SMR reactor with Na$_2$ZrO$_3$ as acceptor at standard conditions.
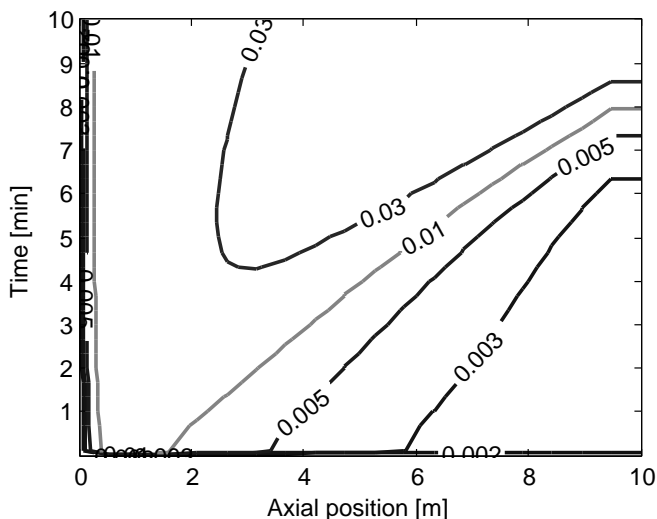
Figure 5.37: Contour plot of the dry CO_2 mole fraction as function of time and axial position in an adiabatic SE-SMR reactor with Na_2ZrO_3 as acceptor at standard conditions.

Downstream of the inlet zone the exothermic capture starts to dominate and the temperature increases. The SMR is thermodynamically favored at higher temperatures and this effect keeps the hydrogen mole fraction at a higher level even when the sorption rate decreases. However, the CO_2 content increases with temperature and this is clearly observed in figure 5.37. The low CO_2 content is kept for a longer time, but the even when the CO_2 dry mole fraction increases to 0.01 the dry hydrogen mole fraction is kept above 0.8. This is due to the thermodynamics of the reforming, where more hydrogen will be produced when increasing the temperature. But when increasing the temperature, the CO_2 content increases and the CO_2 capture will decrease due to the higher partial pressure of CO_2 at higher temperatures. Therefore, it is important to control the outlet temperature to control the amount of CO_2 captured at a desired level. Temperature control is also important to control the CO level. For the isothermal simulations at a temperature of 848 K, the CO content at the outlet will stay below 0.0015 when the dry hydrogen mole fraction is kept above 0.8. When the temperature increases, the water-shift reaction equilibrium moves towards the CO-side. It is noted that parts of the reactor with high temperature are operating outside the range where the empirical expression for the CO_2-capture kinetics was found, we expect that the given trends
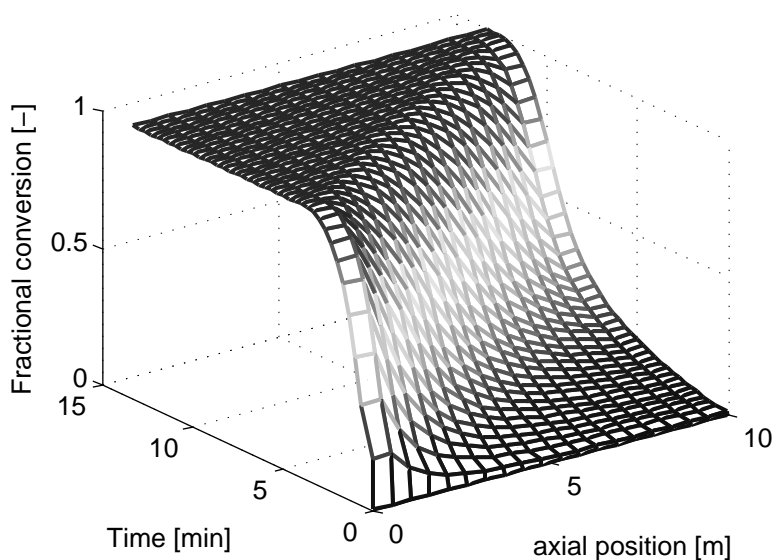
Figure 5.38: Plot of the fraction conversion of acceptor as a function of time and axial position in an adiabatic SE-SMR reactor with Na$_2$ZrO$_3$ as acceptor.

will still yield even if the numerical values may not be accurate.

The total pressure in the reactor affects the process in several ways. Because the reactions have a total production of moles, the reactor is thermodynamically favored at low total pressure. However, a high pressure make the gas volume lower and make the residence times higher. These effects partially cancels out each other, but as seen in figure 5.39 the lowest pressure gives the highest hydrogen purity. The lower pressure gives higher gas velocity, and for 10 bar at these conditions about 2 m/s. The superficial velocity for the 20 bar case is about 1 m/s. This leads to low pressure drop in the system, as seen in figure 5.40. The pressure in the reactor has to be chosen in a total evaluation of the process where the lower pressure drop and the slightly lower conversion with higher pressure has to be taken into consideration with other system variables. The effect of total pressure on SMR can be seen after 12 minutes of simulation where the CO$_2$ capture effect disappears and the resulting process is pure reforming. The hydrogen purity at this stage is clearly lower for the high pressure case. The pressure as function of time and axial position for an outlet pressure of 10 bar is seen in figure 5.41 and it is seen that the pressure in the reactor is slightly dependent of time.
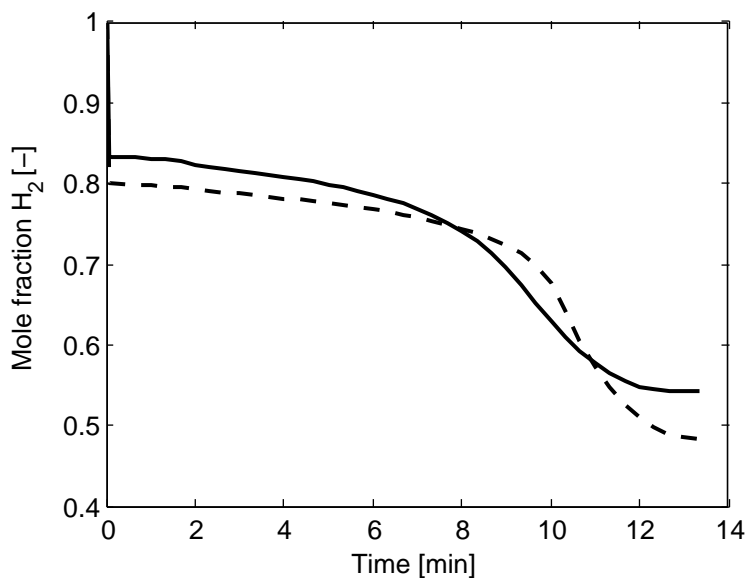
Figure 5.39: Comparison in outlet dry hydrogen mole fractions with outlet pressure of 20 bar (— —) and 10 bar (—) at equal mass flow with Na_2ZrO_3 as acceptor.
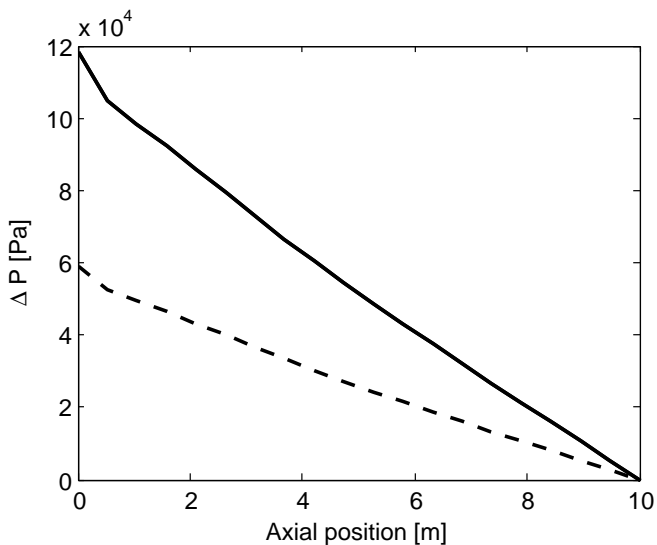
Figure 5.40: Comparison of pressure gradients through an adiabatic SE-SMR reactor with total pressure of 20 bar (—) and 10 bar (— —) with Na_2ZrO_3 as acceptor at equal mass flow .
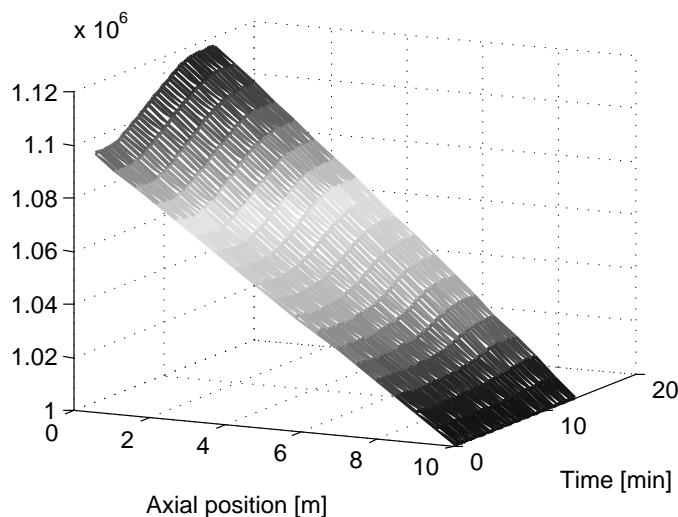
Figure 5.41: The pressure as function of time and axial position in an adiabatic SE-SMR reactor with Na$_2$ZrO$_3$ as acceptor.

The performance of the reactor will be a function of the distribution between catalyst and sorbent in the reactor. To look at the effect of changing the ratio between the two active materials, the reactor have been simulated at different values of α, which is the ratio between the mass of sorbent and the mass of catalyst. A high ratio will make the rate of sorption and the CO$_2$ capture capacity higher. Figure 5.42 shows the outlet dry hydrogen mole fraction as function of time for different values of α. The maximum performance of the reactor is at an α close to 4. When increasing it to 10 the initial hydrogen mole fraction falls from about 0.83 to about 0.82, the curve is flatter, but it does not cross the line for $\alpha = 4$ before a hydrogen fraction of about 0.75. However, the effect is not very large when the amount of sorbent is higher than catalyst, i.e. an α above 1. When lowering the α the effect is much more dramatic, particularly in terms of the time where higher conversion is reached. When α is lowered from 4 to 1, the time where hydrogen mole fraction above 0.8 is reached decreases from 7 to 5 minutes. When decreasing the ratio between the materials even more, the time decreases, and for an α of 0.25 the highest dry hydrogen mole fraction reached is just above 0.8 and it drops immediately.

Another parameter that can be changed in the simulations is the steam to carbon ratio. When the amount of steam is increased the thermodynamics change and more hydrogen can be produced at equilibrium. However, a high steam to
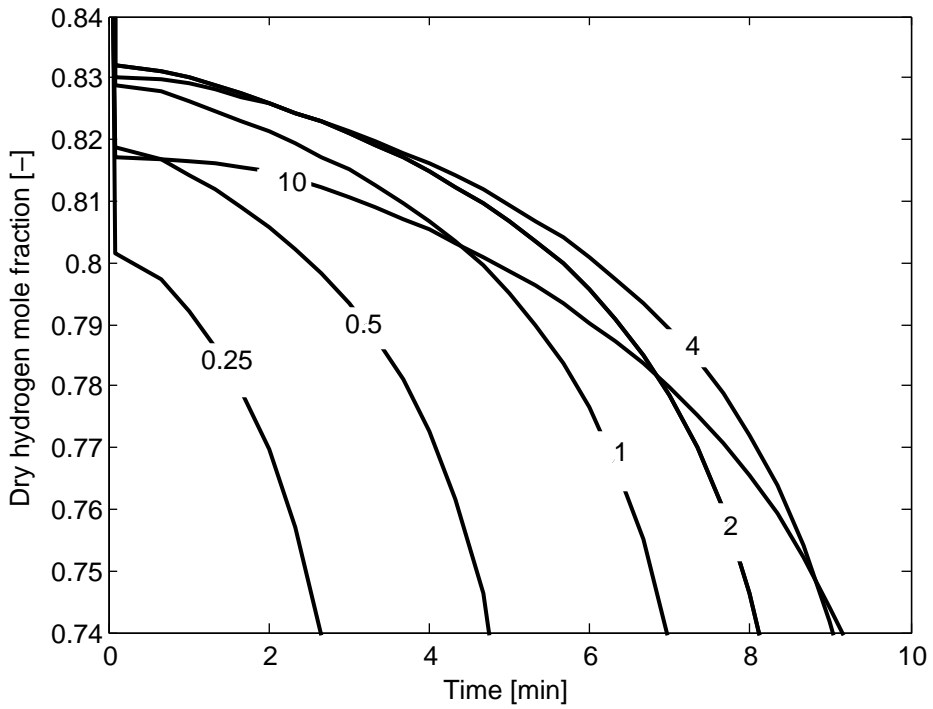
Figure 5.42: Outlet dry hydrogen mole fraction as function of time at different values of α.
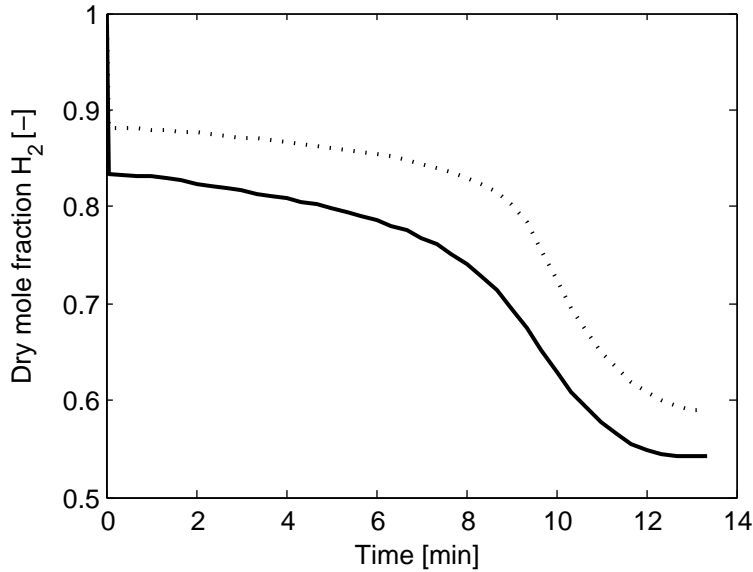
Figure 5.43: Outlet dry hydrogen mole fraction as function of time at S/C-ratios of 4 ($\cdots$) and 3 — for SE-SMR with Na$_2$ZrO$_3$ as acceptor.

carbon ratio will have a negative effect of the overall process efficiency, which will be more looked into in the next chapter of this thesis. Figure 5.43 shows the dry hydrogen mole fraction at S/C-ratios of 3 and 4 and the positive effect of a higher steam to carbon ratio on the conversion is clearly observed. The dry hydrogen mole fraction increases from just above 0.83 to above 0.88 at the same mass throughput in the reactor. A lower velocity in the reactor will also increase the conversion, and the effect of this would be about the same as having a longer reactor. A longer residence time in the reactor will increase the conversion unless equilibrium is reached. When lowering the mass throughput from 5 kg/m^{2}s to 1 kg/m^{2}s the residence time is increased with a factor of 5, which will give an increased conversion. This is observed in figure 5.44. The dry hydrogen mole fraction is just below 0.90 in the first minutes after start-up and falls slowly when more acceptor is filled with CO$_2$. The other effect of lower velocity is that the time before the conversion drops will be much higher due to the lower throughput of gas. The time before the conversion drops dramatically would be expected to be about 5 times longer than for the case with 5 kg/m^{2}s mass flow, and this is also observed in figure 5.44. This means that if higher hydrogen mole fractions is desired out of the reactor there are several ways to do this. One could have a higher steam to carbon ratio, which will give a negative effect on the thermal efficiency of the process or
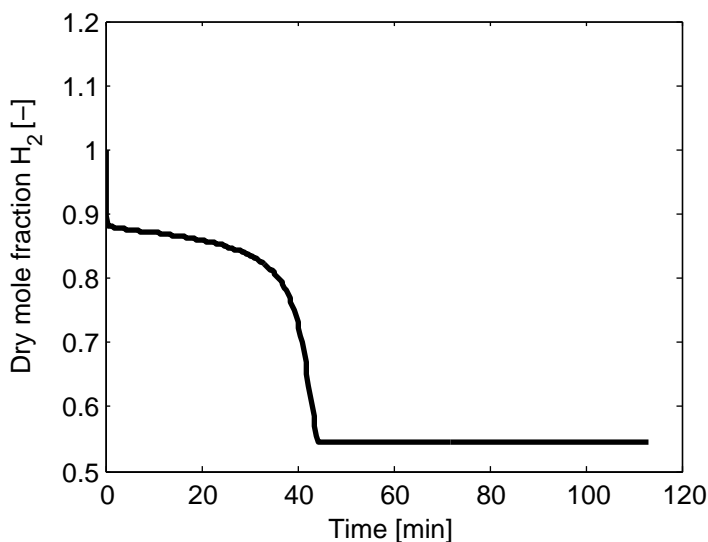
Figure 5.44: Outlet dry hydrogen mole fraction as function of time for a mass input of 1 kg/(m^{2}s) for SE-SMR with Na$_2$ZrO$_3$ as acceptor

a higher residence time in the reactor can be used. For a given inlet flow this can be accomplished either by making the reactor diameter larger, which decreases the velocity, or a longer reactor can be made.

5.3.3   Comparison with fixed bed experiment

The SE-SMR in a fixed bed reactor has been investigated experimentally by Esther Ochoa-Fernández in a small scale reactor.[52] The operating conditions used in this experiment is shown in table 5.6. At these conditions the equilibrium dry hydrogen mole fraction is about 0.99 when using the experimentally found equilibrium partial pressure of CO$_2$. The equilibrium dry hydrogen mole fraction when using literature data[33] is about 0.92. Figure 5.45 shows the comparison of dry hydrogen mole fraction between the experimental data and the simulation results.

Unfortunately there were large unknown volumes in the experimental set-up after the reactor, which make the break-through very difficult to model. It is observed that the time before a steady hydrogen production is reached is much higher than the expected for specified length of reactor and gas velocity. The reactor was initially filled with hydrogen and the hydrogen mole fraction gradually falls down until a "steady-state" hydrogen production rate is reached after about 7 minutes. With a 10 cm long reactor the expected time before the break-through of SE-SMR

Table 5.6: Experimental reactor conditions in SE-SMR with Na$_2$ZrO$_3$ as acceptor

$P_{out}(bar)$	5
$T_f(K)$	848
$T_w(K)$	848
α	5
$\dot{m}_f(kg/m^2s)$	0.0167
L (m)	0.06
d$_t$ (m)	0.016
m$_{cap}$ (g)	7.25
m$_{cat}$ (g)	1.45
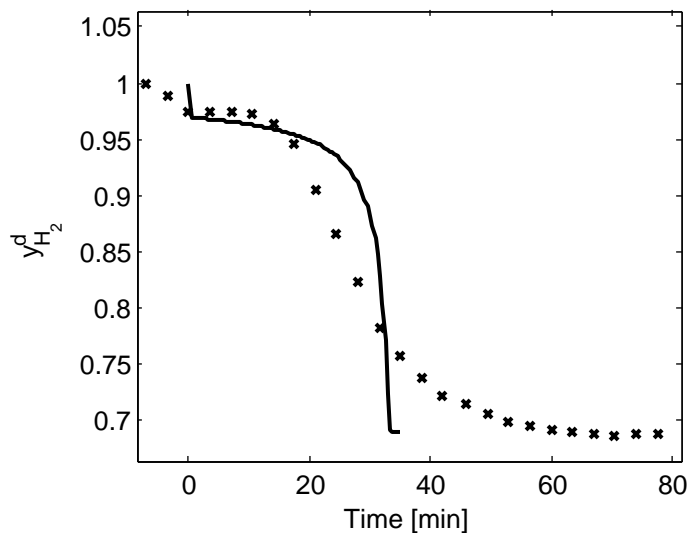
Figure 5.45: Comparison of outlet dry hydrogen mole fraction for SE-SMR with Na$_2$ZrO$_3$ as acceptor between experimental data (x) and model (—).

product should be about 7 seconds. Due to this the starting point of the two data sets has been shifted to try to get a comparison of the reactor outlet conditions. It is observed that the dry hydrogen mole fraction reached is relatively similar. The experimental results give a dry hydrogen mole fraction out of about 0.973 while the simulation results give a dry hydrogen mole fraction of about 0.968. This must be considered a nice fit between the model and the experimental data, and it should be noted that the dry hydrogen mole fraction is not a result of a thermo-dynamical limit, which is at about 0.99, but a result of the kinetics and the flow in the reactor. The dead volumes in the experiment do lead to large discrepancies when the conversion drops, and better knowledge about the dead volumes would be necessary to incorporate this into the model. However, it is considered that the fit to the maximum conversion give a good indication that the reactor model and the capture kinetics are able to describe the process well, and the error is in a small underprediction of the conversion. The simulations and actual SE-SMR experiment also confirms the finding in the capture experiments that the equilibrium partial pressure of CO_2 over Na_2ZrO_3 found in the literature is higher than the actual equilibrium partial pressure for this material.

5.3.4 Comparison with Calcium oxide as acceptor

As discussed in section 2, Calcium Oxide is an alternative material for sorption enhanced steam methane reforming. Li and Cai[42] made a kinetic model for the sorption and desorption of CO_2 on calcium oxide. This model, which was based on the spherical grain model, has been used in simulations of SE-SMR with the models previously described. The equilibrium partial pressure of CO_2 is about the same for CaO and Na_2ZrO_3, but the kinetics of CaO is superior. Figure 5.46 shows a comparison between the capture rate of CO_2 on CaO and Na_2ZrO_3, and a significant difference is observed. Is should be pointed out that this calcium oxide is a synthesized product and not from dolomite, and an optimized structure of the sorption material is very important for the capture properties.

The higher rate of capture leads to better performance in SE-SMR. The hydrogen dry mole fraction at the outlet for simulations with CaO and Na_2ZrO_3 at the standard conditions used in section 5.3 are shown in figure 5.47. The dry hydrogen mole fraction is at the equilibrium at the outlet for the simulations of calcium oxide, and the capacity is also bigger, which means that longer cycle times can be used. Li and Cai also claims that the calcium oxide material they use have a good stability compared to calcium oxide materials used in previous studies. This shows how the capture rate is very important for the SE-SMR process, and with very similar equilibrium partial pressures of CO_2 a much higher conversion is seen with faster kinetics. This means that for Na_2ZrO_3 to be competitive with CaO in
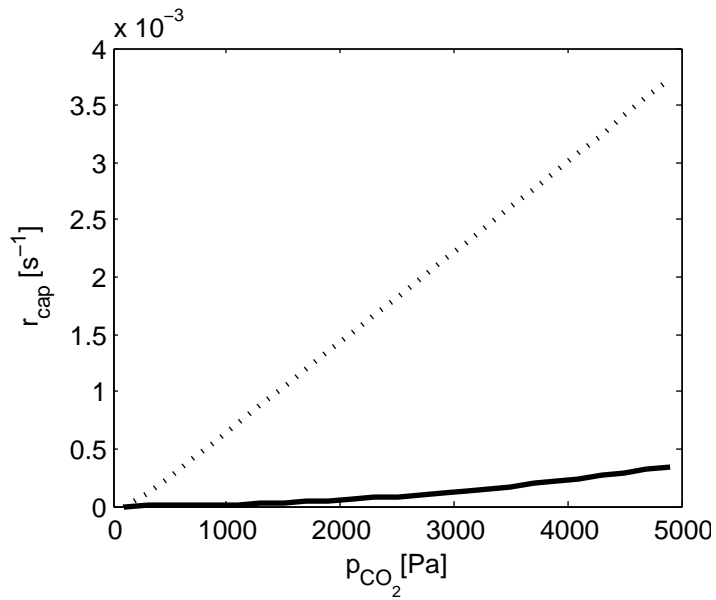
Figure 5.46: Comparison in rate of reaction between capture of CO$_2$ on Na$_2$ZrO$_3$ (—) and CaO ($\cdots$).
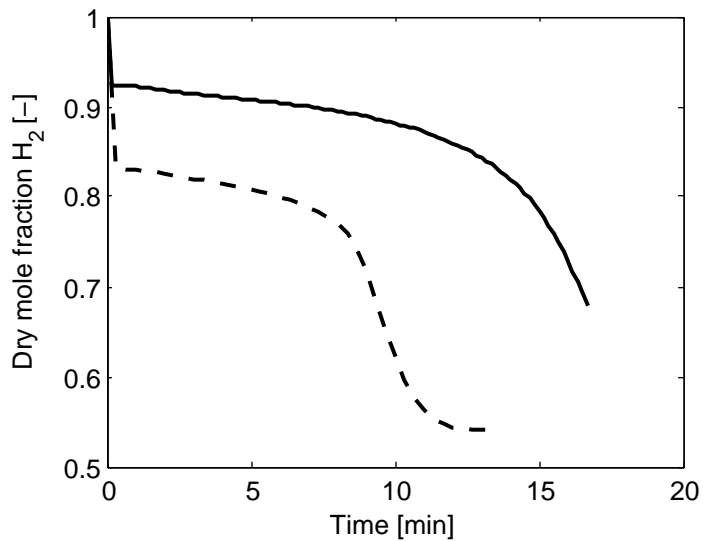
Figure 5.47: Comparison of dry hydrogen mole fraction at outlet for simulations with calcium oxide (—) and sodium zirconate (— —) as acceptor.

a SE-SMR, it must either have much better cycling properties, or the structure of the material have to be optimized to compete with the capture rate of CaO.

Chapter 6

Process design and evaluation

In this part of the thesis the whole SE-SMR process is looked at. The reactor simulations from the previous part are used in a bigger picture with production of hydrogen from natural gas and sequestration of CO_2. The process and the background for it are covered in detail in section 2. As described there, the main reactor concepts that could be used in SE-SMR are fixed and fluidized beds, with variations of these concepts. Here, as in the rest of the thesis the focus has been on fixed bed reactors. For a fixed bed reactor system a minimum of two reactors which are operated in a cyclic manner are needed for the reforming-regeneration cycle.

Using input from the reactor simulations carried out in Matlab, the process has been simulated with the process simulation software Hysys. The main process results, and the energy efficiency in particular, have been calculated using the Hysys simulations for different process conditions and configurations. The size of the process has been chosen to a similar size of the largest autothermal reformers in the world, which give a hydrogen output with lower heating value of 700 MW, and the product specifications has been chosen equal to the specifications of the ENCAP (Enhanced production of CO2) EU-project.[2]

6.1 Overall process description

The process has been based on a traditional hydrogen production by SMR as described in figure 1.1. A clean gas without heavies and sulphur is used as feed, and the sulphur removal and prereforming steps are not necessary for the SE-SMR process described here. For other feed gas compositions, these steps can be included. Because the reforming is done at a low temperature and CO_2 is removed from the reaction zone, the water gas shift reaction will be shifted far to the hydrogen side in equation (6.1).

$$CO + H_2O \leftrightarrow CO_2 + H_2 \qquad (6.1)$$

This means that there is little to gain by installing a shift reactor in an SE-SMR concept. For hydrogen production with CO_2 removal by steam methane reforming there must be a process removing CO_2 from the reforming product, and when the CO_2 is removed inside the reforming reactor, the steps in SE-SMR can be described as in figure 6.1. Based on the steps in figure 6.1 and the reactor cycling
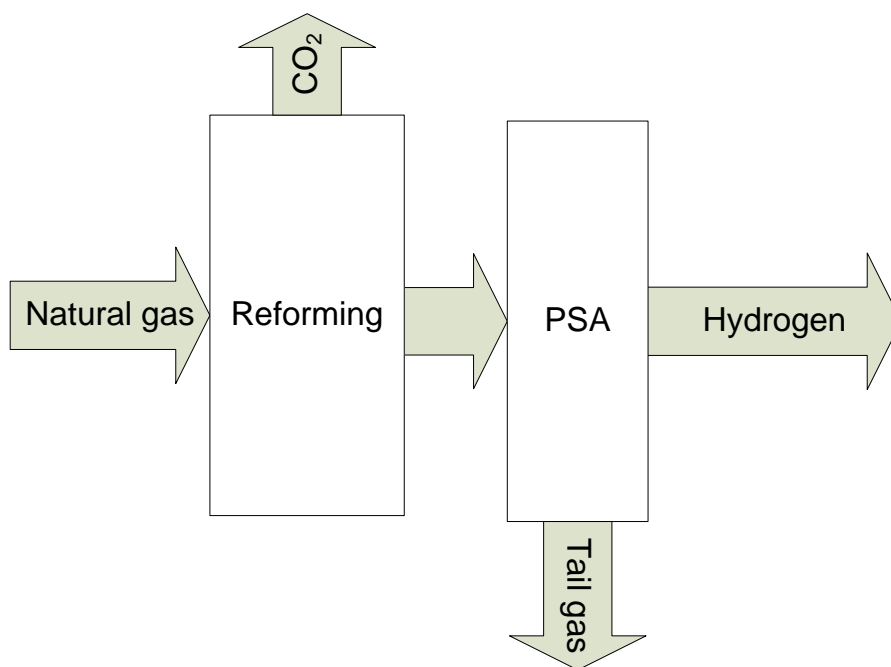
Figure 6.1: An overview of the steps in the SE-SMR-process.

described in the following section, a simplified flow diagram of the process is shown in figure 6.3. The input to the system is natural gas (methane) and demineralised water, and the output is pure hydrogen at a pressure of 60 bar and a stream of carbon dioxide at 110 bar. The reactor must be operated in a cyclic manner and in this figure the reactor operation is split in three steps, reforming, regeneration, and cooling. An overview of a possible reactor cycle is shown in figure 6.2, where the SE-SMR is operated at 575 °C and 20 bar.
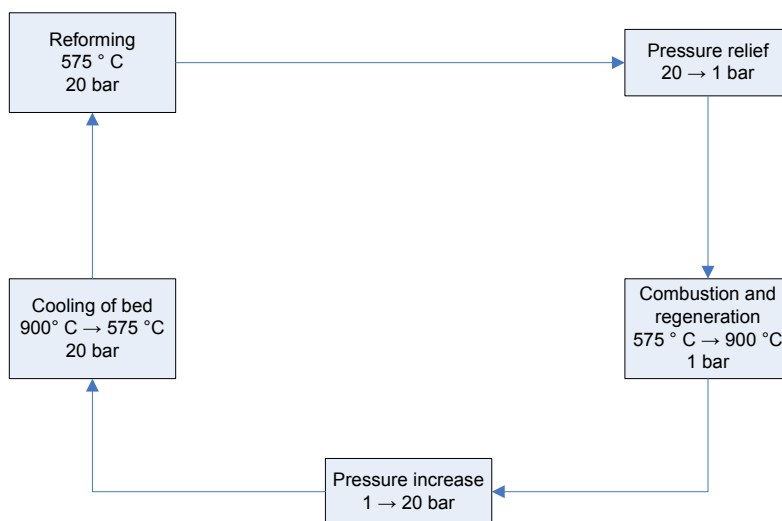
Figure 6.2: An overview of the steps in the operation of a fixed bed reactor system

The reactor is filled with a nickel-based reforming catalyst and a CO_2- accep-
tor, e.g. lithium zirconate or sodium zirconate. Natural gas, parts of it recirculated
from the product purification step, and steam, are fed to the reforming reactor at the
operating temperature and pressure. Through the reforming and sorption reactions
the gas is converted to hydrogen. The product from the reforming reactor consists
mainly of hydrogen, steam, and methane. There are also small contents of carbon
dioxide ($< 0.02\%$) and carbon monoxide($< 0.01\%$). The product stream from the
reforming reactor is heat-exchanged with inlet streams and are cooled down to 25
°C before it enters a knock-out drum where water is removed. After removal of
water the hydrogen is purified by pressure swing adsorption, where the hydrogen
adsorbs on a solid material, while the other species runs through. The hydrogen
recovery is typically 80-90 % dependent on feed gas composition.[74] Although the
PSA unit is shown as one vessel in figure 6.3 the unit consists of several columns
and is operated in four main steps.

- Adsorption.

- Blow down.

- Desorption.

- Repressurization.

During adsorption all other species than hydrogen are produced, while during desorption, a close to pure hydrogen stream is produced. By using several columns in parallel it is possible to produce a continuous stream of pure hydrogen. Dependent on the reactor pressure the gas entering the PSA must be compressed to the 20 bar working pressure of the PSA. The high pressure hydrogen stream from the PSA-unit is at 20 bar, while the low-pressure stream, mainly consisting of methane and unrecovered hydrogen, is close to atmospheric conditions. After the purification the hydrogen product is pressurized and cooled to the outlet specifications, here set to 60 bar and 25 °C. The tail gas from the PSA is compressed and used for heating in the regeneration step, or fed back as feed to the reforming reactor if the recycle gives an excess of fuel gas.

The regeneration step of the reactor cycle can be done in different ways. Indirect heating through the pipe walls and using a sweep gas is one possibility, where the heating could come from combustion of natural gas/hydrogen in air. If combustion in air is used to supply the heat of regeneration, and high CO_2 removal is desired, the flue gas from the combustion must be treated by another process such as an amine solution. Another possibility implies combustion of natural gas/hydrogen in pure oxygen. In this case high CO_2 removal can be accomplished without employing special CO_2 removal processes and the heating can be supplied directly inside the regeneration reactor without removing the possibility of CO_2 sequestration. An option would be to feed natural gas and oxygen simultaneously to the reactor, and the natural gas is combusted directly. To release CO_2, a temperature which gives an equilibrium partial pressure of CO_2 higher than the actual partial pressure is necessary. In the case with combustion of methane in pure oxygen this means an equilibrium partial pressure larger than $0.33p_{tot}$. The heating by combustion in oxygen could also be supplied through the reactor walls or partly through the walls and in the reactor bed. Combustion in oxygen can yield very high temperatures, and although the endothermic regeneration will help controlling the temperature, measures must be taken to avoid extreme temperature gradients in this case.

A possibility that has been looked into by Dupont et al. is to use unmixed combustion. The nickel-catalyst can besides acting as a catalyst also be an oxygen carrier.[17] By first feeding oxygen, the oxygen reacts with nickel creating nickel oxide. When natural gas is fed to the reactor the oxygen is released from the nickel and the natural gas combusted. In all process configurations with SE-SMR in a fixed bed reactor cyclic operation of the reactors is necessary.

In the simulations of the process shown later in the chapter oxygen is used as the main combustion medium, without taking into account if the heating is supplied inside or outside the reactor bed. If the heating is supplied inside the bed, one large reactor bed could be used, while if the heating is supplied through the walls
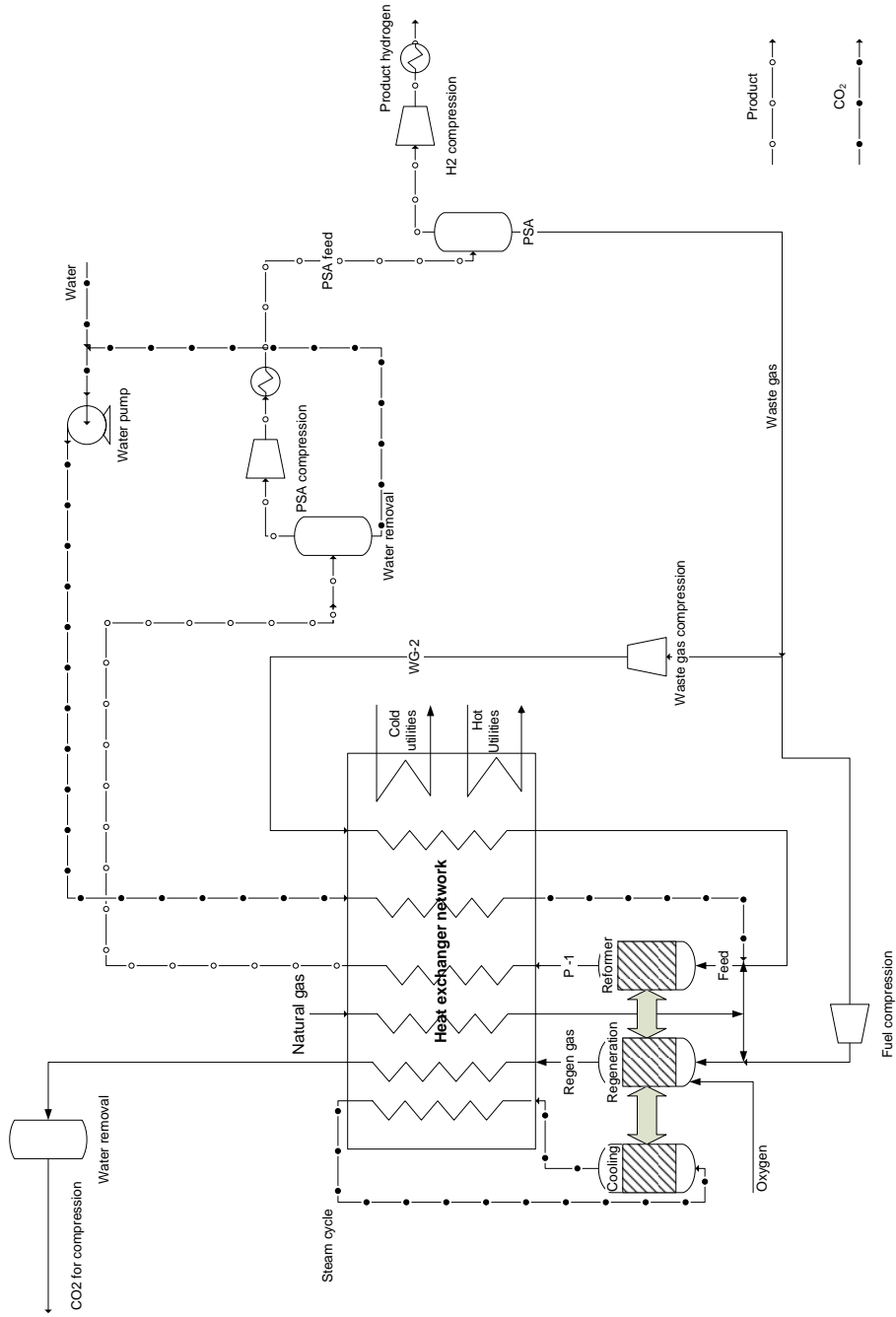
Figure 6.3: An overview of the process configuration for SE-SMR

the reactor must consist of several beds with smaller diameter. To avoid excessive temperature gradients with oxygen as heating medium it could be necessary to recycle some of the CO_2 for temperature control, but the main simulations are done without recycling of CO_2.

After the regeneration of sorbent at high temperature, the reactor bed has to be cooled down to the desired reaction temperature. This is another challenge in this process, where a lot of heat has to be removed in as short time as possible. Here, steam is used for the cooling of the reactor and the hot steam from the reactor cooling is heat exchanged with the inlet steam to the reforming reactor. To avoid too high volume flows in the reactor, the cooling-down should be done after pressurization of the reactor.

The product stream from the regeneration step will consist of steam and carbon dioxide, which is separated by cooling the stream to 25 °C. Before transportation to storage, the CO_2 has to be pressurized. This is done in a step-wise compression, with three compressors followed by cooling and water-removal. The product CO_2 is at 110 bar and in supercritical state.

6.2 Process simulation of SE-SMR

The process described in the previous section is simulated in Aspen Hysys version 2006.5 to evaluate the process performance. Hysys is a modelling tool for process plants with the ability to simulate all common process equipment such as reactors, compressors, heat exchangers, pumps, vessels, etc. The process has been simulated using the Peng Robinson fluid property package with a hypothetic component defined for the solid material. The input and the desired output of the process are shown in table 6.1. The specifications are the same as used in the ENCAP project, and was also used in by Langørgen et. al.[37] In the report by Langørgen et.al hydrogen were produced by autothermal steam methane reforming and CO_2 removed from the reforming product by an amine process giving an hydrogen product of 700 MW LHV. For the regeneration of the sorbent, pure oxygen is used for the combustion which is fired either with natural gas or a mixture of natural gas and hydrogen. A 3% stoichiometric excess of oxygen is used for the combustion. An air separation unit is used to supply oxygen, this unit is not modeled, but the cost for oxygen production was set to 1.0 MJ/kg.[11] The PSA was set as a component splitter, and the hydrogen recovery set to 90%.[74] All compressors and pumps in the process are modeled with a 75 % adiabatic efficiency. For the regeneration combustion it has been assumed that the fuel must be at 2 bar, and predominantly waste gas from the PSA is used as fuel. If there is excess waste gas for fuel, the rest is pressurized to the reformer pressure and recycled back to the process. If the waste gas from the PSA not gives enough fuel for the regenera-

Table 6.1: Feed and product specifications:

Natural gas feed		
	Pressure	70 bar
	Temperature	10 °C
Composition:		
	Methane	100%
Hydrogen product		
	Pressure	60 bar
	LHV	700 MW
Composition:		
	H_2 >99.99%	
CO_2 product		
	Pressure	110 bar
Composition:		
	CO_2	>90%
	H_2O	<500ppm

tion, additional natural gas is fed to the combustion. The SE-SMR is operated as a thermal-pressure swing process, using a reformer pressure of 10/20 bar and a temperature of 575 °C. Due to the pressure drop in the reactor the feed is pressurized to 11 bar. The regeneration with sodium zirconate as acceptor is done at 900°C and 1 atm.

Because there are no complete equilibrium data for the Na_2ZrO_3- material, the regeneration temperature is an estimate based on regeneration data at lower temperatures. It is assumed that the equilibrium partial pressure of CO_2 at 900 °C is above 1 bar, and that there are no thermodynamic limitations at this temperature. With an equilibrium partial pressure of CO_2 higher than the total pressure in the reactor, there will be a driving force for regeneration with any CO_2 content in the stream. When direct combustion is used as heating the CO_2 from the combustion would make a maximum CO_2 content of about 33% on molar basis. This means that the minimum temperature that the regeneration temperature, if the combustion is carried out inside the reaction bed or the combustion products is used as sweep gas, would be the temperature corresponding to a partial pressure of 0.33 bar for regeneration close to atmospheric conditions. To ensure a reasonable driving force, the regeneration should be operated at a temperature corresponding to a partial pressure considerably higher than this, and an atmospheric equilibrium partial pressure is used as a guideline in the simulations. For the simulations with lithium zirconate as acceptor the equilibrium data from Knacke et al.[33] were used in the same way as in section 3.1, and the regeneration temperature were set to the temperature where the partial pressure of Li_2ZrO_3 is 1 bar.

The reactors are modeled as conversion reactors and the conversions based on the Matlab simulations of the fixed bed reactors. In general, the reforming reactions are fast compared to the CO_2-sorption; hence the reforming reactions will be in equilibrium, while the state of the sorption reaction is dependent on the operating conditions.

$$CH_4 + H_2O \leftrightarrow CO + 3H_2 \tag{6.2}$$

$$CO + H_2O \leftrightarrow CO_2 + H_2 \tag{6.3}$$

$$MO + CO_2 \leftrightarrow MCO_3 \tag{6.4}$$
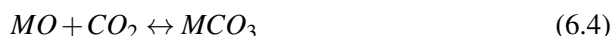
The main reactions in the reactor are given in equation (6.2), (6.3), and (6.4) and the conversion of these three reactions is the input to the Hysys simulations. Equation (6.2) is the main reaction and the one that is most affected by changes in simulation parameters. Equation (6.3) and (6.4) is close to 100 % conversion in the cases looked at, and it is equation (6.2) that gives how much hydrogen that is produced. Equation (6.3) mainly affects the amount of CO in the product, while equation (6.4) mainly affects the amount of CO_2 in the product. A reactor with length of 10 meters is used as a base-case, and the mass flow through the reactor is
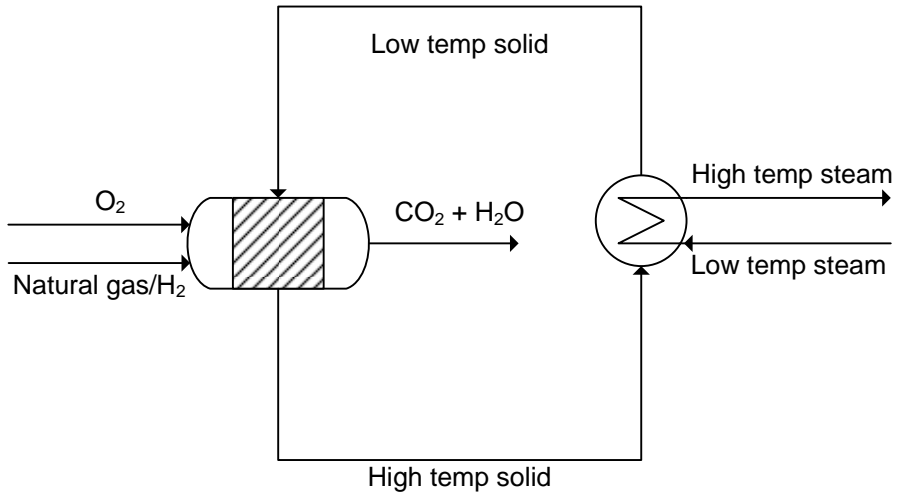
Figure 6.4: How the solid regeneration cycle is implemented in Hysys

adjusted to get a satisfying conversion. A low steam-to-carbon ratio gives higher thermal efficiency, but it was found that for the faster sorbent (Na_2ZrO_3) a lower S/C-ratio than 3 was not possible without considerably lowering the conversion.

The simulations in Hysys are done in steady state, and because the process is of a non steady-state nature some approximations have been done. For the internal solids that are heated in the regeneration step, this is approximated by using a pseudo solid stream defined by the total mass in the reactor divided by the cycling time. For the cooling of the solid this stream is heat exchanged with a steam stream. A sketch of this setup is shown in figure 6.4. This means that the flow of the pseudo stream is calculated as in equation (6.5).

$$\dot{w}_{solid} = \frac{V_{reactor}\rho_{solid}}{t_{cycle}} \tag{6.5}$$

The volume of the reactor is calculated from the actual inlet gas volume flow ($\dot{V}_{gas}$) of the reforming reactor, the superficial gas velocity used in the reactor simulations (v), and the height of the reactor (L), as shown in equation (6.6):

$$V_{reactor} = \frac{\dot{V}_{gas}}{v}L \tag{6.6}$$

In the simulations the regeneration is split in three steps. One reactor is covering the heating of bed to the regeneration temperature where the outlet gas temperature

is set to 575 °C. For the regeneration the outlet gas temperature is set to the temperature of regeneration, and for the cooling down the outlet steam temperature is set equal to the temperature of regeneration.

6.2.1   Thermal efficiency

The thermal efficiency is calculated for the process, and used as a main figure for comparison. Gross efficiency is calculated as the ratio between lower heating value (LHV) of the natural gas feed and LHV of the hydrogen product. The net efficiency is the overall efficiency, calculated as in equation (6.7).

$$\eta_{net} = \frac{LHV_{Product}}{LHV_{Feed} - \text{power input}} \qquad (6.7)$$

There are large quantities of energy transport in the system, and to make use of the heat in an efficient way a simplified pinch methodology has been employed in Hysys. The basic concept of pinch methodology is that heat can only be transferred from hot to cold streams and there must always be a driving force in terms of temperature gradient between the hot and cold streams in a heat exchanger. Typical minimum temperature gradients are 5-20 K and the point where this minimum temperature difference is found is called the *pinch temperature*. To get an optimum heat recovery for the process, no heat should be transferred across this temperature. With lower minimum temperature gradient the driving force in the heat exchangers will be smaller, which means that higher heat transfer area has to be used. This means that there will be a trade-off between a low minimum temperature gradient, which maximizes the heat recovery, and a higher minimum temperature gradient to minimize the heat transfer area. By grouping the streams in the system into cold and hot streams and drawing a graph based on the total heat in the hot and cold streams at different temperatures, the composite diagram can be made.

In Hysys, the LNG exchanger unit operation, several streams can be combined in one heat exchanger, the hot and cold streams are grouped, and the pinch temperature can be specified. In the simulations, a hot or cold utility stream is routed to this multistream exchanger to balance the heat transfer, and the outlet temperature of the hot streams is specified so that the pinch temperature is 10 K. The cooling that must be supplied to the hot streams below the pinch point is done outside the multistream heat exchanger in Hysys and is done by water cooling the streams to a temperature of 25°C. This means that one main unit operation can be used for the heat exchanger network shown in figure 6.3 except the low temperature cooling which is done by single heat exchangers to simplify the control of the process simulation.

In a majority of the simulations there is excess heat above the pinch temperature. If this cooling is supplied as low temperature cooling water with a small
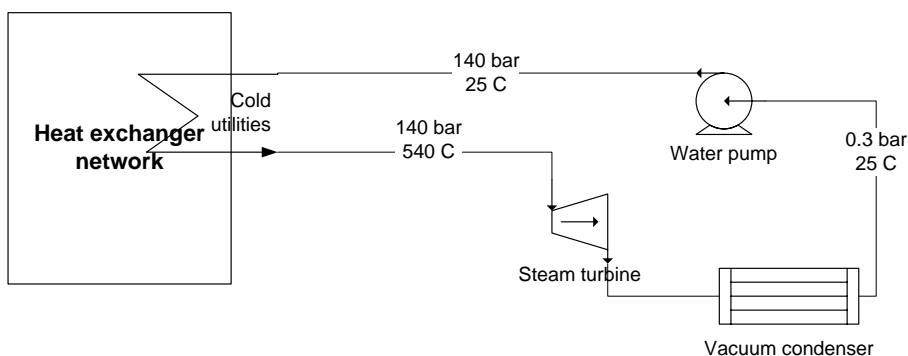
Figure 6.5: An overview of the steam turbine cycle used as cold utility.

temperature increase the heat would be lost. This means that an other cold utility must be supplied in a way that the heat can be recovered. This is done by using a steam turbine cycle, where the excess heat creates high pressure steam, which in turn is expanded in a steam turbine creating power which can be used for the power requirements of the plant or exported. This is the same way as excess heat was accounted for by Langørgen et. al. The steam turbine cycle is shown in figure 6.5. If there is no excess heat, but heat must be supplied to the reactor, this is added by steam at 20 bar. This is accounted for in the calculations by assuming an 85 % efficiency of the steam boiler based on the LHV, and then the necessary fuel gas for the boiler can be calculated. A screenshot from the Hysys simulations is shown in figure 6.6 with the streams named as in figure 6.3. It is used separate reaction vessels for the reforming methane conversion, CO_2 removal, regeneration heating and regeneration. It is in the reforming and CO_2 removal vessels where the conversions found from the Matlab simulations are specified.
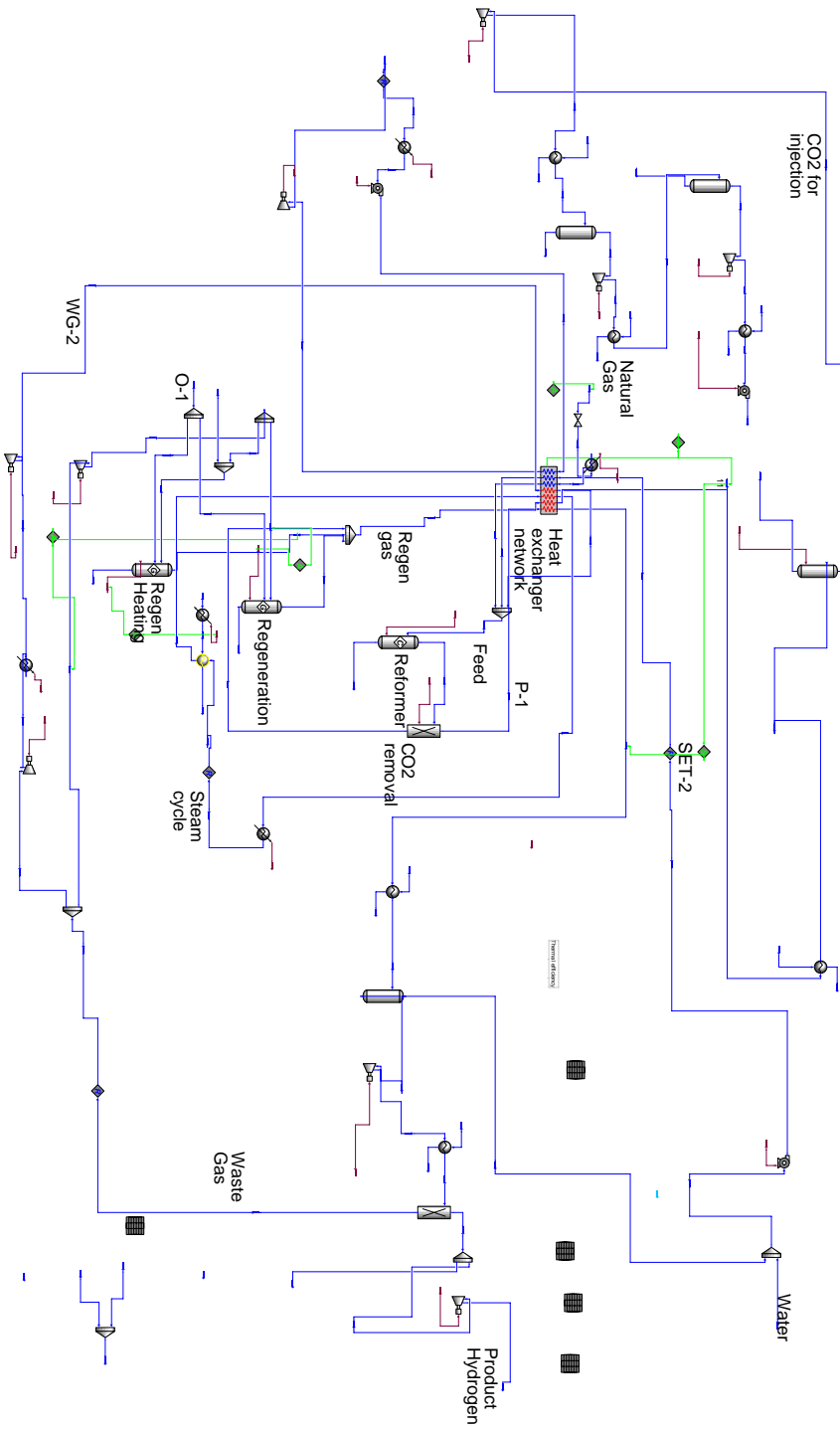
Figure 6.6: Screenshot of the Hysys process simulation set-up.

6.3   Process simulation results

6.3.1   Sodium Zirconate as CO_2 acceptor

Earlier work on thermal efficiencies in SE-SMR has not taking the kinetics of the reactions into consideration.[52] When taking this into account, the possible process designs and thermal efficiencies can change significantly. The process performances using the capture kinetics found in section 3 with lithium zirconate and sodium zirconate as acceptor in SE-SMR have been looked at here. The reactor sizes have been based on the performance of the reforming, because there has not been enough kinetic data available for the regeneration. The main process parameters for the process simulation with Na_2ZrO_3 as acceptor are shown in table 6.2.

Table 6.2: Simulation parameters for SE-SMR with Na_2ZrO_3 as CO_2-acceptor.

Reforming temperature (K)	848
Reforming pressure (bar)	10
Regeneration temperature (K)	1173
Regeneration pressure (bar)	1.013
Reactor length (m)	10
Gas velocity (m/s)	2
S/C- ratio	3

The parameters in table 6.2 have been used in reactor simulations with the models described in section 4. The conversion of methane at these conditions is shown in figure 6.7. From figure 6.7 it is observed that a maximum methane conversion of about 55 % is reached in the reactor and this corresponds to a dry hydrogen mole fraction of about 0.83. The CO_2 dry mole fraction will be about 0.002. In the Hysys models the conversion of the main reactions are found from the reactor simulations and the whole process is then simulated with the input to the conversion reactors from the Matlab simulations. The length of a cycle then determines the reaction conversions, and it also gives the solid flow as given by equation (6.5). A shorter cycle time gives a higher conversion, but it will give a higher pseudo solid flow, which increases the heat that has to be added to the reactor to heat it from reforming temperature to regeneration temperature. For Na_2ZrO_3 as acceptor two different cycle times have been used in the simulations, 4 and 8 minutes. As observed in figure 6.7, at 4 minutes the conversion of methane
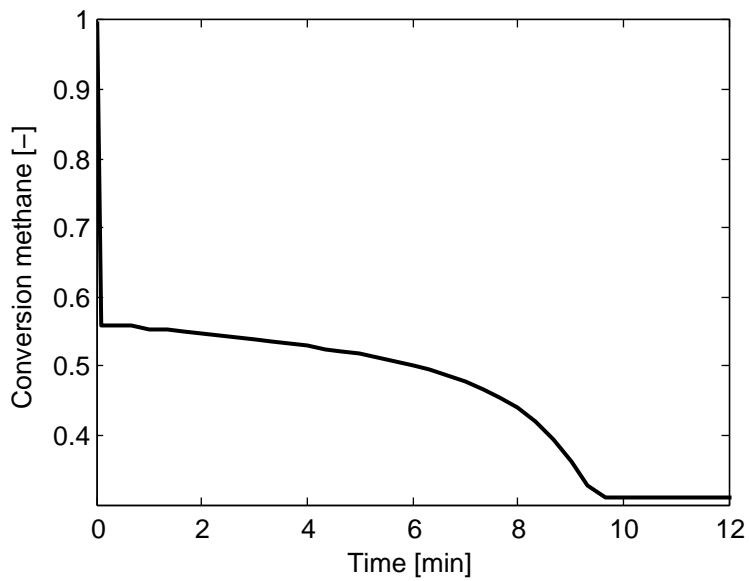
Figure 6.7: The conversion of methane in SE-SMR with Na_2ZrO_3 as sorbent at 575 °C, 10 bar and a S/C ratio of 3.

Table 6.3: Physical properties of the pseudo solid flow.

Density (kg/m^3)	1230
Heat capacity (J/kgK)	1000

is only slightly lower than at the initial conditions, while at 8 minutes the rate of decrease in conversion is high. The average values over the cycle times are used for the conversions in the simulations, and the methane conversion is 0.55 for the simulations with a 4 minute cycle, while it is 0.5 for an 8 minute cycle.

A pseudo-solid was defined in Hysys with the properties for the mixture of Na_2ZrO_3, catalyst and support material given in table 6.3 based on the properties used in the reactor simulations in section 5.3. For the simulations with Na_2ZrO_3 as CO_2 acceptor with main conditions given in table 6.2, the properties of the main streams as named in figure 6.6 are given in appendix A.1. The process thermal efficiency for the 4 and 8 minute cycle has been calculated based on the Hysys simulations, and the main numbers are given in table 6.4. In this table the natural gas feed is the sum of the feed for the reforming, the feed for regeneration and possible natural gas feed for the additional steam boiler in the case where there are no excess heat in the heat exchanger network. All the numbers are based on lower heating value, and the simulations are adjusted to give a lower heating value of the Hydrogen product of 700 MW. Even if the conversion is lower in the 8 minute cycle, the thermal efficiency is much higher. This is due to the large amounts of heat that must be added when heating the bed to regeneration temperature and the large amounts of heat that must be removed when cooling the bed to reforming temperature. Not all the heat can be recovered, and when increasing the rate of heat flow in the systems as in the 4 minute cycle, more heat is lost. Some of the heat is recovered in the steam turbine cycle, 97.4 MW for the 4 minute case, but still there is a lot of low temperature heat that can not be utilized. The higher conversion have a positive effect on the waste gas compression, because less gas is recycled, but more oxygen must be produced for the higher heat flow that is needed, and more fuel is needed, leading to higher fuel compression. The product compression consists of both compression of the product to 20 bar before pressure swing adsorption, and the compression of the hydrogen product.

The reactor cross-section area can be calculated based on the volumetric flow in the reactor and the superficial velocity in the reactor. This is given in table 6.5 together with the thermal efficiency. For the setup used here, the CO_2 removal will be close to 100 %. All CO_2 is captured, except the small amounts that are not separated from H_2 in the PSA unit and the CO_2 soluble in the water separated from

Table 6.4: Process thermal efficiency for simulations with Na_2ZrO_3 as CO_2 acceptor at a reformer pressure of 10 bar and S/C ratio of 3 for cycle times of 4 and 8 minutes.

Cycle time		4 min	8 min
Natural gas feed (LHV)	MW	1114.9	948.0
Hydrogen output (LHV)	MW	700.8	700.5
Fuel compression	MW	1.3	0.9
Oxygen production	MW	22.3	18.9
Waste gas compression	MW	1.8	5.6
Product compression	MW	20.7	20.9
Pumps	MW	1.6	0.5
CO2 compression	MW	20.9	17.7
Power input	MW	68.5	64.4
Power out turbine	MW	97.4	22.1
Net Power	MW	-29.0	42.4
Gross efficiency		0.63	0.74
Net efficiency		0.65	0.71

Table 6.5: Main process simulation results for SE-SMR with Na_2ZrO_3 as acceptor at 10 bar and S/C =3 for cycle times of 4 and 8 min.

Cycle time		4 min	8 min
Reactor cross-section area	m^2	21.0	19.5
Pseudo solid flow	kg/s	1001	539
Thermal efficiency	-	0.65	0.71

the combustion product. Table 6.5 shows the large difference in pseudo-solid flow for the two cycle times, which gives a large difference of heat flow in the system, directly affecting the thermal efficiency. In figure 6.8 and figure 6.9 the composite diagrams for the heat exchanger network for the 8 and 4 minute cycles are shown.

As observed in the figures, there is much higher total heat flow in the 4 minute cycle, and more heat is removed by the steam turbine cycle, shown as the constant line above 300 °C on the cold composite curve for both cycle times. Because more heat is removed in the 4 minute cycle, the constant level is longer for this cycle time. The largest difference between the two cycle times is the amount of heat on the hot composite curve above 575 °C. Due to the large amount of heat that must be transferred to the bed by combustion in the regeneration part, this high temperature heat is reflected in this area of the hot composite curve. When there are more mass that must be heated, as in the 4 minute cycle, more heat must be removed in this temperature area in the heat exchanger network.

Earlier works on hydrogen production by steam reforming have been with traditional steam reforming and amine scrubbing of the flue gas. The thermal efficiency reported for this process is 67.5 % with equal basis and methods of simulation.[37] The thermal efficiency calculated for SE-SMR with the given parameters is then comparable and higher than the thermal efficiency for SMR with CO_2 removal with equal boundary conditions. Metz et al. reports figures of 61.2% and 68.1 % net plant efficiency from two studies on hydrogen production by SMR with a 90% CO_2 removal, but with slightly different conditions.
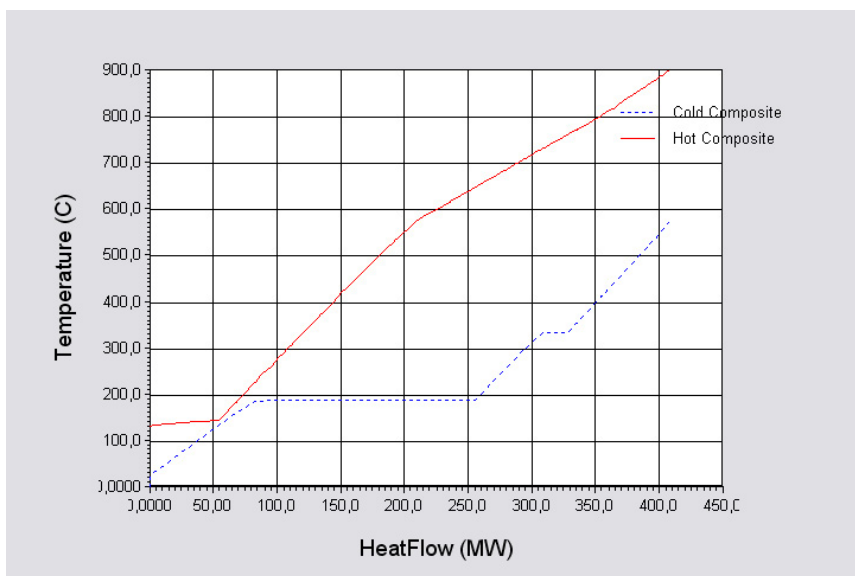
Figure 6.8: Hot and cold composite curves for the heat exchanger network for SE-SMR with Na_2ZrO_3 as acceptor at a pressure of 8 bar an S/C-ratio of 3 and a cycle time of 8 minutes.
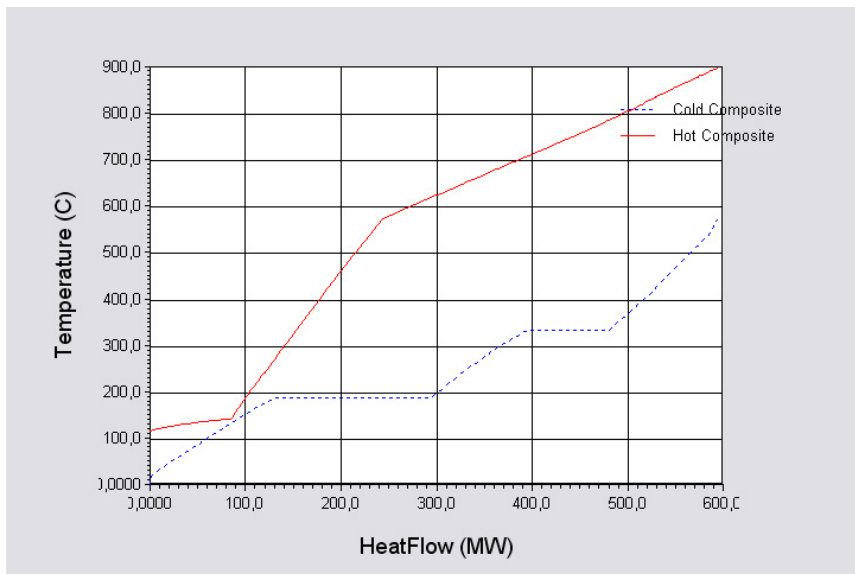
Figure 6.9: Hot and cold composite curves for the heat exchanger network for SE-SMR with Na_2ZrO_3 as acceptor at a pressure of 8 bar an S/C-ratio of 3 and a cycle time of 4 minutes.

6.3.2 The effect of regeneration temperature

The temperature of regeneration will have an impact of the efficiency of the process. As seen for the 4 and 8 minute cycles with Na_2ZrO_3 as sorbent, lower heat flows leads to higher efficiencies. As the regeneration kinetics and equilibrium is not known exactly is has been assumed that with a regeneration temperature of 900 °C, the equilibrium partial pressure of CO_2 would be above 1 atm and desorption is ensured. If the regeneration temperature can be lowered, it would be an advantage. The effect of this has been simulated, and the figures for thermal efficiencies for regeneration at 800, 850, and 900 °C are shown in the table below.

Table 6.6: Process thermal efficiency for SE-SMR with Na_2ZrO_3 as acceptor at a reformer pressure of 10 bar, an S/C ratio of 3 at different regeneration temperatures for a cycle time of 8 minutes.

Regeneration temperature (K)		1173	1123	1073
Natural gas feed (LHV)	MW	948.0	911.8	898.7
Hydrogen output (LHV)	MW	700.5	699.3	700.4
Fuel compression	MW	0.9	0.8	0.7
Oxygen production	MW	18.9	18.2	17.6
Waste gas compression	MW	5.6	6.0	6.5
Product compression	MW	20.9	20.9	20.9
Pumps	MW	0.5	0.2	0.1
CO2 compression	MW	17.7	17.0	16.3
Power input	MW	64.4	63.1	62.1
Power out turbine	MW	22.1	7.7	0.0
Net Power	MW	42.4	55.4	62.1
Gross efficiency		0.74	0.77	0.78
Net efficiency		0.71	0.72	0.73

It is for all these figures assumed that there are no kinetic or equilibrium limitations for the regeneration. As observed in table 6.6 a lower temperature has a positive impact on the thermal efficiency, but not as high impact as the longer cycles times shown previously. A positive effect is that for the 1073 K regeneration temperature there is no excess heat, and the steam turbine cycle is unnecessary.

Table 6.7: Main process simulation results for SE-SMR with Na_2ZrO_3 as acceptor at 10 bar and S/C =3 for different regeneration temperatures for a cycle time of 8 min.

Regeneration temperature (K)		1173	1123	1073
Reactor cross-section area	m^2	19.5	20.9	21.6
Pseudo solid flow	kg/s	539	535	552
Thermal efficiency	-	0.71	0.72	0.73

As observed in table 6.7 the pseudo-solid flow is not significantly different for the three different temperatures, not giving any difference in the heat that must be supplied to the process. But when the same mass must be heated from 575 °C to 900 °C instead of 800 °C the heat for heating the reactor bed will be significantly less, resulting in the difference in natural gas feed shown in table 6.6. This is directly affecting the thermal efficiency, giving the higher figure for regeneration at 800 °C.

6.3.3 Lithium Zirconate as CO_2-acceptor

The thermal efficiency of SE-SMR is dependent of steam to carbon ratio and the conversion in the reactor. With Li_2ZrO_3 as CO_2-acceptor the process performance is affected by the dramatic change in sorbent kinetics and thermodynamics. In section 5.1 the SE-SMR reactor was simulated with Li_2ZrO_3 as CO_2 acceptor. As described in section 5.1 a high steam to carbon ratio must be used to get satisfying conversion, and a ratio of 5 is used in the simulations. The main parameters in the simulations are given in table 6.8, and as seen; the regeneration temperature in addition to the superficial gas velocity and the S/C-ratio are the main differences. The regeneration temperature is set to the temperature where the equilibrium partial pressure of CO_2 is 1 bar, and because of the higher equilibrium partial pressure at equal temperature, the regeneration temperature with Li_2ZrO_3 as sorbent will be significantly lower than for Na_2ZrO_3. The conversion of methane from the reactor simulations at 10 bar, a temperature of 575 °C and an S/C ratio of 5 are shown in

Table 6.8: Simulation parameters for SE-SMR with Li_2ZrO_3 as CO_2-acceptor.

Reforming temperature (K)	848
Reforming pressure (bar)	10
Regeneration temperature (K)	900
Regeneration pressure (bar)	1.013
Gas velocity (m/s)	0.3
Reactor length (m)	10
S/C- ratio	5

figure 6.10. The conversion reached here is marginally higher than for Na_2ZrO_3, but the gas velocity is lower and the steam to carbon ratio is higher. As seen in figure 6.10 the conversion is kept at a high level much longer than for the Na_2ZrO_3, which means that the cycle time will be longer. The CO_2-capacity of Li_2ZrO_3 is marginally higher than for Na_2ZrO_3 (0.22 compared to 0.17 kg CO2/kg acceptor), but the main reason for a longer cycle time is the lower throughput in the reactor which means that the rate of CO_2-production is lower. In the Hysys simulations 50 and 100 minute cycles have been simulated. For the 50 minute cycle an average methane conversion of 60% has been used, and 55% conversion has been used for the 100 minute cycle.

The conversions from the Matlab simulations were in the same way as for the simulations with Na_2ZrO_3 used as input to the Hysys-simulations. The main stream data from the Hysys simulations with the 50 minute cycle are given in appendix A.2. The largest difference from the simulations with Na_2ZrO_3 is the higher fraction of CO_2 in the outlet of the reactor, and the higher steam content in most streams due to the higher steam to carbon ratio. In the same way as for the simulation with Na_2ZrO_3 as sorbent, the thermal efficiency of the process has been calculated. The main figures are shown in table 6.9. It was observed in the simulations with Na_2ZrO_3 as sorbent that the lower temperature of regeneration did not have a large effect on the thermal efficiency and it is other properties of Li_2ZrO_3 that make the thermal efficiency with this sorbent lower. Contrary to the simulations with Na_2ZrO_3 the longer cycle time gives a lower thermal efficiency, which means that there are other effects than the pseudo solid flow that has the largest effect on thermal efficiency. It is also observed that for this set-up of the Li_2ZrO_3 process there is no excess heat for the turbine cycle. This is due to the

Table 6.9: Process thermal efficiency for SE-SMR with Li_2ZrO_3 as acceptor at 10 bar and S/C = 5 with 50 and 100 min cycles compared to the thermal efficiency of the 8 minute cycle with Na_2ZrO_3 as sorbent.

Cycle		50 min Li_2ZrO_3	100 min Li_2ZrO_3	8 min Na_2ZrO_3
Natural gas feed (LHV)	MW	985.9	1012.0	948.0
Hydrogen output (LHV)	MW	699.2	700.1	700.5
Fuel compression	MW	0.7	0.5	0.9
Oxygen production	MW	16.7	15.8	18.9
Waste gas compression	MW	4.8	6.7	5.6
Product compression	MW	20.4	20.7	20.9
Pumps	MW	0.2	0.2	0.5
CO2 compression	MW	15.5	14.6	17.7
Power input	MW	58.2	58.4	64.4
Power out turbine	MW	0.0	0.0	22.1
Net Power	MW	58.2	58.4	42.4
Gross efficiency		0.71	0.69	0.74
Net efficiency		0.67	0.65	0.71
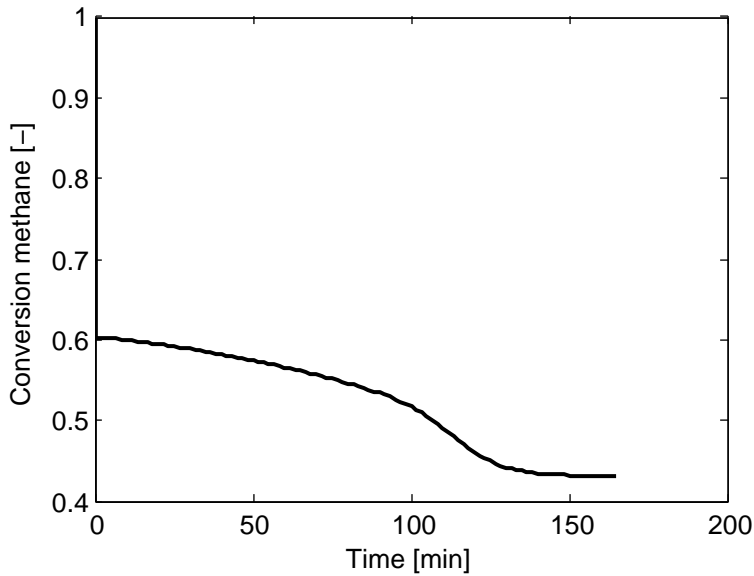
Figure 6.10: The conversion of methane in SE-SMR with Li_2ZrO_3 as sorbent at 575 °C, 10 bar and a S/C ratio of 5.

large amounts of steam that must be heated with a S/C ratio of 5. Instead of a gas turbine cycle it is in this case used steam at a pressure of 20 bar as heating medium in the heat exchanger network, and this is accounted for in the feed gas flow. It is not assumed that this steam boiler is of an oxyfuel type, thus a CO_2 removal below 100 % is calculated. The main results from the process simulations are shown in table 6.10. As observed, the thermal efficiency of the 50 minute cycle is higher than for the 4 minute cycle with Na_2ZrO_3, but lower than for the 8 minute cycle. The pseudo-mass flow for Li_2ZrO_3 as sorbent is 711 kg/s while it is 539 kg/s for the 8 minute Na_2ZrO_3 cycle. For the 100 minute cycle the pseudo-solid flow is lower than for the Na_2ZrO_3 cycle, but it is not reflected in the thermal efficiency. The heating of the reactor from reforming temperature to the regeneration temperature require significantly less heat for the Li_2ZrO_3 cycle than for Na_2ZrO_3, specially for the 100 minute cycle, where the pseudo solid mass flow is lower and the change in temperature is only 52 °C compared to 225°C. However, there are no excess heat in the heat integration in the 50 minute cycle, and the even lower heat rates in the 100 minute cycle does not lead to lower heat losses in the process. This means that the main reason for the lower thermal efficiency with Li_2ZrO_3 compared to Na_2ZrO_3 as CO_2 acceptor for these conditions is the higher steam to carbon ratio.

The lower thermal efficiency of the 100 minute cycle is due to the lower con-

Table 6.10: Main process simulation results for SE-SMR with Li_2ZrO_3 as acceptor at 10 bar and S/C = 5 compared to the results for Na_2ZrO_3 at S/C = 3, 10 bar and with a 8 min. cycle.

Cycle		50 min Li_2ZrO_3	100 min Li_2ZrO_3	8 min Na_2ZrO_3
Reactor cross-section area	m^2	173	186	21
Pseudo solid flow	kg/s	711	388	539
Thermal efficiency	-	0.67	0.65	0.71
CO_2 removal	-	0.86	0.79	1

version in the reactor and more gas is recycled from the PSA. The hot and cold composite curves for the Li_2ZrO_3 cycle for the 100 minute and 50 minute cycles are shown in figure 6.11 and figure 6.12.
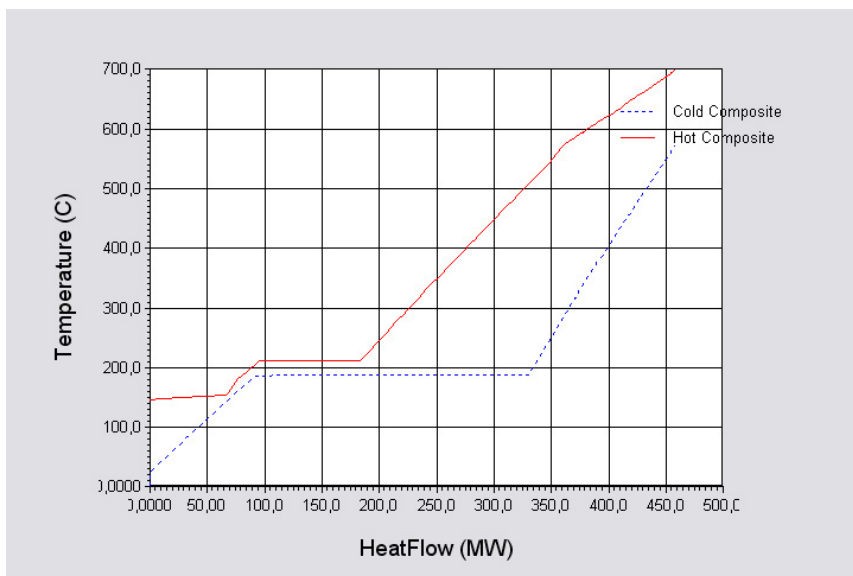
Figure 6.11: Hot and cold composite curves for the heat exchanger network in the 100 minute Li_2ZrO_3 SE-SMR cycle.

Differently from the 8 minute Na_2ZrO_3 cycle at 10 bar and S/C of 3, there is no excess heat in the SE-SMR cycle with Li_2ZrO_3. This means that steam heating
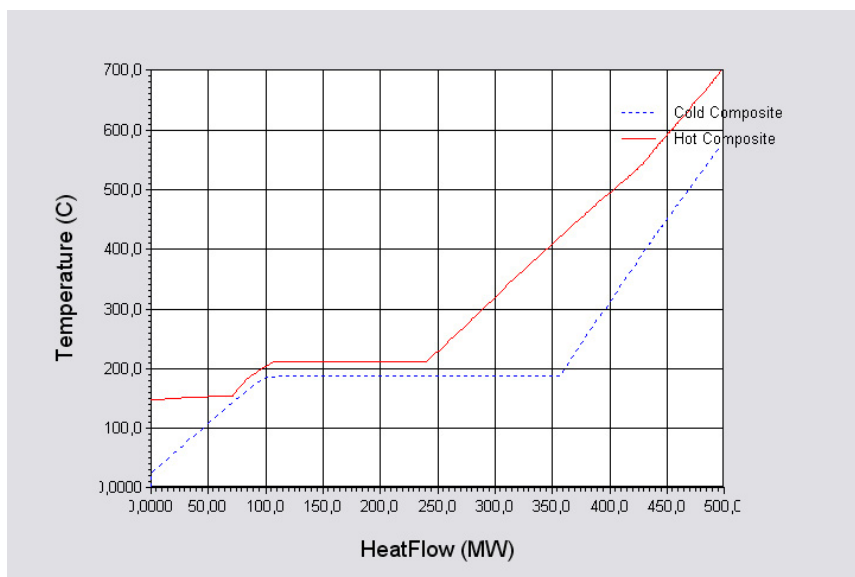
Figure 6.12: Hot and cold composite curves for the heat exchanger network in the 50 minute Li_2ZrO_3 SE-SMR cycle.

is added in the heat integration, seen as the constant level just above 200 °C in the hot composite curve. The vaporization of steam for the reforming is reflected in the constant line just below 200 °C in the cold composite curve, and it is seen that more heat is required for the 100 minute cycle than for the 50 minute cycle in the vaporization. This is due to the lower conversion which means that more methane must be fed to the reactor for the equal amount of product, resulting in a higher steam rate. This directly affects the amount additional heat that must be put into the heat exchanger network.

The other main difference for the process with lithium zirconate is that a much larger reactor has to be used for Li_2ZrO_3 as sorbent for equal hydrogen production capacity. The necessary crossectional area of the reforming bed for the most effective cycle time is 173 m^2 compared to 21 m^2 for Na_2ZrO_3, and not to forget that this is only one of the beds where there must be three or more in parallel. The lower change in temperature from hydrogen production to regeneration will lead to easier operation, and lower temperature can lead to less expensive materials of construction. These are effects that not have been incorporated into the models, and which should be looked at when doing a complete analysis of the process, but the slow kinetics of Li_2ZrO_3 does not make it at attractive sorbent for SE-SMR.

6.3.4   The effect of higher methane conversion

Higher conversion in the reactor without changing the other operating conditions should increase the process performance. Without changing the acceptor properties or the operating conditions, higher conversion can be reached by using a longer reactor. Higher conversion could also be achieved by having a faster sorbent, e.g. CaO as shown in section 5.3.4. A case with Na_2ZrO_3 at equilibrium conversion has been simulated with all other process parameters as given in table 6.2. The equilibrium conversion of methane at equilibrium is 0.77, which is at a partial pressure of CO_2 of 152 Pa. The main stream data for the process simulations are shown in appendix A.3. With higher conversion, the thermal efficiency increases, in this case from about 0.74 to 0.78. The figures for the calculation of thermal efficiency are shown in table 6.11 for a cycle time of 8 minutes. The regeneration has been done at a temperature of 1173 K. It is still assumed a 10 m long reactor which means that for these simulations looks at the effect of having improved CO_2 capture kinetics on Na_2ZrO_3.

It is observed that the thermal efficiency at equilibrium conversion is significantly higher than for the conversion from the Matlab simulations. The thermal efficiency for the 8 minute cycle with kinetic limitations on the reforming and a regeneration temperature of 1173 K gave thermal efficiency of 0.71 compared to 0.74. The pseudo-solid flow and the reactor cross section for the simulations with equilibrium reforming conversion are shown together with the thermal efficiency table 6.12. The change in conversion both means that less natural gas must fed to the process for the production of the necessary amount of hydrogen, and the lower volume flow also reduces the pseudo solid flow in the reactor. The change in pseudo solid flow is 487 kg/s for the high conversion compared to 539 kg/s for the simulated reactor. This has an effect on the thermal efficiency, due to that less heat is lost in the cooling of the reactor bed. It is seen in table 6.11 no power for waste gas compression is required for the equilibrium simulation, also increasing the efficiency. This is due to that with a high conversion the purity of the product stream for the reforming section is high, and less tail gas from the PSA produced. This means that all tail gas is used in the regeneration heating.

Table 6.11: Process thermal efficiency for SE-SMR with Na_2ZrO_3 close to equilibrium, at 10 bar and S/C = 3.

Regeneration limitation		Equilibrium	Kinetic
Natural gas feed (LHV)	MW	932.2	948
Hydrogen output (LHV)	MW	699.7	700.5
Fuel compression	MW	1.0	0.9
Oxygen production	MW	17.7	18.9
Waste gas compression	MW	0.0	5.6
Product compression	MW	19.7	20.9
Pumps	MW	0.5	0.5
CO2 compression	MW	17.4	17.7
Power input	MW	56.5	64.4
Power out turbine	MW	38.4	22.1
Net Power	MW	18.1	42.4
Gross efficiency		0.75	0.74
Net efficiency		0.74	0.71

Table 6.12: Main process simulation results for SE-SMR with Na_2ZrO_3 as acceptor close to equilibrium at 10 bar and S/C =3 for a cycle time of 8 min compared to the results with kinetic limitation.

Regeneration limitation		Equilibrium	Kinetic
Reactor cross-section area	m^2	14.3	19.5
Pseudo solid flow	kg/s	487	539
Thermal efficiency	-	0.74	0.71

6.3.5   The effect of higher reformer pressure

With a high pressure in the reformer the cross-sectional area of the reformer could be lowered if the superficial velocity is kept constant. However, the thermodynamics is favored at a lower total pressure. Therefore, it has been looked at a case where the pressure in the reactor is increased to 20 bar. In figure 5.40 in section 5.3 the effect on dry hydrogen mole fraction is observed at a constant mass input. It is seen that the initial dry hydrogen mole fraction falls from 0.83 at 10 bar to 0.80 with a pressure of 20 bar, and this corresponds to a fractional conversion of 0.5. A cycle time of 8 minutes has been used for the simulations which gives an average methane conversion of 0.47. The results for the 20 bar simulations is compared with the results from the simulations at 10 bar. The superficial velocity at 20 bar is lower, but the conversion of methane is lower because of the thermodynamics. Because the PSA is operated at 20 bar the compression before the PSA-unit is also avoided. The figures for the thermal efficiency for the simulation of the 20 bar process are shown in table 6.13 together with the figures for the process with Na_2ZrO_3 for a cycle time of 8 minutes.

It is observed that a lower product compression power is needed, but more power for the waste gas compression is necessary due to lower methane conversion, leading to higher flow of waste gas, and higher differential pressure. It is seen that even if the net power for the 20 bar case is lower than for the 10 bar case, the net efficiency is lower. This is due to that more feed must added to get a 700 MW LHV product because of the lower conversion, leading to higher pseudo-solid flow and more heat for feed heating. However, the effect of a higher pressure is not very large, and it must be looked at more closely to make definitive conclusions. The compressor in front of the PSA can be removed which will give a positive impact on cost, but the reactor could be more expensive because of higher pressure.

Table 6.13: Process thermal efficiency SE-SMR with Na_2ZrO_3 as sorbent at 20 bar and S/C=3

Reactor pressure		20 bar	10 bar
Natural gas feed (LHV)	MW	967.6	948
Hydrogen output (LHV)	MW	699.9	700.5
Fuel compression	MW	0.9	0.9
Oxygen production	MW	19.3	18.9
Waste gas compression	MW	8.2	5.6
Product compression	MW	11.4	20.9
Pumps	MW	0.7	0.5
CO2 compression	MW	18.1	17.7
Power input	MW	58.5	64.4
Power out turbine	MW	29.8	22.1
Net Power	MW	28.7	42.4
Gross efficiency		0.72	0.74
Net efficiency		0.70	0.71

Table 6.14: Main process simulation results for SE-SMR with Na_2ZrO_3 as acceptor at 20 bar compared to the results at 10 bar for cycle times of 8 minutes.

Reactor pressure		20 bar	10 bar
Reactor cross-section area	m^2	23.4	19.5
Pseudo solid flow	kg/s	600	539
Thermal efficiency	-	0.7	0.71

6.3.6   The effect of higher steam to carbon ratio

Previously, the performance of SE-SMR with Li_2ZrO_3 as acceptor was looked at, and the results was a lower thermal efficiency than with Na_2ZrO_3, partly because of higher steam to carbon ratio. If the S/C-ratio is increased with Na_2ZrO_3 as sorbent, the conversion can be increased. The effect this has on the thermal efficiency has been looked at. All other parameters are the same as given in table 6.2 and when the S/C-ratio is increased to 4, the conversion of methane increases. Figure 5.43 in section 5.3 shows that the dry hydrogen mole fraction at maximum conversion is about 0.88. This corresponds to a methane conversion of 65 %. For an 8 minute cycle the average dry hydrogen mole fraction is 0.87 which corresponds to a methane conversion of 62%.

Table 6.15 shows the overview of the thermal efficiency of the process at an S/C-ratio of 4 and a cycle time of 8 minutes. The conversion in the reactor is higher but the increased amount of steam has a negative effect on the thermal efficiency. By increasing the S/C-ratio from 3 to 4 the thermal efficiency of the process decreases from 0.71 to 0.70. The difference in thermal efficiency for this case is not large, but the difference is due to that with higher steam to carbon ratio a more steam must be heated and there is also a slightly higher pseudo-solid flow due to that higher steam to carbon ratio gives a higher total gas flow through the reactor, even if the amount of recycled gas from the PSA tail gas is lower. The results shows that a low S/C ratio is favorable, but not to a dramatic extent. The increased heat of vaporization is nearly made up for by the increase in conversion. If there were no excess heat for the steam turbine cycle the effect of increasing the steam to carbon ratio would be much more dominant, as for Li_2ZrO_3 as sorbent.

Table 6.15: Process thermal efficiency SE-SMR with Na_2ZrO_3 as sorbent at 10 bar and S/C=4

S/C-ratio		**4**	**3**
Natural gas feed (LHV)	MW	952.1	948
Hydrogen output (LHV)	MW	699.3	700.5
Fuel compression	MW	1.0	0.9
Oxygen production	MW	19.0	18.9
Waste gas compression	MW	2.3	5.6
Product compression	MW	20.3	20.9
Pumps	MW	0.4	0.5
CO2 compression	MW	17.7	17.7
Power input	MW	60.7	64.4
Power out turbine	MW	15.6	22.1
Net Power	MW	45.1	42.4
Gross efficiency		0.73	0.74
Net efficiency		0.70	0.71

Table 6.16: Main process simulation results for SE-SMR with Na_2ZrO_3 as acceptor with S/C-ratio of 4 compared to the results with an S/C-ratio of 3.

S/C-ratio		**4**	**3**
Reactor cross-section area	m^2	21.5	19.5
Pseudo solid flow	kg/s	550	539
Thermal efficiency	-	0.7	0.71

6.3.7   Air as regeneration combustion medium

To get a high CO_2 removal, the regeneration has to be done with pure oxygen if not another process for CO_2-removal is included. An air separation unit, which is necessary to make pure oxygen, is expensive both in investment cost and energy-wise. If a lower CO_2 removal can be tolerated, combustion in air for the regeneration of the sorbent is an option. In that case the combustion product and the CO_2 from regeneration can not be mixed if CO_2 removal is wanted. Only the captured CO_2 from the reforming is sent to injection and the design of the reactor must be equal to a traditional reforming reactor, with firing of the natural gas outside the tubes. When simulating this process it has been assumed that the combustion products exits the regeneration at 900 °C and this stream is used for heating of the air and fuel feed to the regeneration reactor. Table 6.17 shows the thermal efficiency of the process when air is used instead of pure oxygen for the case with Na_2ZrO_3 as sorbent, and all other parameters as shown in table 6.2. Surprisingly it is seen that combustion in air gives a much lower thermal efficiency than the combustion in oxygen. The zero power for oxygen production gives a positive impact, but the net result is negative. The main reason for this is the large amount of low temperature heat that is lost. Due to the 79% nitrogen content in air, the mass flow with high temperature from the regeneration will be much higher. As observed in table 6.17 some of the heat is recovered in the steam turbine cycle, but it is impossible to recover all the heat. This means that the total input of heat to the system is much higher for the case with air than for oxygen as combustion medium. The pseudo-solid flow is in this case more or less equal for the two cases that is compared, and differently from many of the other cases looked at, not the significant factor for the difference in thermal efficiency. The other main drawback with air as combustion medium, in addition to the low efficiency, is that only 55% of the CO_2 is captured. The results here show that oxygen should be more attractive for the regeneration heating than air. The cost of an air separation unit is large, but the changes in CO_2 removal and thermal efficiency is quite dramatic.

Table 6.17: Process thermal efficiency SE-SMR with Na_2ZrO_3 as sorbent, regeneration heat from combustion in air

Combustion medium		Air	Oxygen
Natural gas feed (LHV)	MW	1156.1	948.0
Hydrogen output (LHV)	MW	699.6	700.5
Fuel compression	MW	1.3	0.9
Oxygen production	MW	0.0	18.9
Waste gas compression	MW	2.8	5.6
Product compression	MW	21.0	20.9
Pumps	MW	1.7	0.5
CO2 compression	MW	11.4	17.7
Power input	MW	38.2	64.4
Power out turbine	MW	105.3	22.1
Net Power	MW	-67.1	42.4
Gross efficiency		0.61	0.74
Net efficiency		0.64	0.71

Table 6.18: Main process simulation results for SE-SMR with Na_2ZrO_3 as acceptor at 10 bar and S/C = 3 in 8 minute cycles with a comparison of regeneration firing in air or pure oxygen.

Combustion medium		Air	Oxygen
Reactor cross-section area	m^2	21.3	21
Pseudo solid flow	kg/s	555	539
Thermal efficiency	-	0.64	0.71
CO_2 removal	-	0.55	1

6.3.8   Mixed methane hydrogen product

If the product stream is used in a combustion power plant and not in fuel cells, there is no specific limit on the hydrogen purity, and the unconverted methane can be burned with hydrogen in gas turbines. The degree of methane conversion in SE-SMR would then mostly be dependent on how high CO_2 removal rate that is desired. In this case the PSA-unit would be obsolete and the stream before the PSA unit in figure 6.3 is the product stream going to the power plant. The product hydrogen pressure is here set to 30 bar, a typical fuel pressure for gas turbines. The process has been simulated for the case described, and it naturally leads to an increased efficiency of the process. But because non-converted methane is not recirculated the fraction CO_2 captured will be less, when the CO_2 in the product methane is calculated as CO_2-equivalents. The main stream data for the simulations without H_2-purification are given in appendix A.4.

For the case where pure oxygen is used for regeneration the figures for the calculation of thermal efficiency are shown in table 6.19. The figures for the thermal efficiency show that there are several places where energy is saved compared to the case with purification of hydrogen. There is of course no need for waste gas recompression or fuel compression, because all fuel is taken from the high pressure inlet natural gas. The reason that less hydrogen is produced is because methane here is included in the LHV of the product. The power for CO_2-compression will also be less in this case, due to that less CO_2 is captured and compressed. The fraction of CO_2 captured is shown together with the other main results in table 6.20. As seen here, the thermal efficiency for this process will be significantly higher than for the one with pure H_2 as product, but it comes at the cost of lower fraction of CO_2 sequestrated. If a higher CO_2 removal is desired the solution would be to have a higher conversion in the reforming, which could be done by increasing

Table 6.19: Process thermal efficiency of SE-SMR without H_2-purification with Na_2ZrO_3 as sorbent.

Product		H_2 +CH_4	H_2
Natural gas feed (LHV)	MW	818.2	948.0
Hydrogen output (LHV)	MW	700.6	700.5
Fuel compression	MW	0.0	0.9
Oxygen production	MW	12.6	18.9
Waste gas compression	MW	0.0	5.6
Product compression	MW	12.3	20.9
Pumps	MW	0.2	0.5
CO2 compression	MW	9.2	17.7
Power input	MW	34.4	64.4
Power out turbine	MW	9.2	22.1
Net Power	MW	25.2	42.4
Gross efficiency		0.86	0.74
Net efficiency		0.83	0.71

Table 6.20: Main process simulation results for SE-SMR with Na_2ZrO_3 as acceptor without H_2-purification.

Reactor cross-section area	m^2	10
Pseudo solid flow	kg/s	258
Thermal efficiency	-	0.83
CO_2 sequestration	-	0.62

the residence time in the reactor or having a faster CO_2 acceptor. The volume flow through the reactor will be much smaller because less feed is needed to get the specified LHV of product, and no gas is recycled back to the reforming. The product hydrogen in this case is about 80 mole% and the majority of the rest is methane. The carbon in the methane is also accounted for in the CO_2-removal given in table 6.20.

6.3.9 CO_2 recycle for combustion temperature control

As mentioned earlier in this chapter, excessive temperatures could be a problem with O_2 as combustion medium even if no detailed analysis have been carried out on this subject. One solution to this could be to recycle CO_2 to lower the concentration of fuels and oxygen in the combustion. Two different ways of doing this have been investigated. A cold CO_2 stream at about 130 °C after the integration could be used, or the high temperature CO_2 content stream directly from the regeneration could be recycled. To be able to recycle this a fan has to be installed and it has been assumed a 2 bar exit pressure from the recycling fan. A 50% recycle of the CO_2 stream has been assumed in the simulations. It is not considered if a fan operating at a temperature above 800 °C is practically feasible. The figures for the thermal efficiency are given in table 6.21, where the CO_2 recycle fan power has been added to the CO_2 compression power. The figures in the table above give a similar thermal efficiency for the hot recycling as without recycling, while the cold recycle gives a significantly lower thermal efficiency. The reason for this is that when a cold recycle stream is introduced in the regeneration more fuel must be added to keep the high temperature, which results in a higher total fuel consumption. For the hot recycle the gross efficiency actually is higher than for the simulation without the recycle. The reason for this is that heat is added to the stream when it is pressurized and this heat will reduce the amount of fuel that has to be added in the regeneration. However, the effect of this naturally lost on the net efficiency, when the fan power is taken into account. This means that if CO_2 is to be recycled it should be done at as high temperature as possible to avoid losses of thermal efficiency, but naturally the effect on temperature control in the combustion would be higher with a colder stream. These effects has to be weighed against each other together with the feasibility of having a fan operating with a hot gas when evaluating the recycling of CO_2 in the regeneration heating.

Table 6.21: Process thermal efficiency of SE-SMR with CO_2 recirculation at low (LT) and high temperature (HT) with Na_2ZrO_3 as sorbent compared to the process without recirculation. All simulations at S/C =3, 10 bar reforming pressure and 8 minute cycle time

CO_2 recirculation		HT	LT	None
Natural gas feed (LHV)	MW	908	1046	948
Hydrogen output (LHV)	MW	700.6	699.8	700.5
Fuel compression	MW	0.8	1	0.9
Oxygen production	MW	18.2	20.9	18.9
Waste gas compression	MW	5.9	4.2	5.6
Product compression	MW	20.7	21.0	20.9
Pumps	MW	0.5	1.1	0.5
CO2 compression	MW	33.2	28.2	17.7
Power input	MW	79.3	76.5	64.4
Power out turbine	MW	15.9	65.6	22.1
Net Power	MW	63.4	10.8	42.4
Gross efficiency		0.76	0.67	0.74
Net efficiency		0.71	0.66	0.71

6.3.10   Concluding remarks on the reactor simulation results

The simulations carried out in this part of the thesis shows that it is possible to reach high thermal efficiencies when using actual kinetics for the CO_2 capture. This can be done without using too large reactors, a typical reactor size for the process with Na_2ZrO_3 as acceptor would have a length of 10 meters and a diameter of about 4.5-5 meters if the heat of regeneration is supplied inside the bed. To have a high CO_2-removal(85 %) the heat for regeneration must be supplied from combustion in pure oxygen. When a lot of high temperature heat must be supplied the oxygen alternative is also more efficient than with air. It is also shown that the capture-kinetics of sorbent is important, and to have high thermal efficiency the kinetics must be fast enough for SE-SMR with relatively low residence times and steam to carbon ratios, and if the kinetics of sorption on Na_2ZrO_3 could be improved further, this would increase the thermal efficiency of SE-SMR. The heating of the bed from reaction temperature to regeneration demands a lot of heat and this heat is dominating the heat flow in the system and the thermal efficiency of the process. As long as there are excess high temperature heat in the system it is advantageous to have a longer cycle time and a lower conversion. For optimization of the process it should be set up in a way that the necessary heating and cooling above the pinch point are as much in balance as possible. For this optimization more reliable data for the regeneration is necessary, and both the thermodynamics and kinetics have to be looked at in detail. The change in temperature from reforming to regeneration can also lead to difficulties with construction material. However the relative change is not that high compared to e.g. dehydration with mol sieves where typical changes in temperature is from 30 °C to 250 °C with similar cycle times used for the simulations here. Perhaps the most promising process seems to be a process with a production of a mixed methane/hydrogen product. This increases the thermal efficiency of the process dramatically, and if a faster sorbent were used the CO_2 removal could be in the region of typical SMR with an amine CO_2 removal process(85-90%). With some methane in the product this also eases the design of gas turbines for power production because the combustion would yield lower temperatures. The necessary reactor area for this process would also be about half of the area for a production of a pure hydrogen product.

Chapter 7

Conclusions and proposed further work

7.1 Conclusions

The work in this thesis has focused on simulation of hydrogen production by sorption enhanced steam methane reforming in a fixed bed reactor. A robust transient one dimensional model has been formulated and implemented for the simulations of the reforming reactor. Three main models have been formulated, one pseudo-homogeneous model and two heterogeneous model that account for intraparticle mass and heat transfer. The two heterogeneous models are different in the way the solid materials are placed in the reactor. The 1-particle model considers one type of pellet in the reactor consisting of both catalytic and sorbent material, while the 2-particle model considers two separate pellet types with catalytic and sorbent material.

To simulate sorption enhanced steam methane reforming reactors, kinetic models for all major reactions must be formulated. The steam methane reforming reactions have been extensively studied earlier, and the kinetic model of Xiu and Froment was used in the simulations. Different solid synthetic materials for the high temperature CO_2 capture have been studied and kinetic models for the capture of CO_2 on these materials have been formulated in this thesis. Two of the materials, nanocrystalline lithium zirconate and sodium zirconate have been synthesized at NTNU, while the lithium silicate was obtained from Toshiba. The materials synthesized at NTNU showed quite similar kinetic properties, and the capture rate of CO_2 was described by a first order rate reaction with respect to fractional conversion of the solid. This can indicate that the kinetics are limited by nucleation as described by the Avrami-Erofeev model. Others have also used the first order model, without using it to describe a specific mechanism. The two zirconates had

been synthesized by the same method, and it is reasonable to believe that this is the reason for why the same formulation could be used to model the capture kinetics on both materials. Contrary the lithium silicate material showed a CO_2 capture rate which were dependent on the squared fractional conversion. This does not indicate any specific mechanism, but can be the result of changes in mechanism during the course of reaction. However, while the shape of the rate expression was similar for the two zirconates, the reaction rates did differ substantially. The lithium zirconate had the slowest capture rate of the materials, with a kinetic constant about 100 times lower than the one for sodium zirconate, which showed the fastest kinetics. The capture rate on lithium silicate was found to be between the two other materials.

The simulations of SE-SMR show that it is possible to produce hydrogen with a purity above 80 % on a dry basis in a fixed bed reactor with the investigated sorbents. The conversion is very dependent on the kinetics of the sorbent and the steam to carbon ratio. With lithium zirconate as acceptor a steam to carbon ratio of 5 had to be used to reach a dry hydrogen purity above 80%. The superficial velocity used for the simulations with Li_2ZrO_3 was 0.3 m/s for the base case and a dry hydrogen mole fraction of about 0.86 was reached after 10 meters at this velocity. This is low compared to traditional SMR, which often uses gas velocities above 2 m/s, and a very large reactor would be needed to produce the same amount of hydrogen as traditional SMR with Li_2ZrO_3 as acceptor in SE-SMR.

The capture kinetics on Li_2ZrO_3 are slow, and no need for heterogeneous models were found for the pellet size used in the simulations. However, if the pellet size was increased there would be mass transfer effects, and a simple pseudo homogeneous model would over predict the conversion of methane. The model used in the simulations incorporates the effect of mass removal from the gas phase due to CO_2 capture. The effect of including this part was looked at, and it showed that there was significant difference in the solutions when compared to models with constant mass flow or constant gas velocity. When comparing the results with lithium silicate as acceptor to the results with lithium zirconate, it was seen that much higher gas velocities could be used at equal steam to carbon ratios, and still obtain dry hydrogen mole fractions at the outlet of the reactor above 0.8. For the simulations with Li_4SiO_4 it was observed that a pseudo homogenous model gave the same results as the heterogeneous model when the acceptor and the catalyst were localized in the same pellet. When two different pellets were used, a difference in reactor performance was observed due to mass transfer limitations. This shows that the distribution of the active materials has an effect on the overall performance, and if possible, one particle should be used for best possible performance. A comparison with a fluidized bubbling bed reactor has also been done, and it showed that while the temperature gradients in the fluidized bed were much smaller, a longer reactor

was needed to reach the same conversion as in a fixed bed reactor.

Sodium zirconate was the last acceptor where a kinetic expression for the capture rate was found from in-house experimental data. This acceptor showed clearly better performance in SE-SMR than the previous two, due to both superior kinetics and lower equilibrium partial pressure. The change in properties meant that hydrogen with above 80% purity could be produced with as low steam to carbon ratios as 3, and with gas velocities up to 2 m/s in a 10 meter long reactor. The simulations with a heterogeneous model showed that there would be mass transfer limitations with the pellet size used, and the one-particle heterogeneous model was used for the simulations.

An important result from all simulations is that it is seen that there will be large temperature gradients in the reactor even if the total reaction not is very endothermic. If a fixed bed reactor is operated without external heating, the temperature close to the inlet will decrease dramatically, while the outlet temperature will increase. This means that temperature control could be necessary during hydrogen production, and that heating/cooling not only has to be supplied during regeneration.

The simulations of the SE-SMR with Na_2ZrO_3 ere also compared to experimental data. The simulations showed that the models gave a good prediction of the conversion in the reactor. However, the experimental set-up had too large dead volumes to be able to predict the whole cycle until the sorbent was fully saturated. The results from the simulations with Na_2ZrO_3 were finally compared to results from simulations with a synthetic CaO as sorbent. It showed that even if the Na_2ZrO_3 has very good properties compared to Li_4SiO_4 and Li_2ZrO_3 the kinetics of CaO were superior.

The SE-SMR process as a whole has been studied, from the inlet stream of natural gas to production of hydrogen and compression/injection of CO_2. This has been done by incorporating the results from the reactor simulations in simulations of the whole process. The analysis ware done using the conversion results from the reactor simulations and it has been shown that a process thermal efficiency comparable to and higher than SMR with CO_2 capture can be reached. The efficiency is very dependent on the amount of heat that must be supplied to the reactor in the regeneration step and the kinetics of the sorbent. A thermal efficiency of 0.71 was calculated for an SE-SMR process with Na_2ZrO_3 as sorbent with a gas velocity of 2 m/s, a 10 m long reactor, a pressure of 10 bar, a reforming temperature of 848 K and a steam to carbon ratio of 3. The heat for regeneration was in this case supplied by combustion of methane in pure oxygen and yielded high degree of CO_2-removal ($\approx 100\%$). The temperature of regeneration used for Li_2ZrO_3 as sorbent were only 52 °C higher than the reforming temperature, while it was 325 °C higher for Na_2ZrO_3. When Li_2ZrO_3 replaced Na_2ZrO_3 as CO_2-acceptor the

lower temperature increase for regeneration, which lead to less heat supplied, did make up for some of the disadvantages of Li_2ZrO_3, but in total the slower kinetics make it a less promising sorbent for SE-SMR. With all other parameters equal the thermal efficiency fell from 0.71 to 0.67 when using Li_2ZrO_3 as acceptor instead of Na_2ZrO_3. At the same time the cross-section area of the reactor had to be increased almost 10 times to get the throughput that was necessary to have equal production of hydrogen.

The process efficiency can be increased for Na_2ZrO_3 if better kinetics or a longer reactor are used. If the conversion of methane could reach equilibrium the thermal efficiency of the process would increase from 0.71 to 0.74. High degree of CO_2 removal is only reached if the heat of regeneration is supplied by combustion in pure oxygen and the simulations show that only about 55 % of the carbon can be captured if the combustion is carried out in air. In this case the only captured carbon is from the reforming and not from the combustion of methane for regeneration heating.

The possibility of not producing pure hydrogen, but a mixture of hydrogen and methane has also been investigated. With the low conversion of methane the CO_2 capture simulated for this process was only 62 % when the methane content in the product is calculated as CO_2-equivalents. The thermal efficiency of this process was about 0.83, compared to the 0.71 for the case with pure hydrogen as product. If the kinetics of CO_2-sorption could be increased, giving higher hydrogen content in the product, an increased CO_2 removal can be reached without lowering the thermal efficiency.

7.2   Proposed further work

This work has focused on the reforming reactor and the kinetics of capture and has shown that it is possible to produce hydrogen with high purity by SE-SMR. There has not been enough data available for the regeneration kinetics to be modeled and simulated, and this should be the main focus in further work on SE-SMR. The regeneration could pose a challenge when large amounts of heat has to be supplied to release the CO_2. Accurate models of this will help in the work of finding the optimum operating point and the way of doing the regeneration. The heating to the regeneration could be done indirectly through the pipe wall or by combustion inside the reactor volume. In any case it is important to describe the heat transfer and reactions in the regeneration reactor. Na_2ZrO_3 had the best properties of the materials that was characterized, and had kinetics properties which make it an interesting challenger to CaO. A comparison with a synthetic CaO material showed that Na_2ZrO_3 was not as fast as CaO, and for the more expensive materials like zirconates to be alternatives they have to have better properties than CaO or MgO.

Even if the Na_2ZrO_3 showed lower performance the problem with CaO has been that it does not withstand thousands of cycles, and how the material performance declines after cycles should be incorporated into the models to get a complete picture.

There are problems with operating the fixed bed reactor that could be difficult to overcome. Large changes in temperature between cycles and internal temperature gradients are problems that could be diminished by using a fluidized bed reactor concept. The temperature gradients in a fluidized bed reactor are much smaller and when using one reactor as reformer and the other as regenerator the cycling in temperature is removed. The small endothermic heat of the reforming section can then be supplied as hot regenerated particles. Though, the challenge in supplying the heat to the regenerator is still there, and modelling of the whole reforming-regeneration cycle in a fluidized bed reactor with the possibility of incorporate different type of heat sources, both indirect and combustion inside the reactor volume is something that should be looked into.

For a fixed bed reactor system unmixed combustion could be a concept that would make it easier to control temperature and CO_2 release. This is something that could an alternative for the heat supply during regeneration. By first feeding oxygen that reacts with nickel in the catalyst and then the methane for combustion, it could be possible to lower the temperature of combustion. For fixed bed reactor concept it is important to control the temperature at a level as low as possible while CO_2 still is released at a reasonable rate.

As the comments here suggests, most of the work on SE-SMR has been on the reforming, and now it is time to go deeper into detail on the regeneration, and to combine the modelling of the reforming and the regeneration, with special care given to how the heat is supplied during regeneration.

Bibliography

(1) High level group for hydrogen and fuel cells technologies: Hydrogen energy and fuel cells: A vision of our future. European commision, 2003.

(2) Encap d1.1.1 &d1.1.2. reference cases and guidelines for technology concepts. ref. mp. 29623, 2004.

(3) A. M. Adris, B. B. Pruden, C. J. Lim, and J. R. Grace. On the reported attempts to radically improve the performance of the steam methane reforming reactor. *Canadian Journal of Chemical Engineering*, 74:177–186, 1996.

(4) M. Avrami. Kinetics of phase change. i. general theory. *Journal of Chemical Physics*, 7:1103–12, 1939.

(5) M. Avrami. Kinetics of phase change. ii. transformation-time relations for random distribution of nuclei. *Journal of Chemical Physics*, 8:212–24, 1940.

(6) M. Avrami. Granulation, phase change and microstructure. kinetics of phase change. iii. *Journal of Chemical Physics*, 9:177–84, 1941.

(7) L. Bernstein, P. Bosch, O. Canziani, Z. Chen, R. Christ, W. H. Ogunlade Davidson, S. Huq, D. Karoly, V. Kattsov, Z. Kundzewicz, J. Liu, U. Lohmann, M. Manning, T. Matsuno, B. Menne, B. Metz, M. Mirza, L. N. Neville Nicholls, R. Pachauri, J. Palutikof, M. Parry, D. Qin, N. Ravindranath, A. Reisinger, J. Ren, K. Riahi, C. Rosenzweig, M. Rusticucci, Y. S. Stephen Schneider, S. Solomon, P. Stott, R. Stouffer, T. Sugiyama, D. T. Rob Swart, C. Vogel, and G. Yohe. *IPCC, 2007: Climate Change 2007: Synthesis Report. Contribution of Working Groups I, II and III to the Fourth Assessment Report of the Intergovernmental Panel on Climate Change*. IPCC, Geneva, Switzerland, 2008.

(8) S. K. Bhatia and D. D. Perlmutter. A random pore model for fluid-solid reactions. i. isothermal, kinetic control. *AIChE Journal*, 26:379–86, 1980.

(9) R. B. Bird, W. E. Stewart, and E. N. Lightfoot. *Transport Phenomena*. Wiley, New York, 1960.

(10) R. B. Bird, W. E. Stewart, and E. N. Lightfoot. *Transport Phenomena*. Wiley, New York, 2nd edition, 2002.

(11) O. Bolland and H. Undrum. A novel methodology for comparing CO_2 capture options for natural gas-fired combined cycle plants. *ADVANCES IN ENVIRONMENTAL RESEARCH*, 7(4):901–911, JUN 2003. ISSN 1093-0191.

(12) A. Bruun-Tsekhovoi, A. Zadorin, Y. Katsobashvili, and S. Kourdyumov. The process of catalytic steam reforming of hydrocarbons in the presence of carbon dioxide acceptor. In *Hydrogen Energy Progress VII, Proceedings of the World hydrogen Energy Conference*, pages 885–900. Pergamon Press, 1988.

(13) A. Burghardt and J. Aerts. Pressure changes during diffusion with chemical reaction in a porous pellet. *Chemical Engineering and Processing*, 23:77–87, 1988.

(14) Y. Ding and E. Alpay. Equilibria and kinetics of CO_2 adsorption on hydrotalcite adsorbent. *Chemical Engineering Science*, 55:3461–3474, 2000.

(15) Y. Ding and E. Alpay. Adsorption-enhanced steam-methane reforming. *Chemical Engineering Science*, 55:3929–3940, 2000.

(16) A. G. Dixon. Correlations for wall and particle shape effects oon fixed bed bulk voidage. *The Canadian Journal of Chemical Engineering*, 66:705–708, 1988.

(17) V. Dupont, A. Ross, I. Hanley, and M. Twigg. Unmixed steam reforming of methane and sunflower oil: A single reactor process for H_2-rich gas. *Int. J. Hydrogen Energy*, 32:67–79, 2007.

(18) M. F. Edwards and J. Richardson. Gas dispersion in packed beds. *Chemical Engineering Science*, 23:109–123, 1968.

(19) K. Essaki, K. Nakagawa, M. Kato, and H. Uemoto. CO_2 absorption by lithium silicate at room temperature. *Journal of Chemical Engineering of Japan*, 37:772–777, 2004.

(20) G. F. Froment and K. B. Bischoff. *Chemical reactor analysis and design*. Jonh Wiley & sons, 2nd edition edition, 1990.

(21) A. Gomez-Barea and P. Ollero. An approximate method for solving gas-solid non-catalytic reactions. *Chemical Engineering Science*, 61:3725–3735, 2006.

(22) C. Han and D. P. Harrison. Simultaneous shift reaction and carbon dioxide separation for the direct production of hydrogen. *Chemical Engineering Science*, 49:5875–83, 1994.

(23) R. E. Hicks. Pressure drop in packed beds of spheres. *Industrial & Engineering Chemistry Fundamentals*, 9:500–2, 1970.

(24) M. M. Hossain and H. I. de Lasa. Reactivity and stability of Co-Ni/Al2O3 oxygen carrier in multicycle CLC. *AIChE Journal*, 53:1817–1829, 2007.

(25) N. Y. Hu and A. Scaroni. *Fuel*, 75:177–186, 1996.

(26) F. Hufton, S. Mayorga, and S. Sircar. Sorption-enhanced reaction process for hydrogen production. *Aiche J.*, 45:248, 1999.

(27) J. Ida and Y. S. Lin. Mechanism of high-temperature CO_2 sorption on lithium zirconate. *Environmental Science and Technology*, 37:1999–2004, 2003.

(28) J.-i. Ida, R. Xiong, and Y. S. Lin. Synthesis and CO_2 sorption properties of pure and modified lithium zirconate. *Separation and Purification Technology*, 36:41–51, 2004.

(29) H. A. Jakobsen, H. Lindborg, and V. Handeland. A numerical study of the interactions between viscous flow, transport and kinetics in fixed bed reactors. *Computers & Chemical Engineering*, 26:333–357, 2002.

(30) K. Johnsen, J. Grace, S. Elnashaie, L. Kolbeinsen, and D. Eriksen. Modeling of sorption-enhanced steam reforming in a dual fluidized bubbling bed reactor. *Industrial & Engineering Chemistry Research*, 45:4133, 2006.

(31) M. Kato and K. Nakagawa. New series of lithium containing complex oxides, lithium silicates, for application as a high temperature CO_2 absorbent. *Journal of the Ceramic Society of Japan*, 109:911–914, 2001.

(32) M. Kato, S. Yoshikawa, and K. Nakagawa. Carbon dioxide absorption by lithium orthosilicate in a wide range of temperature and carbon dioxide concentrations. *Journal of Materials Science Letters*, 21:485–487, 2002.

(33) O. Knacke, O. Kubaschewski, K. Hesselmann, and I. Barin. *Thermochemical properties of inorganic substances*. Springer Verlag, 1991.

(34) A. L. Kohl and R. Nielsen. *Gas purification*. Gulf pub., Houston, 5th edition, 1997.

(35) G. C. Koumpouras, E. Alpay, A. Lapkin, Y. Ding, and F. Stepanek. The effect of adsorbent characteristics on the performance of a continuous sorption-enhanced steam methane reforming process. *Chemical Engineering Science*, 62:5632–5637, 2007.

(36) G. C. Koumpouras, E. Alpay, and F. Stepanek. Mathematical modelling of low-temperature hydrogen production with in situ CO_2 capture. *Chemical Engineering Science*, 62:2833–2841, 2007.

(37) O. Langørgen, J. Jakobsen, N. Eldrup, and P. Røkke. Large scale co-production of hydrogen and electricity from natural gas with co_2-capture. Technical report, Sintef, 2006.

(38) D. K. Lee. An apparent kinetic model for the carbonation of calcium oxide by carbon dioxide. *Chemical Engineering Journal (Amsterdam, Netherlands)*, 100:71–77, 2004.

(39) D. K. Lee, I. H. Baek, and W. L. Yoon. Modeling and simulation for the methane steam reforming enhanced by in situ CO_2 removal utilizing the CaO carbonation for H_2 production. *Chemical Engineering Science*, 59:931–942, 2004.

(40) D. K. Lee, I. H. Baek, and W. L. Yoon. A simulation study for the hybrid reaction of methane steam reforming and in situ CO_2 removal in a moving bed reactor of a catalyst admixed with a CaO-based CO_2 acceptor for H_2 production. *International Journal of Hydrogen Energy*, 31:649–657, 2006.

(41) K. B. Lee, M. G. Beaver, H. S. Caram, and S. Sircar. Production of fuel-cell grade hydrogen by thermal swing sorption enhanced reaction concept. *International Journal of Hydrogen Energy*, 33:781–790, 2008.

(42) Z.-S. Li and N.-S. Cai. Modeling of multiple cycles for sorption-enhanced steam methane reforming and sorbent regeneration in fixed bed reactor. *Energy & Fuels*, 21:2909–2918, 2007.

(43) H. Lindborg, M. Lysberg, and H. Jakobsen. Practical validation of the two-fluid model applied to dense gas-solid flows in fluidized beds. *Submittet to Chemical Engineering Science*, 2007.

(44) A. López-Ortiz and D. Harrison. Simultaneous shift reaction and carbon dioxide separation for the direct production of hydrogen. *Chemical engineering science*, 40:5102–5109, 2001.

(45) A. López-Ortiz, N. Perez Rivera, A. Reyes Rojas, and D. Lardizabal Gutier-rez. Novel carbon dioxide solid acceptors using sodium containing oxides. *Separation Science and Technology*, 39:3559–3572, 2004.

(46) G. Marbán and T. Valdés-Solís. Towards the hydrogen economy? *Internation journal of hydrogen energy*, 32:1625 – 1637, 2007.

(47) D. Marquardt. An algortithm for least-squares estimation of non-linear pa-rameters. *SIAM journal on applied mathematics*, 11:431–441, 1963.

(48) G. Metz, O. Davidson, H. de Coninck, M. Loos, and L. Meyer, editors. *IPCC 2005: Special report on carbon dioxide capture and storage*. Cambridge university press, 2005.

(49) F. Mueller-Langer, E. Tzimas, M. Kaltschmitt, and S. Peteves. Techno-economic assesment of hydrogen production processes for the hydrogen economy for the short and medium term. *International journal of hydrogen energy*, 2007.

(50) B. N. Nair, T. Yamaguchi, H. Kawamura, S.-I. Nakao, and K. Nakagawa. Processing of lithium zirconate for applications in carbon dioxide separation: Structure and properties of the powders. *Journal of the American Ceramic Society*, 87:68–74, 2004.

(51) K. Nakagawa and T. Ohashi. A novel method of CO_2 capture from high temperature gases. *Journal of the Electrochemical Society*, 145:1344–1346, 1998.

(52) E. Ochoa-Fernández. *CO_2-acceptors for sorption enhanced steam methane reforming*. PhD thesis, NTNU, 2007.

(53) E. Ochoa-Fernández, T. Grande, H. K. Rusten, H. A. Jakobsen, A. Holmen, M. Rønning, and D. Chen. Novel solid high temperature CO_2 absorbents for the production of H_2 by sorption enhanced steam reforming. EuropaCat-VII;, August 2005.

(54) E. Ochoa-Fernández, H. K. Rusten, H. A. Jakobsen, M. Rønning, A. Holmen, and D. Chen. Sorption enhanced hydrogen production by steam methane re-forming using Li_2ZrO_3 as sorbent: Sorption kinetics and reactor simulation. *Catalysis Today*, 106:41–46, 2005.

(55) E. Ochoa-Fernández, H. K. Rusten, M. Rønning, A. Holmen, H. A. Jakob-sen, and D. Chen. H_2 production by CO_2 sorption enhanced steam methane reforming. gas-fuel 05. Oral presentation, 14-16 November 2005.

(56) E. Ochoa-Fernández, T. Zhao, G. Haugen, H. K. Rusten, M. Rønning, H. A. Jakobsen, and D. Chen. Application of CO_2 sorption enhanced hydrogen production with CO_2 removing: precombustion in power generation. the third trondheim conference on CO_2 capture, transport and storage. Oral presentation, 10-11 October 2005.

(57) E. Ochoa-Fernández, G. Haugen, T. Zhao, M. Rønning, I. Aartun, B. Børresen, E. Rytter, M. Rønnekleiv, and D. Chen. Evaluation of potential CO_2 acceptors for application in hydrogen production by sorption enhanced steam reforming. *Am. Chem. Soc., Div. Fuel Chem*, 51(2):598, 2006.

(58) E. Ochoa-Fernández, G. Haugen, T. Zhao, H. K. Rusten, J.-P. Andreassen, M. Rønning, H. A. Jakobsen, I. Aartun, B. Børresen, E. Rytter, M. Rønnekleiv, and D. Chen. Design, preparation and applications of CO_2 acceptors in power generation with CO_2 management. 12th international conference on greenhouse gas control technologies, GHGT-8. Oral presentation, 19 - 22 June 2006.

(59) E. Ochoa-Fernández, M. Rønning, T. Grande, and D. Chen. Synthesis and CO_2 capture properties of nanocrystalline lithium zirconate. *Chem. Mater. Accepted*, 18:1383–1385, 2006.

(60) S. Patankar. *Numerical Heat Transfer and Fluid Flow*. Hemisphere Publishing Corporation, Taylor and Francis Group, New York, 1980.

(61) B. E. Poling, J. M. Prausnitz, and J. P. O'Connell. *The Properties of Gases and Liquids*. McGraw-Hill, fifth edition, 2001.

(62) J. A. Ritter and A. D. Ebner. State-of-the-art adsorption and membrane separation processes for hydrogen production in the chemical and petrochemical industries. *Separation Science and Technology*, 42:1123–1193, 2007.

(63) J. Rostrup-Nielsen. *Catalysis:Science and technology*, chapter Catalytic steam reforming, pages 1–117. Springer, Berlin, 1984.

(64) J. R. Rostrup-Nielsen and T. Rostrup-Nielsen. Large-scale hydrogen production. *Cat Tech*, 6(4):150 – 159, 2002.

(65) H. K. Rusten, E. Ochoa-Fernández, D. Chen, E. T. Hessen, and H. A. Jakobsen. Modeling and simulation of sorption enhanced hydrogen production. the second trondheim conference on CO_2 capture, transport and storage. Oral presentation, 10-11 October 2005.

(66) H. K. Rusten, E. Ochoa-Fernández, D. Chen, E. T. Hessen, H. Lindborg, and H. A. Jakobsen. Modelling and simulation of sorption enhanced hydrogen production. 8th international conference on greenhouse gas control technologies (GHGT-8). Oral presentation, 19-22 June 2006.

(67) H. K. Rusten, E. Ochoa-Fernández, D. Chen, and H. A. Jakobsen. Heterogeneous and pseudo-homogeneous reactor models with solution of the velocity-pressure coupling for simulation of sorption enhanced steam reforming. 17th international congress of chemical and process engineering CHISA. Oral presentation, 27-31 August 2006.

(68) H. K. Rusten, E. Ochoa-Fernández, C. De, and H. A. Jakobsen. Modelling and simulation of hydrogen production by sorption enhanced steam reforming; integration of catalyst and adsorbent. ISCRE 19 - 19th international symposium on chemical reaction engineering. Oral presentation, 3-6 September 2006.

(69) H. K. Rusten, E. Ochoa-Fernández, D. Chen, and H. A. Jakobsen. Numerical investigation of sorption enhanced steam methane reforming using CO_2 as CO_2-acceptor. *Industrial & Engineering Chemistry Research*, 46(13):4435–4443, 2007.

(70) H. K. Rusten, E. Ochoa-Fernández, H. Lindborg, D. Chen, and H. A. Jakobsen. Hydrogen production by sorption-enhanced steam methane reforming using lithium oxides as CO_2-acceptor. *Industrial & Engineering Chemistry Research*, 46:8729–8737, 2007.

(71) M. D. Shieh and C. Lee. A more general structural model which includes the induction time for gas-solid reactions. i. nonporous solids. *Chemical Engineering Science*, 47:4017–25, 1992.

(72) A. Silaban, M. Narcida, and D. P. Harrison. Characteristics of the reversible reaction between $CO_2(g)$ and calcined dolomite. *Chemical Engineering Communications*, 146:149–162, 1996.

(73) D. Simbeck. CO_2 capture and storage - the essential bridge to the hydrogen economy. *Energy*, 29:1633 – 1641, 2004.

(74) S. Sircar and T. Golden. Purification of hydrogen by pressure swing adsorption. *Separation science and technology*, 35(5):667 – 687, 2000.

(75) J. Szekely and J. Evans. A structural model for gas-solid reactions with a moving boundary. *Chemical Engineering Science*, 25:1091–1107, 1970.

(76) J. Szekely, J. W. Evans, and H. Y. Sohn. *Gas-solid reactions*. Academic Press, 1976.

(77) L. H. Thomas. Elliptic problems in linear difference equations over a network. Technical report, Watson Sci. Comput. Lab. Report, Comubia, New York, 1949.

(78) M. Twigg. *Catalyst Handbook*. Wolfe Publishing Ltd., UK, 1989.

(79) M. J. Venegas, E. Fregoso-Israel, R. Escamilla, and H. Pfeiffer. Kinetic and reaction mechanism of CO_2 sorption on Li_4SiO_4: study of the particle size effect. *Industrial & Engineering Chemistry Research*, 46:2407–2412, 2007.

(80) H. K. Versteeg and W. Malalasekera. *An introduction to computational fluid dynamics The finite volume method*. Longman Scientific and Technical, 1995.

(81) N. Wakao and T. Funazkri. Effect of fluid dispersion coefficients on particle-to-fluid mass transfer coefficients in packed beds. correlation of sherwood numbers. *Chemical Engineering Science*, 33:1375–84, 1978.

(82) W. E. Waldron, J. R. Hufton, and S. Sircar. Production of hydrogen by cyclic sorption enhanced reaction process. *AIChE Journal*, 47(6):1477–1479, 2001.

(83) C. Y. Wen. Noncatalytic heterogeneous solid-fluid reactions models. *Industrial and Engineering Chemistry*, 60:34–54, 1968.

(84) R. Xiong, J. Ida, and Y. S. Lin. Kinetics of carbon dioxide sorption on potassium-doped lithium zirconate. *Chemical Engineering Science*, 58: 4377–4385, 2003.

(85) G.-h. Xiu, P. Li, and A. E. Rodrigues. Sorption-enhanced reaction process with reactive regeneration. *Chemical Engineering Science*, 57(18):3893–3908, 2002.

(86) G.-h. Xiu, J. L. Soares, P. Li, and A. E. Rodrigues. Simulation of five-step one-bed sorption-enhanced reaction process. *AIChE Journal*, 48:2817–2832, 2002.

(87) G.-h. Xiu, P. Li, and A. E. Rodrigues. New generalized strategy for improving sorption-enhanced reaction process. *Chemical Engineering Science*, 58: 3425–3437, 2003.

(88) G.-h. Xiu, P. Li, and A. E. Rodrigues. Sorption-enhanced reaction process with intraparticle-diffusion limitations. *Chemical Engineering Journal*, 95: 83–93, 2003.

(89) J. Xu and G. F. Froment. Methane steam reforming, methanation and water-gas shift: I. intrinsic kinetics. *AIChE Journal*, 35(1):88–96, 1989.

(90) S. Yagi, D. Kunii, and N. Wakao. Effective thermal conductivities in packed beds. *AIChE Journal*, 6:543–6, 1960.

(91) A. N. Zagoruiko and A. G. Okunev. Sorption-enhanced steam reforming of hydrocarbons with autothermal sorbent regeneration in a moving heat wave of a catalytic combustion reaction. *Reaction Kinetics and Catalysis Letters*, 91:315–324, 2007.

(92) T. J. Zhao, E. Ochoa-Fernández, M. Ronning, and D. Chen. Preparation and high-temperatureCO_2 capture properties of nanocrystalline Na_2ZrO_3. *Chemistry Of Materials*, 19(13):3294–3301, 2007.

Appendix A

Simulation mass balances

A.1 SE-SMR with Na_2ZrO_3, 10 bar, S/C = 3, 8 minute cycle.

	NORWEGIAN UNIV SCI&TECH Calgary, Alberta CANADA	Case Name:	SESMRFIX10BARNAZR700MWWPOWERLNG750KGSxml8min.hsc
		Unit Set:	SI
		Date/Time:	Thu Feb 04 21:09:08 2010

Workbook: Case (Main)

Material Streams   Fluid Pkg: All

Name		Added fuel	CO2 for injection	Cold solid	Condensate	Feed
Vapour Fraction		1.0000	1.0000	0.0000	0.0000	1.0000
Temperature	(C)	25.00	25.00	575.0	25.23	574.0
Pressure	(kPa)	7000	101.3	101.3	1200	1100
Molar Flow	(kgmole/h)	0.0000	4479	1.938e+004	1.703e+004	2.371e+004
Mass Flow	(kg/h)	0.0000	1.924e+005	1.940e+006	3.069e+005	4.026e+005
Actual Volume Flow	(m3/h)	0.0000	1.090e+005	1577	304.6	1.514e+005
Mole fraction [-] (Methane)		1.0000	0.0000	0.0000	0.0000	0.2395
Mole fraction [-] (CO2)		0.0000	0.9486	0.0000	0.0000	0.0020
Mole fraction [-] (H2O)		0.0000	0.0312	0.0000	1.0000	0.7189
Mole fraction [-] (Nitrogen)		0.0000	0.0000	0.0000	0.0000	0.0000
Mole fraction [-] (Hydrogen)		0.0000	0.0000	0.0000	0.0000	0.0389
Mole fraction [-] (CO)		0.0000	0.0000	0.0000	0.0000	0.0007
Mole fraction [-] (Oxygen)		0.0000	0.0202	0.0000	0.0000	0.0000
Mole fraction [-] (Solid*)		0.0000	0.0000	1.0000	0.0000	0.0000
Name		Natural Gas	O-1	P-1	P-2	Product Hydrogen
Vapour Fraction		1.0000	1.0000	1.0000	0.8225	1.0000
Temperature	(C)	10.00	25.00	575.0	133.0	157.0
Pressure	(kPa)	7000	200.0	1000	1000	6000
Molar Flow	(kgmole/h)	4252	3378	2.661e+004	2.661e+004	1.042e+004
Mass Flow	(kg/h)	6.821e+004	1.081e+005	2.804e+005	2.804e+005	2.102e+004
Actual Volume Flow	(m3/h)	1201	4.180e+004	1.877e+005	7.345e+004	6333
Mole fraction [-] (Methane)		1.0000	0.0000	0.1067	0.1067	0.0000
Mole fraction [-] (CO2)		0.0000	0.0000	0.0035	0.0035	0.0000
Mole fraction [-] (H2O)		0.0000	0.0000	0.4278	0.4278	0.0000
Mole fraction [-] (Nitrogen)		0.0000	0.0000	0.0000	0.0000	0.0000
Mole fraction [-] (Hydrogen)		0.0000	0.0000	0.4608	0.4608	1.0000
Mole fraction [-] (CO)		0.0000	0.0000	0.0012	0.0012	0.0000
Mole fraction [-] (Oxygen)		0.0000	1.0000	0.0000	0.0000	0.0000
Mole fraction [-] (Solid*)		0.0000	0.0000	0.0000	0.0000	0.0000
Name		PSA feed	Regen gas	Regen-2	Warm solid	Waste Gas
Vapour Fraction		0.9984	1.0000	1.0000	0.0000	1.0000
Temperature	(C)	25.00	801.6	133.0	900.0	21.83
Pressure	(kPa)	2000	101.3	101.3	101.3	131.7
Molar Flow	(kgmole/h)	1.528e+004	8103	8103	1.938e+004	4853
Mass Flow	(kg/h)	7.619e+004	2.577e+005	2.577e+005	1.940e+006	5.516e+004
Actual Volume Flow	(m3/h)	1.898e+004	7.146e+005	2.690e+005	1577	9.027e+004
Mole fraction [-] (Methane)		0.1858	0.0000	0.0000	0.0000	0.5850
Mole fraction [-] (CO2)		0.0062	0.5246	0.5246	0.0000	0.0194
Mole fraction [-] (H2O)		0.0033	0.4642	0.4642	0.0000	0.0102
Mole fraction [-] (Nitrogen)		0.0000	0.0000	0.0000	0.0000	0.0000
Mole fraction [-] (Hydrogen)		0.8027	0.0000	0.0000	0.0000	0.3790
Mole fraction [-] (CO)		0.0020	0.0000	0.0000	0.0000	0.0064
Mole fraction [-] (Oxygen)		0.0000	0.0112	0.0112	0.0000	0.0000
Mole fraction [-] (Solid*)		0.0000	0.0000	0.0000	1.0000	0.0000

		Case Name:	SESMRFIX10BARNAZR700MWWPOWERLNG750KGSxml8min.hsc		
	NORWEGIAN UNIV SCI&TECH Calgary, Alberta CANADA	Unit Set:	SI		
		Date/Time:	Thu Feb 04 21:09:08 2010		

Workbook: Case (Main) (continued)

Material Streams (continued)   Fluid Pkg: All

Name		Water	WG-2			
Vapour Fraction		0.0000	1.0000			
Temperature	(C)	25.00	157.8			
Pressure	(kPa)	101.3	1200			
Molar Flow	(kgmole/h)	5699	2437			
Mass Flow	(kg/h)	1.027e+005	2.771e+004			
Actual Volume Flow	(m3/h)	101.9	7277			
Mole fraction [-] (Methane)		0.0000	0.5852			
Mole fraction [-] (CO2)		0.0000	0.0194			
Mole fraction [-] (H2O)		1.0000	0.0102			
Mole fraction [-] (Nitrogen)		0.0000	0.0000			
Mole fraction [-] (Hydrogen)		0.0000	0.3787			
Mole fraction [-] (CO)		0.0000	0.0064			
Mole fraction [-] (Oxygen)		0.0000	0.0000			
Mole fraction [-] (Solid*)		0.0000	0.0000			

Licensed to: NORWEGIAN UNIV SCI&TECH

A.2   SE-SMR with Li$_2$ZrO$_3$, 10 bar, S/C = 3, 50 minute cycle.

	NORWEGIAN UNIV SCI&TECH	Case Name:	SESMRLizrxml.hsc		
aspentech	Calgary, Alberta	Unit Set:	SI		
	CANADA	Date/Time:	Thu Feb 04 21:29:33 2010		

Workbook: Case (Main)

Material Streams   Fluid Pkg: All

Name		Added fuel	CO2 for injection	Cold solid	Condensate	Feed
Vapour Fraction		1.0000	1.0000	0.0000	0.0000	1.0000
Temperature	(C)	25.00	25.00	575.0	25.25	574.1
Pressure	(kPa)	7000	101.3	101.3	1200	1100
Molar Flow	(kgmole/h)	0.0000	3928	2.557e+004	2.359e+004	2.936e+004
Mass Flow	(kg/h)	0.0000	1.690e+005	2.559e+006	4.250e+005	5.078e+005
Actual Volume Flow	(m3/h)	0.0000	9.555e+004	609.3	421.8	1.872e+005
Mole fraction [-] (Methane)		1.0000	0.0000	0.0000	0.0000	0.1607
Mole fraction [-] (CO2)		0.0000	0.9544	0.0000	0.0001	0.0040
Mole fraction [-] (H2O)		0.0000	0.0312	0.0000	0.9999	0.8024
Mole fraction [-] (Nitrogen)		0.0000	0.0000	0.0000	0.0000	0.0000
Mole fraction [-] (Hydrogen)		0.0000	0.0000	0.0000	0.0000	0.0321
Mole fraction [-] (CO)		0.0000	0.0000	0.0000	0.0000	0.0008
Mole fraction [-] (Oxygen)		0.0000	0.0145	0.0000	0.0000	0.0000
Mole fraction [-] (Solid*)		0.0000	0.0000	1.0000	0.0000	0.0000
Name		Natural Gas	O-1	P-1	P-2	Product Hydrogen
Vapour Fraction		1.0000	1.0000	1.0000	0.8127	1.0000
Temperature	(C)	10.00	25.00	575.0	147.2	157.2
Pressure	(kPa)	7000	200.0	1000	1000	6000
Molar Flow	(kgmole/h)	3750	2356	3.232e+004	3.232e+004	1.040e+004
Mass Flow	(kg/h)	6.016e+004	7.538e+004	3.891e+005	3.891e+005	2.098e+004
Actual Volume Flow	(m3/h)	1059	2.914e+004	2.277e+005	9.057e+004	6324
Mole fraction [-] (Methane)		1.0000	0.0000	0.0584	0.0584	0.0000
Mole fraction [-] (CO2)		0.0000	0.0000	0.0071	0.0071	0.0000
Mole fraction [-] (H2O)		0.0000	0.0000	0.5544	0.5544	0.0000
Mole fraction [-] (Nitrogen)		0.0000	0.0000	0.0000	0.0000	0.0000
Mole fraction [-] (Hydrogen)		0.0000	0.0000	0.3787	0.3787	1.0000
Mole fraction [-] (CO)		0.0000	0.0000	0.0015	0.0015	0.0000
Mole fraction [-] (Oxygen)		0.0000	1.0000	0.0000	0.0000	0.0000
Mole fraction [-] (Solid*)		0.0000	0.0000	0.0000	0.0000	0.0000
Name		PSA-feed	Regen gas	Regen-2	Warm solid	Waste Gas
Vapour Fraction		0.9984	1.0000	1.0000	0.0000	1.0000
Temperature	(C)	25.00	675.5	147.2	700.0	22.00
Pressure	(kPa)	2000	101.3	101.3	101.3	131.7
Molar Flow	(kgmole/h)	1.445e+004	6564	6564	2.557e+004	4045
Mass Flow	(kg/h)	6.714e+004	2.165e+005	2.165e+005	2.559e+006	4.616e+004
Actual Volume Flow	(m3/h)	1.796e+004	5.110e+005	2.256e+005	609.3	7.530e+004
Mole fraction [-] (Methane)		0.1306	0.0000	0.0000	0.0000	0.4665
Mole fraction [-] (CO2)		0.0157	0.5713	0.5713	0.0000	0.0561
Mole fraction [-] (H2O)		0.0033	0.4200	0.4200	0.0000	0.0116
Mole fraction [-] (Nitrogen)		0.0000	0.0000	0.0000	0.0000	0.0000
Mole fraction [-] (Hydrogen)		0.8471	0.0000	0.0000	0.0000	0.4539
Mole fraction [-] (CO)		0.0034	0.0000	0.0000	0.0000	0.0120
Mole fraction [-] (Oxygen)		0.0000	0.0086	0.0086	0.0000	0.0000
Mole fraction [-] (Solid*)		0.0000	0.0000	0.0000	1.0000	0.0000

aspentech NORWEGIAN UNIV SCI&TECH Calgary, Alberta CANADA	Case Name:	SESMRLizrxml.hsc	
	Unit Set:	SI	
	Date/Time:	Thu Feb 04 21:29:33 2010	

Workbook: Case (Main) (continued)

Material Streams (continued)   Fluid Pkg: All

Name		Water	WG-2		
Vapour Fraction		0.0000	1.0000		
Temperature	(C)	25.00	160.3		
Pressure	(kPa)	101.3	1200		
Molar Flow	(kgmole/h)	5715	2075		
Mass Flow	(kg/h)	1.030e+005	2.368e+004		
Actual Volume Flow	(m3/h)	102.2	6236		
Mole fraction [-] (Methane)		0.0000	0.4664		
Mole fraction [-] (CO2)		0.0000	0.0561		
Mole fraction [-] (H2O)		1.0000	0.0116		
Mole fraction [-] (Nitrogen)		0.0000	0.0000		
Mole fraction [-] (Hydrogen)		0.0000	0.4539		
Mole fraction [-] (CO)		0.0000	0.0120		
Mole fraction [-] (Oxygen)		0.0000	0.0000		
Mole fraction [-] (Solid*)		0.0000	0.0000		

A.3   SE-SMR with Na$_2$ZrO$_3$ at equilibrium.

	NORWEGIAN UNIV SCI&TECH Calgary, Alberta CANADA	Case Name:	SESMRFIX10BARNAZR700MWWPOWERLNG750KGSxml8mineq.HSC
aspentech		Unit Set:	SI
		Date/Time:	Thu Feb 04 21:27:56 2010

Workbook: Case (Main)

Material Streams   Fluid Pkg: All

Name		Added fuel	CO2 for injection	Cold solid	Condensate	Feed
Vapour Fraction		1.0000	1.0000	0.0000	0.0000	1.0000
Temperature	(C)	25.00	25.00	575.1	25.20	574.0
Pressure	(kPa)	7000	101.3	101.3	1200	1100
Molar Flow	(kgmole/h)	203.2	4410	1.746e+004	1.193e+004	1.603e+004
Mass Flow	(kg/h)	3260	1.894e+005	1.747e+006	2.150e+005	2.809e+005
Actual Volume Flow	(m3/h)	62.45	1.073e+005	416.0	213.4	1.023e+005
Mole fraction [-] (Methane)		1.0000	0.0000	0.0000	0.0000	0.2482
Mole fraction [-] (CO2)		0.0000	0.9476	0.0000	0.0000	0.0000
Mole fraction [-] (H2O)		0.0000	0.0312	0.0000	1.0000	0.7518
Mole fraction [-] (Nitrogen)		0.0000	0.0000	0.0000	0.0000	0.0000
Mole fraction [-] (Hydrogen)		0.0000	0.0000	0.0000	0.0000	0.0000
Mole fraction [-] (CO)		0.0000	0.0000	0.0000	0.0000	0.0000
Mole fraction [-] (Oxygen)		0.0000	0.0212	0.0000	0.0000	0.0000
Mole fraction [-] (Solid*)		0.0000	0.0000	1.0000	0.0000	0.0000
Name		Natural Gas	O-1	P-1	P-2	Product Hydrogen
Vapour Fraction		1.0000	1.0000	1.0000	0.8189	1.0000
Temperature	(C)	10.00	25.00	575.0	112.0	157.7
Pressure	(kPa)	7000	200.0	1000	1000	6000
Molar Flow	(kgmole/h)	3978	3249	1.909e+004	1.909e+004	1.041e+004
Mass Flow	(kg/h)	6.381e+004	1.040e+005	1.463e+005	1.463e+005	2.100e+004
Actual Volume Flow	(m3/h)	1124	4.020e+004	1.348e+005	5.005e+004	6336
Mole fraction [-] (Methane)		1.0000	0.0000	0.0479	0.0479	0.0000
Mole fraction [-] (CO2)		0.0000	0.0000	0.0001	0.0001	0.0000
Mole fraction [-] (H2O)		0.0000	0.0000	0.3103	0.3103	0.0000
Mole fraction [-] (Nitrogen)		0.0000	0.0000	0.0000	0.0000	0.0000
Mole fraction [-] (Hydrogen)		0.0000	0.0000	0.6415	0.6415	1.0000
Mole fraction [-] (CO)		0.0000	0.0000	0.0001	0.0001	0.0000
Mole fraction [-] (Oxygen)		0.0000	1.0000	0.0000	0.0000	0.0000
Mole fraction [-] (Solid*)		0.0000	0.0000	0.0000	0.0000	0.0000
Name		PSA feed	Regen gas	Regen-2	Warm solid	Waste Gas
Vapour Fraction		0.9984	1.0000	1.0000	0.0000	1.0000
Temperature	(C)	25.00	814.5	112.0	900.0	22.36
Pressure	(kPa)	2000	101.3	101.3	101.3	131.7
Molar Flow	(kgmole/h)	1.321e+004	8391	8391	1.746e+004	2800
Mass Flow	(kg/h)	4.033e+004	2.612e+005	2.612e+005	1.747e+006	1.933e+004
Actual Volume Flow	(m3/h)	1.645e+004	7.489e+005	2.639e+005	416.0	5.221e+004
Mole fraction [-] (Methane)		0.0692	0.0000	0.0000	0.0000	0.3268
Mole fraction [-] (CO2)		0.0002	0.4983	0.4983	0.0000	0.0010
Mole fraction [-] (H2O)		0.0033	0.4906	0.4906	0.0000	0.0153
Mole fraction [-] (Nitrogen)		0.0000	0.0000	0.0000	0.0000	0.0000
Mole fraction [-] (Hydrogen)		0.9271	0.0000	0.0000	0.0000	0.6562
Mole fraction [-] (CO)		0.0002	0.0000	0.0000	0.0000	0.0008
Mole fraction [-] (Oxygen)		0.0000	0.0112	0.0112	0.0000	0.0000
Mole fraction [-] (Solid*)		0.0000	0.0000	0.0000	1.0000	0.0000

NORWEGIAN UNIV SCI&TECH Calgary, Alberta CANADA	Case Name:	SESMRFIX10BARNAZR700MWWPOWERLNG750KGSxml8mineq.HSC
	Unit Set:	SI
	Date/Time:	Thu Feb 04 21:27:56 2010

Workbook: Case (Main) (continued)

Material Streams (continued)　　　　　Fluid Pkg:　　　All

Name		Water	WG-2		
Vapour Fraction		0.0000	---		
Temperature	(C)	25.00	---		
Pressure	(kPa)	101.3	1200		
Molar Flow	(kgmole/h)	6051	0.0000		
Mass Flow	(kg/h)	1.090e+005	0.0000		
Actual Volume Flow	(m3/h)	108.2	---		
Mole fraction [-] (Methane)		0.0000	0.3268		
Mole fraction [-] (CO2)		0.0000	0.0010		
Mole fraction [-] (H2O)		1.0000	0.0153		
Mole fraction [-] (Nitrogen)		0.0000	0.0000		
Mole fraction [-] (Hydrogen)		0.0000	0.6562		
Mole fraction [-] (CO)		0.0000	0.0008		
Mole fraction [-] (Oxygen)		0.0000	0.0000		
Mole fraction [-] (Solid*)		0.0000	0.0000		

Licensed to: NORWEGIAN UNIV SCI&TECH

A.4 SE-SMR with Na$_2$ZrO$_3$ with mixed product.

aspentech	NORWEGIAN UNIV SCI&TECH	Case Name:	SESMRFIX10BARNAZR700MWWPOWERLNG750KGSxml8mineq.HSC	
	Calgary, Alberta	Unit Set:	SI	
	CANADA	Date/Time:	Thu Feb 04 21:27:56 2010	

Workbook: Case (Main)

Material Streams   Fluid Pkg: All

Name	Added fuel	CO2 for injection	Cold solid	Condensate	Feed
Vapour Fraction	1.0000	1.0000	0.0000	0.0000	1.0000
Temperature (C)	25.00	25.00	575.1	25.20	574.0
Pressure (kPa)	7000	101.3	101.3	1200	1100
Molar Flow (kgmole/h)	203.2	4410	1.746e+004	1.193e+004	1.603e+004
Mass Flow (kg/h)	3260	1.894e+005	1.747e+006	2.150e+005	2.809e+005
Actual Volume Flow (m3/h)	62.45	1.073e+005	416.0	213.4	1.023e+005
Mole fraction [-] (Methane)	1.0000	0.0000	0.0000	0.0000	0.2482
Mole fraction [-] (CO2)	0.0000	0.9476	0.0000	0.0000	0.0000
Mole fraction [-] (H2O)	0.0000	0.0312	0.0000	1.0000	0.7518
Mole fraction [-] (Nitrogen)	0.0000	0.0000	0.0000	0.0000	0.0000
Mole fraction [-] (Hydrogen)	0.0000	0.0000	0.0000	0.0000	0.0000
Mole fraction [-] (CO)	0.0000	0.0000	0.0000	0.0000	0.0000
Mole fraction [-] (Oxygen)	0.0000	0.0212	0.0000	0.0000	0.0000
Mole fraction [-] (Solid*)	0.0000	0.0000	1.0000	0.0000	0.0000
Name	Natural Gas	O-1	P-1	P-2	Product Hydrogen
Vapour Fraction	1.0000	1.0000	1.0000	0.8189	1.0000
Temperature (C)	10.00	25.00	575.0	112.0	157.7
Pressure (kPa)	7000	200.0	1000	1000	6000
Molar Flow (kgmole/h)	3978	3249	1.909e+004	1.909e+004	1.041e+004
Mass Flow (kg/h)	6.381e+004	1.040e+005	1.463e+005	1.463e+005	2.100e+004
Actual Volume Flow (m3/h)	1124	4.020e+004	1.348e+005	5.005e+004	6336
Mole fraction [-] (Methane)	1.0000	0.0000	0.0479	0.0479	0.0000
Mole fraction [-] (CO2)	0.0000	0.0000	0.0001	0.0001	0.0000
Mole fraction [-] (H2O)	0.0000	0.0000	0.3103	0.3103	0.0000
Mole fraction [-] (Nitrogen)	0.0000	0.0000	0.0000	0.0000	0.0000
Mole fraction [-] (Hydrogen)	0.0000	0.0000	0.6415	0.6415	1.0000
Mole fraction [-] (CO)	0.0000	0.0000	0.0001	0.0001	0.0000
Mole fraction [-] (Oxygen)	0.0000	1.0000	0.0000	0.0000	0.0000
Mole fraction [-] (Solid*)	0.0000	0.0000	0.0000	0.0000	0.0000
Name	PSA feed	Regen gas	Regen-2	Warm solid	Waste Gas
Vapour Fraction	0.9984	1.0000	1.0000	0.0000	1.0000
Temperature (C)	25.00	814.5	112.0	900.0	22.36
Pressure (kPa)	2000	101.3	101.3	101.3	131.7
Molar Flow (kgmole/h)	1.321e+004	8391	8391	1.746e+004	2800
Mass Flow (kg/h)	4.033e+004	2.612e+005	2.612e+005	1.747e+006	1.933e+004
Actual Volume Flow (m3/h)	1.645e+004	7.489e+005	2.639e+005	416.0	5.221e+004
Mole fraction [-] (Methane)	0.0692	0.0000	0.0000	0.0000	0.3268
Mole fraction [-] (CO2)	0.0002	0.4983	0.4983	0.0000	0.0010
Mole fraction [-] (H2O)	0.0033	0.4906	0.4906	0.0000	0.0153
Mole fraction [-] (Nitrogen)	0.0000	0.0000	0.0000	0.0000	0.0000
Mole fraction [-] (Hydrogen)	0.9271	0.0000	0.0000	0.0000	0.6562
Mole fraction [-] (CO)	0.0002	0.0000	0.0000	0.0000	0.0008
Mole fraction [-] (Oxygen)	0.0000	0.0112	0.0112	0.0000	0.0000
Mole fraction [-] (Solid*)	0.0000	0.0000	0.0000	1.0000	0.0000

Licensed to: NORWEGIAN UNIV SCI&TECH

aspentech NORWEGIAN UNIV SCI&TECH Calgary, Alberta CANADA	Case Name:	SESMRFIX10BARNAZR700MWWPOWERLNG750KGSxml8mineq.HSC
	Unit Set:	SI
	Date/Time:	Thu Feb 04 21:27:56 2010

Workbook: Case (Main) (continued)

Material Streams (continued)   Fluid Pkg: All

Name		Water	WG-2		
Vapour Fraction		0.0000	---		
Temperature	(C)	25.00	---		
Pressure	(kPa)	101.3	1200		
Molar Flow	(kgmole/h)	6051	0.0000		
Mass Flow	(kg/h)	1.090e+005	0.0000		
Actual Volume Flow	(m3/h)	108.2	---		
Mole fraction [-] (Methane)		0.0000	0.3268		
Mole fraction [-] (CO2)		0.0000	0.0010		
Mole fraction [-] (H2O)		1.0000	0.0153		
Mole fraction [-] (Nitrogen)		0.0000	0.0000		
Mole fraction [-] (Hydrogen)		0.0000	0.6562		
Mole fraction [-] (CO)		0.0000	0.0008		
Mole fraction [-] (Oxygen)		0.0000	0.0000		
Mole fraction [-] (Solid*)		0.0000	0.0000		

Licensed to: NORWEGIAN UNIV SCI&TECH

Appendix B

Papers

Numerical Investigation of Sorption Enhanced Steam Methane Reforming Using Li₂ZrO₃ as CO₂-acceptor

Hans Kristian Rusten,* Esther Ochoa-Fernández, De Chen, and Hugo Atle Jakobsen

The Norwegian University of Science and Technology (NTNU), NO-7491 Trondheim, Norway

A fixed-bed reactor for the production of hydrogen via sorption-enhanced steam methane reforming (SE-SMR) is investigated. Pseudo-homogeneous and heterogeneous models have been formulated and used to simulate the process performance. The capture kinetics of CO_2 on Li_2ZrO_3 have been characterized experimentally for determination of a kinetic model that is used in the simulations of SE-SMR. The simulations show that hydrogen with purities of >87 mol % can be produced at a temperature of 848 K and a total pressure of 10 bar, but with long reactors and low production capacities. To make SE-SMR an industrial alternative, materials with better capture properties are required.

1. Introduction

Hydrogen is an important raw material in the chemical and petroleum industries; large quantities are used in the manufacture of ammonia and methanol and in a variety of petroleum hydrotreating processes. In addition, hydrogen might become a new generation clean energy source for transport, especially for fuel cell application, which would cause a huge increase in hydrogen demand.

Steam methane reforming (SMR) is currently the major process for the large-scale production of hydrogen. The process involves multiple steps and severe operating conditions in which the reformer is normally operated at 800−850 °C and 20−35 bar, followed by high and low-temperature shift reactors. For hydrogen production with CO_2 capture, another cost-effective process is desirable. Within the past few years, the concept of multifunctional reactors that combine reaction and separation, especially the concept of the sorption-enhanced reaction process (SERP), have received increased attention. A CO_2 acceptor can be installed, together with a catalyst, to remove CO_2 from the gas phase, normal equilibrium limits of reforming and shift reactions are changed, and a product that contains more than 98% H_2 (dry basis) is possible.[1] Sorption-enhanced steam reforming can be performed at a much lower temperature (450−630 °C) than normal steam reforming, which will significantly lower investment and operation cost. The primary impurity is methane and relative low levels of carbon oxides.[2] A lower concentration of CO and higher concentration of hydrogen will reduce the coking potential, which is a serious problem in normal steam reforming.

The capture is an exothermic reaction, which is contrary to the endothermic steam reforming, and the heat of sorption will make the need for external heating less than that for the traditional steam reforming process.

$$CH_4 + 2H_2O + Li_2ZrO_3(s) \leftrightarrow 4H_2 + Li_2CO_3(s) + ZrO_2(s)$$
$$(\Delta H_{848K} = 15 \text{ kJ/mol}) \quad (1)$$
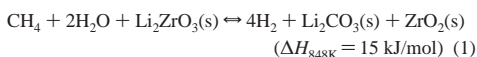
The net change of enthalpy for the reaction, calculated at the working temperature, is positive; hence, energy still must be supplied, but the quantity required is considerably less than that for the traditional SMR process.

There has been extensive research on the equilibrium of CO_2 capture on different solids at ambient temperature and atmospheric pressure. Recently, there has been increased attention to high-temperature acceptors. High-temperature CO_2 solid sorbents in SE-SMR should fulfill certain requirements: high capacity, fast sorption rate, good multicycling stability, relatively low temperature for regeneration, and inert for steam reforming catalysts.[3] Carbon-based materials, metal oxides, zeolites, and hydrotalcite-like materials are potential acceptors for CO_2. Recently it has been reported that lithium-containing materials (mainly Li_2ZrO_3 and Li_4SiO_4) are promising candidates with high CO_2 capture capacity and high stability.[4,5] The regeneration temperature is also much lower than that for other oxides such as CaO and MgO.

In this work, we study the reactor performance using Li_2ZrO_3 as the CO_2 acceptor.[6] A tapered element oscillating microbalance has been used for the CO_2 uptake measurements. From these data, a kinetic expression for the capture kinetics, as a function of CO_2 partial pressure and temperature, has been developed.

Previous modeling work on SE-SMR has been performed for hydrotalcite and CaO as CO_2 acceptors, using simpler models.[7,8] The objective of this work has been to develop a model to describe the SE-SMR process in a fixed-bed reactor that is easily adapted for different types of CO_2 capture kinetics. Different reactor models have been assessed and a model with full solution of the pressure velocity coupling has been chosen based on an evaluation of various model formulations. Heterogeneous and pseudo-homogeneous reactor models have been formulated to study the integration between the catalyst and the sorbent.

2. Kinetics of the CO₂ Acceptor

Nanocrystalline lithium zirconate has been synthesized by a novel soft-chemistry route presented by Ochoa et al.[6] The CO_2 capture properties of this material has been investigated in a tapered element oscillating microbalance with flow rates high enough to ensure no external mass-transfer limitations. The uptake of CO_2 is measured at three temperatures (530, 550, and 575 °C) and at partial pressures in the range of 0.3−1 bar. A mathematical model for the capture kinetics is needed to enable utilization of the kinetic data in reactor simulations. Several models for gas−solid reactions have been proposed in the literature,[9] and for the sorption of gas on solid, the shrinking-

Table 1. Parameters Fitted to Eq 2

parameter	value
K_{10} (s^{-1})	$8.07 \times 10^{-13} \pm 7 \times 10^{-15}$
E_1 (J/mol)	$7.7 \times 10^4 \pm 2 \times 10^3$

core model is commonly applied.[10] The model has been used to explain the mechanism of CO_2 capture on Li_2ZrO_3,[11] where the diffusion of CO_2 in the product Li_2CO_3 shell is observed to be the rate-determining step. However, the shrinking-core model and several other models failed to explain the results obtained in our experiments. The original shrinking-core model is linearly dependent on the partial pressure of CO_2, and some modified versions have a dependency of P_{CO_2} between 0 and 1.[8] The measured data show a dependency of the CO_2 partial pressure close to 2, which is a number that is not explained by the shrinking-core model or other proposed mechanistic models. With respect to fractional coverage (x), a linear function of $(1 - x)$ gives the best fit to the data. The higher-order dependency of the partial pressure of CO_2 indicates that the limiting step is the chemical reaction itself; however, further work is needed to derive a detailed kinetic model that explains the actual reaction mechanism. The primary objective of this work is to model and simulate the SE-SMR process, and, in this context, a simpler model was determined to be sufficient. The work on developing more detailed kinetics is continuing as well. Because no mechanistic model that explained the experimental results was found, an empirical model was chosen. This relation is given in eq 2.

$$\frac{dx}{dt} = K_1(p_{CO_2} - p_{eq,CO_2})^2(1 - x) \quad (2)$$

The equilibrium partial pressure of CO_2 (p_{eq,CO_2}) is modeled using thermodynamic data;[12] x is the fractional conversion and has a value of 1 at full saturation of the CO_2 acceptor.

$$x = \frac{q}{q_{max}} \quad (3)$$

Here, q is the mass of CO_2 captured per mass of lithium

zirconate, and q_{max} is the value of q at maximum capture and is determined to have a value of 0.22 for this sample of Li_2ZrO_3. K_1 is the effective reaction rate constant for which an Arrhenius expression is used for the temperature dependence.

$$K_1 = K_{10} \exp\left[-\left(\frac{E}{R}\right)\left(\frac{1}{T} - \frac{1}{T_0}\right)\right] \quad (4)$$

T_0 was chosen as 848 K and the fitted parameters in eqs 2 and 4 are given with standard deviations in Table 1.
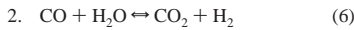
An in-house code for nonlinear model fitting using a secant version of Marquardt's method of least squares was used to determine the parameters in the model. The experimental data and the model fit at different partial pressures of CO_2 and temperatures are shown in Figure 1. A short induction period is observed at lower partial pressures, which gives a small discrepancy between the experiments and the predictions; however, the model is considered appropriate, in regard to simulating the SE-SMR process. The model is not able to reproduce the maximum in the capture kinetics that is observed at ~585 °C; thus, the model should not be used at higher temperatures.

3. The Reactor Models

Transient one-dimensional reactor models with axial dispersion have been developed to simulate a fixed-bed reactor. A transient model is chosen because the capture of CO_2 has a time-dependent nature, and axial dispersion is included because relatively low gas velocities are used in the simulations. Three different models have been developed: two heterogeneous models and a pseudo-homogeneous model. The difference between the two heterogeneous models is the manner in which the sorbent is installed in the reactor. One model considers that Li_2ZrO_3 and the reforming catalyst are separated in two different particles, whereas, in the other case, there is one particle with both catalytic and capture properties. The SMR and the water-gas shift reaction kinetics can be described by three equations, two of which are independent:
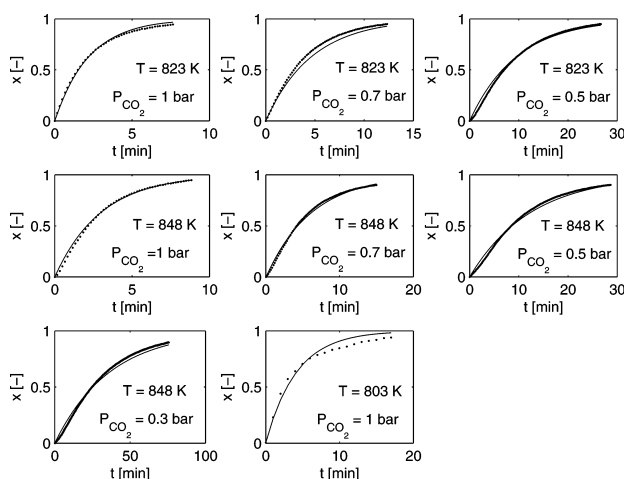
Figure 1. ($\cdot\cdot\cdot$) Experimental data and ($-$) kinetic model for CO_2 capture on lithium zirconate.

1. $CH_4 + H_2O \leftrightarrow CO + 3H_2$ (5)

2. $CO + H_2O \leftrightarrow CO_2 + H_2$ (6)

3. $CH_4 + 2H_2O \leftrightarrow CO_2 + 4H_2$ (7)

The kinetics of these reactions are described by Xu and Froment:[13]

$$R_1 = \frac{k_1}{p_{H_2}^{2.5}} \left[\frac{p_{CH_4}p_{H_2O} - (p_{H_2}^{3}p_{CO}/K_1)}{DEN^2} \right] \quad (8)$$

$$R_2 = \frac{k_2}{p_{H_2}} \left[\frac{p_{CO}p_{H_2O} - (p_{H_2}p_{CO_2}/K_2)}{DEN^2} \right] \quad (9)$$

$$R_3 = \frac{k_3}{p_{H_2}^{3.5}} \left[\frac{p_{CH_4}p_{H_2O}^{2} - (p_{H_2}^{4}p_{CO_2}/K_3)}{DEN^2} \right] \quad (10)$$

DEN is given as $1 + K_{CO}p_{CO} + K_{H_2}p_{H_2} + K_{CH4}p_{CH_4} + K_{H_2O}p_{H_2O}/p_{H_2}$ and all constants are taken from Xu and Froment.[13]

3.1. Bulk Gas Equations. The general mass balance equation for a chemical species i in reacting fluid flow with varying density, temperature, and composition is written as

$$\frac{\partial \rho_i}{\partial t} + \nabla \cdot (\rho_i u) + \nabla \cdot J_i = R_i \quad (11)$$

A cross-sectional average of eq 11 reduces the model to one dimension, and after introducing mass fractions, the transport equation for porous media flows is given as

$$\epsilon_b \frac{\partial \rho_g \omega_i}{\partial t} + \frac{\partial}{\partial z}(\rho_g \omega_i u) = \frac{\partial}{\partial z}\left(\epsilon_b D_{z,i}\rho_g \frac{\partial \omega_i}{\partial z}\right) + S_i \quad (12)$$

Equation 12 is solved for the components H_2, CO, CH_4, and CO_2. H_2O is the dominating component in the system, and the mass fraction of H_2O is obtained from eq 13:

$$\sum_{i=1}^{5} \omega_i = 1 \quad (13)$$

The source term (S_i) is different in the various models, with the expressions shown in eq 14.

$$S_i = \begin{cases} a_{v,cat}k_i\rho_g(\omega_{cat,i}^s - \omega_i) + a_{v,cap}k_i\rho_g(\omega_{cap,i}^s - \omega_i) & \text{(2-P)} \\ a_{v,p}k_i\rho_g(\omega_{p,i}^s - \omega_i) & \\ & \text{(1-P)} \\ \left(\frac{1-\epsilon_b}{1+\alpha(\epsilon_{p,cap}/\epsilon_{p,cat})}\right)(1-\epsilon_{p,cat})\rho_{cat}r_i + & \\ & \text{(P-H)} \\ \frac{1-\epsilon_b}{1-[\epsilon_{p,cat}/(\epsilon_{p,cat}+\epsilon_{p,cap}\alpha)]}(1-\epsilon_{p,cap})\rho_{cap}r_{i,cap} & \\ & (14) \end{cases}$$

For the one particle (1-P) and two-particle (2-P) heterogeneous models, the source terms contain particle−bulk mass-transfer terms. For the pseudo-homogeneous (P−H) model, S_i is a reaction-rate term.

For the two-particle model (2-P), the mass-transfer term considers both mass transfer from the catalyst and CO_2-acceptor particles; hence, two terms are included. There are also two terms in the source term for the pseudo-homogeneous model: one for the reforming reactions and one for the CO_2 capture kinetics. For all components but CO_2, the capture rate is zero. The parameter α is the ratio between the mass of the CO_2 acceptor and that of the catalyst. For a case with both materials in one particle, the void fractions ($\epsilon_{p,cat}$ and $\epsilon_{p,cap}$) will be the same and the source term for the pseudo-homogeneous model can be simplified.

An averaged one-dimensional energy equation is formulated in terms of temperature:

$$(\rho_g C_{pg}\epsilon_b + \rho_s C_{ps})\frac{\partial T}{\partial t} + \rho_g u C_{pg}\frac{\partial T}{\partial z} = \frac{\partial}{\partial z}\left(\lambda_z \frac{\partial T}{\partial z}\right) + S_i' \quad (15)$$

In the same way as that for the component transport, the source term, S_i', is different for the different models, as defined in eq 16.

$$S_i' = \begin{cases} a_{v,cat}h(T - T_{cat}^s) + a_{v,cap}h(T_{cat}^s - T) & \text{(2-P)} \\ a_{v,p}h(T_p^s - T) & \text{(1-P)} \\ \frac{1-\epsilon_b}{1+\alpha(\epsilon_{p,cap}/\epsilon_{p,cat})}(1-\epsilon_{p,cat})\rho_{cat}\sum_{i}^{3}\Delta H_{R_i}R_i + & \\ & \text{(P-H)} \\ \frac{1-\epsilon_b}{1-[\epsilon_{p,cat}(\epsilon_{p,cat}+\epsilon_{p,cap}\alpha)]}(1-\epsilon_{p,cap})\rho_{cap}\Delta H_{cap}r_{cap} & \\ & (16) \end{cases}$$

The source terms are analogous to the terms in the component transport equation, with heat-transfer terms for the heterogeneous models and heat-of-reaction terms for the pseudo-homogeneous model.

For the 1-D model, a momentum equation and a continuity equation are solved to predict the pressure−velocity coupling in the reactor. The continuity equation is given by eq 17:

$$\epsilon_b \frac{\partial \rho_g}{\partial t} + \frac{\partial}{\partial z}(\rho_g u) = -R_{cap} \quad (17)$$

The capture kinetics, R_{cap}, are taken into consideration in the continuity, because mass, in terms of CO_2, is removed from the gas phase of the reactor bed. The cross-sectional average momentum equation for a fixed-bed reactor can be given as[14]

$$\frac{\partial}{\partial t}(\rho_g u) + \frac{\partial}{\partial z}\left(\frac{\rho_g uu}{\epsilon_b}\right) = \epsilon_b \frac{\partial p}{\partial z} - \epsilon_b f \frac{\rho_g |u|u}{d_p} \quad (18)$$

Viscous forces, gravitational forces, and the wall shear forces are small, compared to the friction term in porous media for reactor conditions used in these simulations and, hence, are neglected in the momentum equation. Compared to a standard momentum equation for gas flow, a porous media friction term, $(-\epsilon_b f\rho_g |u|u/d_p)$, is added to the right-hand side. Relations for the friction factor and the others parameters used in the simulations are given in Table 2.

3.2. Particle Equations. Inside the catalyst and capture pellets, convective terms are assumably not significant, and the balance equation for the chemical components is expressed by

$$\epsilon_p \frac{\partial \rho_g \omega_{p,i}}{\partial t} = \frac{1}{r^2}\frac{\partial}{\partial r}\left(r^2 D_{p,i}\rho_g \frac{\partial \omega_{p,i}}{\partial r}\right) + \bar{r}_i \quad (19)$$

Table 2. Relations for Parameters Used in the Model

parameter	equation/comments
Axial dispersion coefficient, D_L:[15]	$D_{z,i} = 0.73 D_{im} + \dfrac{0.5 u d_p}{1 + 9.49 D_{im}/(u d_p)}$ where D_{im} is calculated from the Wilke equation[16] and the molecular binary diffusivities are calculated from relations in Poling et al.[17] The effective diffusivities in the particles are calculated from $D_{p,i} = \dfrac{D_{im} \epsilon_p}{\tau}$
Mass-transfer coefficient between particles and bulk:[18]	$Sh = 2 + 1.1(Sc)^{1/3}(Re_p)^{0.6}$ where $Sc = \dfrac{\mu}{\rho_g D_m}$, $Sh = \dfrac{D_m}{k d_p}$, and $Re_p = \dfrac{d_p \rho_g}{\mu}$ The analogy between heat and mass transfer allow us to use a similar expression for the heat-transfer coefficient, replacing Sh and Sc with Nu and Pr:
Heat-transfer coefficient between particles and bulk	$Nu = 2 + 1.1(Pr)^{1/3}(Re_p)^{0.6}$ $Pr = \dfrac{C_{pg}\mu}{\lambda_g}$ and $Nu = \dfrac{\lambda_g}{h d_p}$
Effective axial bed conductivity:[19]	$\dfrac{\lambda_z}{\lambda_g} = \dfrac{\lambda_z^0}{\lambda_g} + 0.75(Pr)(Re_p)$ where $\dfrac{\lambda_z^0}{k_g} = \epsilon + \dfrac{1 - \epsilon}{0.139\epsilon - 0.0339 + 2/[3(\lambda_g/\lambda_p)]}$ Gas conductivities λ_g are estimated from the Eucken formula.[20]
The bed void fraction is calculated from a relationship valid for $(d_p/d_t) \leq 0.5$:[21]	$\epsilon_b = 0.4 + 0.05\left(\dfrac{d_p}{d_t}\right) + 0.412\left(\dfrac{d_p}{d_t}\right)^2$
Friction factor for flow in porous media:[22]	$f = 6.8\left[\dfrac{(1 - \epsilon_b)^{1.2}}{\epsilon_b^{\,3}}\right]Re^{-0.2}$

Two different models, based on these equations, are simulated: one model that has one particle (1-P), consisting of both the sorbent and the catalyst, and one model with two different particles (2-P). For the model with one type of particle, the term $\bar{r}_i$ consists of both the reforming reaction and the capture reaction rates. For all components but CO_2, the capture rate is zero. The reaction rates in the pellets can then be expressed as

$$\bar{r}_i = \begin{cases} \left(\dfrac{1 - \epsilon_p}{1 + \alpha}\right)\rho_{cat} r_i + \left[\dfrac{1 - \epsilon_p}{1 - 1/(1 + \alpha)}\right]\rho_{cap} r_{i,cap} & \text{(1-P)} \\ (1 - \epsilon_{p,cat})\rho_{cat} r_i & \text{(2-P, catalyst)} \\ (1 - \epsilon_{p,cap})\rho_{cap} r_{i,cap} & \text{(2-P, acceptor)} \end{cases}$$

(20)

In the model with two types of particles, eq 19 is solved for both of them. The catalyst particle equations are solved for all components, with the reforming kinetics. Similar to the equations for bulk component transport, eq 19 is solved for the same four components and H_2O is calculated from the sum of mass fractions (eq 13). In the sorbent particle, all components but CO_2 are inert, and only one component in eq 19 is solved, in addition to the energy equation (eq 21).

$$[\epsilon_p \rho_g C_{pg} + (1 - \epsilon_p)\rho_p C_{ps}]\frac{\partial T_p}{\partial t} = \frac{1}{r^2}\frac{\partial}{\partial r}\left(r^2 \lambda_p \frac{\partial T_p}{\partial r}\right) + \Delta H_R$$

(21)

The temperature equation for the particles (eq 21) is solved in

the same manner as the component equations, with different ΔH_R values for the different models.

$$\Delta H_R = \begin{cases} \left(\dfrac{1 - \epsilon_p}{1 + \alpha}\right)\rho_{cat} \sum_i^3 (-\Delta H_{R_i})R_i + \\ \dfrac{1 - \epsilon_p}{1 - [1/(1 + \alpha)]}\rho_{cap} r_{i,cap}(-\Delta H_{r,cap}) & \text{(1-P)} \\ \\ (1 - \epsilon_{p,cat})\rho_{cat} \sum_i^3 (-\Delta H_{R_i})R_i & \text{(2-P, catalyst)} \\ \\ (1 - \epsilon_{p,cap})\rho_{cap} r_{i,cap}(-\Delta H_{r,cap}) & \text{(2-P, acceptor)} \end{cases}$$

(22)

3.3. Boundary Equations. The inlet boundary conditions are given by

$$\left.\begin{array}{l} \omega_i = \omega_{i,f} \\ T = T_f \\ u = u_f \\ \dot{m} = \dot{m}_f \end{array}\right\} \text{ at } z = 0$$

(23)

Boundary conditions at the outlet are also needed, and are given as

$$\left.\begin{array}{l} \dfrac{\partial \omega_i}{\partial z} = 0 \\ \dfrac{\partial T}{\partial z} = 0 \\ P = P_{out} \end{array}\right\} \text{ at } z = L$$

(24)

Table 3. Physical Parameters Used in the Simulations

parameter	value
d_p	0.005 m
d_t	0.1 m
L	4 m
ϵ_p	0.5 m
τ	3
$\rho_{cap,p}$	2500 kg/m^3
$\rho_{cat,p}$	2300 kg/m^3
λ_p	0.2 W m^{-1} K^{-1}
C_{ps}	1000 J kg^{-1} K^{-1}

Table 4. Standard Reactor Conditions

parameter	value
P_{out}	10 bar
T_f	848 K
T_w	848 K
$\dot{m}_f$	0.77 kg m^{-2} s^{-1}
α	4

Boundary conditions for the particle phase are as follows:

$$\left(D_{p,i}\frac{\partial \omega_i}{\partial r}\right)_{r=r_p} = -k_i(\omega_{p,i} - \omega_i) \tag{25}$$

$$\left(\lambda_p\frac{\partial T_p}{\partial r}\right)_{r=r_p} = -h(T_p - T) \tag{26}$$

$$\left(\frac{\partial \omega_i}{\partial r}\right)_{r=0} = 0 \tag{27}$$

$$\left(\frac{\partial T_p}{\partial r}\right)_{r=0} = 0 \tag{28}$$

3.4. The Algorithm. The governing equations are discretized using a finite volume scheme with uniform cell sizes and a staggered grid. This means that pressure, temperature, mass fractions, and density are evaluated at ordinary nodal points, whereas the velocity is solved on a staggered grid centered around the scalar cell faces. First-order forward differences are used for the discretization in time, which gives an implicit set of equations. The pressure—velocity coupling is solved using the semi-implicit method for pressure-linked equations (SIMPLE)[23] and a time splitting scheme is used to make the algorithm more efficient. At $t = 0$, the pressure—velocity coupling is implicitly solved without the component and energy transport equations in an initialization procedure to start the algorithm with consistent flow and pressure fields. For $t > 0$, the algorithm can be sketched as follows:

(1) The temperature and component species equations are solved implicitly in an iteration procedure until convergence is reached. The pressure and the velocity are held constant in these calculations while the gas density (ρ_g) is updated continuously with the change in gas composition and temperature.

(2) The pressure—velocity coupling is solved by an adapted SIMPLE algorithm.

(3) The variables are stored and the algorithm proceeds to the next time step with calculation of new temperature and component mass fractions.

In the heterogeneous models, the particle equations are solved in step 1 simultaneously with the bulk transport equations, using an implicit scheme. The particle equations and the bulk transport equations are thus solved in an iteration loop until convergence is reached in the specific time step, because the reaction rate terms and heat of reaction are nonlinear. For all the transport equations, the TDMA algorithm is used to solve the discretized algebraic equations.

4. Results and Discussion

A tube reactor with dimensions given in Table 3 is simulated. The dimensions chosen are based on the regular SMR, where reactor tubes with a diameter of 10 cm is typical. The length of the reactor is a case chosen for this particular project, because shorter reactors than those used in the conventional SMR are

desired, to save investment costs. The reactor is operated at a total pressure of 10 bar. Because the reforming kinetics are fast, compared to the sorption rate, a high ratio between the CO_2 acceptor and the catalyst is used. The reactor is filled with steam (97 mol %) and a small amount of hydrogen at the desired temperature (848 K) at startup. The input to the reactor is methane and steam, in which the steam-to-methane ratio is set to 6. A high steam-to-carbon (S/C) ratio is necessary to reach high conversions. A typical set of reactor conditions are presented in Table 4, and these are referenced as standard conditions in the subsequent parts of the paper. The inlet mass flux, which is set to 0.77 kg m^{-2} s^{-1} in the simulations, corresponds to a superficial gas velocity of 0.3 m/s. Physical properties of the reactor and materials are given in Table 3.

A measure used for the performance of the reactor is the dry hydrogen mole fraction, which is the hydrogen mole fraction of the gas after steam is removed. The dry mole fractions are calculated as in eq 29:

$$y_i^d = \frac{y_i}{1 - y_{H_2O}} \tag{29}$$

4.1. Assessing the Need for Heterogeneous Models. For steam reforming, heterogeneous models or pseudo-homogeneous models that include an efficiency factor have been used to simulate the process. The SMR has been determined to be strongly intraparticular diffusion-controlled,[24] and to check whether this is also the case for the SE-SMR, heterogeneous models have been formulated. Dry hydrogen mole fractions at $t = 200$ s are plotted in Figure 2, and no significant differences are observed in the reactor performances for the pseudo-homogeneous, one-particle heterogeneous, and two-particle heterogeneous models.

No advantage of heterogeneous models is observed under standard conditions, because the capture of CO_2 is the limiting step of the process. In contrast to the SMR, where the reactions are very fast, compared to the diffusion processes, the capture kinetics are slow, compared to the diffusion processes. The search for new and better CO_2 acceptors is in progress, and with faster kinetics, heterogeneous models or pseudo-heterogeneous with efficiency factors could be necessary. In the present case, a pseudo-homogeneous model
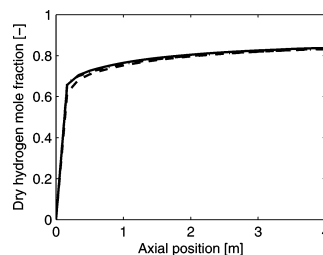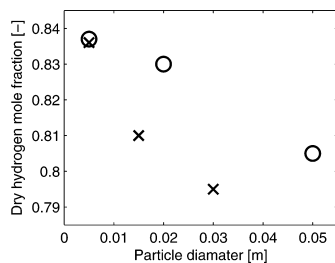
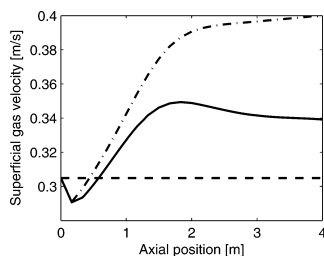**Figure 2.** Comparison in dry hydrogen mole fraction with (—) the pseudo-homogeneous model, (− · −) the one-particle heterogeneous model, and (- - -) two-particle heterogeneous model at $t = 200$ s, $P = 10$ bar, $T_f = 848$ K, steam-to-carbon (S/C) ratio = 6, $u_f = 0.3$ m/s.

Figure 3. Outlet dry hydrogen mole fraction at standard conditions for different particle sizes from (○) one-particle and (×) two-particle heterogeneous models at $t = 50$ s.
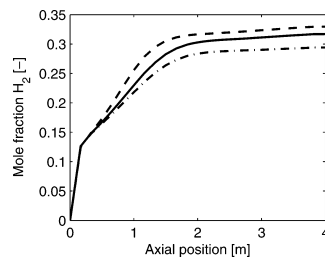

Figure 5. Comparisons of hydrogen mole fraction in the reactor with full solution of (—) the momentum and continuity equations, (— · —) constant mass flux, and (- - -) constant velocity; reactor profiles at $t = 200$ s, standard conditions.

Figure 4. Comparisons of velocity in the reactor with full solution of (—) the momentum and continuity equations, (— · —) constant mass flux, and (- - -) constant velocity; reactor profiles at $t = 200$ s, standard conditions.

Figure 6. Pressure in the reactor as function of axial position, at $t = 200$ s; standard conditions.

with an efficiency factor of 1 gives satisfying results for the dimensions of particles used.

With larger particles, the process will move toward being controlled by intraparticle diffusion. Figure 3 shows the dry hydrogen outlet mole fraction under standard conditions for both one and two particles after 50 s. The conversion in the reactor decreases with larger particles. The effect is, as expected, greater for the two-particle model and occurs at smaller particle sizes. The reason for this is that, for two particles, the CO_2 must diffuse out of the catalyst particle, through the bulk phase, and into the sorbent, and this becomes the limiting step. For the one-particle model, the diffusion of the reacting species to and from the bulk phase becomes the limiting step at larger particle diameters.

4.2. Effects of Solving the Momentum Equation. The pressure−velocity coupling is solved for the models described in section 3. This part of the simulation is computationally expensive, and the necessity for this model part is tested by comparing its results with other simpler model formulations. The two alternative approaches used are to assume constant gas velocity through the reactor or assume a constant mass flux through the reactor. Comparisons of the velocity and hydrogen mole fraction that were obtained in the reactor are shown in Figures 4 and 5, respectively. As seen in Figure 4, the velocity in the reactor is clearly different in these three cases. These phenomena affect the solution of all other transport equations and the impact on the hydrogen mole fractions is observed in Figure 5. There is a 10%−15% discrepancy between the rigorous model and the others for the output mole fractions. The effect of removal of mass can be observed in the results from the rigorous model in Figure 4. After a decrease in velocity in the first part of the reactor, because of changes in temperature and gas composition, the velocity reaches a maximum before
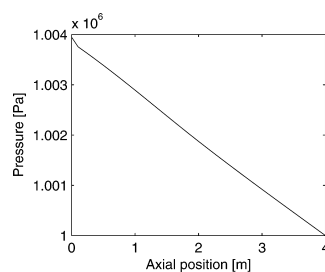
it slightly decreases in the last part of the reactor. Without the removal of mass, the results from the rigorous model would be very similar to the model with constant mass flux. An important future goal in the process development is to find CO_2 acceptors with faster kinetics than those used in this work. In cases with faster capture kinetics, the effect of not solving the continuity equation is most likely larger, and a model that includes this is even more important.

An important drawback associated with requiring solution of the momentum and continuity equations is the computational cost. The simulations with the complete model can require as much as four times the computational time used for the other two cases.

The pressure drop over the porous bed is determined by the friction factor in eq 18. The overall pressure drop in the reactor is small, because small velocities must be used to obtain satisfactory conversion. Figure 6 shows the pressure as a function of axial position. It is observed that the pressure is approximately constant through the reactor. It is known that low pressure drops in the reactor might lead to a misdistribution of flow; nevertheless, this effect is not taken into account in the model. With faster capture kinetics, higher gas velocities can be used, which will lead to significantly higher pressure gradients in the reactor and, thus, remove a possible misdistribution of flow.

To calculate the pressure and velocity profiles, a rigorous model that includes the transient and convective terms in the momentum equation (eq 18) are used. Other models for transient sorption reactors contain a simpler formulation, with only the Ergun equation for the pressure;[7] however, a complete formulation was chosen, because it makes the model much more robust. The simpler Ergun formulation (eq 30) is sufficient in reactors with small changes in gas volume; however, with changes both
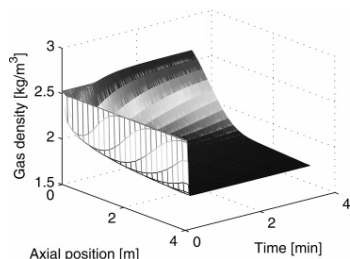
Figure 7. Gas density as function of time and axial position; standard conditions.
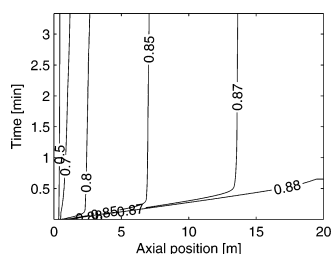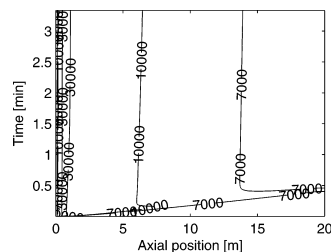

Figure 8. Contour plots of the dry hydrogen mole fraction, as a function of time and axial position, under standard conditions.

Figure 9. Contour plots of the partial pressure of CO_2 [Pa], as a function of time and axial position, under standard conditions.

Figure 10. Contour plot of the dry CO_2 mole fraction, as a function of time and axial position, under standard condtitions.

Figure 11. Contour plot of the dry CO mole fraction, as a function of time and axial position, under standard conditions.

in gas composition, temperature, and removal of CO_2, these terms should be included.

$$\frac{\mathrm{d}p}{\mathrm{d}z} = f\frac{\rho_\mathrm{g}|u|u}{d_\mathrm{p}} \qquad (30)$$

Figure 7 shows the density profile in the reactor, and the large changes in gas density are observed. The Ergun equation is not on a transient form; hence, the pressure will be set up instantaneously as a function of velocity. Because the pressure, in reality, has a fast but dynamic nature, the simplifications in the Ergun equation can lead to numerical problems. With certain combinations of initial and operating conditions, nonphysical solutions such as a reversal of the flow in the reactor may occur: these are solutions that are not observed when using the more rigorous model. Therefore, the rigorous model is chosen to be able to handle different types of operating conditions, although it is computationally more expensive.

4.3. Reactor Performance. A tube reactor of 20 m is simulated to show the performance of the reactor as a function of length. The thermodynamic upper limit of hydrogen purity, on a dry basis at 10 bar total pressure and a temperature of 848 K, using lithium zirconate as an acceptor, is 91 mol %. Very long reactors and low space velocities are required to reach the equilibrium composition, because of the limitations of the CO_2-capture kinetics. Contour plots of the dry hydrogen mole fraction are shown in Figure 8. It is observed that a dry hydrogen mole fraction of 0.8 is attained just after 2 m of the reactor; however, to get close to the thermodynamic limit, a significantly longer reactor is needed. At 10 m, a dry mole fraction of 0.86 is reached, but after 10 more meters, the dry hydrogen mole fraction has only increased by ∼0.02 and equilibrium conversion is not reached. The main reason for this is the slow capture kinetics at low partial pressures of CO_2. A reaction order of 2, with respect to the partial pressure of CO_2 in eq 2, makes the process slow as it reaches the thermodynamic limitation. The
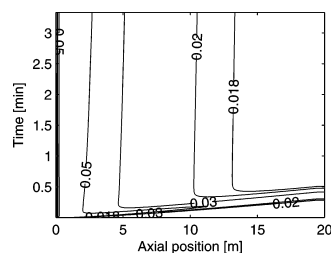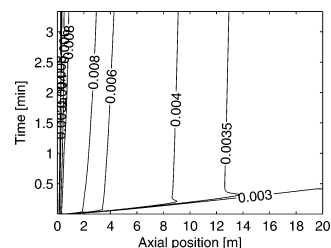
partial pressure contour profiles of CO_2 are shown in Figure 9, and it can be observed that the partial pressure is decreasing very slowly in the second half of the reactor. The partial pressure is ∼7000 Pa after 4 m; thereafter, the capture kinetics decreases considerably and 14 m of reactor are needed to attain a partial pressure of 7000 Pa. The equilibrium partial pressure is ∼3500 Pa at 848 K. The CO_2 content is also shown in Figure 10, but here, it is shown in terms of dry mole fraction. This mole fraction is considerably less than that for the traditional SMR, where the outlet dry CO_2 mole fraction is in the region of 0.10−0.15. This is obviously due to the capture of CO_2 in the reactor, and it also affects the CO content, which is shown in terms of dry mole fraction in Figure 11. For SMR, typical values for dry CO mole fractions is 0.02−0.03; hence, the amount of CO in the reactor is considerably less for the SE-SMR.

The same tendency as that experienced with longer reactors is observed when the gas velocity is reduced. Figure 12 shows the dry hydrogen purity as a function of axial position in a 4-m-long reactor at $t = 200$ s, and the conversion is strongly dependent on the gas velocity.
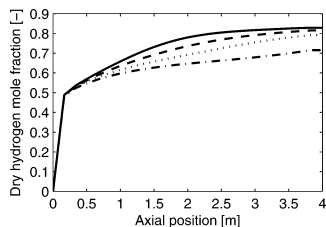
As mentioned, there are equilibrium limitations for the process, and with lower S/C ratios, the equilibrium conversion
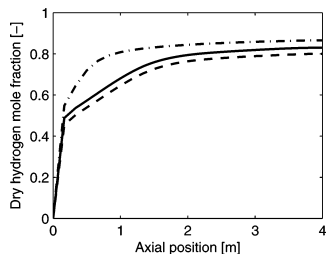
Figure 12. Comparison in dry hydrogen mole fraction at different inlet superficial gas velocities (u_f = (- - -) 0.6 m/s, (—) 0.3 m/s, and (— · —) 0.1 m/s) at t = 200 s.
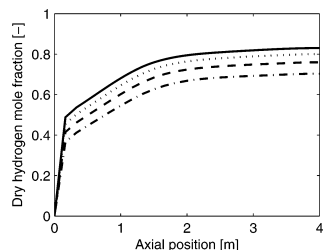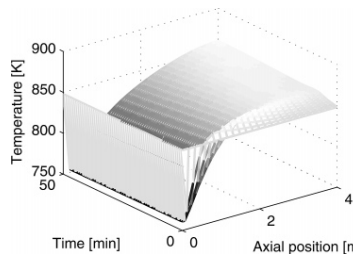

Figure 13. Comparison in dry hydrogen mole fraction at different steam-to-carbon (S/C) ratios at t = 200 s: S/C = (—) 6, (···) 5, (- - -) 4, and (— · —) 3.
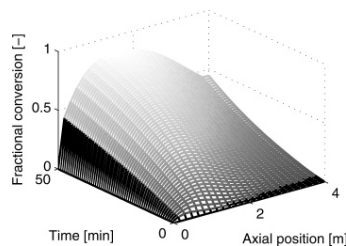

Figure 14. Dry hydrogen mole fraction as a function of axial position at different times: (—) after 5 min, (- - -) after 20 min, (···) after 40 min, and (— · —) after 70 min.

Figure 15. Temperature in the reactor, as a function of time and axial position.

Figure 16. Fractional conversion of the acceptor, as a function of time and axial position.

will be reduced. A relatively low throughput of steam is desirable to obtain a more energy-efficient process, but as observed in Figure 13, the product purity is reduced considerably when the S/C ratio is reduced. This ratio is an important aspect for the process and must be evaluated carefully in a complete design. Traditional SMR uses S/C ratios as small as 3 and has, at this point, an advantage, compared to the SE-SMR with Li$_2$-ZrO$_3$ as an acceptor.[1]

The CO$_2$-capture kinetics are dependent on the fractional conversion of the CO$_2$ acceptor. Thus, the sorption kinetics will become slower with time. This will lead to lower conversion in the reactor, as shown in Figure 14. The contour plot shows that a dry hydrogen mole fraction of >0.83 only is reached in the first minutes. The hydrogen content then decreases, and, after 70 min, it is down to just above 70%, which is close to the thermodynamic limit for SMR without a CO$_2$ acceptor under these conditions. The lower dry hydrogen mole fraction in the reactor is due to the decreasing capture kinetics. The decrease in kinetics is mainly due to the dependence of fractional conversion, but it is also attributable to a reduction in the temperature in the reactor. The reactor is heated with a constant

temperature at the wall, which is set equal to the inlet gas temperature. As observed in Figure 15, this is not sufficient to sustain the temperature in the reactor. This leads to slower sorption kinetics and, hence, lower conversion. Figure 16 shows the fractional conversion of the acceptor. In the time span used in the simulations, which is approximately an hour, the acceptor has reached ~80% of its capacity.

5. Conclusions

Heterogeneous and pseudo-homogeneous models with calculation of the pressure−velocity coupling in the reactor have been formulated. Simulations show that the solutions are dependent on including the pressure−velocity coupling. Dry hydrogen mole fractions of >87% can be obtained in sorption-enhanced steam methane reforming (SE-SMR) with Li$_2$ZrO$_3$ as a CO$_2$ acceptor, but they require long reactors and low gas velocities. The work on new acceptors with improved kinetics is in progress and it is very important for improving the process. Simulations show that the kinetics of the CO$_2$ capture is the rate-determining step in the process under the given conditions and indicate that there are no significant intraparticular resistances. This means that a pseudo-homogeneous model with an efficiency factor of 1 can be used instead of more rigorous heterogeneous models. For particles >5 mm in diameter, an efficiency factor must be included in the pseudo-homogeneous model or heterogeneous models should be used.

Notation

a_v = surface area of particles (m^{-1})
C = concentration (mol/m^3)
C_p = heat capacity (J mol^{-1} K^{-1})
d = diameter (m)
d_t = diameter of reactor tube (m)
D = dispersion factor or diffusivity (m^2/s)
E = Arrhenius activation energy (J/mol)

f = friction factor
h = bulk-particle heat-transfer coefficient (W m^{-1} K^{-1})
$-\Delta H$ = heat of reaction (J/kg)
J = mass flux vector (kg/m^2)
k = mass-transfer coefficient (m/s)
K = constant in capture kinetics (s^{-1})
L = length of reactor (m)
$\dot{m}$ = mass flux (kg m^{-1} s^{-1})
n = constant in capture kinetics
p = pressure (Pa)
q = mass of CO_2 per mass of acceptor
r = radius (m)
r = reaction rate of components (kg kg^{-1} s^{-1})
R = reaction rate (kg m^{-3} s^{-1})
R = gas constant (J K^{-1} mol^{-1})
S = component mass source term (kg m^{-3} s^{-1})
S' = heat source term (J m^{-3} s^{-1})
t = time (s)
T = temperature (K)
u = superficial space velocity (m/s)
x = fractional conversion
y = mole fraction
z = axial position (m)

Greek Symbols

α = ratio between the volume of the acceptor and the volume of the catalyst
ϵ = void fraction
λ = conductivity (J m^{-1} s^{-1})
μ = viscosity (Pa s)
ρ = density (kg/m^3)
τ = tortuosity
ω = mass fraction

Subscripts

b = bed
cap = capture, CO_2 acceptor
cat = catalyst
eq = equilibrium
f = feed
g = gas
i = component i
m = molar
max = maximum
p = particle
s = solid
w = wall
z = axial direction

Superscripts

d = dry
s = surface

Literature Cited

(1) Ochoa-Fernández, E.; Haugen, G.; Zhao, T.; Rønning, M.; Aartun, I.; Børresen, B.; Rytter, E.; Rønnekleiv, M.; Chen, D. Evaluation of potential co$_2$ acceptors for application in hydrogen production by sorption enhanced steam reforming. *Am. Chem. Soc., Div. Fuel Chem.* **2006**, *51*, 598.

(2) Hufton, J.; Waldron, S.; Weigel, S.; Nataraj, S.; Rao, M.; Sircar, S. Sorption enhanced reaction process for the production of hydrogen. In *Proceedings of the 2000 Hydrogen Program Review*, **2000**.

(3) Hufton, F.; Mayorga, S.; Sircar, S. Sorption-enhanced reaction process for hydrogen production. *AIChE J.* **1999**, *45*, 248.

(4) Nakagawa, K.; Ohashi, T. A novel method of CO_2 capture from high temperature gases. *J. Electrochem. Soc.* **1998**, *145*, 1344−1346.

(5) Kato, M.; Nakagawa, K. New series of lithium containing complex oxides, lithium silicates, for application as a high temperature CO_2 absorbent. *J. Ceram. Soc. Jpn.* **2001**, *109*, 911−914.

(6) Ochoa-Fernández, E.; Rønning, M.; Grande, T.; Chen, D. Synthesis and CO_2 capture properties of nanocrystalline lithium zirconate. *Chem. Mater.* **2006**, *18*, 1383−1385.

(7) Xiu, G.-H.; Li, P.; Rodrigues, A. E. Sorption-enhanced reaction process with intraparticle-diffusion limitations. *Chem. Eng. J.* **2003**, *95*, 83−93.

(8) Johnsen, K.; Grace, J.; Elnashaie, S.; Kolbeinsen, L.; Eriksen, D. Modeling of SESMR. *Ind. Eng. Chem. Res.* **2006**, *45*, 4133.

(9) Szekely, J.; Evans, J. W.; Sohn, H. Y. *Gas−Solid Reactions*; Academic Press: New York, 1976.

(10) Ishida, M.; Wen, C.-Y. Comparison of kinetic and diffusional models for solid−gas reactions. *AIChE J.* **1968**, *14*, 311−17.

(11) Ida, J.; Lin, Y. S. Mechanism of high-temperature CO_2 sorption on lithium zirconate. *Environ. Sci. Technol.* **2003**, *37*, 1999−2004.

(12) Knacke, O.; Kubaschewski, O.; Hesselmann, K.; Barin, I. *Thermochemical Properties of Inorganic Substances*; Springer−Verlag: Berlin, 1991.

(13) Xu, J.; Froment, G. F. Methane steam reforming, methanation and water-gas shift: I. intrinsic kinetics. *AIChE J.* **1989**, *35*, 88−96.

(14) Jakobsen, H. A.; Lindborg, H.; Handeland, V. A numerical study of the interactions between viscous flow, transport and kinetics in fixed bed reactors. *Comput. Chem. Eng.* **2002**, *26*, 333−357.

(15) Edwards, M. F.; Richardson, J. Gas dispersion in packed beds. *Chem. Eng. Sci.* **1968**, *23*, 109−123.

(16) Bird, R. B.; Stewart, W. E.; Lightfoot, E. N. *Transport Phenomena*; Wiley: New York, 1960.

(17) Poling, B. E.; Prausnitz, J. M.; O'Connell, J. P. *The Properties of Gases and Liquids,* Fifth Edition; McGraw−Hill: New York, 2001.

(18) Wakao, N.; Funazkri, T. Effect of fluid dispersion coefficients on particle-to-fluid mass transfer coefficients in packed beds. correlation of sherwood numbers. *Chem. Eng. Sci.* **1978**, *33*, 1375−1384.

(19) Yagi, S.; Kunii, D.; Wakao, N. Effective thermal conductivities in packed beds. *AIChE J.* **1960**, *6*, 543−546.

(20) Bird, R. B.; Stewart, W. E.; Lightfoot, E. N. *Transport Phenomena*, 2nd Edition; Wiley: New York, 2002.

(21) Dixon, A. G. Correlations for wall and particle shape effects on fixed bed bulk voidage. *Can. J. Chem. Eng.* **1988**, *66*, 705−708.

(22) Hicks, R. E. Pressure drop in packed beds of spheres. *Ind. Eng. Chem. Fundam.* **1970**, *9*, 500−502.

(23) Patankar, S. *Numerical Heat Transfer and Fluid Flow*; Hemisphere Publishing Corporation, and Taylor and Francis Group: New York, 1980.

(24) Froment, G. F.; Bischoff, K. B. *Chemical Reactor Analysis and Design,* 2nd Edition; Wiley: New York, 1990.

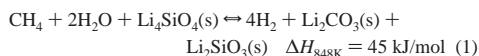# Hydrogen Production by Sorption-Enhanced Steam Methane Reforming Using Lithium Oxides as CO₂-Acceptor

Hans Kristian Rusten,* Esther Ochoa-Fernández, Håvard Lindborg, De Chen, and Hugo A. Jakobsen

The Norwegian University of Science and Technology (NTNU), NO-7491 Trondheim, Norway

The kinetics of CO_2-capture on Li_4SiO_4 has been examined experimentally and described by a mathematical reaction-rate model. Sorption-enhanced steam methane reforming has been simulated with a fixed-bed reactor model using the formulated capture kinetics. At working conditions of 20 bar, 848 K, a steam-to-carbon ratio of 5, and a superficial inlet gas velocity of 1 m/s, a dry hydrogen mole fraction at the outlet of 0.87 can be reached. The performance of the process with Li_4SiO_4 is compared to that with Li_2ZrO_3 as CO_2-acceptor. Li_4SiO_4 gives higher conversion and production capacity at lower steam-to-carbon ratios. A drawback for the process with Li_4SiO_4 as acceptor is that high conversion is only reached at low fractional conversion of the acceptor. This is due to the fact that the capture kinetics is second order with respect to unreacted solid. The total reaction is endothermic, and effective heat exchange is necessary to avoid a dramatic drop in the reactor temperature. A fluidized-bed reactor has also been simulated, and the results have been compared to those of the fixed-bed reactor. The fluidized-bed reactor has some advantages in terms of easier heat integration and continuous regeneration of CO_2-acceptor, but compared to the fixed bed, a longer reactor is needed to reach the same conversion.

1. Introduction

An increased demand for hydrogen as an energy-carrier and as a fuel for clean power generation is expected during the 21st century. The Kyoto protocol states that the world has to decrease its CO_2 emissions to the atmosphere. A concept combining hydrogen production and sequestration of CO_2 is the sorption-enhanced steam methane reforming (SE-SMR) process. This is an alternative to the traditional steam methane reforming (SMR). SE-SMR is a concept that has received increased attention in recent years. The process utilizes a solid CO_2-acceptor to capture CO_2 in the reforming reactor and thereby change the normal thermodynamic limitations of steam methane reforming. As a consequence, the SE-SMR can be run at lower temperatures than the traditional SMR process, which will reduce energy consumption, coking and sintering of the catalyst, and investment costs. Different metal oxides have been proposed as high-temperature CO_2-acceptors for SE-SMR, and lithium-containing materials have shown promising properties. Lithium zirconate and lithium silicate are two potential candidates as CO_2-acceptors at high temperatures having high capacity and relatively low regeneration temperature.[1,2] The total reaction for SE-SMR with Li_4SiO_4 as CO_2-acceptor is shown in

$$CH_4 + 2H_2O + Li_4SiO_4(s) \leftrightarrow 4H_2 + Li_2CO_3(s) + Li_2SiO_3(s) \quad \Delta H_{848K} = 45 \text{ kJ/mol} \quad (1)$$

In the SE-SMR process, the solid CO_2-acceptor will be regenerated by temperature swing or pressure swing and a product stream of CO_2 can be transported to storage.

In this paper, a kinetic model for the capture of CO_2 on Li_4SiO_4 is presented and mathematical reactor models are used to study the performance of the SE-SMR with Li_4SiO_4 as CO_2-acceptor. In a previous paper,[3] a relation for the capture kinetics of CO_2 on Li_2ZrO_3 was found, and a fixed-bed SE-SMR reactor

was simulated. The performance of the process with Li_2ZrO_3 is compared to the process with Li_4SiO_4 as acceptor.

Both fixed-bed reactors and fluidized-bed reactors have been proposed for the process. Johnsen et al.[4] modeled a dual fluidized bed using calcium oxide as CO_2-acceptor. Xiu et al.[5] simulated a fixed-bed reactor using hydrotalcite as sorbent. The fluidized-bed reactor offers some advantages in terms of heat integration and continuous operation. For this reason, a fluidized-bed SE-SMR reactor has been simulated in this work for comparison with the fixed-bed reactor.

2. Apparent Kinetic Model for the CO₂ Capture

The kinetics of CO_2-capture on a Li_4SiO_4-based material from Toshiba have been examined in a tapered element oscillating microbalance (TEOM) at three different temperatures, 803, 823, and 848 K, and at partial pressures of CO_2 in the range 0.05−1 bar. The synthesis method of the lithium orthosilicate material used is reported by Kato et al.[6] The material was ground to a fine powder before the experiments, and the flow rates used in the measurements were high enough to ensure no external mass-transfer limitations. The experimental setup and procedures of the TEOM measurements are described in detail by Ochoa-Fernández et al.[7]

To be able to utilize the experimental data in a mathematical reactor model, a kinetic rate expression for the CO_2 capture on Li_4SiO_4 has to be found. A typical model for gas−solid reactions is given by eq 2.

$$\frac{dx}{dt} = Kf(P_a)F(x) \quad (2)$$

Different expressions for $F(x)$ have been given in the literature, and a selection of these is listed by Gomez-Barea and Ollero.[8] A commonly applied model is the shrinking unreacted core model[9] where $F(x) = (1 - x)^{2/3}$. Other used models are the random pore model[10] and the volumetric model.[9] None of these models or variations of these, like the shrinking core model

with different geometries and including an induction period,[11] showed a satisfying fit to the experimental data over the whole range of operating conditions. For the gathered experimental data, an expression with $F(x) = (1 - x)^n$ and an n-value of 2 gave the best fit to the data. This formulation does not explain the capture mechanism, but it indicates that the rate-limiting step is changing with fractional conversion, as reported by Lee[12] for the reaction of calcium oxide with CO_2. A rigorous mechanistic model for the CO_2 capture should include the change in the rate-limiting step during the course of the reaction and with the change in temperature and partial pressure of CO_2, but for the purpose of this work, which is the modeling of SE-SMR, a simpler model is considered sufficient. To be able to formulate a more descriptive model that explains the different steps in the capture of CO_2, further experimental analysis is needed.

After the determination of the expression for $F(x)$ in eq 2, the reaction rate expression is given as

$$\frac{dx}{dt} = Kf(p_{CO_2})(1 - x)^2 \tag{3}$$

Mechanistic models based on first-order reaction kinetics with respect to the CO_2 partial pressure use $f(p_{CO_2}) = p_{CO_2} - p_{CO_2,eq}$, but the experimental data clearly showed that the kinetics were not first order with respect to partial pressure. Similar to the function of fractional conversion, this indicates that the rate-limiting step changes with partial pressure. Nonlinear dependencies of the partial pressure have also been found and modeled for other gas–solid reactions, like the reaction of CO_2 with calcium oxide.[4] The expression found for the modeling of the capture kinetics is shown in eq 4:

$$\frac{dx}{dt} = K(p_{CO_2} - p_{CO_2,eq})^n (1 - x)^2 \tag{4}$$

Experiments have also been carried out to get the equilibrium partial pressure of CO_2 for the material, and this was done by finding the highest partial pressure of CO_2 at different temperatures, which did not lead to weight gain after several hours in the TEOM. From these experimental data, an expression for the equilibrium partial pressure of CO_2 as a function of temperature was found.

$$\ln\left(\frac{1}{p_{CO_2}}\right) = -0.0066T - 2.25 \tag{5}$$

To get the values of the parameters in the kinetic model, an in-house code for nonlinear model fitting based on Marquardt's secant model was used. By integrating eq 4 in time, the expression fitted to the experimental data was found:

$$x = 1 - \frac{1}{1 + K(p_{CO_2} - p_{CO_2,eq})^{n_t}} \tag{6}$$

x is the fractional conversion of sorbent, defined as q/q_{max} where q is the mass uptake of CO_2 per mass of sorbent and q_{max} is the maximum of q found for this material, which was 0.20. For the kinetic constant (K), an Arrhenius expression (eq 7) is used for the temperature dependence.

$$K = K_0 \exp\left[-E_{cap}/R\left(\frac{1}{T} - \frac{1}{T_0}\right)\right] \tag{7}$$

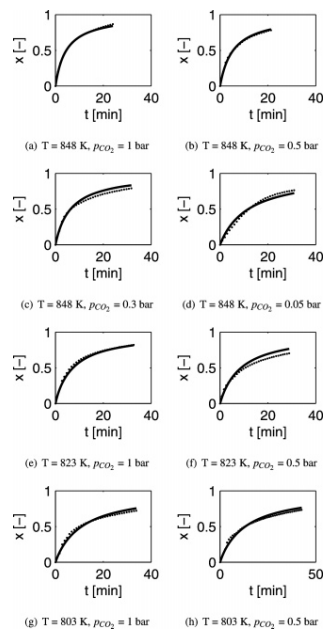The fitted parameters in eqs 4 and 7 with standard deviations are given in Table 1.

Figure 1. Experimental data (···) and kinetic model (—) for the capture of CO_2 on lithium orthosilicate.
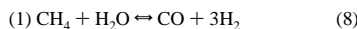
Table 1. Capture Kinetic Parameters

K_0 (s^{-1})	$1.84 \times 10^{-4} \pm 1.7 \times 10^{-5}$
E_{cap} (J/mol)	$1.1 \times 10^5 \pm 3 \times 10^3$
n	0.26 ± 0.01

Figure 1 shows the experimental data and the model fit at all examined partial pressures and temperatures. The fit is reasonably good, particularly since the material will undergo minor changes as it is used in several cycles. Changes in the morphology during the capture–regeneration cycles will have some effect on the sorption kinetics, which will lead to discrepancies to any kinetic model. However, the model fit is found to be sufficient to model the SE-SMR with Li_4SiO_4 as CO_2-acceptor.

3. Reactor Models

Transient one-dimensional reactor models with axial dispersion have been developed to simulate a fixed-bed reactor. A transient model is chosen because the capture of CO_2 has a time-dependent nature, and axial dispersion is included because relatively low gas velocities are used in the simulations. Three different models have been developed, two heterogeneous models and a pseudo-homogeneous model. The difference between the two heterogeneous models is the manner in which the sorbent is installed in the reactor. One model considers that the acceptor and the reforming catalyst are separated in two different particles, whereas, in the other case, there is one particle with both catalytic and capture properties.

The steam methane reforming and the water gas shift reaction kinetics can be described by three equations, two of which are independent:

$$(1)\ CH_4 + H_2O \leftrightarrow CO + 3H_2 \tag{8}$$

$$(2)\ CO + H_2O \leftrightarrow CO_2 + H_2 \tag{9}$$

$$(3)\ CH_4 + 2H_2O \leftrightarrow CO_2 + 4H_2 \tag{10}$$

The kinetics of these reactions have been described by Xu and Froment:[13]

$$R_1 = \frac{k_1}{p_{H_2}^{2.5}}(p_{CH_4}p_{H_2O} - p_{H_2}^{3}p_{CO}/K_1)/DEN^2 \tag{11}$$

$$R_2 = \frac{k_2}{p_{H_2}}(p_{CO}p_{H_2O} - p_{H_2}p_{CO_2}/K_2)/DEN^2 \tag{12}$$

$$R_3 = \frac{k_3}{p_{H_2}^{3.5}}(p_{CH_4}p_{H_2O} - p_{H_2}^{4}p_{CO_2}/K_3)/DEN^2 \tag{13}$$

DEN is given as $1 + K_{CO}p_{CO} + K_{H_2}p_{H_2} + K_{CH_4}p_{CH_4} + K_{H_2O}p_{H_2O}/p_{H_2}$, and all constants are taken from Xu and Froment.[13]

3.1. Bulk Gas Equations. The general mass-balance equation for a chemical species i in reacting fluid flow with varying density, temperature, and composition is written as

$$\frac{\partial \rho_i}{\partial t} + \nabla \cdot (\rho_i u) + \nabla \cdot J_i = R_i \tag{14}$$

A cross-sectional average of eq 14 reduces the model to one dimension, and after introducing mass fractions, the transport equation for porous media flows is given as

$$\epsilon_b \frac{\partial \rho_g \omega_i}{\partial t} + \frac{\partial}{\partial z}(\rho_g \omega_i u) = \frac{\partial}{\partial z}\left(\epsilon_b D_{z,i}\rho_g \frac{\partial \omega_i}{\partial z}\right) + S_i \tag{15}$$

Equation 15 is solved for the components H_2, CO, CH_4, and CO_2. H_2O is the dominating component in the system, and the mass fraction of H_2O is obtained from eq 16.

$$\sum_{i=1}^{5} \omega_i = 1 \tag{16}$$

The axial dispersion coefficient ($D_{z,i}$) is calculated from eq 17:[14]

$$D_{z,i} = 0.73D_{im} + \frac{0.5ud_p}{1 + 9.49D_{im}/(ud_p)} \tag{17}$$

The molecular diffusivities (D_{im}) of component i in the gas mixture are calculated from the Wilke equation,[15] and the molecular binary diffusivities are calculated from relations by Poling et al.[16] The source term (S_i) is different in the various models, with the expressions shown in eq 18. For the one-particle (1-P) and two-particle (2-P) heterogeneous models, the source term contains particle–bulk mass-transfer terms, and for the pseudo-homogeneous model (P–H), S_i is a reaction-rate term.

$$S_i = \begin{cases} a_{v,cat}k_i\rho_g(\omega_{i,cat}^{s} - \omega_i) + a_{v,cap}k_i\rho_g(\omega_{i,cap}^{s} - \omega_i) & 2-P \\ a_{v,p}k_i\rho_g(\omega_{p,i}^{s} - \omega_i) & 1-P \\ \dfrac{1-\epsilon_b}{1+\alpha\dfrac{1-\epsilon_{p,cat}}{1-\epsilon_{p,cap}}}(1-\epsilon_{p,cat})\rho_{cat}r_i + \dfrac{1-\epsilon_b}{1+\dfrac{1-\epsilon_{p,cap}}{\alpha(1-\epsilon_{p,cat})}}(1-\epsilon_{p,cap})\rho_{cap}r_{cap,i} & P-H \end{cases} \tag{18}$$

For the two-particle model, the mass-transfer term considers mass transfer from both the catalyst and the CO_2-acceptor particles; hence, two terms are included. There are also two terms in the source term for the pseudo-homogeneous model: one each for volume of CO_2-acceptor and of catalyst. For a case with both materials in one particle, the void fractions ($\epsilon_{p,cat}$ and $\epsilon_{p,cat}$) will be the same and the source term can be simplified. The capture reaction rate ($r_{cap,i}$) is given by eq 19 where the relation for dx/dt is found in Section 2.

$$r_{cap} = q_{max}\frac{dx}{dt} \tag{19}$$

The mass-transfer coefficient between the gas phase and the particle is given by[17]

$$Sh = 2 + 1.1(Sc)^{1/3}(Re_p)^{0.6} \tag{20}$$

From the Sherwood number (Sh), the mass-transfer coefficient can be found from eq 21.

$$Sh = \frac{D_m}{kd_p} \tag{21}$$

An averaged one-dimensional energy equation is formulated in terms of temperature:

$$(\rho_g C_{pg}\epsilon_b + \rho_s C_{ps})\frac{\partial T}{\partial t} + \rho_g u C_{pg}\frac{\partial T}{\partial z} = \frac{\partial}{\partial z}\left(\lambda_z \frac{\partial T}{\partial z}\right) + S_i' \tag{22}$$

A relation for the effective axial bed conductivity is given by Yagi et al.:[18]

$$\frac{\lambda_z}{\lambda_g} = \frac{\lambda_z^0}{\lambda_g} + 0.75(Pr)(Re_p) \tag{23}$$

λ_z^0/k_g in eq 23 is given by eq 24:

$$\frac{\lambda_z^0}{k_g} = \epsilon + \frac{1-\epsilon}{0.139\epsilon - 0.0339 + 2/3(\lambda_g/\lambda_p)} \tag{24}$$

Gas conductivities (λ_g) are estimated from the Eucken formula.[19]

In the same way as that for the component transport, the source term (S_i') is different for the different models, as defined in eq 25.

$$S_i' = \begin{cases} a_{v,cat}h(T - T_{cat}^s) + a_{v,cap}h(T_{cap}^s - T) & 2-P \\ a_{v,p}h(T_p^s - T) & 1-P \\ \dfrac{1-\epsilon_b}{1 + \alpha \dfrac{1-\epsilon_{p,cat}}{1-\epsilon_{p,cap}}}(1-\epsilon_{p,cat})\rho_{cat}\sum_i^3 \Delta H_{R_i}R_i + \dfrac{1-\epsilon_b}{1 + \dfrac{1-\epsilon_{p,cat}}{\alpha(1-\epsilon_{p,cap})}}(1-\epsilon_{p,cap})\rho_{cap}\Delta H_{cap}r_{cap} & P-H \end{cases} \tag{25}$$

The terms are analogous to the terms in the component transport equation, with heat-transfer terms for the heterogeneous models and a heat-of-reaction term for the pseudo-homogeneous model. The heat-transfer coefficient between the gas phase and the particles is calculated using the analogy between heat and mass transfer, replacing Sh and Sc with Nu and Pr, respectively, in eq 20.

$$Nu = 2 + 1.1(Pr)^{1/3}(Re_p)^{0.6} \tag{26}$$

$$Nu = \frac{\lambda_g}{hd_p} \tag{27}$$

For the 1-D model, a momentum equation and a continuity equation are solved to predict the pressure−velocity coupling in the reactor. The continuity equation is as given in eq 28.

$$\epsilon_b \frac{\partial \rho_g}{\partial t} + \frac{\partial}{\partial z}(\rho_g u) = -R_{cap} \tag{28}$$

The capture kinetics, R_{cap}, are accounted for in the continuity since mass in terms of CO_2 is removed from the gas phase of the reactor bed. The momentum equation for an averaged 1-D fixed-bed reactor can be given as[20]

$$\frac{\partial}{\partial t}(\rho_g u) + \frac{\partial}{\partial z}\left(\frac{\rho_g uu}{\epsilon_b}\right) = \epsilon_b \frac{\partial p}{\partial z} - \epsilon_b f \frac{\rho_g |u|u}{d_p} \tag{29}$$

Viscous forces, gravitational forces, and the wall shear forces are small compared to the friction term in porous media for reactor conditions used in these simulations and, hence, are neglected in the momentum equation. Compared to a standard momentum equation for gas flow, a porous media friction term, ($-\epsilon_b f\rho_g|u|u/d_p$), is added to the right-hand side. A relation for the friction factor is given in eq 30.[21]

$$f = 6.8\frac{(1-\epsilon_b)^{1.2}}{\epsilon_b^3}Re_p^{-0.2} \tag{30}$$

3.2. Particle Equations. Inside the catalyst and capture pellets, convective terms are assumed to be insignificant and the balance equation for the chemical components is expressed by

$$\epsilon_p \frac{\partial \rho_g \omega_{p,i}}{\partial t} = \frac{1}{r^2} \frac{\partial}{\partial r}\left(r^2 D_{p,i}\rho_g \frac{\partial \omega_{p,i}}{\partial r}\right) + \bar{r}_i \tag{31}$$

In eq 31, the effective diffusion coefficient in the particle ($D_{p,i}$) is calculated from the relationship in eq 32.

$$D_{p,i} = D_{im}\epsilon_p/\tau \tag{32}$$

Two different models based on these equations are simulated: one model with one particle (1-P) consisting of both the sorbent and the catalyst and one model with two different particles (2-P). For the model with one type of particle, the term $\bar{r}_i$ consists of both the reforming reaction rates and the capture reaction rate. For all components but CO_2, the capture rate is zero. The reaction rates in the pellets can then be expressed as

$$\bar{r}_i = \begin{cases} \dfrac{1-\epsilon_p}{1+\alpha}\rho_{cat}r_i + \dfrac{1-\epsilon_p}{1+\dfrac{1}{\alpha}}\rho_{cap}r_{cap,i} & 1-P \\ (1-\epsilon_{p,cat})\rho_{cat}r_i & 2-P, \text{catalyst} \\ (1-\epsilon_{p,cap})\rho_{cap}r_{cap,i} & 2-P, \text{acceptor} \end{cases} \tag{33}$$

In the model with two types of particles, eq 31 is solved for both of them. The catalyst particles are solved for all components, with the reforming kinetics. Similarly to the equations for bulk-component transport, eq 31 is solved for four components and H_2O is calculated from the sum of mass fractions (eq 16). In the sorbent particle, all components but CO_2 are inert, and only one component equation is solved in addition to the energy eq 34.

$$(\epsilon_p\rho_g C_{pg} + (1-\epsilon_p)\rho_p C_{ps})\frac{\partial T_p}{\partial t} = \frac{1}{r^2}\frac{\partial}{\partial r}\left(r^2\lambda_p \frac{\partial T_p}{\partial r}\right) + \Delta H_R \tag{34}$$

The temperature equation for the particles (eq 34) is solved in the same manner as the component equations, with different ΔH_R for the different models.

$$\Delta H_R = \begin{cases} \dfrac{1-\epsilon_p}{1+\alpha}\rho_{cat}\sum_i^3(-\Delta H_{R_i})R_i + \dfrac{1-\epsilon_p}{1+\dfrac{1}{\alpha}}\rho_{cap}r_{cap,i}(-\Delta H_{r,cap}) & 1-P \\ (1-\epsilon_{p,cat})\rho_{cat}\sum_i^3(-\Delta H_{R_i})R_i & 2-P, \text{catalyst} \\ (1-\epsilon_{p,cap})\rho_{cap}r_{cap,i}(-\Delta H_{r,cap}) & 2-P, \text{acceptor} \end{cases} \tag{35}$$

The given set of equations is discretized using a finite volume scheme, and the resulting algebraic equations are solved using a TDMA solver. The algorithm is described in detail by Rusten et al.[3]

4. Results and Discussion

A 6 m long reactor is simulated with an outlet pressure of 20 bar. The reactor is a multitube reactor with tube diameters of 10 cm, which is a typical diameter in SMR. At start-up, the reactor is filled with steam and a small amount of hydrogen at a temperature of 848 K. The feed to the reactor is steam and methane at a steam-to-carbon ratio of 5 with a temperature of 848 K. The inlet mass flux is set to 5 kg/(m² s). This gives an inlet superficial gas velocity of ~1 m/s. In the reactor, an acceptor-to-catalyst ratio of 4 is used. The operating conditions are chosen to yield a dry hydrogen mole fraction out of the reactor above 0.85 and the highest production capacity possible. The steam-to-carbon ratio is an important parameter for the energy efficiency of the process. High S/C ratios give lower thermal efficiency but higher equilibrium conversion. For traditional SMR, typical S/C ratios are ~3, but in SE-SMR with Li_4SiO_4 as acceptor, a S/C ratio of 5 is needed to get satisfying conversion. This gives a feed to the reactor consisting of 16.7% methane and 83.3% steam on a molar basis. The physical parameters of the reactor and the materials are given in Table 2.

A measure used for the performance of the reactor is the dry hydrogen mole fraction, which is is the hydrogen mole fraction of the gas after steam is removed. The dry mole fractions are calculated as in eq 36.
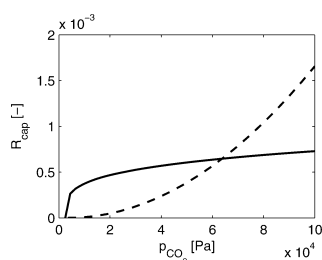
$$y_i^d = \frac{y_i}{1 - y_{H_2O}} \tag{36}$$
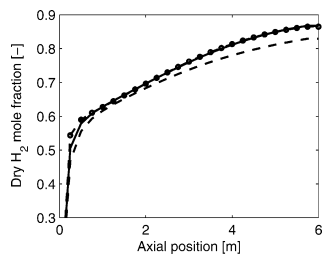
Figure 2. Comparison of dry hydrogen mole fraction between pseudo-homogeneous model, (—) one-particle heterogeneous model (OOO) and two-particle heterogeneous model (− −) with Li_4SiO_4 as acceptor, $P = 20$ bar, $T_f = 848$ K, S/C ratio = 5, $u_f = 1$ m/s.


Figure 3. CO_2-capture kinetics for fresh sorbent as a function of partial pressure of CO_2 for Li_2ZrO_3 (− −) and Li_4SiO_4 (—).

Table 2. Physical Parameters Used in the Simulations

d_p (m)	0.005
d_t (m)	0.1
L (m)	6
ϵ_p	0.5
τ	3
$\rho_{cap,p}$ (kg/m^3)	2600
$\rho_{cat,p}$ (kg/m^3)	2300
λ_p (W/(m K))	0.2
C_{ps} (J/(kg K))	1000

4.1. Assessing the Need for a Heterogeneous Model. Heterogeneous models or pseudo-homogeneous models including an efficiency factor are conventionally used to simulate the steam methane reforming. The sorption-enhanced process has been simulated with heterogeneous models to see if there were any significant intraparticular resistances. Two different ways of installing the CO_2-acceptor in the reactor are looked into: one particle with both catalytic and capture properties or two different types of particles with catalytic and capture properties. Figure 2 shows the dry hydrogen mole fraction as function of axial position at $t = 50$ s. Particles with diameters of 5 mm have been used, and the results from the heterogeneous simulations with one type of particle are about the same as those for the pseudo-homogeneous model; for the two-particle model, the results are different. With two particles, the CO_2 has to diffuse out of the catalytic particle, through the bulk phase, and into the acceptor particle, and according to the simulations, this is a limiting step in the process. With one particle, this is not a problem, since the CO_2 is captured in the same particle as it is produced. This is contrary to the results with Li_2ZrO_3 as acceptor, where no mass-transfer limitations were found for two particles.[3] A pseudo-homogeneous model with efficiency factors of 1 is used for simulating the fixed-bed reactor in the latter parts of this article; thus, one particle with both properties is assumed.
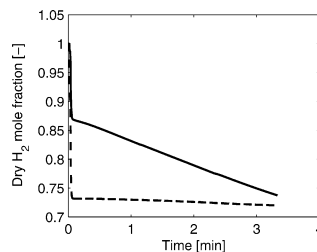
Figure 4. Dry hydrogen mole fraction at the outlet as function of time for Li_2ZrO_3 (− −) and Li_4SiO_4 (—), $P = 20$ bar, $T_f = 848$ K, S/C ratio = 5, $u_f = 1$ m/s.
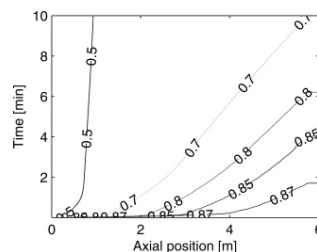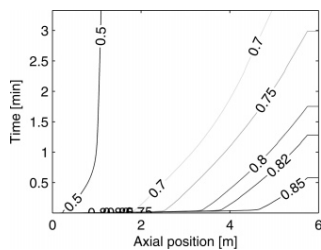

Figure 5. Contour plot of dry hydrogen mole fraction as function of time and axial position at an inlet mass flux of 2 kg/(m^2 s) with Li_4SiO_4 as acceptor, $P = 20$ bar, $T_f = 848$ K, S/C ratio = 5.

Earlier work on SE-SMR from our group has been with Li_2ZrO_3 as the CO_2-acceptor, and the results show that the kinetics of Li_2ZrO_3 are slow, particularly at low partial pressures of CO_2, which leads to low production capacities if a dry hydrogen fractions in the range 0.8−0.85 should be reached.[3] The kinetics of Li_4SiO_4 are faster, and this can be clearly observed in Figure 3, where the capture kinetics of both Li_2ZrO_3 and Li_4SiO_4 are shown as functions of partial pressure of CO_2.

Figure 4 shows the outlet dry hydrogen mole fraction as a function of time, and the large difference in performance with the two different acceptors is seen. A dry hydrogen mole fraction of 0.87 can be reached at the outlet of the reactor when Li_4SiO_4 is used as acceptor, compared to 0.75 for the Li_2ZrO_3. However, it is observed that a high purity of hydrogen can only be sustained for a short period of time in the case of Li_4SiO_4 as acceptor. This is due to the fact that the capture kinetics is decreasing with fractional conversion of the sorbent and the conversion of methane is not sustained when the kinetics is slower.

Figures 5 and 6 show contour plots for inlet mass fluxes of, respectively, 2 and 5 kg/(m^2 s), and it is observed that the maximum conversion is the same in both cases but that the conversion is sustained for a longer period for the lower throughput. The equilibrium dry hydrogen mole fraction with Li_4SiO_4 as acceptor is just below 0.88 at the working conditions, and as observed in Figures 4 and 6, the conversion is close to equilibrium at low fractional conversion of the acceptor.

Figure 7 shows the fractional conversion of sorbent as a function of time and space, and at a fractional conversion of 0.1, the kinetics has decreased in such a way that the conversion of CH_4 reached at the outlet of the reactor is lowered considerably. The capture kinetics is second order with respect

Figure 6. Contour plots of dry hydrogen mole fraction as function of time and axial position at an inlet mass flux of, $P = 20$ bar, $T_f = 848$ K, S/C ratio = 5.
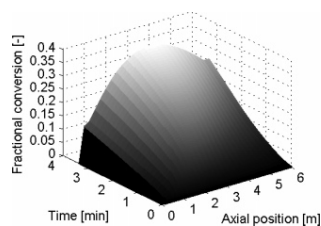
Figure 7. Fractional conversion of CO_2-acceptor as function of time and space, $P = 20$ bar, $T_f = 848$ K, S/C ratio = 5, $u_f = 1$ m/s.
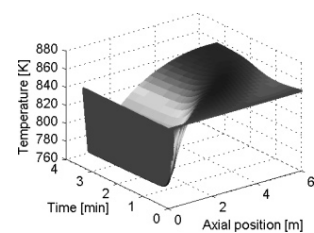
**Figure 8.** Reactor temperature as function of time and space with Li_4SiO_4 as CO_2-acceptor, $P = 20$ bar, $T_f = 848$ K, S/C ratio = 5, $u_f = 1$ m/s.

to fractional conversion and decreases rapidly as CO_2 reacts with the sorbent. Clearly, this is also the reason why the conversion is high for a longer period at lower gas throughput, where the sorbent is kept at lower fractional conversion for a longer period of time. Longer reactors and/or less gas throughput are necessary if the dry hydrogen fraction should be kept at a high level for longer periods in a fixed-bed reactor.

Figure 8 shows the temperature in the reactor as a function of time and space for a simulation of 200 s. It can be observed that the temperature in the reactor is dropping dramatically, especially near the inlet. A wall temperature of 848 K is used to heat the reactor, but that is not enough to attain the temperature at a constant level. The total enthalpy of reaction is positive for the process, and energy has to be supplied if the temperature in the reactor should be kept constant; this has to be done more efficiently than in the simulations.

4.2. Comparisons with Fluidized Bed. A possible alternative to the fixed-bed reactor is a fluidized-bed reactor. The fluidized bed offers some advantages in terms of heat integration and possibilities for continuous regeneration of the sorbent. Simulations of a bubbling-bed reactor have been carried out to compare some of the results to those of the fixed-bed reactor. The model used to simulate the fluidized-bed reactor is a rigorous 2-dimensional dynamic model based on granular theory described
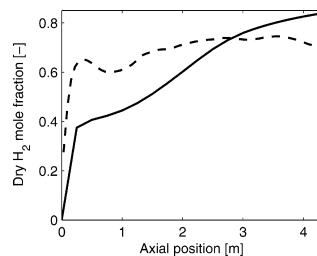
Figure 9. Comparison of dry hydrogen mole fraction as function of axial position between the fixed-bed reactor model (—) and fluidized bed reactor model (− −) with Li_4SiO_4 as acceptor at $t = 85$ s, adiabatic conditions, $P = 20$ bar, $T_f = 848$ K, S/C ratio = 5, $u_f = 0.4$ m/s.
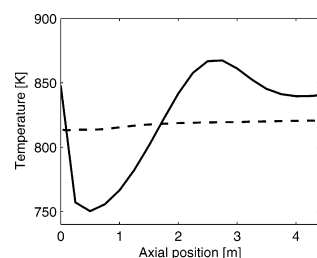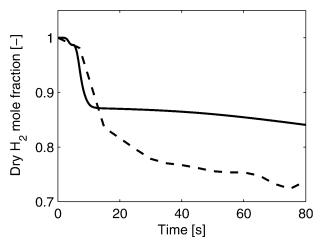

Figure 10. Comparison of temperature as function of axial position between the fixed-bed reactor model (—) and fluidized bed reactor model (− −) with Li_4SiO_4 as acceptor at $t = 85$ s, adiabatic conditions, $P = 20$ bar, $T_f = 848$ K, S/C ratio = 5, $u_f = 0.4$ m/s.

by Lindborg et al.[22] In Figure 9, the dry hydrogen mole fraction as a function of axial position is shown for a fixed-bed reactor and a fluidized-bed reactor. The reactor beds have equal length, and the reactors are operated adiabatically at the same operating conditions.

It is observed in Figure 9 that the conversion in the fixed-bed reactor is considerably higher than that for the fluidized-bed reactor at equal bed heights. This could result from several reasons: the bubbles in the fluidized-bed reactor give inferior contact between the gas phase and the particles, the fluidized-bed reactor has a higher void fraction that gives lower particle density, and the fluidized-bed reactor gives a lower outlet temperature. The difference in temperature profiles can be seen in Figure 10, and an almost constant temperature in the fluidized bed is observed. This could be an advantage compared to the fixed-bed reactor in terms of easier heat supply, but in these simulations, which are adiabatic, it leads to a lower outlet temperature. This results in a lower equilibrium conversion, and the importance of controlling the outlet temperature is seen.

The lower particle density in the fluidized bed does not have a large effect on the simulated composition. In the fluidized-bed reactor, an average void fraction of ~0.6 is observed, while the void fraction in the fixed-bed reactor is just above 0.4. A fixed-bed reactor with the same void fraction as the average void fraction in the fluidized bed was simulated to test for the effect of lower particle density. The results from these simulations are quite similar to the results from the lower void fraction. This is due to the fact that the actual local gas velocity is lowered when the void fraction is increased, which weighs up for the lowered total reaction rates due to lower particle density, and the conversion is not effected significantly.

Figure 11. Comparison of the outlet dry hydrogen mole fraction between the fixed-bed reactor model ($-$) and fluidized bed reactor model ($- -$) as a function of time with Li_4SiO_4 as acceptor at adiabatic conditions, $P = 20$ bar, $T_f = 848$ K, S/C ratio = 5, $u_f = 0.4$ m/s.
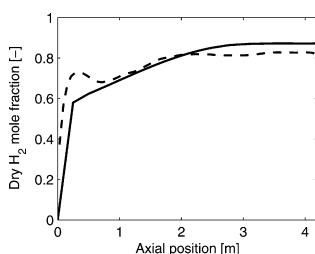
Figure 12. Comparison of the outlet dry hydrogen mole fraction between the fixed-bed reactor model ($-$) and fluidized bed reactor model ($- -$) as a function of time with Li_4SiO_4 as acceptor at $t = 85$ s, isothermal conditions, $P = 20$ bar, $T_f = 848$ K, S/C ratio = 5, $u_f = 0.4$ m/s.

In Figure 11, the outlet dry hydrogen mole fraction as a function of time is shown, and the conversion is consistently lower in the fluidized-bed reactor for the already listed reasons.

Isothermal simulations for the two reactor concepts were also carried out. This was done to see if the lower conversion was solely due to the lower outlet temperature or if there is a combination of mechanisms. Figure 12 shows the dry hydrogen mole fractions in the reactors at isothermal conditions. Here, it is observed that the conversion in the fluidized-bed reactor also is lower for the isothermal case. This means that the inferior gas-particle contact in the fluidized bed gives a significant decrease in the reactor performance. In a reactor design, this means that, even if the heat integration is in such an efficient manner that the reactor is close to isothermal, a longer fluidized-bed reactor is needed to reach comparable conversions with the fixed-bed reactor. To reach more definite conclusions in the comparison between the reactor concepts, the regeneration of the sorbent also has to be looked into, and this work is in progress.

5. Conclusions

The simulations performed show that hydrogen with a purity of 0.87 can be produced at a temperature of 848 K, a steam-to-carbon ratio of 5, and a pressure of 20 bar with Li_4SiO_4 as CO_2-acceptor. This is a significant improvement compared to the process with Li_2ZrO_3 as CO_2-acceptor. The capture rate decreases with fractional conversion of the sorbent, and high conversion of CH_4 cannot be sustained for more than a couple of minutes with high gas throughput in the reactor. Simulations also show that, if one type of particle with both catalytic and capture properties is used, the capture rate is the limiting step

of the process. This changes when two particles are used, where some intraparticular diffusion resistance occurs. This yields a particle diameter of 5 mm.

Energy needs to be supplied to the reactor, and a wall temperature of 848 K is not sufficient to keep the temperature from dropping dramatically. To attain the temperature in the reactor, better heating or another reactor concept is needed. A fluidized-bed reactor is an alternative for this process, presenting the mentioned advantages. The large temperature gradients will be smaller, and heat can be added to the reactor by recirculating the particles. The simulations also show that, for larger production capacities, the cycling times for the fixed-bed reactor will be very short, a problem that will vanish when using a fluidized-bed reactor with continuous regeneration of particles. The simulations on a fluidized-bed reactor show that a longer reactor bed is needed to reach satisfying conversions compared to a fixed-bed reactor. In the simulations, the lower conversion in the fluidized bed is because of the lower outlet temperature and because of inferior gas-particle contact due to gas bubbles.

Notation

Roman Symbols

a_v = surface area of particles (1/m)
C = concentration (mol/m^3)
C_p = heat capacity (J/(mol K))
d = diameter (m)
d_t = diameter of reactor tube (m)
D = dispersion factor or diffusivity (m^2/s)
E = Arrhenius activation energy (J/mol)
f = friction factor
h = bulk$-$particle heat transfer coefficient (W/(m K))
$-\Delta H$ = heat of reaction (J/kg)
J = mass flux vector (kg/m^2)
k = mass-transfer coefficient (m/s)
K = constant in capture kinetics (1/s)
L = length of reactor (m)
$\dot{m}$ = mass flux (kg/(m^2 s))
n = constant in capture kinetics
p = pressure (Pa)
q = mass of CO_2 per mass of acceptor
r = radius (m), or reaction rate of components (kg/(kg s))
R = reaction rate (kg/(m^3 s)), or gas constant (J/(K mol))
S = component mass source term (kg/(m^3 s))
S' = heat source term (J/(m^3 s))
t = time (s)
T = temperature (K)
u = superficial space velocity (m/s)
x = fractional conversion
y = mole fraction
z = axial position (m)

Greek Symbols

α = ratio between volumes of acceptor and catalyst
ϵ = void fraction
λ = conductivity (J/(m s))
μ = viscosity (Pa s)
ρ = density (kg/m^3)
τ = tortuosity
ω = mass fraction

Subscripts

b = bed
cap = capture, CO_2-acceptor

185

cat = catalyst
eq = equilibrium
f = feed
g = gas
i = component i
m = molar
max = maximum
p = particle
s = solid
w = wall
z = axial direction

Superscripts

d = dry
s = surface

Literature Cited

(1) Kato, M.; Nakagawa, K. New series of lithium containing complex oxides, lithium silicates, for application as a high temperature CO_2 absorbent. *J. Ceram. Soc. Jpn.* **2001**, *109*, 911.

(2) Ida, J.; Lin, Y. S. Mechanism of high-temperature CO_2 sorption on lithium zirconate. *Environ. Sci. Technol.* **2003**, *37*, 1999.

(3) Rusten, H. K.; Ochoa-Fernàndez, E.; Chen, D.; Jakobsen, H. A. Numerical investigation of sorption enhanced steam methane reforming using Li_2ZrO_3 as CO_2-acceptor. *Ind. Eng. Chem. Res.* **2007**, *46*, 4435.

(4) Johnsen, K.; Grace, J.; Elnashaie, S.; Kolbeinsen, L.; Eriksen, D. Modeling of sorption-enhanced steam reforming in a dual fluidized bubbling bed reactor. *Ind. Eng. Chem. Res.* **2006**, *45*, 4133.

(5) Xiu, G.-h.; Li, P.; Rodrigues, A. E. Sorption-enhanced reaction process with intraparticle-diffusion limitations. *Chem. Eng. J.* **2003**, *95*, 83.

(6) Kato, M.; Yoshikawa, S.; Nakagawa, K. Carbon dioxide absorption by lithium orthosilicate in a wide range of temperature and carbon dioxide concentrations. *J. Mater. Sci. Lett.* **2002**, *21*, 485.

(7) Ochoa-Fernández, E.; Haugen, G.; Zhao, T.; Rønning, M.; Aartun, I.; Børresen, B.; Rytter, E.; Rønnekleiv, M.; Chen, D. Evaluation of potential CO_2 acceptors for application in hydrogen production by sorption enhanced steam reforming. *Am. Chem. Soc., Div. Fuel Chem.* **2006**, *51*, 598.

(8) Gomez-Barea, A.; Ollero, P. An approximate method for solving gas-solid non-catalytic reactions. *Chem. Eng. Sci.* **2006**, *61*, 3725.

(9) Szekely, J.; Evans, J. W.; Sohn, H. Y. *Gas-solid reactions*; Academic Press: New York, 1976.

(10) Bhatia, S. K.; Perlmutter, D. D. A random pore model for fluid-solid reactions. i. isothermal, kinetic control. *AIChE J.* **1980**, *26*, 379.

(11) Shieh, M. D.; Lee, C. A more general structural model which includes the induction time for gas-solid reactions. I. Nonporous solids. *Chem. Eng. Sci.* **1992**, *47*, 4017.

(12) Lee, D. K. An apparent kinetic model for the carbonation of calcium oxide by carbon dioxide. *Chem. Eng. J.* **2004**, *100*, 71.

(13) Xu, J.; Froment, G. F. Methane steam reforming, methanation and water-gas shift: I. Intrinsic kinetics. *AIChE J.* **1989**, *35*, 88.

(14) Edwards, M. F.; Richardson, J. Gas dispersion in packed beds. *Chem. Eng. Sci.* **1968**, *23*, 109.

(15) Bird, R. B.; Stewart, W. E.; Lightfoot, E. N. *Transport Phenomena*; Wiley: New York, 1960.

(16) Poling, B. E.; Prausnitz, J. M.; O'Connell, J. P. *The Properties of Gases and Liquids, fifth edition*; McGraw-Hill: New York, 2001.

(17) Wakao, N.; Funazkri, T. Effect of fluid dispersion coefficients on particle-to-fluid mass transfer coefficients in packed beds. Correlation of Sherwood numbers. *Chem. Eng. Sci.* **1978**, *33*, 1375.

(18) Yagi, S.; Kunii, D.; Wakao, N. Effective thermal conductivities in packed beds. *AIChE J.* **1960**, *6*, 543.

(19) Bird, R. B.; Stewart, W. E.; Lightfoot, E. N. *Transport Phenomena, 2nd edition*; Wiley: New York, 2002.

(20) Jakobsen, H. A.; Lindborg, H.; Handeland, V. A numerical study of the interactions between viscous flow, transport and kinetics in fixed bed reactors. *Comput. Chem. Eng.* **2002**, *26*, 333.

(21) Hicks, R. E. Pressure drop in packed beds of spheres. *Ind. Eng. Chem. Fundam.* **1970**, *9*, 500.

(22) Lindborg, H.; Lysberg, M.; Jakobsen, H. Practical validation of the two-fluid model applied to dense gas-solid flows in fluidized beds. *Chem. Eng. Sci.* **2007**, *62*, 5854.